# Electronic Structure/function Relationship in Metal Ligand Multiple Bonds for C-H Functionalization Chemistry

Dissertation Advisor: Professor Theodore A. Betley Matthew John Taylor Wilding

**Electronic structure/function relationship in metal ligand multiple bonds for C-H functionalization chemistry**

## Abstract

The factors that enable intermolecular C–H amination by iron complexes supported by dipyrromethene ligands ($^{R}$L, L=1,9-R$_2$-5-mesityldipyrromethene R = 2,4,6-Ph$_3$C$_6$H$_2$ (Ar), Ad) were investigated. Despite the diversity of characterized iron imide complexes ($Fe^{II}$, $S = 0$; $Fe^{III}$, $S = {}^1/_2, 1, {}^3/_2$; $Fe^{IV}$, $S = 0, 1$; $Fe^{V}$, $S = {}^1/_2$), group transfer reactivity by these molecules into unactivated C–H bonds is unique to the dipyrrin supported complex ($^{Ar}$L)FeCl(NC$_6$H$_4$$^{t}$Bu), which consists of a high-spin ($S = {}^5/_2$) $Fe^{III}$ center antiferromagnetically coupled to an imido-centered radical ($Fe^{III}$–$^{\bullet}$NR). However, the complex electronic structure complicates analysis of the salient features of the electronic structure that enable such unprecedented chemistry.

Therefore, a family of dipyrrin-supported iron imide complexes that do not possess *N*-radical character were synthesized. Extensive spectroscopy and magnetic characterization support a view of these complexes as the first crystallographically characterized $S = {}^5/_2$ $Fe^{III}$ imide complexes ($Fe^{III}$=NR). The unprecendented electronic structure supports the first examples of intermolecular C–H amination from isolated $Fe^{III}$ imides and indicates that the presence of a high-spin metal-ligand multiple bond is sufficient to engender the desired C–H functionalization chemistry.

The redox relationship between the $Fe^{III}$–$^{\bullet}$NR and $Fe^{III}$=NR electronic structure was exploited to prepare an $Fe^{III}$ (alkyl)iminyl complex, the direct analogue to the intermediate formed during the catalytic C–H amination chemistry reported previously by our group. X-ray absorption

spectroscopy demonstrates a constant iron oxidation upon redox, suggesting *N*-atom valence chemistry at the transferrable imide moiety. Kinetic analysis implies that oxidation to the $Fe^{III}$–$^{\bullet}NR$ lowers the enthalpic barrier to C–H functionalization which contributes to a 1,000-fold increase in reactivity towards C–H bonds.

Finally, these studies lead to the development of a new generation of dipyrrin-supported iron catalysts for the intramolecular cyclization of alkyl azides into *N*-Boc-pyrrolidines that can function at 0.01 mol % catalyst loading – a decrease in loading by three-orders of magnitude as compared to our previous catalytic system. These catalysts manifest high tolerance to Lewis bases, and have enabled the cyclization of a new class of substrates featuring activation by a variety of heteroatom-containing functional groups.

# Table of Contents

# Acknowledgements

A list of every person who has helped to bring this dissertation to fruition would be too long and somehow still not exhaustive. In brief, I would like to thank my labmates over my five years in the group; my friends throughout the Chemistry departments of Harvard, MIT, Boston College, and Brandeis; and my family, specifically Ashley Biernesser. The degree program has been a cruicual formative experience and I am so grateful to have been provided the opportunity.

# List of Schemes

# List of Figures

# List of Tables

# List of Chemical Abbreviations

| | |
|---|---|
| ACN | acetonitrile |
| Ad or $^{1}$Ad | 1-adamantyl |
| Ar | 2,4,6-triphenylphenyl |
| Boc | tert-butylcarbamate |
| Bn | benzyl |
| bpy | 2,2'-bipyridine |
| CHD | cyclohexadiene |
| Cp | cyclopentadienyl |
| Cy | cyclohexyl |
| CyPhos | 2-dicyclohexylphosphinobiphenyl |
| dba | dibenzylideneacetone |
| DCM | dichloromethane |
| DDQ | 2,3-dichoro-5,6-dicyano-1,4-benzoquinone |
| dipp | 2,6-diisopropylphenyl |
| dpma | dipyrromethane |
| dpme | dipyrromethene or dipyrrin |
| Et | ethyl |
| $Et_2O$ | diethylether |
| Fc | ferrocene |
| $Fc^{+}$ | ferrocenium |
| $^{i}$Pr or iPr | isopropyl |
| L | ligand |
| Me | methyl |
| Mes | mesityl or 2,4,6-trimethylphenyl |
| OTf | trifluoromethylsulfonate or triflate |
| PDI | pyridine diimine, 2,6-bis[1-(2,6-diisopropylphenylimino)ethyl]pyridine |
| Ph | phenyl |
| OPh | phenoxide |
| PPTS | pyridinium *para*-toluenesulfonate |
| py | pyridine |
| SPhos | 2-dicyclohexylphosphino-2',6'-dimethoxybiphenyl |
| TBA | tetrabutylammonium |
| $^{t}$Bu or tBu | *tert*-butyl |
| TFA | trifluoroacetic acid |
| thf or THF | tetrahydrofuran |
| TMS | trimethylsilyl |
| tol | toluene |
| Ts | *para*-toluenesulfonyl or tosyl |

# List of Acronyms, Symbols, and Units

| | |
|---|---|
| $^{\bullet}$ | radical |
| $\{^1H\}$ | proton decoupled |
| $^{13}C$ | carbon-13 |
| $^1H$ | proton |
| Å | angstrom, $10^{-10}$ meters |
| avg | average |
| br | broad |
| CHN% | combustion or elemental analysis percentages for carbon, hydrogen, and nitrogen |
| $cm^{-1}$ | wavenumbers or inverse centimeters |
| CV | cyclic voltammetry or cyclic voltammogram |
| *D* | axial zero field splitting parameter |
| d | doublet in NMR |
| D or $^2H$ | deuterium |
| d.r. | diasteromeric ratio |
| dc | direct current |
| $d_n$ | deuterated (*n* is the number of positions where $^2H$ replaces $^1H$) |
| DPV | differential pulse voltammetry or differential pulse voltammogram |
| *e* | elementary charge, charge of a single proton or electron, $1.602 \times 10^{-19}$ coulombs |
| *E* | rhombic zero field splitting parameter |
| $e^-$ | electron |
| EPR | electron paramagnetic resonance |
| $ESI^+$ | positive ion electron spray ionization |
| G | gauss |
| *g* | Landé g-factor (but may also refer to the anomalous gyromagnetic ratio, 2.0023) |
| GHz | gigahertz, $10^9$ Hertz or $10^9$ $s^{-1}$ |
| ***H*** | Hamiltonian operator |
| *H* | magnetic field |
| HAT | hydrogen atom transfer |
| HOMO | highest occupied molecular orbital |
| *I* | current in microamperes |
| IR | infrared spectroscopy (NIR denotes near infrared spectroscopy) |
| *J* | coupling constant |
| *k* | Boltzmann constant, 0.695 $cm^{-1}/K$ |
| K | kelvin |
| KIE | kinetic isotope effect |
| LC/MS | liquid chromatography/mass spectrometry |
| LUMO | lowest unoccupied molecular orbital |
| M | molar, moles per liter |
| m | multiplet in NMR |
| *m*- | *meta* position on an aryl ring, indicating a 1,3 relationship |
| *m*/*z* | mass to charge ratio |
| MHz | megahertz, $10^6$ Hertz or $10^6$ $s^{-1}$ |

| | |
|---|---|
| MLMB | metal-ligand multiple bond |
| mmol | millimole, $10^{-3}$ moles |
| MO | molecular orbital |
| mV | millivolt, $10^{-3}$ volts |
| $N$ | Avogadro constant, $6.022 \times 10^{23}$ mol$^{-1}$ |
| nm | nanometer, $10^{-9}$ meters |
| NMR | nuclear magnetic resonance |
| *o*- | *ortho* position on an aryl ring, indicating a 1,2 relationship |
| Oe | oersted |
| *p*- | *para* position on an aryl ring, indicating a 1,4 relationship |
| ppm | parts per million |
| q | quartet in NMR |
| rt | room temperature |
| s | singlet in NMR or second |
| $S$ | spin |
| $\boldsymbol{S}$ | spin operator |
| sh | shoulder |
| SOMO | singly-occupied molecular orbital |
| SQUID | superconducting quantum interference device |
| T | tesla |
| t | triplet in NMR |
| $T$ or T | temperature |
| TS | transition state |
| UV/Vis | ultraviolet-visible absorption spectroscopy |
| $V$ | potential in mV or V |
| V | volt |
| *w/w* | mass fraction or percentage weight solute per weight solution |
| $\delta$ | delta, chemical shift in ppm |
| $\delta$ | isomer shift for $^{57}$Fe Mössbauer in mm/s |
| $\Delta E_Q$ | quadrupole splitting for $^{57}$Fe Mössbauer in mm/s |
| $\Delta H$ | enthalpy |
| $\varepsilon$ | epsilon, extinction coefficient or molar absorptivity in $M^{-1}cm^{-1}$ |
| $\eta^n$ | eta, hapticity or the number, n, of contiguous atoms in a ligand bound to a metal |
| $\kappa^n$ | kappa, denticity or the number, *n*, of atoms in a polydentate ligand bound to the metal |
| $\lambda$ | lambda, wavelength in nm |
| $\mu$A | microampere, $10^{-6}$ ampere |
| $\mu_B$ | Bohr magneton, $9.274 \times 10^{-21}$ erg/G |
| $\mu_{eff}$ | mu effective, effective magnetic moment in Bohr magnetons |
| $\nu$ | frequency |
| $\chi$ | magnetic susceptibility |
| $\chi_M$ or $\chi_m$ | molar magnetic susceptibility in cm$^3$/mol |

# Chapter 1: The Electronic Structure-Function Relationship

## 1.1 Introduction

Greater than 90 % of organic materials produced by chemical industry are derived from petroleum (crude oil) or natural gas sources.[1] Direct conversion of these primarily hydrocarbon feedstocks into value-added products is challenging due to the relative chemical inertness of aliphatic C–H bonds, which have bond dissociation energies of 95 to 105 kcal/mol.[2] Overcoming this inherent stability is key to utilizing these commodities as chemical synthons, and current industrial processes to do so consume greater than one-third of the total U.S. delivered energy consumption.[3] Therefore, a practical methodology for the direct and atom-economic construction of carbon-heteroatom bonds from unactivated C–H bonds would greatly impact the broader landscape of energy consumption in chemical industry.

The field of organometallic chemistry has sought to lower the barrier to achieve C–H functionalization by utilizing transition metals to affect reactive intermediates along the reaction trajectory.[4] The nature of interaction between metal ion and reactive intermediate dictates the mechanism of bond activation and provides a means of classification for systems that are active for transition metal-mediated C–H functionalization. Oxidative addition of the carbon-hydrogen bond to a low-valent metal center, electrophilic substitution (with concomitant loss of a proton), and σ- bond metathesis all yield species containing a metal-carbon σ-bond, which can then be

1. Heaton, C. A. *An Introduction to Industrial Chemistry*; Springer Science & Business Media, **2012**.
2. Luo, Y.-R. Handbook of Bond Dissociation Energies in Organic Compounds; CRC Press, **2002**.
3. Department of Energy, *Annual Energy Outlook 2015*; Washington D.C., **2015**.
4. Hartwig, J. F. Organotransition Metal Chemistry: From Bonding to Catalysis; University Science Books, **2010**.

**Scheme 1.1** Modes of C–H bond activation commonly utilized in transition metal catalysis.

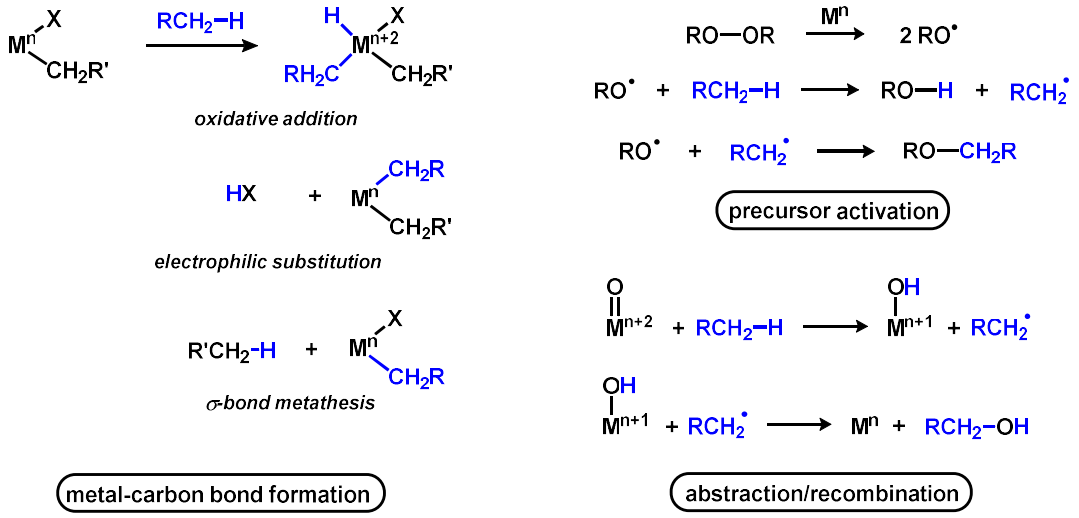


used as a synthetic intermediate for further functionalization (). While this methodology for C–H activation has been demonstrated to be effective for aromatic C–H bond functionalization, it has been much less productive for aliphatic C–H bonds due to the poor spatial and energetic accessibility of the C–H bonding and antibonding orbitals.

The challenges associated with forming a discrete metal-carbon bonding interaction can be circumvented by instead utilizing a transition metal ion to catalyze an orthogonal reaction that subsequently effects C–H functionalization (, top right). In this process, the redox activity and Lewis acidity of the metal ion facilitates the decomposition of high-potential energy precursors into species that are competent for activation of the C–H bond donor, most commonly via hydrogen atom abstraction or direct C–H insertion.[5] As the metal does not directly interact with the C–H bond substrate, reactions employing this methodology often manifest non-productive

5. (a) Wiese, S.; Badiei, Y. M.; Gephart, R. T.; Mossin, S.; Varonka, M. S.; Melzer, M. M.; Meyer, K.; Cundari, T. R.; Warren, T. H. *Angew. Chem. Int. Ed. Engl.* **2010**, *49*, 8850–8855. (b) Jang, E. S.; McMullin, C. L.; Käß, M.; Meyer, K.; Cundari, T. R.; Warren, T. H. *J. Am. Chem. Soc.* **2014**, *136*, 10930–10940. (c) Chen, M. S.; White, M. C. *Science* **2010**, *327*, 566–571. (d) White, M. C. *Science* **2012**, *335*, 807–809.

**Scheme 1.2** Mechanism of C–H hydroxylation by cytochrome $P_{450}$ via generation of a high-valent iron oxo intermediate termed *compound I*, hydrogen atom abstraction from substrate, and radical recombination.

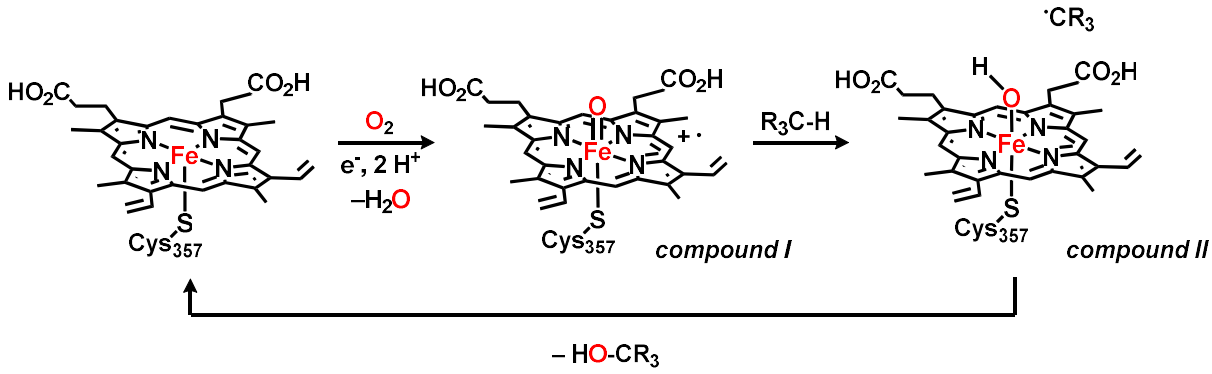


radical homocoupling and are difficult to tune for chemo- and regioselectivity. As such, current pathways for aliphatic C–H functionalization require directing groups, strong chemical oxidants, or preoxidation of substrate to manifest productive reactivity.[6] Despite these challenges, the enzyme cytochrome P450 activates strong C–H bonds under physiological physiological conditions utilizing a distinct mechanistic approach ().[7] A high-valent iron-oxo intermediate is generated upon reaction of the heme iron active site with molecular oxygen. A powerful oxidizing intermediate (compound I, ) possesses two electrons residing in Fe–O π* orbitals, which serves to both weaken and induce radical character within the Fe–O bond. By activating substrates along this metal-ligand multiple bond vector, cytochrome P450 circumvents the difficult aliphatic oxidative addition in favor of a hydrogen atom abstraction pathway. Subsequent radical recombination of the resulting iron-hydroxide with the newly formed substrate radical furnishes the hydroxylated product under mild conditions and in a controlled manner. Direct insertion of the oxo into the C–H bond donor via a concerted process can also occur.

6. (a) Labinger, J. A.; Bercaw, J. E. *Nature* **2002**, *417*, 507–514. (b) Dick, A. R.; Sanford, M. S. *Tetrahedron* **2006**, *62*, 2439–2463. (c) Zalatan, D. N.; Bois, J. Du. Yu, J.-Q.; Shi, Z., Eds.; Springer Berlin Heidelberg: Berlin, Heidelberg, **2010**; 347–378. (d) Ryabov, A. D. *Chem. Rev.* **1990**, *90*, 403–424.
7. (a) Ortiz de Montellano, P. R. Kluwer Academic/Plenum Publishers: New York, **2005**. (b) Rittle, J.; Green, M. T. *Science* **2010**, *330*, 933–937. (c) Green, M. T. *Curr. Opin. Chem. Biol.* **2009**, *13*, 84–88. (d) Green, M. T.; Dawson, J. H.; Gray, H. B. *Science* **2004**, *304*, 1653–1656. (e) Fujii, H. *Coord. Chem. Rev.* **2002**, *226*, 51–60.

Inspired by the precedent of hydroxylation by cytochrome P450, metal-ligand multiple bonds have been implicated as intermediates in a variety of transformations, both biologically[8] and abiologically.[9] The structure-function relationship linking the presence of a metal-ligand multiple bond to productive C–H functionalization chemistry has thus prompted significant efforts to prepare synthetic systems supporting metal-ligand multiple bonds and exhibiting the desired chemistry. Mononuclear, terminal iron oxo and imido complexes were thus targeted as potential group transfer reagents for the functionalization of C–H bonds. However, direct C–H functionalization has been observed for only two isolated iron oxo compounds and not observed for any isolated iron imido compound.

An analysis of the body of work comprising synthetic iron -oxo and -imido complexes highlights the importance of an electronic structure-function relationship in metal-ligand multiple bonds for C–H functionalization and provides a rationalization for the lack of desired reactivity that has been observed. The exact properties of compound I () that leads to the desired hydroxylation reactivity observed for cytochrome P450 have not been systemactially studied in a synthetic system to date.

8. Solomon, E. I.; Brunold, T. C.; Davis, M. I.; Kemsley, J. N.; Lee, S.-K.; Lehnert, N.; Neese, F.; Skulan, A. J.; Yang, Y.-S.; Zhou, J. *Chem. Rev.* **2000**, *100*, 235–350.
9. (a) Mehn, M. P.; Peters, J. C. *J. Inorg. Biochem.* **2006**, *100*, 634–643. (b) Bess, E. N.; Deluca, R. J.; Tindall, D. J.; Oderinde, M. S.; Roizen, J. L.; Du Bois, J.; Sigman, M. S. *J. Am. Chem. Soc.* **2014**, *136*, 5783–5789. (c) Liu, W.; Groves, J. T. *J. Am. Chem. Soc.* **2010**, *132*, 12847–12849.

## 1.2 Synthetic Iron Oxos

Initially, iron oxo compounds were targeted to repliacate the oxo-transfer chemistry exhibited by compound I (). The first spectroscopically characterized iron-oxo complex was prepared by Groves *et al*. via treatment of $Fe^{III}$(TMP)Cl (TMP = *meso*-tetramesitylporphyrin) with *m*-chloroperbenzoic acid at –78 °C.[10] Since then, numerous examples of porphyrin-supported iron-oxo complexes have been reported[11] and have been implicated as intermediates in the oxygenation of strong C–H bonds.[12] Porphyrin ligands possess a distinctive visible spectrum arising from $\pi \rightarrow \pi^*$ transitions that are sensitive to the nature of the coordinated metal ion, making their complexes amenable to characterization with UV/visible spectroscopy.[13] The porphyrin ligand is redox active and able to relieve oxidative strain at the metal center while still maintaining a high overall molecular oxidation state. Further, despite their anionic nature, porphyrins are relatively weak σ- and π-donating ligands (as the nitrogen atom lone pairs are engaged in π-bonding throughout the ligand backbone and not available for donation to the metal center) which support open-shell electronic configurations at the transition metal ion.[14] For example, the Groves porphyrin iron-oxo displays a solution magnetic moment that is most consistent with an $S = {}^3/_2$ spin state, the maximum spin state possible for the formally $Fe^V$ species. This electronic structure places radical density in the iron-oxygen antibonding orbitals, weakening the bond and engendering the desired reactivity.

The utility of porphyrin ligands has inspired significant efforts towards the isolation and characterization of highly reactive porphyrin iron-oxo species. However, none have been

10. Groves, J. T.; Nemo, T. E.; Myers, R. S. *J. Am. Chem. Soc.* **1979**, *101*, 1032–1033.
11. Fujii, H. *Coord. Chem. Rev.* **2002**, *226*, 51–60 and references therein.
12. Groves, J. T. *J. Inorg. Biochem.* **2006**, *100*, 434–447 and references therein.
13. Lippard, S. J.; Berg, J. M. *Principles of Bioinorganic Chemistry*; University Science Books, 1994.
14. Solomon, E. I.; Lever, A. B. P. Inorganic Electronic Structure and Spectroscopy: Applications and Case Studies; 2nd ed.; Wiley, **2006**.

crystallographically characterized, likely due to their thermal sensitivity. This thermal instability can be overcome by utilizing non-porphyrin ligands to support the iron-oxo moiety, although identification and spectral characterization becomes more challenging in the absence of the porphyrin chromophore. In fact, the first high-resolution crystal structure of an isolable iron-oxo complex,[15] obtained from the reaction of $[(TMC)(ACN)Fe^{IV}(O)][CF_3SO_3]_2$ (TMC = 1,4,8,11-tetramethyl-1,4,8,11-tetraazacyclotetradecane) and iodosobenzene at –40 °C, was not reported until 2003, more than 20 years after the initial work by Groves.

The solid state structure reveals the tetradentate TMC ligand and an exogenous acetonitrile molecule bound *trans* to an Fe–O moiety, yielding an overall distorted octahedral symmetry at the metal center. This molecular geometry causes a significant energetic splitting of the primarily metal-based frontier molecular orbitals such that the mean pairing energy of the *d*-electrons is significantly lower than the energetic penalty incurred upon population of these high-lying anti-bonding orbitals. The substantial ligand field, coupled with the short Fe–O bond distance of 1.646

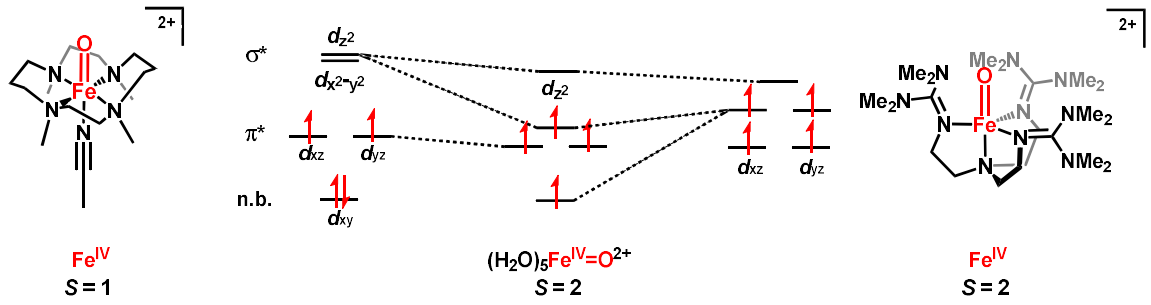


**Figure 1.1** Frontier molecular orbital diagram for selected iron oxo complexes. Substitution of more weakly donating aquo-ligands for the nitrogenous ligands of $[(TMC)(ACN)Fe^{IV}(O)][CF_3SO_3]_2$ lowers the energy of the $d_{x2-y2}$ orbital sufficiently that the mean spin pairing energy can be overcome to provide a high-spin complex. Removal of an axial ligand from the pseudo-octahedral geometry corresponding to the trigonal bipyramidal geometry of the tris(guanidine)amine-supported iron oxo complex on the right destabilizes the $d_{xy}$, again promoting the formation of a high spin complex. Despite their high-spin electronic configuration, these complexes are not reactive for C–H hydroxylation, likely a result of either the sterically-demanding nature of the supporting ancillary ligands or their high instability, as in the case of cationic penta(aqua) iron(IV) oxo.

15. Rohde, J.-U.; In, J.-H.; Lim, M. H.; Brennessel, W. W.; Bukowski, M. R.; Stubna, A.; Münck, E.; Nam, W.; Que, L. *Science* **2003**, *299*, 1037–1039.

Å which symmetrically destabilizes the $d_{xz}$ and $d_{yz}$ orbitals with respect to the nonbonding $d_{xy}$ orbital, leads to an observed $S = 1$ ground state for the $d^4$ metal ion (**Figure 1.1**). This analysis was validated via magnetic circular dichroism spectroscopy, $^{57}$Fe Mössbauer spectroscopy, and electron paramagnetic resonance measurements, which confirm the $S = 1$ configuration of iron in $[(TMC)(ACN)Fe^{IV}(O)][CF_3SO_3]_2$. A combination of the intermdiate-spin electronic state and bulky TMC ligand necessary for thermal stability leads to an iron-oxo complex that is competent for the oxidation of triphenylphosphine but exhibits no activity towards C–H bond donors.

Substitution for the tetrapyridine-based ligand *N*,*N*-bis(2-pyridylmethyl)-bis(2-pyridyl)methylamine ($N_4$py) enabled crystallographic characterization of a similar $S = 1$ iron oxo complex;[16] however, this species manifests hydroxylation reactivity of unactivated aliphatic C–H bonds with substrates as inert as cyclohexane.[17] As both $[(TMC)(ACN)Fe^{IV}(O)][CF_3SO_3]_2$ and $[(N_4py)(ACN)Fe^{IV}(O)][CF_3SO_3]_2$ share common spin states ($S = 1$), molecular geometries, and frontier molecular orbital diagrams, the difference in reactivity has been attributed to the presence of low-lying excited states during the C-H hydroxylation reaction trajectory,[18] demonstrating that ground state electronic considerations can be insufficient to fully describe the reactivity of a system. Nevertheless, this example suggests that accessing higher spin states, even transiently, may lead to enhanced reactivity towards C-H functionalization.

The significant energetic splitting of the frontier molecular orbitals manifest in $[(TMC)(ACN)Fe^{IV}(O)][CF_3SO_3]_2$ is challenging to overcome in an octahedral molecular geometry. A number of octahedral iron-oxo complexes have been characterized to date. Among

16. Klinker, E. J.; Kaizer, J.; Brennessel, W. W.; Woodrum, N. L.; Cramer, C. J.; Que, L. *Angew. Chem. Int. Ed. Engl.* **2005**, *44*, 3690–3694.
17. Kaizer, J.; Klinker, E. J.; Oh, N. Y.; Rohde, J. U.; Song, W. J.; Stubna, A.; Kim, J.; Münck, E.; Nam, W.; Que Jr., L. *J. Am. Chem. Soc.* **2004**, *126*, 472–473.
18. Kumar, D.; Hirao, H.; Que Jr., L.; Shaik, S. *J. Am. Chem. Soc.* **2005**, *127*, 8026–8027.

these, only $[(H_2O)_5Fe^{IV}(O)]^{2+}$ possesses an $S = 2$ molecular spin state, although assignment of the electronic structure is significantly complicated by the short half-life of the molecule ($t_{1/2}$ = 10 sec. at 25 °C) and inability to lower the requisite aqueous solution of precursors below 0 °C, causing significant (> 40 %) amounts of an impurity that cannot be separated.[19] As compared to the nitrogen-based TMC ligand, the weaker donor strength of the supporting aqua ligands decreases the splitting of the frontier orbitals. The orbital energetic separation decreases below the mean spin pairing energy, leading to a high-spin configuration at the metal center.

An alternative strategy for engendering high-spin electronic structures can be realized by altering the coordination geometry of the complex in an effort to tune the overlap between the metal-based *d*-orbitals and ancillary ligands such that metal-ligand bonding becomes more equitable and no single *d*-orbital is maximally destabilized.[20] By modifying the ligand framework to support a trigonal bipyramidal (TBP) geometry in the corresponding iron-oxo compound, the Que group has prepared a crystallographically-characterized iron oxo complex in a high-spin ($S = 2$) molecular spin state.[21] To counter the decrease in steric shielding that occurs upon moving from octahedral to TBP geometry (associated with removal of an axial ligand), the tris(guanidine)amine ligand employed features very sterically demanding substituents in the primary coordination sphere. The steric shielding imparts significant thermal stability, although it prevents substrate access to the iron oxo moiety and precludes intermolecular C–H functionalization reactivity. Substitution with a bis(guanidine)amine ligand allowed the preparation of an analogous iron oxo compound with less steric shielding at the iron center that

19. Pestovsky, O.; Stoian, S.; Bominaar, E. L.; Shan, X. P.; Münck, E.; Que Jr., L.; Bakac, A. *Angew. Chemie-International Ed.* **2005**, *44*, 6871–6874.
20. Betley, T. A.; Wu, Q.; Van Voorhis, T.; Nocera, D. G. *Inorg. Chem.* **2008**, *47*, 1849–1861.
21. England, J.; Guo, Y. S.; Farquhar, E. R.; Young, V. G.; Münck, E.; Que Jr., L. *J. Am. Chem. Soc.* **2010**, *132*, 8635–8644.

demonstrates enhanced rates for C–H abstraction chemistry, although no C–H functionalization was observed.[22] In line with this observation, a less sterically-demanding tris(benzimidazole)amine ligand was utilized to generate a transient iron oxo complex that is competent for hydroxylation of strong C–H bonds at room temperature via a low lying excited state; however, this species, as well as any other TBP $S = 2$ iron oxo complexes, has yet to be structurally characterized.[23]

In the absence of sterically demanding ancillary ligands, coordination to the oxygen rather than the iron atom may be exploited to provide both an electronic and steric stabilization to the reactive fragment and facilitate isolation. Work by Borovik,[24] Chang,[25] and Que[26] have utilized protons, alkali metals, and rare earth elements, respectively, to promote formation/stabilization of a high-valent iron oxo moiety. Even if an interaction between Lewis acidic additives and the iron oxo complex is not evident in the solid state molecular structures, potential interactions during synthesis cannot be excluded as the addition of Lewis acids has been shown to dramatically impact both the formation and reactivity of iron oxo complexes.[26] In general, the strength of coordination to the oxygen atom significantly alters the reactivity of the Lewis acid/base pair. For example, the potassium counter-cation of an anionic tris(pyrrolide)amine iron(II) complex is coordinatively saturated with solvent molecules in the solid state and effectively separated from the transition

22. England, J.; Guo, Y.; Van Heuvelen, K. M.; Cranswick, M. A.; Rohde, G. T.; Bominaar, E. L.; Münck, E.; Que, L. *J. Am. Chem. Soc.* **2011**, *133*, 11880–11883.
23. (a) Seo, M. S.; Kim, N. H.; Cho, K.-B.; So, J. E.; Park, S. K.; Clémancey, M.; Garcia-Serres, R.; Latour, J.-M.; Shaik, S.; Nam, W. *Chem. Sci.* **2011**, *2*, 1039. (b) Kaizer, J.; Klinker, E. J.; Oh, N. Y.; Rohde, J.-U.; Song, W. J.; Stubna, A.; Kim, J.; Münck, E.; Nam, W.; Que, L. *J. Am. Chem. Soc.* **2004**, *126*, 472–473. (c) Nam, W. *Acc. Chem. Res.* **2007**, *40*, 522–531.
24. Lacy, D. C.; Gupta, R.; Stone, K. L.; Greaves, J.; Ziller, J. W.; Hendrich, M. P.; Borovik, A. S. *J. Am. Chem. Soc.* **2010**, *132*, 12188–12190.
25. Bigi, J. P.; Harman, W. H.; Lassalle-Kaiser, B.; Robles, D. M.; Stich, T. A.; Yano, J.; Britt, R. D.; Chang, C. J. *J. Am. Chem. Soc.* **2012**, *134*, 1536–1542.
26. Li, F.; Van Heuvelen, K. M.; Meier, K. K.; Münck, E.; Que, L. *J. Am. Chem. Soc.* **2013**, *135*, 10198–10201.

metal ion. Reaction of this precursor complex with trimethylamine-*N*-oxide generates an isolable $S = 2$ oxoiron complex that can perform intramolecular C–H hydroxylation of the tris(pyrrolide)amine ligand or intermolecular C–H abstraction.[25] Conversely, proton-coupled electron transfer from a tris(urea)amine hydroxoiron(III) complex results in an oxoiron(IV) complex supported by the three urea-based protons of the ligand. Productive C–H functionalization chemistry from this complex is nonexistent, despite a high-spin electronic configuration, likely a consequence of the strength of the Lewis acid/base pair which passivates the otherwise reactive iron oxo complex.[24]

Based on the studies by Que, Nam, Borovik, and Cheng, the presence of a metal-ligand multiple bond is not sufficient to engender the desired chemistry, as evidenced by the wealth of isolated $S = 1$ iron oxo complexes that are unreactive towards C–H bonds. However, a correlation between high spin state and reactivity towards hydrogen atom abstraction does emerge.[27] Further, the lone example of C–H hydroxylation from a crystallographically characterized metal ligand multiple bond ($[(N_4py)(ACN)Fe^{IV}(O)][CF_3SO_3]_2$, $S = 1$) has been theorized to necessitate state crossing to the quintet ($S = 2$) potential energy surface prior to productive C–H functionalization.[28] Computational studies have suggested than this quintet state is broken symmetry in nature, implying an iron(III)-oxyl radical ($S_{Fe}\ ^5/_2 - S_O\ ^1/_2 = S_{total}\ 2$) as the active intermediate rather than a high-spin iron(IV)-oxo.[29] Similar observations have been made for both mononuclear[30] and

27. Puri, M.; Que, L. *Acc. Chem. Res.* **2015**, *48*, 2443–2452.
28. (a) Kumar, D.; Hirao, H.; Que, L.; Shaik, S. *J. Am. Chem. Soc.* **2005**, *127*, 8026–8027. (b) Hirao, H.; Kumar, D.; Que, L.; Shaik, S. *J. Am. Chem. Soc.* **2006**, *128*, 8590–8606. (c) Seo, M. S.; Kim, N. H.; Cho, K.-B.; So, J. E.; Park, S. K.; Clémancey, M.; Garcia-Serres, R.; Latour, J.-M.; Shaik, S.; Nam, W. *Chem. Sci.* **2011**, *2*, 1039.
29. Ye, S.; Neese, F. *Proc. Natl. Acad. Sci. U. S. A.* **2011**, *108*, 1228–1233.
30. Mai, B. K.; Kim, Y. *Inorg. Chem.* **2016**, *55*, 3844–3852.

dinuclear[31] non-heme iron hydroxylase enzymes and suggest commonality for the iron(III)-oxyl radical intermediate in both biological and synthetic hydroxylation systems. For the non-heme iron enzyme TauD dioxygenase, the majority of the activation energy (89 %) for the overall transformation is utilized to establish the $Fe^{III}$–•O state while the barrier towards abstraction is very low.[30] The small activation energy, coupled with the absence of heavy atom movement at the transition state, has been implicated as a source of tunneling that leads to the very high observed kinetic isotope effects in both synthetic and biological systems (ca. 28-50).

## 1.3 Synthetic Iron Imides

The synthetic challenges associated with the isolation and manipulation of highly reactive oxygen-based C–H functionalization intermediates may be partially alleviated via the use of imido fragments instead. The organic functionality bound to the nitrogen atom donor of the *pro*-imido ligand can be systematically altered to provide a range of steric protection and electronic perturbations to the metal-ligand multiple bond. From a ligand field theory perspective, the ligand field strength of an imido is reduced from its oxo counterpart due to the presence of the pendant organic group which can delocalize the molecular orbitals involved in metal-imide binding. Further, while oxo ligands participate in bonding to metal centers via both σ- and π-symmetry molecular orbitals, the σ-symmetric interaction of imide ligands is significant reduced due to its interactions with the *N*-functional group. Nevertheless, the resulting metal ligand multiple bond is isostructural to and can potentially manifest similar C–H functionalization reactivity with that observed in the corresponding oxo complex, although with augmented stability against deleterious

31. (a) Khanh Mai, B.; Kim, Y. *Chem. - A Eur. J.* **2013**, *19*, 3568–3572. (b) Mai, B. K.; Kim, Y. *Chem. - A Eur. J.* **2014**, *20*, 6532–6541.

decomposition.

The enhanced stability of imido complexes as compared to oxo complexes has resulted in a wealth of iron imido complexes that are stable to characterization ($Fe^{II}$, $S = 0$;[32] $Fe^{III}$, $S = {}^{1}/_{2}, {}^{3}/_{2}$;[33] $Fe^{IV}$, $S = 0, 1$;[34] $Fe^{V}$, $S = {}^{1}/_{2}$;[35] Fe–N = 1.622 – 1.700(5) Å). The reactivity of these complexes is dominated by two-electron group transfer chemistry, including insertion by CO to form isocyanates,[36] insertion by isocyanides to form carbodiimides,[37] and hydrogenation to afford the corresponding amines.[38] In direct analogy to the field of iron oxo chemistry, strong donicity of the ancillary ligands leads to the formation of exclusively low- or intermediate-spin states for these complexes. While some species do contain unpaired electron density, it is not localized along the iron imide bond vector as the molecular orbital of $\pi^*_{Fe–Nimide}$ symmetry is additionally destabilized via interactions with the ancillary ligand and is energetically inaccessible. For this reason, only three groups of iron imide complexes have shown single electron chemistry in the form of hydrogen atom abstraction: the tris(carbeno)borate-supported $Fe^{IV}$ imide of Smith,[34a] the β-

32. Brown, S. D.; Peters, J. C. *J. Am. Chem. Soc.* **2005**, *127*, 1913–1923.
33. (a) Scepaniak, J. J.; Young, J. A.; Bontchev, R. P.; Smith, J. M. *Angew. Chem. Int. Ed. Engl.* **2009**, *48*, 3158–3160. (b) Betley, T. A.; Peters, J. C. *J. Am. Chem. Soc.* **2003**, *125*, 10782–10783. (c) Lu, C. C.; Saouma, C. T.; Day, M. W.; Peters, J. C. *J. Am. Chem. Soc.* **2007**, *129*, 4–5. (d) Cowley, R. E.; Holland, P. L. *Inorg. Chem.* **2012**, *51*, 8352–8361. (e) Brown, S. D.; Betley, T. A.; Peters, J. C. *J. Am. Chem. Soc.* **2003**, *125*, 322–323. (f) Bart, S. C.; Lobkovsky, E.; Bill, E.; Chirik, P. J. *J. Am. Chem. Soc.* **2006**, *128*, 5302–5303. (g) Cowley, R. E.; DeYonker, N. J.; Eckert, N. A.; Cundari, T. R.; DeBeer, S.; Bill, E.; Ottenwaelder, X.; Flaschenriem, C.; Holland, P. L. *Inorg. Chem.* **2010**, *49*, 6172–6187.
34. (a) Nieto, I.; Ding, F.; Bontchev, R. P.; Wang, H.; Smith, J. M. *J. Am. Chem. Soc.* **2008**, *130*, 2716–2717. (b) Verma, A. K.; Nazif, T. N.; Achim, C.; Lee, S. C. *J. Am. Chem. Soc.* **2000**, *122*, 11013–11014. (c) Thomas, C. M.; Mankad, N. P.; Peters, J. C. *J. Am. Chem. Soc.* **2006**, *128*, 4956–4957. (d) Searles, K.; Fortier, S.; Khusniyarov, M. M.; Carroll, P. J.; Sutter, J.; Meyer, K.; Mindiola, D. J.; Caulton, K. G. *Angew. Chemie Int. Ed.* **2014**, *53*, 14139–14143. (e) Searles, K.; Fortier, S.; Khusniyarov, M. M.; Carroll, P. J.; Sutter, J.; Meyer, K.; Mindiola, D. J.; Caulton, K. G. *Angew. Chemie Int. Ed.* **2014**, *53*, 14139–14143. (f) Wang, L.; Hu, L.; Zhang, H.; Chen, H.; Deng, L. *J. Am. Chem. Soc.* **2015**, *137*, 14196–14207.
35. Ni, C.; Fettinger, J. C.; Long, G. J.; Brynda, M.; Power, P. P. *Chem. Commun. (Camb).* **2008**, 6045–6047.
36. (a) Brown, S. D.; Betley, T. A.; Peters, J. C. *J. Am. Chem. Soc.* **2003**, *125*, 322–323. (b) Bart, S. C.; Lobkovsky, E.; Bill, E.; Chirik, P. J. *J. Am. Chem. Soc.* **2006**, *128*, 5302–5303.
37. (a) Cowley, R. E.; Eckert, N. A.; Elhaik, J.; Holland, P. L. *Chem. Commun.* **2009**, 1760–1762. (b) Cowley, R. E.; Golder, M. R.; Eckert, N. A.; Al-Afyouni, M. H.; (c) Holland, P. L. *Organometallics* **2013**, *32*, 5289–5298.
38. Bart, S. C.; Lobkovsky, E.; Bill, E.; Chirik, P. J. *J. Am. Chem. Soc.* **2006**, *128*, 5302–5303.

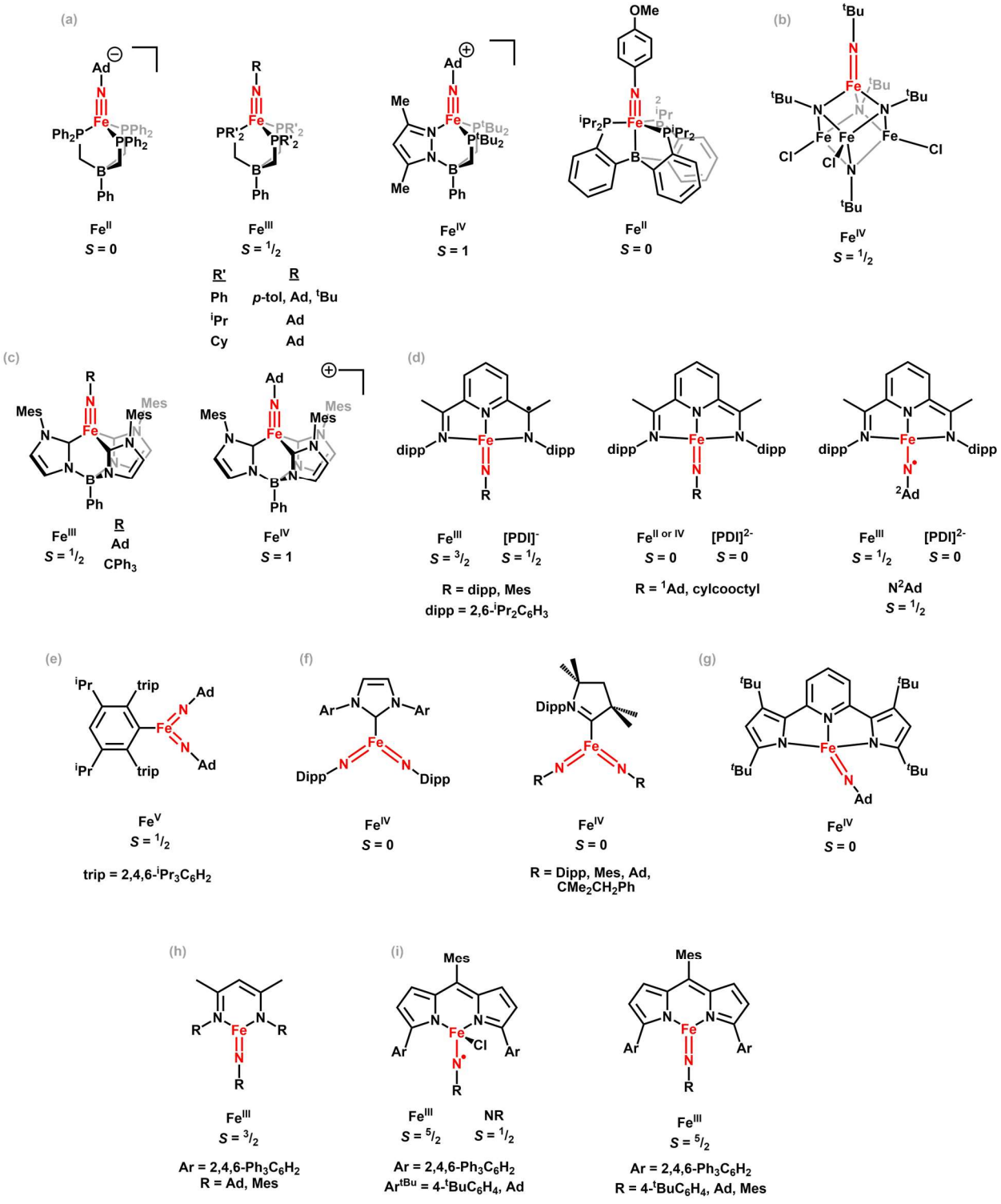


**Figure 1.2**. Crystallographically characterized mononuclear, terminal iron imides known in the literature from the groups of (a) Peters,[32, 33b,c,e, 33e, 34c, 36a] (b) Lee,[34b] (c) Smith,[33a,34a] (d) Chirik,[33f, 36b, 38] (e) Power,[35] (f) Deng,[34f] (g) Caulton,[34e] (h) Holland,[33d,g, 37a,c] and (i) Betley.[39]

diketiminate-supported $Fe^{III}$ imides of Holland, [33d,g, 37a,c] and the dipyrrin-supported $Fe^{III}$ imides/iminyls of Betley.[39]

The abstraction chemistry observed from the tris(carbeno)borate-supported $Fe^{IV}$ imide has been imputed as a primarily thermodynamic phenomena due to the high basicity of the N–H bond in the resulting iron amide product ($pK_a$ = 37(3)). Regardless of the stepwise or concerted mechanism of $H^{\bullet}$ transfer, the N–H BDE of 88(5) kcal/mol enables hydrogen atom abstraction from the weak C–H bond of 9,10-dihydroanthracene in 25 % yield at 100 °C. The forcing conditions are likely a consequence of the significant activation energy required for the HAT process due to the electronic structure of the starting imide complex ($S = 1$). By accessing high spin states and populating $\pi^*_{Fe–Nimide}$ orbitals, the single electron required to form the bond between the $N_{imide}$ and incoming H-atom would bear stronger positional similarity to that required during the transition state of N–H bond formation and should lower the barrier towards HAT processes.[40] In fact, a terminal iron(III) imide complex ($S = {}^3/_2$) prepared by Holland and coworkers decomposes *in situ* over several hours at room temperature to cleanly afford the product of hydrogen atom abstraction from the supporting β-diketiminate ligand framework. Addition of weak C–H bond donors instead encourages intermolecular hydrogen atom transfer, furnishing the first example of HAT to an isolated iron imide complex. Both the intra- and intermolecular HAT occur only in the presence of exogenous pyridine, which was rationalized by invoking the intermediacy of a high-spin ($S = {}^5/_2$) pyridine adduct of the iron(III) imide as the active agent for HAT.

Similar ligand functionalization was observed upon treatment of a dipyrrin-supported $Fe^{II}$

39. King, E. R.; Hennessy, E. T.; Betley, T. A. *J. Am. Chem. Soc.* **2011**, *133*, 4917–4923.
40. (a) Warren, J. J.; Tronic, T. A.; Mayer, J. M. *Chem. Rev.* **2010**, *110*, 6961–7001. (b) Mayer, J. M. *Acc. Chem. Res.* **2011**, *44*, 36–46.

complexes with adamantyl azide.[41] Removal of weak C–H bonds from the ligand periphery enabled the catalytic intermolecular, direct C–H amination of toluene and provided an isolable iron imide complex as the first example of direct C–H functionalization from an isolate iron imide complex.

## 1.4 C–H Amination Chemistry from High-Spin (Dipyrrinato)Iron Imides

Preparation of a dipyrrin ligand that does not feature weak C-H bonds ($^{Ar}$L = 1,9-Ar$_2$-5-mesityl-dipyrromethene, Ar = 2,4,6-Ph$_3$C$_6$H$_2$) to prevent intramolecular functionalization permitted the isolation and crystallographic characterization of a related dipyrrin-supported high-valent iron imide species featuring a very long Fe–N bond (1.768(2) Å) and asymmetric carbon-carbon bond lengths in the *N*–aryl substituent of the imido fragment.[39] Zero-field $^{57}$Fe Mössbauer analysis revealed features consistent with a trivalent iron center. In concert, the data suggest the electronic structure is best described as a high-spin ($S = {}^5/_2$) iron(III) antiferromagnetically coupled to an imide centered radical ($S = {}^1/_2$) to yield the overall $S = 2$ ground state determined via solid-state magnetometry. Notably, the species is competent for the C–H amination of toluene at room temperature, the first example of such a reaction from an isolated iron imide complex. A similar species featuring a *N*–dipp (dipp = di-isopropylphenyl) substituent was also prepared and possesses a similar Fe$^{III}$–$^{\bullet}$NR electronic motif, providing additional confidence in its assignment.[42]

The broken symmetry electronic configuration disrupts the covalency within the metal imide fragment, enhancing radical character of the Fe–N π* orbitals and weakening the metal ligand multiple bond. These factor combine to make the imide moiety more labile and the overall complex

41. King, E. R.; Betley, T. A. *Inorg. Chem.* **2009**, *48*, 2361–2363.
42. Iovan, D. A.; Betley, T. A. *J. Am. Chem. Soc.* **2016**, *138*, 1983–1993.

more highly reactive towards C–H bonds. This observation hints at the correlation between spin state and C–H functionalization reactivity. Of the isolated iron imide complexes in $S = 0$, $S = {}^{1}/_{2}$, or $S = 1$ spin states, only one is known to perform hydrogen atom abstraction and none are capable of direct C–H amination. As the spin state of the molecule is increased to $S = {}^{3}/_{2}$ as observed in β-diketiminate-supported iron imides, hydrogen atom abstraction becomes more facile and takes place at room temperature as opposed to the forcing conditions necessitated previously. Finally, only the high-spin ($S = 2$) iron iminyl complexes can perform both hydrogen atom abstraction as well as direct C–H functionalization of unactivated substrates.

Despite the observed correlation, the relative complexity of the iron iminyl electronic structure complicates the analysis. Specifically, the spin state at iron has been increased to $S = {}^{5}/_{2}$ while imide *N*–atom possesses an $S = {}^{1}/_{2}$ electronic configuration. Ideally, a molecule that possess an $S = {}^{5}/_{2}$ spin state (with no nitrogen centered radical character) would serve as a better comparison and help to elucidate the correlation between electronic structure and reactivity towards C–H amination from a metal ligand multiple bond.

The following paragpraphs provide synopses of the Thesis chapters presented herein to address the correlation of metal ligand multiple bond electronic structure to efficacy for functional group transfer.

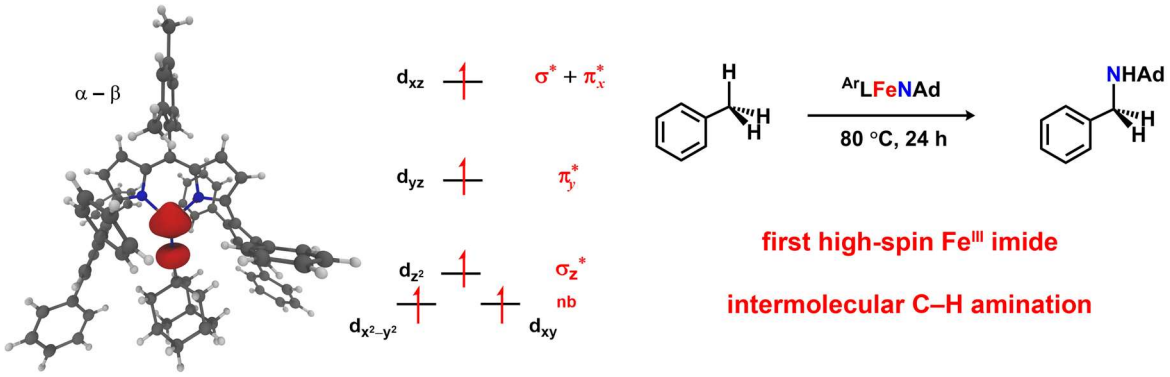


**Chapter 2** details the synthesis, characterization, and reactivity of two such dipyrrin-supported iron imide complexes. These complexes were characterized by $^{1}$H NMR, cryogenic EPR, zero-field $^{57}$Fe Mossbauer spectroscopy, and solid-state magnetometry to establish a spin ground state of $S = {}^{5}/_{2}$ and represent the first examples of isolated, high-spin Fe$^{III}$ imides in the literature. In line with the relationship between higher spin states and propensity for C–H amination, these iron imide complexes are competent for intermolecular hydrogen atom abstraction as well as the direct C–H amination of toluene. As such, population of Fe–N π* orbitals in the $S = {}^{5}/_{2}$ state is sufficient to engender the desired functionalization reactivity and enables unprecedented amination from an isolated iron imide complex.

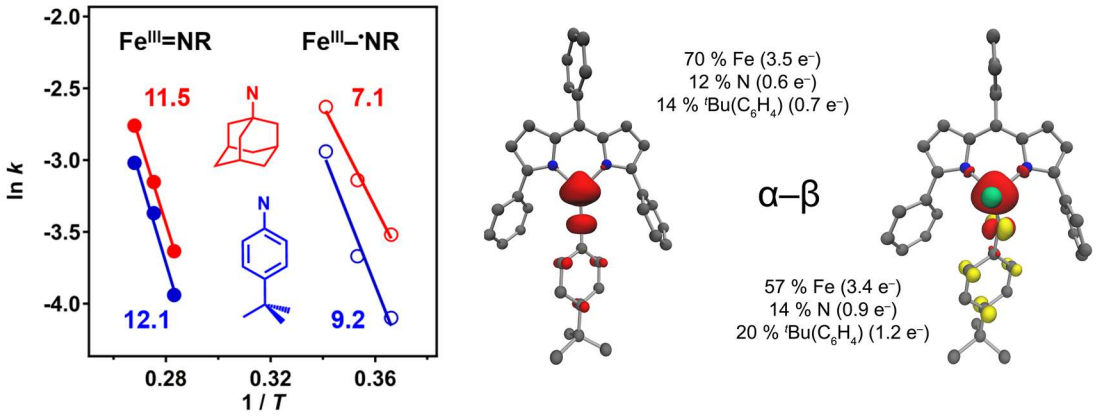


Based on electronic structure analysis, the primary difference between the $Fe^{III}$ imide and previously prepared $Fe^{III}$ iminyl complexes lies in the population of a primarily imide-based molecular orbital. **Chapter 3** exploits this relationship to prepare a family of iron imide complexes in both $Fe^{III}$ imide and $Fe^{III}$ iminyl oxidation states with varying *N*-functional groups. Again, $^{1}H$ NMR, cryogenic EPR, zero-field $^{57}Fe$ Mossbauer spectroscopy, solid-state magnetometry, and computational studies enable electronic structure analysis in this family of complexes, and suggest that the $Fe^{III}$ iminyl electronic structure is a general feature of dipyrrin-supported iron imide complexes in the formal 4+ oxidation state. The effect of oxidation state and *N*-functional group on both hydrogen atom transfer and intermolecular C–H amination can be correlated to the amount of spin density localized within the metal-ligand multiple bond. X-ray absorption spectroscopy and extended X-ray fine structure analysis verify the commonality of the iron oxidation state, even upon redox of these complexes, suggesting *N*-imide centered valence chemistry. Further, the structure of the first iron (alkyl)iminyl complex was determined via EXAFS analysis and bears direct analogy to the intermediate species formed during the catalytic cyclization of alkyl azide to form *N*-heterocycles reported previously.

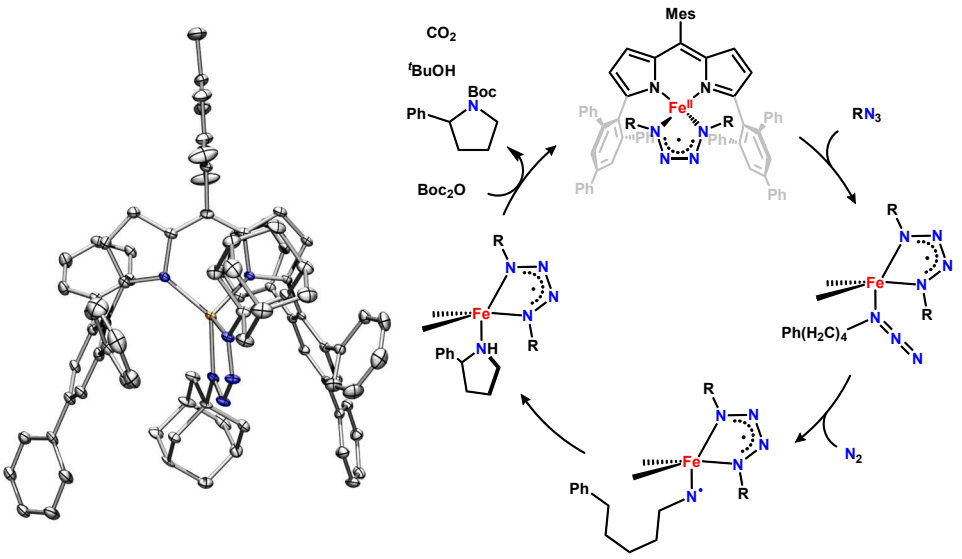


In an attempt to similarly investigate the effects of oxidation state on intramolecular C–H amination chemistry, we utilized a low valent iron(I) precursor as precatalyst for the cyclization of alkyl azide in the presence of di-*tert*-butyldicarbonate to form *N*-boc-pyrrolidines. The work presented in **Chapter 4** demonstrates that the catalytically active species is best described as an iron tetrazene complex that forms rapidly upon exposure of the precatalyst to substrate. We detail the synthesis and characterization of a family of (dipyrrinato)iron tetrazene complexes that differ in the tetrazene *N*-atom substituent. This family of complexes are robust catalysts for the cyclization of alkyl azides into pyrrolidine products in the presence of ditertbutyldicarbonate. Kinetic analysis supports a mechanistic view of the reaction as first-order with respect to both catalyst and substrate. The iron tetrazene catalysts are much more stable to Lewis basic functional groups and can enable productive cyclization with as little as 0.01 mol % of iron complex. In addition, the enhanced stability towards Lewis bases has enabled the cyclization of a new family of substrates featuring activation of the C–H bond by a variety of heteroatom-containing functional groups.

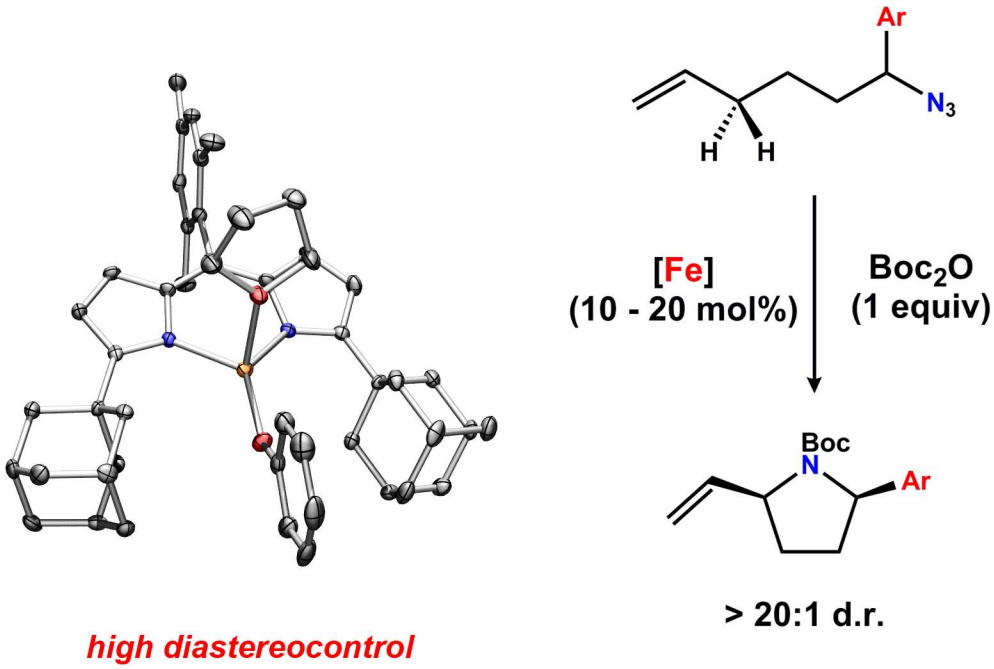


Structural information obtained on the iron (alkyl)iminyl intermediate in **Chapter 3** allowed us to computationally explore the diastereoselectivity of *N*-heterocycle formation as catalyzed by ($^{Ad}$L)FeCl(OEt$_2$) in **Chapter 5**. Upon cyclization of linear alkyl azide substrates with substitution at the α- and δ-positions, two possible diastereomers are formed in unequal ratios. Substrate modification to systematically vary steric parameters of these substituents result in modest changes in diastereoselectivity while preserving the *syn*-diastereomer as the favored product. To determine the origins of this bias, the reaction trajectory was calculated at the Def2-TZVP level of theory of uB3LYP. The reaction proceeds via a selectivity-determining hydrogen atom abstraction where steric interaction between the cyclizing substrate and the dipyrrin catalyst can be observed. The bridgehead position as well as the anionic ligand of the dipyrrin catalyst both destabilize the *pro*-anti transition state by 0.9 $^{kcal}/_{mol}$, which predicts a 4.6:1 d.r. that is in good agreement with the experimentally observed 3.9:1 selectivity. Enhancing the steric projection of the anionic ligand provided the most dramatic enhancement in diasteroselectivity to greater than 20:1 d.r. for nearly

all substrates investigated.

The results presented herein comment on the salient electronic features of intermediates for C–H functionalization. The presence of a high-spin metal-ligand multiple bond is sufficient to engender the desired chemistry, and the amount of radical density localized within the MLMB vector tunes the barrier toward amination. Given sufficient tuning of the supporting ligands, first-row transition metal catalysts can manifest good catalytic turnover in C–H functionalization reactivity.

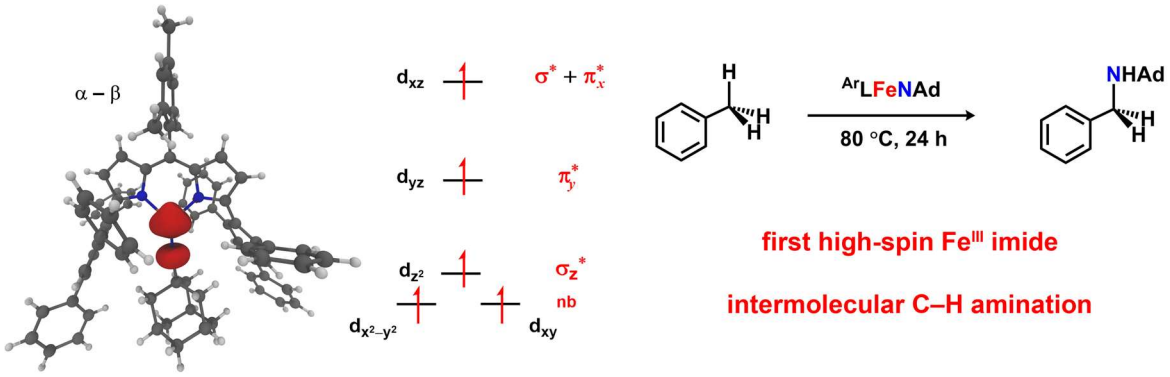


# Chapter 2: High spin iron imido complexes competent for C-H bond amination

## 2.1 Introduction

Coordination complexes featuring metal ligand multiple bonds (MLMBs) are implicated as intermediates in a variety of catalytic transformations both biologically[1] and abiologically.[2] The pursuit of MLMBs is driven by their capacity to facilitate atom- and group-transfer catalysis to unreactive C–H bond and olefinic functionalities, key to biological metabolism. Factors that govern MLMB reactivity and, conversely, stability include metal oxidation state, molecular oxidation level, and electronic structure.[3] Efficacy for group transfer reactivity is often reliant on accessing high molecular oxidation [4] levels to provide the driving force for substrate functionalization (e.g., cytochtrome P450), though the direct impact differing electronic structures

1. Mehn, M. P.; Peters, J. C. *J. Inorg. Biochem.* **2006**, *100*, 634–643. Bess, E. N.; Deluca, R. J.; Tindall, D. J.; Oderinde, M. S.; Roizen, J. L.; Du Bois, J.; Sigman, M. S. *J. Am. Chem. Soc.* **2014**, *136*, 5783–5789.
2. Liu, W.; Groves, J. T. *J. Am. Chem. Soc.* **2010**, *132*, 12847–12849.
3. Betley, T. A.; Peters, J. C. *J. Am. Chem. Soc.* **2003**, *125*, 10782–10783.
4. Rittle, J.; Green, M. T. *Science* **2010**, *330*, 933–937.

**Scheme 2.1.**

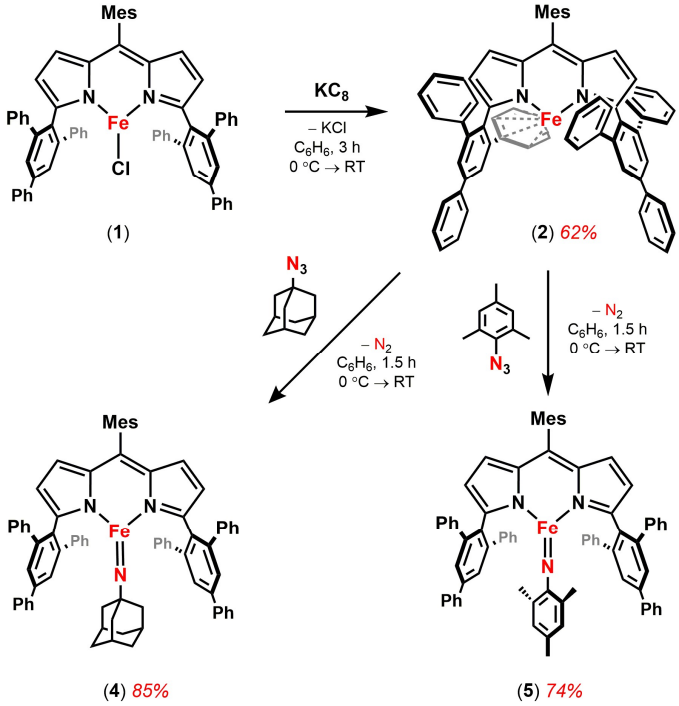


has not yet been fully explored. We hypothesized that targeting high-spin configurations could provide a similar driving force: electronic population of MLMB antibonding orbitals limits the MLMB covalency, enhancing its electrophilicity and reactivity group transfer processes. We have demonstrated enhanced reactivity for group transfer from cobalt imido and iron iminyl complexes capable of activating and functionalizing C–H bonds, respectively.[5] The dipyrrin's weak ligand field strength engenders the high-spin electronic structure despite the inherent strong field MLMB component. Ferric imido complexes have been isolated in $S = {}^{1}/_{2}$ and ${}^{3}/_{2}$ configurations,[6] but the

5. (a) King, E. R.; Sazama, G. T.; Betley, T. A. *J. Am. Chem. Soc.* **2012**, *134*, 17858–17861. (b) King, E. R.; Betley, T. A. *Inorg. Chem.* **2009**, *48*, 2361–2363. (c) King, E. R.; Hennessy, E. T.; Betley, T. A. *J. Am. Chem. Soc.* **2011**, *133*, 4917–4923. (d) Hennessy, E. T.; Betley, T. A. *Science* **2013**, *340*, 591–595.
6. (a) Lu, C. C.; Saouma, C. T.; Day, M. W.; Peters, J. C. *J. Am. Chem. Soc.* **2007**, *129*, 4–5. (b) Scepaniak, J. J.; Young, J. A.; Bontchev, R. P.; Smith, J. M. *Angew. Chem. Int. Ed. Engl.* **2009**, *48*, 3158–3160. (c) Cowley, R. E.; Holland, P. L. *Inorg. Chem.* **2012**, *51*, 8352–8361. (d) Brown, S. D.; Betley, T. A.; Peters, J. C. *J. Am. Chem. Soc.* **2003**, *125*, 322–323. (e) Bart, S. C.; Lobkovsky, E.; Bill, E.; Chirik, P. J. *J. Am. Chem. Soc.* **2006**, *128*, 5302–5303. (f) Cowley, R. E.; DeYonker, N. J.; Eckert, N. A.; Cundari, T. R.; DeBeer, S.; Bill, E.; Ottenwaelder, X.; Flaschenriem, C.; Holland, P. L. *Inorg. Chem.* **2010**, *49*, 6172–6187.

putative high-spin $^{5}/_{2}$ configuration has thus far eluded isolation. Thus, we sought to prepare and evaluate the reaction chemistry of a high-spin iron(III) imido complex against the literature examples and determine the impact of the electronic structure for group transfer processes.

## 2.2 Results and Discussion

The synthesis of metal imido complexes typically utilize oxidative group transfer from organic azides or hypervalent iodine reagents to a reactive coordination complex capable of nitrene capture. Thus, we prepared a suitable iron(I) reagent following chemical reduction of the three coordinate ferrous dipyrrin complex ($^{Ar}$L)FeCl (**1**) ($^{Ar}$L: 5-mesityl-1,9-(2,4,6-$Ph_3C_6H_2$)dipyrrin). Cyclic voltammetry on **1** in dichloromethane revealed a reversible $Fe^{II/III}$ couple at –460 mV and an irreversible reduction event at –1.80 V (both versus $[Cp_2Fe]^{0/+}$, **Figure 2.1**) which was attributed to an iron-centered reduction. Accordingly, treatment of **1** with a slight excess (1.05 equiv) of potassium graphite in thawing benzene cleanly afforded the reduced complex ($^{Ar}$L)Fe (**2**), as evidenced by the single quadrupole doublet (δ: 0.62 $^{mm}$/s, $|\Delta E_Q|$: 0.86 $^{mm}/_{s}$) in the $^{57}$Fe Mössbauer spectrum (**Figure 2.2**).

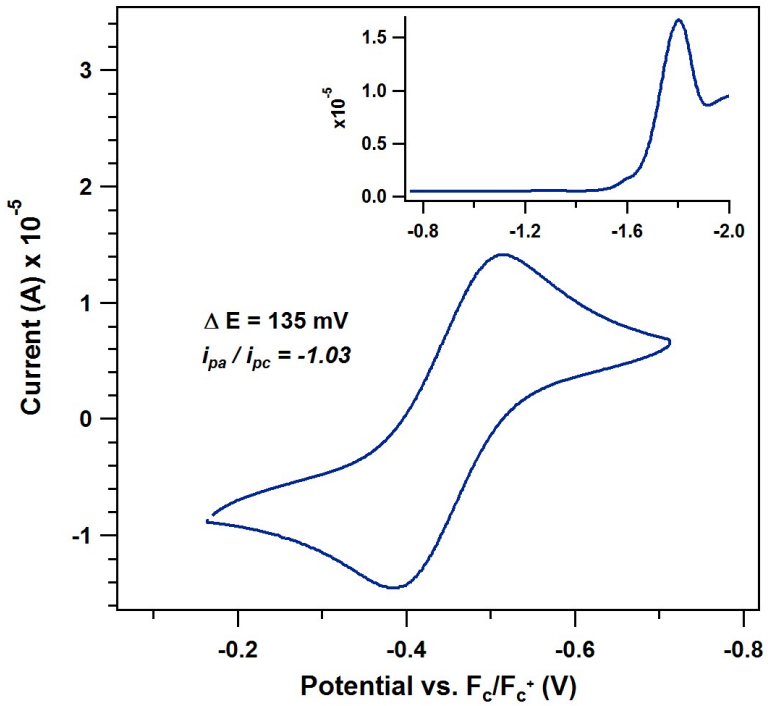


**Figure 2.1.** Cyclic voltammogram of ($^{Ar}$L)FeCl (**1**) obtained in $CH_2Cl_2$ at 25 °C, with 0.1 M ($nBu_4N$)($PF_6$) as supporting electrolyte and a scan rate of 100 mV/s showing a quasi-reversible oxidation event at -460 mV (OCP: -690 mV) with (inset) differential pulse voltammetry showing an irreversible reduction event at $E_{red}$ = -1.80 V.

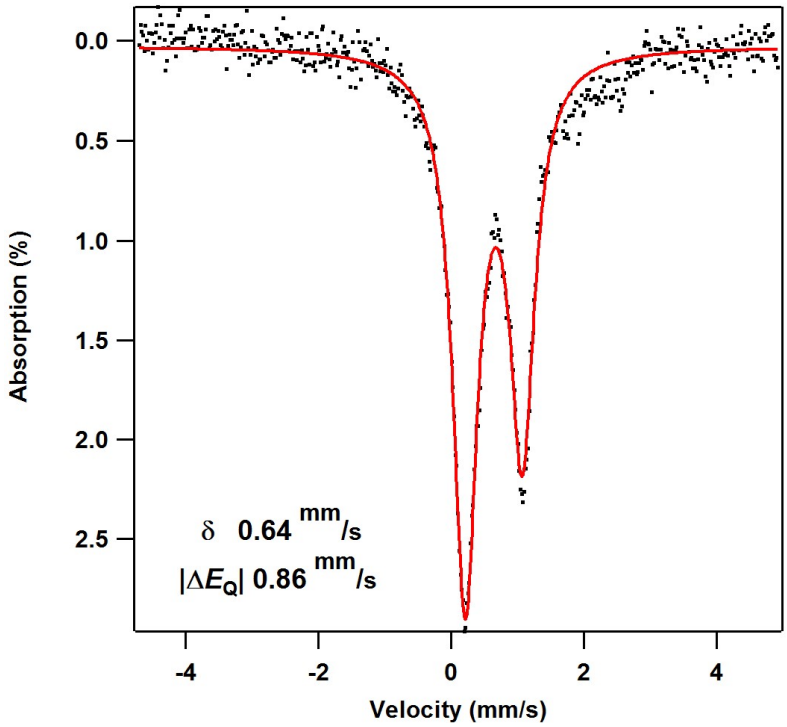


**Figure 2.2.** Zero-field $^{57}$Fe Mössbauer spectrum of ($^{Ar}$L)Fe (**2**). Asymmetry of peaks was reproducible and fit with a peak asymmetry ratio of 0.58. Isomer shift and quadrupole splitting are reported relative to Fe foil at room temperature.

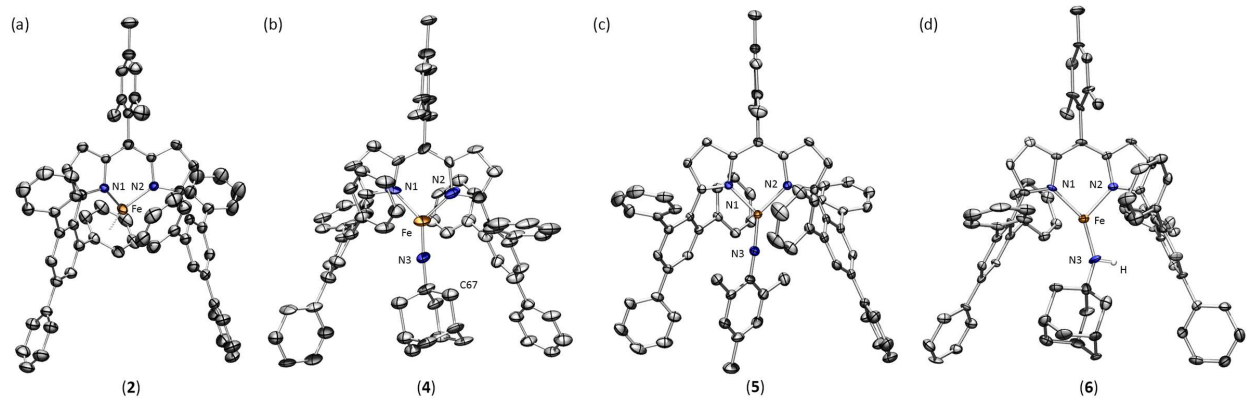


**Figure 2.3**. Solid-state structure of (a) ($^{Ar}$L)Fe (**2**), (b) ($^{Ar}$L)Fe(NAd) (**4**) at 100 K with 20% probability ellipsoids and (c) ($^{Ar}$L)Fe(NMes) (**5**) and (d) ($^{Ar}$L)Fe(NHAd) (**6**) at 100 K with 35 % probability ellipsoids. H atoms and solvent molecules have been omitted for clarity. Colors: Fe, orange; C, gray; H, white; N, blue.

Structural elucidation of **2** reveals an $\eta^6$-interaction between the iron and an *ortho*-phenyl substituent of the 2,4,6-$Ph_3C_6H_2$ aryl flanking unit of the dipyrrin (**Figure 2.3**). The arene binding interaction is inert to displacement by coordinating ligands (THF, diethyl ether, pyridine, trimethylphosphine, primary amines).

Although the $^1$H NMR displays no observable resonances (295 K), the frozen toluene EPR spectrum of **2** at 77 K consists of a rhombic signal ($g_{eff}$ = 2.24, 2.04, 1.98), consistent for an $S = {}^1/_2$ spin state. SQUID magnetometry corroborates this assignment with $\mu_{eff} = 1.7\ \mu_b$ at 75 K, complete overlay of the isofield curves by reduced magnetization (**Figure 2.4**), and good fit of the field-dependence of low-temperature magnetization to the $S = {}^1/_2$ Brillouin function (**Figure 2.5**).

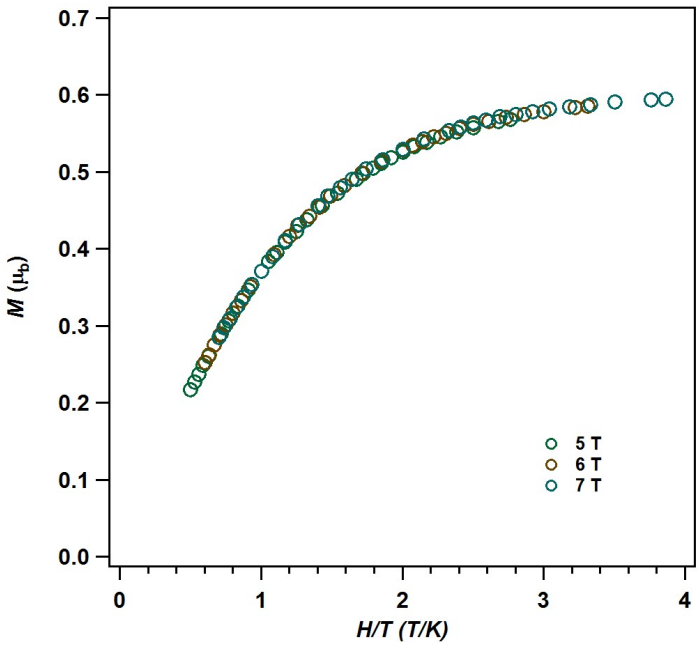


**Figure 2.4.** Reduced magnetization data for ($^{Ar}$L)Fe (**2**) collected at 3 fields (5-7 T) over the temperature range (1.8 K – 10 K) showing overlay of isofield curves.

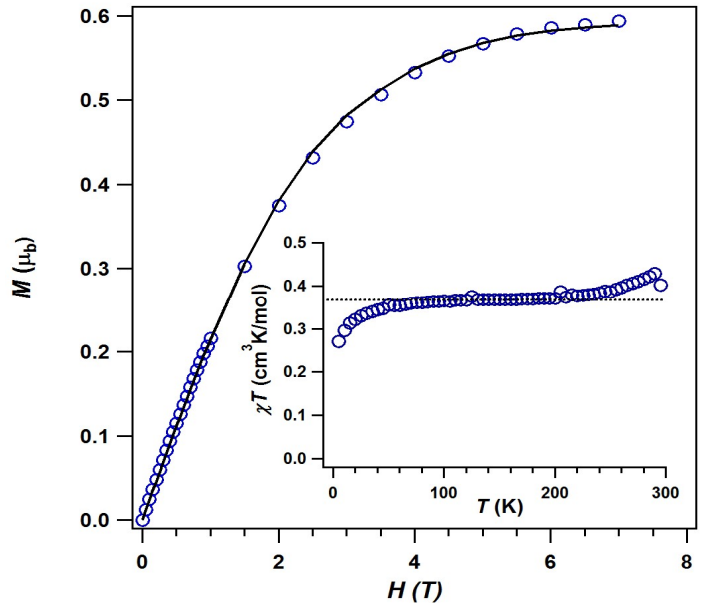


**Figure 2.5.** Brillouin function fitting to low-temperature (1.8 K) magnetization data of ($^{Ar}$L)Fe (**2**). Fit parameters: S = $^1/_2$, g = 2.03, $M_{sat}$ = 0.60 $\mu_b$ (obtained from least squares fitting). The inset shows $\chi_M$T vs. T at 0.5 T with $\chi_M$T = 0.37 cm$^3$K/mol at 125 K. The downturn of $\chi_M$T at low temperature is likely due to intermolecular interactions and/or normal field saturation effects.

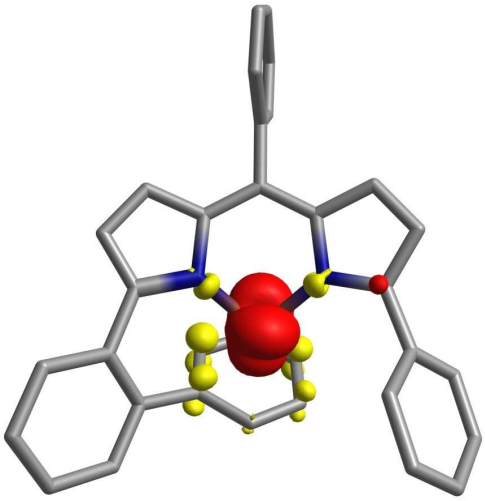

**Figure 2.6.** Mulliken spin density plot derived from a single point calculation on a truncated version of ($^{Ar}$L)Fe (**2**), showing 75 % spin localization on the metal and 16 % delocalized throughout the first coordination sphere (of which 11 % occurs on the $\eta^6$-arene) with the residual density distributed throughout the remainder of the molecule.

A single-point DFT calculation[7] on a truncated structural model of **2** suggests a high degree of covalency between the iron and $\eta^6$-bound arene (**Figure 2.6**), although the predominance of spin density (75 % based on Mulliken spin population analysis) is localized on the metal center and no broken-symmetry solution was found (e.g., $S_{Fe} = 1$, $S_{arene} = -^1/_2$).

The VT magnetic susceptibility data for **2** does not plateau at higher temperature, instead it manifests a gradual increase at ca. 250 K that continues to the temperature limit of the magnetometer. Thus, we assign the ground state of **2** as a low-spin ($S$ = ½) Fe$^{I}$ that may thermally populate higher spin states.

Dropwise addition of a dilute (0.03 % *w/w*) solution of adamantyl azide to ($^{Ar}$L)Fe$^{I}$ was sufficient to suppress the formation of the iron-tetrazinato complex ($^{Ar}$L)Fe($\kappa^2$-N$_4$Ad$_2$) (**3**), and provide the targeted iron-imido complex ($^{Ar}$L)Fe(NAd) (**4**) in good yield (85%). Treatment of **2** with mesitylazide cleanly affords the arylimido complex ($^{Ar}$L)Fe(NMes) (**5**, 74%) without the competing tetrazinato formation, presumably due to the steric protection of the imido aryl

7. Neese, F. Wiley Interdiscip. Rev. Comput. Mol. Sci. **2012**, 2, 73–78.

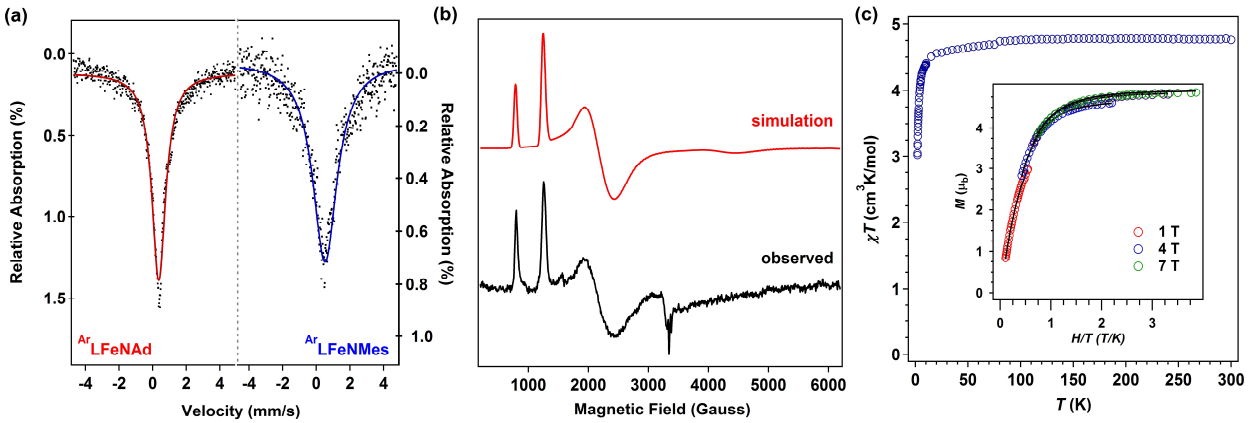


**Figure 2.7.** (a) Zero-field $^{57}$Fe Mössbauer of **4** (red) and **5** (blue) (δ, $|\Delta E_Q|$, Γ ($^{mm}/_{s}$): **4**, 0.37, *0.00*, 0.50; **5**, 0.47, *0.00*, 0.82). (b) X-band EPR of **4** (fit parameters: $S = {}^{5}/_{2}$, g = 2.0, $^{E}/_{D}$ = 0.145). (c) VT dc magnetic susceptibility for **4** collected at 0.5 T (blue circles). Inset: VTVH magnetization data collected on increasing temperature from 1.8 to 10 K at increasing field for 1, 4, and 7 T with the fit parameters as described in the text.

*ortho* substituents. The molecular structures of **4** and **5** were obtained by single crystal X-ray diffraction studies on single crystals grown from a concentrated toluene solution layered with pentane at –35 °C (**Figure 2.3**). Both molecular structures feature distorted trigonal planar iron(III) centers supported by the dipyrrin ligand and single imido moieties.

The Fe–N3 distance of 1.674(11) Å in **4** and 1.708(2) Å in **5** are consistent with the reported range for three- and four-coordinate iron-alkylimido species [1.622 – 1.700(5) Å] with established multiple bond character. In addition, the ∠Fe–N3–$C_{imido}$ angle of 174.7° in **4** and 172.3(2)° in **5** suggest biaxial π contributions, supporting the view of **4** and **5** as iron(III) complexes featuring doubly-bonded imidos.

The Mössbauer spectra of **4** and **5** feature single broad transitions (δ, $|\Delta E_Q|$, Γ ($^{mm}/_{s}$): **4**, 0.37, *0.00*, 0.50; **5**, 0.47, *0.00*, 0.82) at 200 K (**Figure 2.7**). The isomer shift values are close to those previously reported for the iminyl radical ($^{Ar}$L)Fe$^{III}$Cl(•NAr) (δ, $|\Delta E_Q|$ ($^{mm}/_{s}$): 0.29, *2.29*)[8] and the bimolecularly-coupled [($^{Ar}$L)Fe$^{III}$Cl]$_2$(κ$^2$-N(Ph)(C$_6$H$_5$)N) (δ, $|\Delta E_Q|$ ($^{mm}/_{s}$): 0.33, *2.15*)[8] suggesting a

8. King, E. R.; Hennessy, E. T.; Betley, T. A. *J. Am. Chem. Soc.* **2011**, *133*, 4917–4923.

common iron oxidation state assignment among these molecules and **4**, whereas the metrical parameters for **5** are presumably affected by the conjugation to the imido mesityl functionality. Spectra obtained below ca. 150 K suffer from significant broadening and low signal-to-noise ratio, likely due to incomplete resolution of hyperfine splitting at 90 K or more complex relaxation broadening phenomena[9] often observed in high-spin $Fe^{III}$ compounds.[10]

In accordance with the observed temperature dependent phenomena (*vide supra*), **4** and **5** do not exhibit an EPR signal above ca. 50 K. The frozen toluene EPR spectrum of **4** obtained at 4 K displays a rhombic signal ($g_{eff}$ = 8.62, 5.35, 3.10), well reproduced by an $S = {}^5/_2$ simulation treating each intra-doublet transition as an effective $S = {}^1/_2$ system (in the weak-field limit) and including the effects of both rhombicity ($^E/_D$) and *D*-strain (simulation parameters: g = 2.0, $^E/_D$ = 0.145, linewidth = 15 G). The inclusion of *D*-strain is necessary to account for the randomness in spatial confirmation of the frozen solution and provide an effective powder pattern for a given *S* and $^E/_D$.[11] The data and corresponding simulation are shown in **Figure 2.7**. No satisfactory agreement with experiment was found for simulations employing the $S = {}^3/_2$ assignment. Accordingly, solid-state magnetometry of **4** is consistent with a high spin state as evidenced by a $\mu_{eff}$ of 5.3 $\mu_B$ ($\chi_M T$ = 4.76 $cm^3$ K/mol) at 295 K (**Figure 2.7**). The value of $\chi_M T$ over the temperature range surveyed is consistent with an $S = {}^5/_2$ configuration (spin-only value anticipated is 4.38 $cm^3$ K/mol). The spin state suggested by the magnetic susceptibility data is further corroborated by variable-temperature, variable-field magnetization data collected on heating from 1.8 to 10 K and at increasing fields of

9. Stoian, S. A.; Yu, Y.; Smith, J. M.; Holland, P. L.; Bominaar, E. L.; Munck, E. *Inorg. Chem.* **2005**, *44*, 4915–4922.
10. (a) Greenwood, N. N.; Gibb, T. C. *Mossbauer Spectroscopy*; John Wiley & Sons, Incorporated, **1971**. (b) Gütlich, P.; Bill, E.; Trautwein, A. X. *Mössbauer Spectroscopy and Transition Metal Chemistry: Fundamentals and Applications*; Springer Science & Business Media, **2010**.
11. Hagen, W. R. *Mol. Phys.* **2007**, *105*, 2031–2039

1–7 T (Figure 2c inset). Magnetization saturation occurs at 4.86 $\mu_B$ at 1.8 K and 7 T. The lower than expected saturation (5.92 $\mu_B$ for an ideal $S = {}^5/_2$ with g = 2) and the observation of nonsuperimposable isofield curves indicates the presence of zero-field splitting, which was quantifed by fitting the date to the spin Hamiltonian $\hat{H} = D\hat{S}_z^2 + E(\hat{S}_x^2 - \hat{S}_y^2) + g_{iso}\mu_B$ **S•H**. The fit parameters considering an $S = {}^5/_2$ that best reproduce the data are $g = 2.02$, D = 1.0 $cm^{-1}$, |E/D| = 0.01 (**Figure 2.7**, inset, continuous black traces).

A single-point DFT calculation on **4** corroborates the $S = {}^5/_2$ ground state assignment and the calculated Mössbauer parameters match well with those observed for **4** (calculated δ ($^{mm}/_s$): 0.35). The calculated spin density plot (α – β) for **4**, shown in **Figure 2.8**, illustrates the contributions to the total spin contributed by iron (78%) and the imide nitrogen atom (16%). The molecular orbital ordering indicated is governed by the type of bonding and overlap between the metal center, the dipyrrin ligand, and the imido fragment, each singly populated in the high-spin

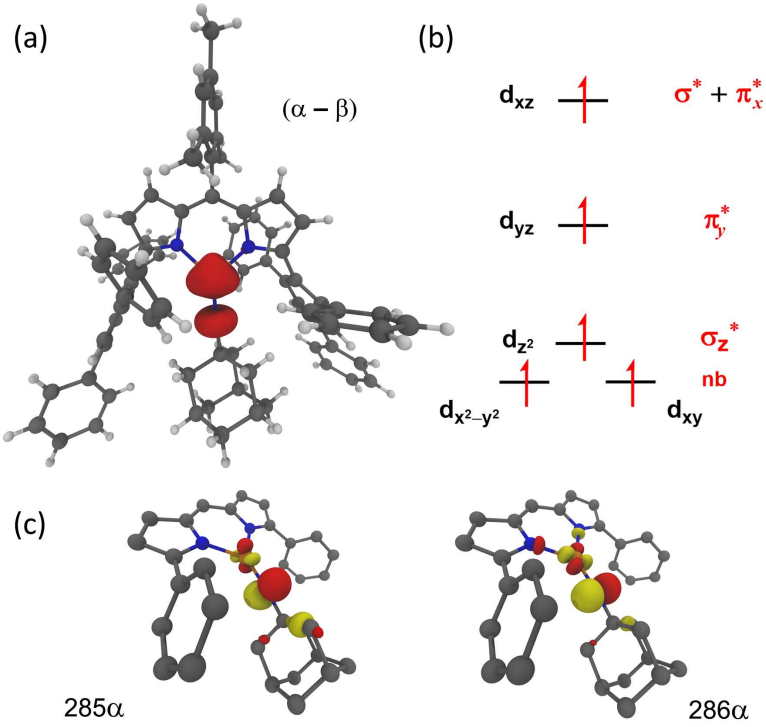


**Figure 2.8**. The calculated spin density population (α – β) for **4** ($S = {}^5/_2$) (a), the qualitative orbital energetic ordering (b), and the highest singly occupied orbitals for ($Fe_{yz}$ – $NR_{py}$, 285α) and ($Fe_{xz}$ – $NR_{px}$, 286α) (c) as suggested by DFT (B3LYP/6-31g(d); Gaussian 09).

configuration: 286α ($d_{xz}$: $\sigma^*$ to dipyrrin; $\pi^*$ to imido N$p_x$), 285α ($d_{yz}$: $\pi^*$ to imido N$p_y$), 280α ($d_z^2$: $\sigma^*$ to imido N$p_z$), 273α–274α ($d_{x^2-y^2}$, $d_{xy}$: nominally non-bonding). The density functional modeling and magnetic data acquired for imido complexes **4** and, by extension, **5** are assigned as the first high-spin ($S = {}^5/_2$) complexes thus far observed on iron.

With the isolated high-spin imidos **4** and **5** in hand, we were thus interested in assessing whether the reactivity of these two complexes diverge from that reported for the low- and intermediate spin analogues. Low-spin ($S$ = ½) complexes have been shown to exhibit nitrene transfer to tertiary phosphines and CO,[12] whereas the intermediate spin imido complexes have displayed this reactivity in addition to facilitating H-atom abstraction from weak C–H bonds.[13] A reaction between **4** and excess $PMe_2Ph$ (100 equivalents) proceeded instantaneously at room temperature to produce the phosphinimide $Me_2PhP$(NAd) and regenerate **2**. Heating a mixture of **4** and 1,4-cyclohexadiene at 45 °C resulted in slow consumption of **4** and formation of a new paramagnetic complex as evidenced by $^1$H NMR (**Figure 2.9**), to afford the amido product of H-atom abstraction ($^{Ar}$L)Fe(NHAd). This assignment was verified by comparison of the reaction mixture $^1$H NMR spectrum with an authentic sample of ($^{Ar}$L)Fe(NHAd) (**6**) afforded by the direct metathesis of **1** with LiNHAd in benzene.

12. Brown, S. D.; Betley, T. A.; Peters, J. C. *J. Am. Chem. Soc.* **2003**, *125*, 322–323.
13. (a) Cowley, R. E.; Eckert, N. A.; Elhaik, J.; Holland, P. L. *Chem. Commun.* **2009**, 1760–1762. (b) Eckert, N. A.; Vaddadi, S.; Stoian, S.; Lachicotte, R. J.; Cundari, T. R.; Holland, P. L. *Angew. Chemie Int. Ed.* **2006**, *45*, 6868–6871. (c) Cowley, R. E.; Holland, P. L. *Inorganica Chim. Acta* **2011**, *369*, 40–44. (d) Cowley, R. E.; Eckert, N. A.; Vaddadi, S.; Figg, T. M.; Cundari, T. R.; Holland, P. L. *J. Am. Chem. Soc.* **2011**, *133*, 9796–9811.

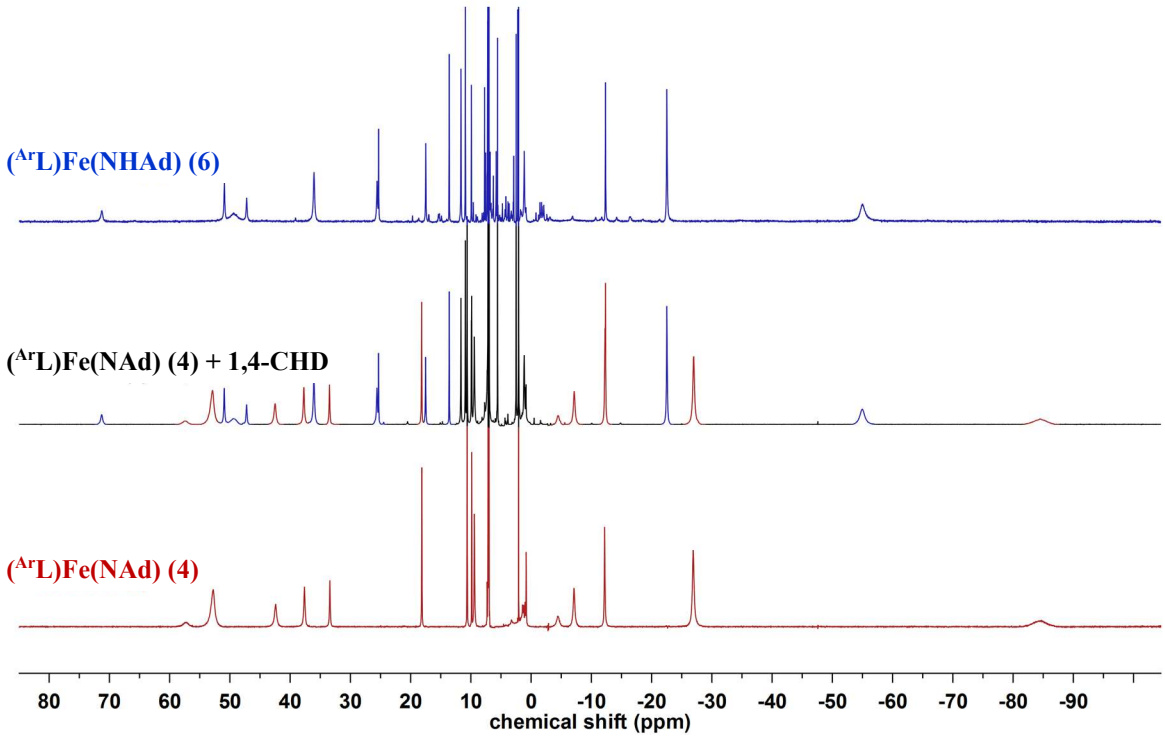


**Figure 2.9.** $^{1}$H NMR spectra of (bottom) ($^{Ar}$L)Fe(NAd) (**4**), (middle) upon addition of 1,4-cyclohexadiene ( 45 °C, 7 d), and (top) ($^{Ar}$L)Fe(NHAd) (**6**) in $C_6D_6$, showing hydrogen atom transfer.

The amide is not stable to prolonged heating, preventing the full consumption of **4** prior to decomposition. Nevertheless, a significant amount of product can be observed after 7 days incubating at 45 °C. In a similar fashion, **5** partially (ca. 50% completion) converts to the amide ($^{Ar}$L)Fe(NHMes) following treatment with 2,4,6-$^{t}$Bu$_3$C$_6$H$_2$OH (BDE O–H: 81 kcal/mol) at 60 °C for 6h, as shown in the $^{1}$H NMR overlay with authentic ($^{Ar}$L)Fe(NHMes) (**7**) in **Figure 2.10**. While production of the amide **7** is evident, further reaction between **7** and the aryloxide radical is also apparent (**Figure 2.10**).

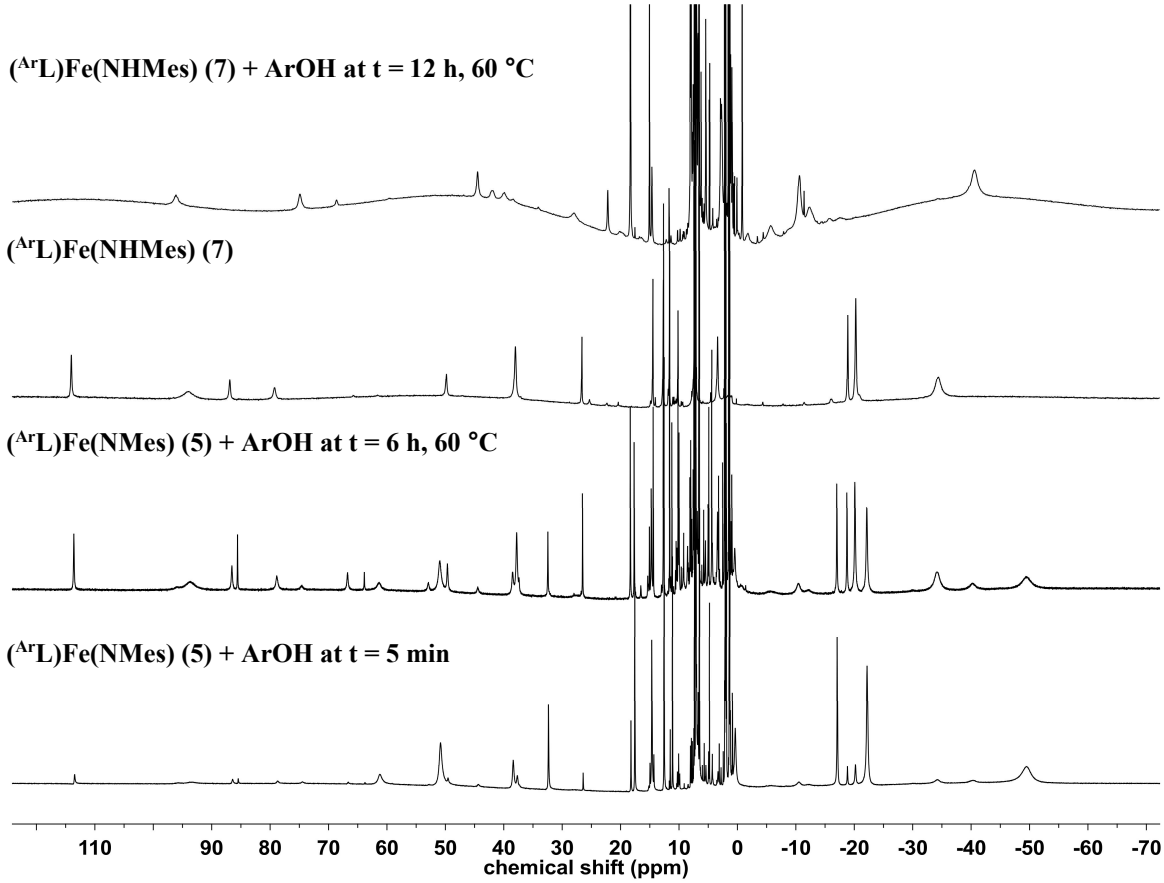


**Figure 2.10**. $^{1}$H NMR spectra showing conversion of ($^{Ar}$L)Fe(NMes) (**5**) to ($^{Ar}$L)Fe(NHMes) (**7**) upon treatment with 2, 4, 6- tri-*tert*-butylphenol at 60 °C. The additional peaks at t = 6 h are presumably due to an adduct between $^{Ar}$LFeNHMes the resulting aryloxide radical, as shown in the top spectrum.

The reactivity of three coordinate **4** and **5** should be contrasted with the quartet imido reported by Holland that does not undergo intermolecular HAT reactivity except in the presence of a Lewis base (e.g. pyridine, lutidine).[14] The authors propose the intermediacy of an $S = {}^{5}/_{2}$ pyridine adduct that possesses sufficient potency to engender reactivity towards C–H bonds. While imide variants that do not necessitate pyridine coordination prior to HAT have since been prepared

14. Cowley, R. E.; DeYonker, N. J.; Eckert, N. A.; Cundari, T. R.; DeBeer, S.; Bill, E.; Ottenwaelder, X.; Flaschenriem, C.; Holland, P. L. *Inorg. Chem.* **2010**, *49*, 6172–6187.

($S = {}^3/_2$), their rate of reaction with cyclohexadiene, for example, is between one and four orders of magnitude slower than postulated $S = {}^5/_2$ adduct complex.[15]

While **4** is stable in toluene solutions below or at room temperature, heating toluene solutions of **4** to 80 °C resulted in amination of the solvent benzylic C–H bond. Analysis of the reaction mixture by LC-MS revealed intermolecular C–H amination and formation of *N*-adamantyl-benzylamine (14 %), *N*-adamantyl-benzylimine (3 %), and significant amounts of 1,2-diphenylethane. Kinetic isotope effects ($k_H/k_D$) of 15.5(3) and 11(1) were determined for intermolecular ($C_7H_8$ vs. $C_7D_8$) and intramolecular ($d_1$-toluene $C_6H_5CH_2D$ activation) competition experiments, respectively, based on analysis of the resulting insertion products by LC-MS (see Supporting Information). These data are reminiscent of the intermolecular C–H amination chemistry with ($^{Ad}$L)FeCl($OEt_2$) reported previously (KIE: 12.8(5), presence of 1,2-diphenylethane at elevated temperatures as a result of solvent cage breakdown and coupling of two benzylic radicals), and are similarly consistent with a stepwise abstraction/recombination mechanism. Although **4** does not possess the radical density on the iminyl fragment proposed for ($^{Ar}$L)FeCl($^{\bullet}$NAr), C–H functionalization chemistry is still possible with **4**.

The large KIE observed in the reaction of **4** with toluene suggests that the C–H bond breaking event contributes significantly to the rate limiting step of the reaction sequence illustrated in Figure 4a. A consideration of the frontier molecular orbitals (FMOs) that complete this process include the two iron imido π interactions and the toluene C–H σ bond (see Figure 4). The two *N* π FMOs consist of the non-degenerate π interactions: $\pi_x$ [$\sigma^*_{(dxz - L\sigma)} \pm Np_x$] which includes a Fe–$L_{dipyrrin}$ $\sigma^*$ component, and the orthogonal $\pi_y$ (Fe $d_{yz} \pm Np_y$). We propose the $\pi_y^*$ FMO dictates the primary orbital interaction with the incoming toluene C–H substrate given its steric accessibility and more

15. Cowley, R. E.; Holland, P. L. *Inorg. Chem.* **2012**, *51*, 8352–8361.

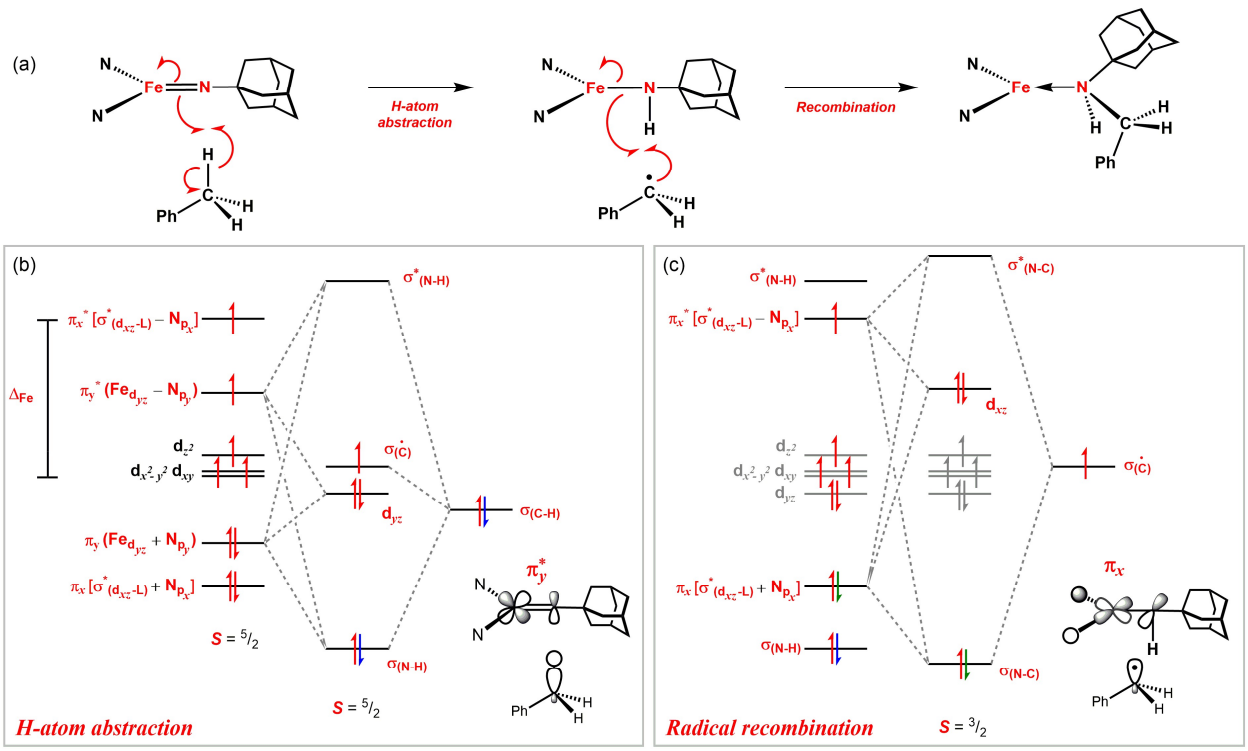


**Figure 2.11.** Frontier molecular orbital description of $Fe^{III}$(NAd) reaction profile for H-atom abstraction from $PhCH_3$ and the subsequent radical rebound event.

favorable energetic overlap. The H-atom abstraction step is highlighted in Figure 4b, where the homolyzed C–H orbital (yielding $PhC^{\bullet}H_2$ and H 1s) combine with $\pi_y/\pi_y^*$ to yield four orbital combinations: $(\sigma_{N-H})^2(Fe\ 3d_{yz})^2(PhC^{\bullet}H_2)^1(\sigma^*_{N-H})^0$, constituting a one-electron reduction at the iron center to $Fe^{II}$. The H-atom abstraction step conserves total spin-angular momentum as the resulting radical pair complex remains in a sextet spin configuration. The recombination step (Fig. 4c) should proceed combining the benzylic radical with the remaining $\pi_x$ $[\sigma^*_{(dxz\ -\ L\sigma)} \pm Np_x]$ pair yielding three product orbitals: $(\sigma_{N-C})^2(Fe\ 3d_{xz})^2(\sigma^*_{N-C})^0$, requiring a spin inversion to avoid population of $\sigma^*_{N-C}$, and thus constituting a net reduction of the iron center to $Fe^{I}$.

While **4** is operative for C–H bond amination, the (β-diketiminate)$Fe^{III}$(NAd)[14] ($S = {}^3/_2$) congener described by Holland was reported to be active for the H-atom abstraction reaction but not for the radical rebound mechanism. The principal difference between the two nearly isostructural materials is the spin ground states resulting from the ligand field strengths of the two

ancillary ligand sets. From an orbital perspective, the $\pi_y$ components are largely the same between the β-diketiminate and dipyrrin complexes, thus the HAA step is largely unchanged and could proceed by similar mechanisms. The $\pi_x/\pi_x^*$, however, does change between the two ancillary ligands. The stronger σ-donating β-diketiminate destabilizes $\pi_x^*$ which remains unpopulated in the ground state. Similarly, the corresponding bonding $\pi_x$ would be lowered in energy with respect to **4**. Thus the radical recombination step could be affected by the orbital energy changes and diminish the probability for the recombination step.

## 2.3 Conclusions

Akin to (dipyrrin)Co(NR) imido complexes which thermally access open shell configurations permitting C–H bond activation to occur, the high-spin $Fe^{III}$ imido complexes reported herein can facilitate nitrene transfer including C–H bond functionalization. Furthermore, the high-spin imido complexes can be synthesized utilizing both alkyl and aryl-imido fragments, suggesting the sextet configuration is energetically preferred even when the MLMB unit ligand field strength is increased. Comparing the results demonstrated herein with the known reactivity of ferric imido complexes spanning electronic configurations of $S = ½ \rightarrow {}^5/_2$, the sextet configuration is the only electronic structure that permits both H-atom abstraction and the subsequent recombination reaction to occur. Thus, one could envision catalytic intra- or intermolecular nitrene delivery reactions to be developed, so long as the high-spin electronic structure is maintained for the MLMB fragment. Given both the ferric imido and iminyl radical species have been shown to be competent for intermolecular nitrene delivery into C–H bonds, we are now interested in understanding how the oxidative potency is varied between the species. Research is currently underway to probe this factor for group transfer catalysis.

## 2.4 Experimental Methods

### *2.4.1 General Considerations*

All manipulations of metal complexes were carried out in the absence of water and dioxygen using standard Schlenk techniques, or in an MBraun inert atmosphere drybox under a dinitrogen atmosphere. Ligand and ligand precursor syntheses were carried out in air, except where noted. All glassware was oven dried for a minimum of 1 h and cooled in an evacuated antechamber prior to use in the drybox. Benzene, *n*-hexane, and toluene were dried and deoxygenated on a Glass Contour System (SG Water USA, Nashua, NH) and stored over 4 Å molecular sieves (Strem) prior to use. Benzene-$d_6$ was purchased from Cambridge Isotope Labs, degassed, stored over 4 Å molecular sieves prior to use. Pentane was purchased from Sigma-Aldrich and stored over 4 Å molecular sieves prior to use. Iron(II) chloride was purchased from Strem and ground under inert atmosphere. The ligand $^{Ar}$LH and lithium salt ($^{Ar}$L)Li were synthesized as previously reported.[16] Synthesis of (4-azidobutyl)benzene and protocol for quantification of yield under catalytic conditions were performed as previously reported or is otherwise noted.[17] Potassium graphite was prepared by heating potassium with 8 equivalents of graphite powder at 80 °C in an evacuated flask for 4 h. Toluene-α-$d_1$ was prepared with 95 % deuterium enrichment by treating a suspension of benzyl potassium[18] in pentane with $D_2O$ dropwise. Celite® 545 (J. T. Baker) was dried in a Schlenk flask for 24 h under dynamic vacuum while heating to at least 150 °C prior to drybox use.

16. King, E. R.; Hennessy, E. T.; Betley, T. A. *J. Am. Chem. Soc.* **2011**, *133*, 4917-4923.
17. Hennessy, E. T.; Betley, T. A. *Science* **2013**, *340*, 591–595.
18. Bailey, P. J.; Coxall, R. A.; Dick, C. M.; Fabre, S.; Henderson, L. C.; Herber, C.; Liddle, S. T.; Loroño-González, D.; Parkin, A.; Parsons, S. *Chemistry* **2003**, *9*, 4820–4828.

### *2.4.2 Characterization and Physical Measurements*

$^{1}$H NMR spectra were recorded on Varian Mercury 400 MHz or Varian Unity/Inova 500 MHz spectrometers. $^{1}$H and $^{13}$C NMR chemical shifts are reported relative to $SiMe_4$ using the chemical shift of residual solvent peaks as reference. Elemental analyses (%CHN) were carried out by Complete Analysis Laboratories, Inc. (Parsippany, NJ).

Zero-field $^{57}$Fe Mössbauer spectra were measured with a constant acceleration spectrometer (SEE Co, Minneapolis, MN) at 90K. Isomer shifts are quoted relative to Fe foil at room temperature. Data was analyzed and simulated with Igor Pro 6 software (WaveMetrics, Portland, OR) using Lorentzian fitting functions. Samples were prepared by suspending 50-100 mg of compound in sufficient Paratone oil and immobilizing by rapid freezing in liquid nitrogen.

EPR spectra were obtained on a Bruker EleXsys E-500 CW-EPR spectrometer. Spectra were measured as frozen toluene glasses at a microwave power of 0.6325–2 mW. Effective g-values were obtained from spectral simulations of $S = {}^{1}/_{2}$ systems using the program Easyspin.[19] Spectral simulations incorporating spin state and rhombicity were performed using VisualRhombo.[20]

Magnetic data were collected using a Quantum Design MPMS-5S SQUID magnetometer. Measurements for were obtained for finely ground microcrystalline powders restrained in a frozen eicosane matrix within polycarbonate capsules. Samples were prepared under a dry nitrogen atmosphere by packing the powder in a gelcap and adding warm liquid eicosane, which formed a solid wax upon cooling. Dc susceptibility measurements were collected in the temperature range 5-300 K under a dc field of 5000 or 10000 Oe. Dc magnetization measurements were obtained in

19. Stoll, S.; Schweiger, A. *J. Magn. Reson.* **2006**, 178, 42–55.
20. Hagen, W. R. Mol. *Phys.* **2007**, *105*, 2031–2039.

the temperature range 1.8-10 K under dc fields of 1, 2, 3, 4, 5, 6, and 7 T. The susceptibility data was corrected for contributions from the sample holder and eicosane, as well as the core diamagnetism of the sample using Pascal's constants. The reduced magnetization data were fit using PHI.[21]

### *2.4.3 Syntheses*

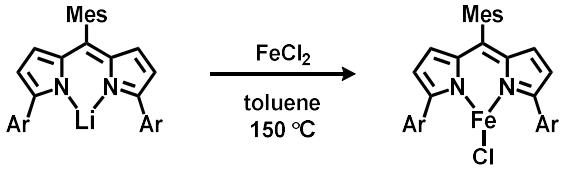


**($^{Ar}$L)FeCl (1)**: To a 50 mL pressure vessel was added ($^{Ar}$L)Li (0.500 g, 0.57 mmol, 1 equiv.), $FeCl_2$ (0.078 mg, 0.61 mmol, 1.07 equiv.), and 20 mL toluene. The vessel was equipped with a magnetic stir bar, capped, removed from the glovebox, and placed in an oil bath thermostated at 150 °C for 14 h. The dark purple mixture was cooled to room temperature, returned to the glovebox, and filtered through a coarse glass frit with celite to remove lithium chloride and excess iron. The celite was washed with benzene until the filtrate was nearly colorless. The solvent was removed *in vacuo* and the resulting purple material recrystallized at -40 °C from 18 mL of 2:1 ratio of hexanes to benzene. The following morning, the mother liquor was decanted and the crystals washed with 4 mL cold (-40 °C) hexanes and dried *in vacuo* to afford ($^{Ar}$L)FeCl (**1**) as a purple crystals (0.400 g, 73%). Characterization data for this compound matches that previously reported.[16] $\mu_{eff}$ (295 K, SQUID) = 5.3 $\mu_B$.

21. Chilton, N. F.; Anderson, R. P.; Turner, L. D.; Soncini, A.; Murray, K. S. *J. Comput. Chem.* **2013**, *34*, 1164–1175.

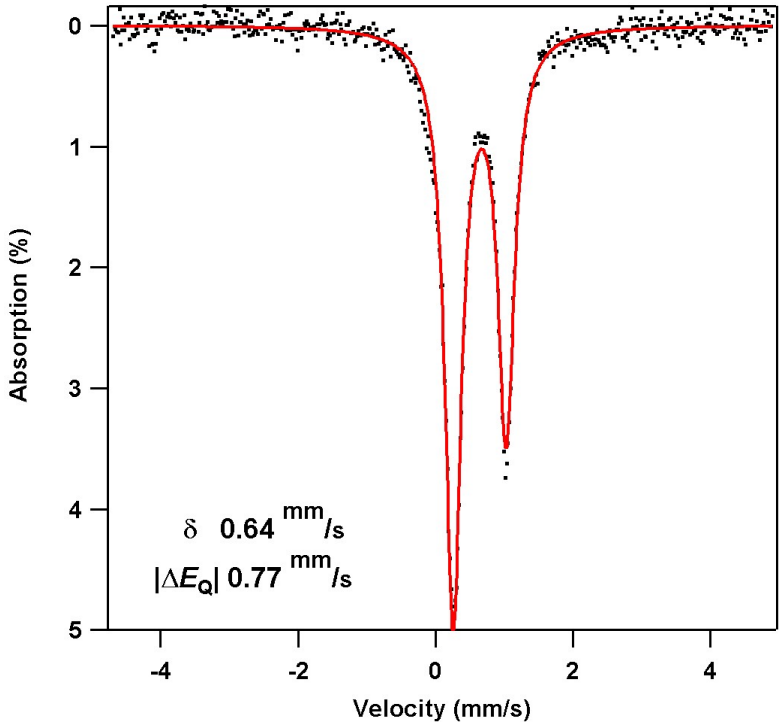


**Figure 2.12.** Zero-field $^{57}$Fe Mössbauer spectrum of micro-crystalline ($^{Ar}$L)FeCl (**1**). Asymmetry of peaks was reproducible and fit with a peak asymmetry ratio of 0.60. Isomer shift and quadrupole splitting are reported relative to Fe foil at room temperature. Parameters calculated via single-point DFT: $\delta$= 0.69 $^{mm}/_{s}$, $\Delta E_Q$: +0.78 $^{mm}/_{s}$.

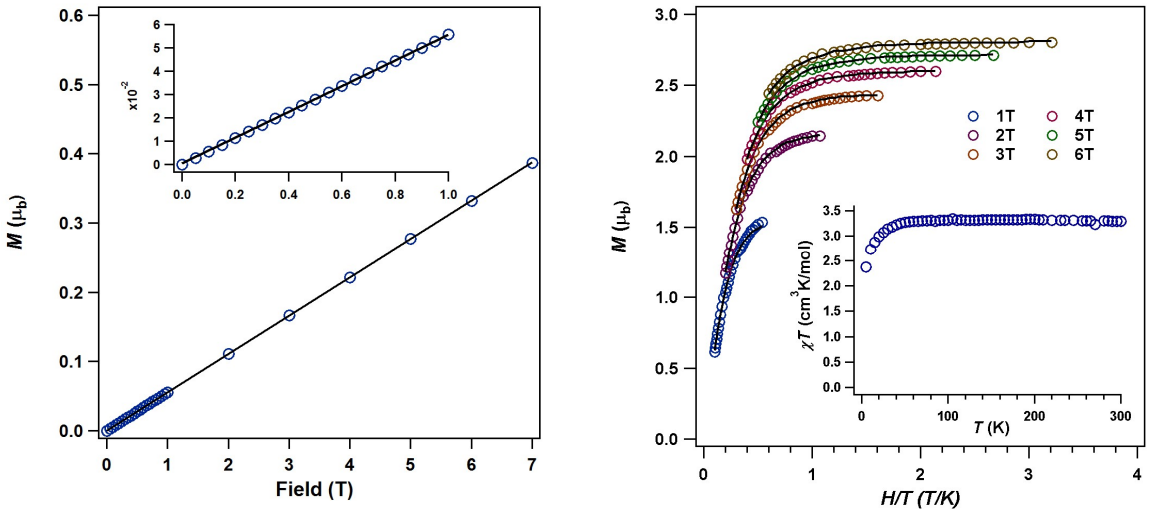


**Figure 2.13.** Magnetometry for ($^{Ar}$L)FeCl (**1**). (left) M vs. H at 100 K is linear, showing absence of ferromagnetic impurity even at low fields (left, inset), (right, inset) $\chi_M$T vs. T at 0.5 T with $\chi_M$T = 3.46 cm$^3$K/mol at 295 K, and (right) reduced magnetization data (M vs. H/T) collected at 6 fields (1-6 T) over the temperature range (1.8 K – 10 K). Reduced magnetization fit parameters: g = 2.63, D = -16.85 cm$^{-1}$, E/D = 0.30 from PHI.[21]

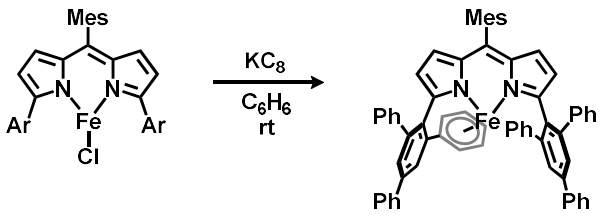


**($^{Ar}$L)Fe (2):** In a 20 mL vial, potassium graphite ($KC_8$, 0.055 g, 0.41 mmol, 1.2 equiv.) was slurried in 1 mL benzene and frozen. A thawing solution of ($^{Ar}$L)FeCl (**1**) (0.322 g, 0.33 mmol, 1.0 equiv.) in benzene was pipetted on top of the frozen slurry and the reaction allowed to stir while warming to room temperature, during which time the color changed from pink to bright purple. After 3 hours, the reaction was filtered through celite and the filter cake eluted with excess benzene until the filtrate was nearly colorless. The solvent was removed *in vacuo* and the solids were dissolved in benzene and again filtered through celite. The solvent was removed *in vacuo* and the resulting material dissolved in minimal benzene and transferred to a 20 mL vial. The solution was frozen and the solvent removed via sublimation *in vacuo* to afford ($^{Ar}$L)Fe (**2**) as a purple powder (0.191 g, 62%). Crystals suitable for X-ray diffraction were grown from a 2:1 *n*-hexane/benzene mixture at −38 °C. $^1$H NMR (400 MHz, 295 K, $C_6D_6$): no observable peaks. $\mu_{eff}$ (150 K, SQUID): 1.7 $\mu_B$. EPR (toluene, 77 K): $g_{eff}$ = 2.24, 2.04, 1.98. Zero-field $^{57}$Fe Mössbauer (90 K) (δ, $|\Delta E_Q|$ ($^{mm}/_s$)): 0.64, *0.86* ($\gamma$ = 0.22 $^{mm}/_s$). %CHN Calc. for $C_{66}H_{49}FeN_2$: C 85.61, H 5.33, N 3.03; Found: C 85.38, H 5.13, N 2.89. HRMS (ESI$^+$) *m/z* calcd $C_{66}H_{49}FeN_2^+$ [M$^+$]: 925.3240, found: 925.3219.

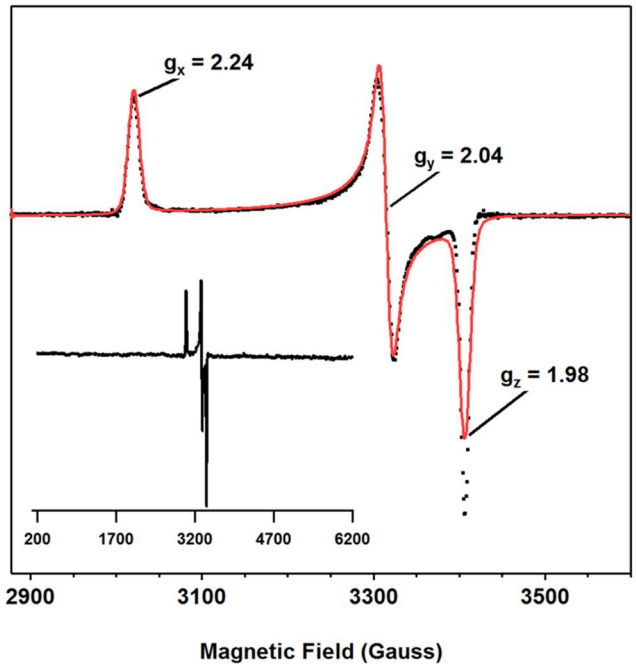


**Figure 2.14.** Frozen toluene EPR spectrum of ($^{Ar}$L)Fe (**2**) at 77K expanded to show rhombic signal with full spectrum shown in the inset. The red line represents a simulation with Easyspin[19] resulting from the labeled $g_{eff}$ values and S = $^1/_2$ spin state as input.

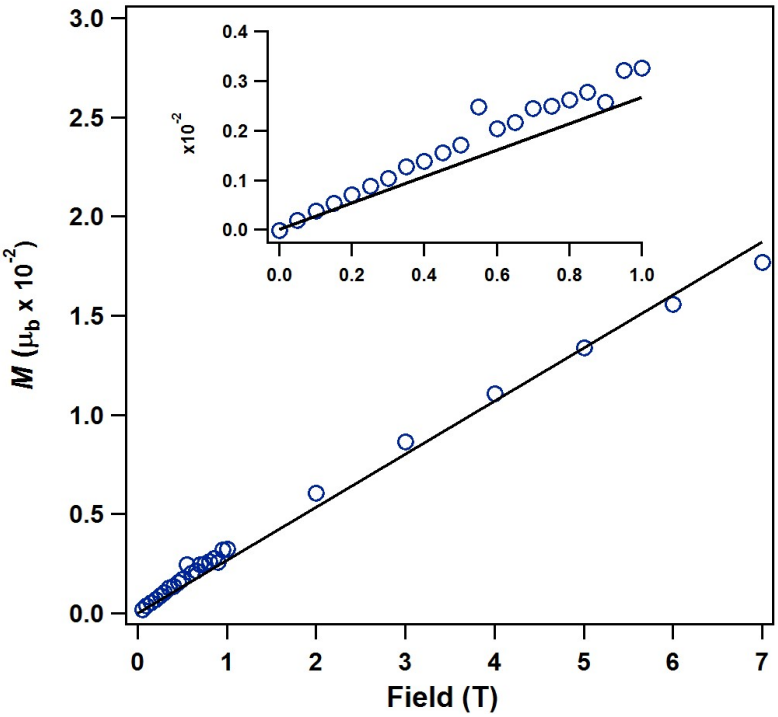


**Figure 2.15.** Solid state magnetometry data for ($^{Ar}$L)Fe (**2**) of M vs. H at 100 K showing absence of a ferromagnetic impurity.

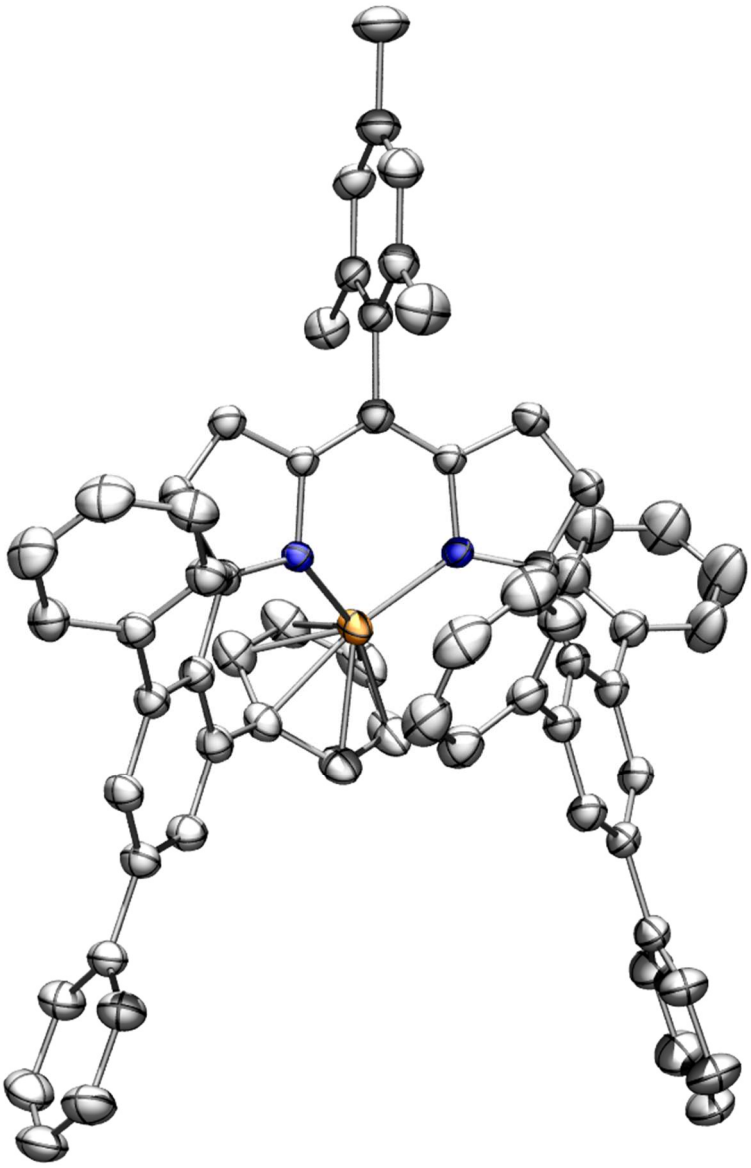

**Figure 2.16.** Solid-state molecular structure for ($^{Ar}$L)FeCl (**1**) with thermal ellipsoids at 35% probability level. Hydrogen atoms not shown. Iron = orange, nitrogen = blue, carbon = gray.

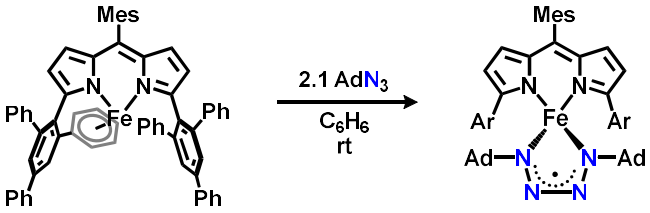


**($^{Ar}$L)Fe(κ$^2$-N$_4$Ad$_2$) (3):** In a 20 mL vial ($^{Ar}$L)Fe (**2**) (80 mg, 0.09 mmol, 1 equiv.) was dissolved in 10 mL of bezene. A solution of adamantyl azide in benzene (3.21 g, 1% *w/w*, 0.18 mmol, 2 equiv) was added resulting in an immediate color change from dark purple to dark red. After stirring for 30 min the solvent was removed *in vacuo*, and the residue washed with *n*-hexane to give the tetrazene complex, **($^{Ar}$L)Fe(κ$^2$-N$_4$Ad$_2$)**, as a dark red powder (98.3 mg, 91%). Crystals suitable for X-ray diffraction were grown from a concentrated toluene solution layered with pentane at −38 °C. $^1$H NMR (400 MHz, $C_6D_6$) δ 31.05, 20.84, 15.40, 15.05 (br s), 14.64, 13.63, 8.76 (br s), 6.73 (d, $J$ = 27.2 Hz), 5.67 (t, $J$ = 7.0 Hz), 5.40 (t, $J$ = 7.2 Hz), 5.30, 4.79, 3.56 (d, $J$ = 7.3 Hz), 1.76, 1.60, 1.55, 1.32 (q, $J$ = 11.4 Hz), -3.49, -5.40, -5.96 (br s), -7.08, -8.68, -9.52, -18.01 (br s), -27.70, -30.73. $\mu_{eff}$ (295 K, SQUID) 4.1 $\mu_B$. EPR (toluene, 4 K): $g_{eff}$ = 6.25, 2.07. Zero-field $^{57}$Fe Mössbauer (90 K) (δ, $|\Delta E_Q|$ ($^{mm}/_s$)): 0.70, *2.74* (γ = 0.27 $^{mm}/_s$). %CHN Calc. for $C_{86}H_{79}FeN_6$: C 82.47, H 6.36, N 6.71; Found: C 82.30, H 6.21, N 6.57. HRMS (ESI$^+$) *m/z* calcd $C_{86}H_{80}FeN_6^+$ [M$^+$]: 1252.5791 found: 1252.5780.

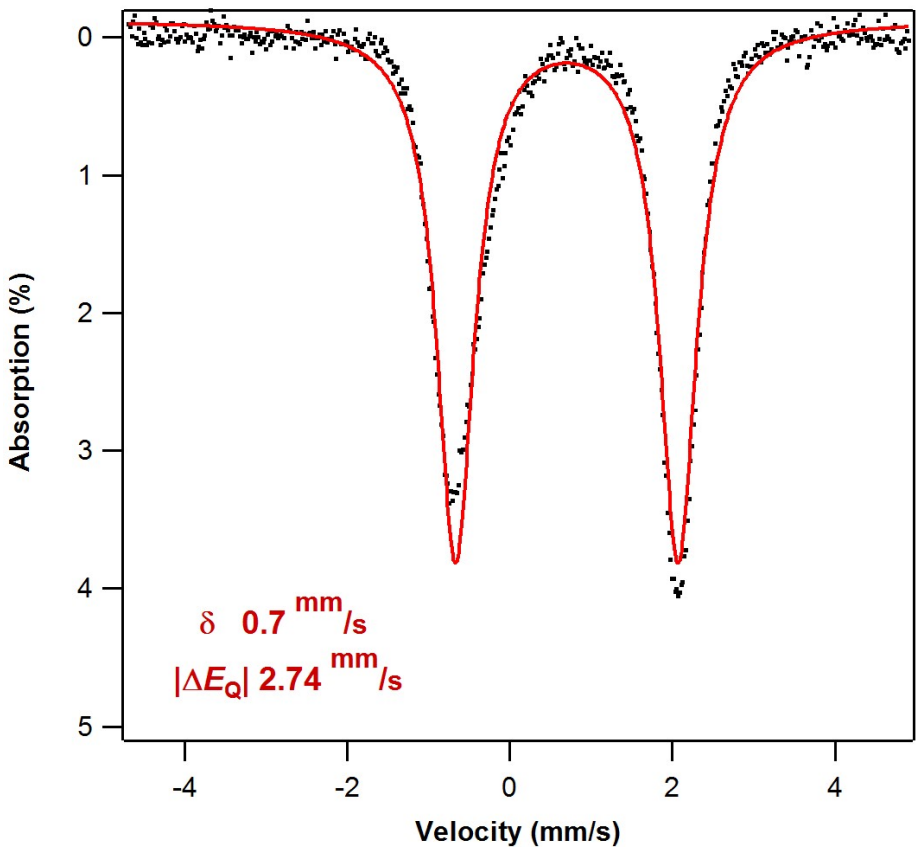


**Figure 2.17.** Zero-field $^{57}$Fe Mössbauer spectrum of ($^{Ar}$L)Fe($\kappa^2$-$N_4Ad_2$) (**3**). Isomer shift and quadrupole splitting are reported relative to Fe foil at room temperature. Parameters calculated via single-point DFT: $\delta$= 0.69 $^{mm}/_{s}$, $\Delta E_Q$= +3.39 $^{mm}/_{s}$.

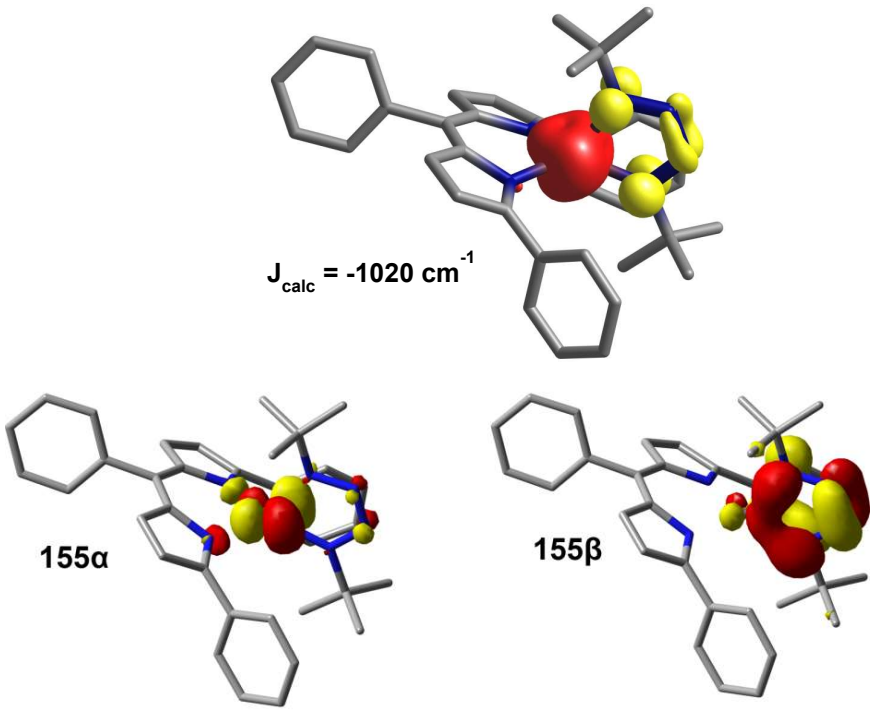


**Figure 2.18.** Mulliken spin density plot for ($^{Ar}$L)Fe($\kappa^2$-$N_4Ad_2$) (**3**) derived from the broken symmetry (4,1) solution demonstrating antiferromagnetic coupling between a high-spin (S = 2) $Fe^{II}$ center and a tetrazene-based radical (S = -$^1/_2$) for an overall S = $^3/_2$ spin state. Shown below are the unrestricted corresponding orbitals for the spin-coupled pair (155α,155β).

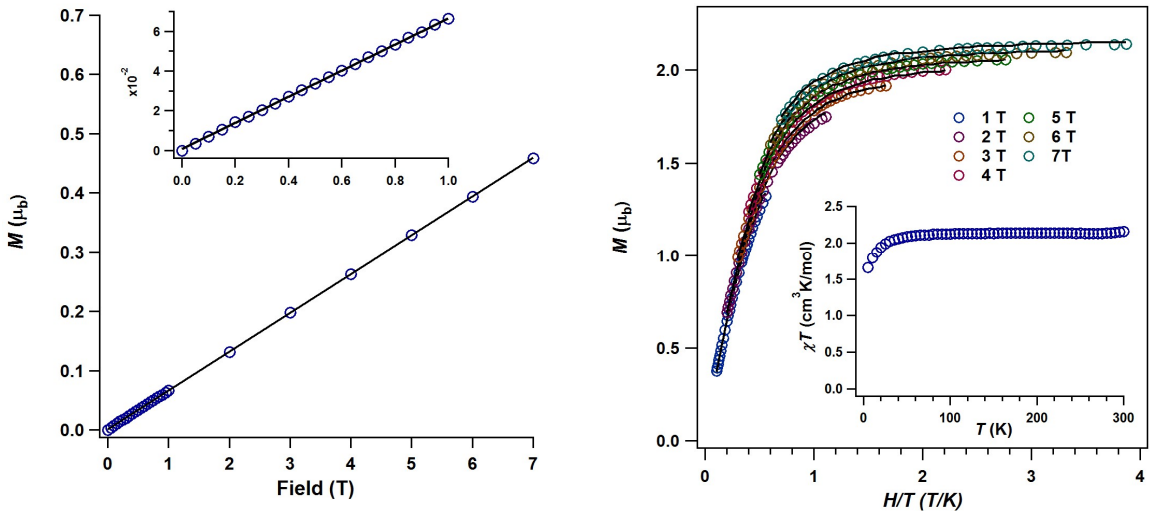


**Figure 2.19.** Magnetometry for ($^{Ar}$L)Fe($\kappa^2$-$N_4Ad_2$) (**3**). (left) M vs. H at 100 K is linear, showing absence of ferromagnetic impurity even at low fields (left, inset), (right, inset) $\chi_M$T vs. T at 0.5 T with $\chi_M$T = 2.15 $cm^3$K/mol at 295 K, and (right) reduced magnetization data (M vs. H/T) collected at 7 fields (1-7 T) over the temperature range (1.8 K – 10 K). Reduced magnetization fit parameters: g = 2.49, D = -20.62 $cm^{-1}$, E/D = 0.02 from PHI.[21]

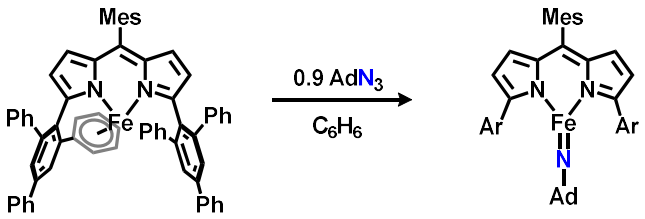


**($^{Ar}$L)Fe(NAd) (4):** A solution of ($^{Ar}$L)Fe (**2**) (101 mg, 94 μmol, 1 equiv.) in 50 mL benzene was transferred to an oven-dried 100 mL round bottom flask. A solution of adamantyl azide in benzene (7.90 g, 0.2% *w/w*, 89 μmol, 0.95 equiv) was added dropwise over the course of 1.5 hours, during which time the color changed from purple to pink. The solvent was removed in vacuo and the resulting solid washed extensively with hexanes to remove unreacted azide and ($^{Ar}$L)Fe and yield ($^{Ar}$L)FeNAd (**4**) as a pink/purple solid (81 mg, 85 %). To remove trace ($^{Ar}$L)Fe($\kappa^2$-$N_4Ad_2$) (**3**), the product was recrystallized from a concentration toluene solution layered with pentane at -40 °C to yield ($^{Ar}$L)Fe(NAd), as purple microcrystals suitable for X-ray diffraction. $^1$H NMR (500 MHz, $C_6D_6$) δ 136.50 (br s), 56.28 (br s), 51.87, 41.60, 37.00, 32.96, 17.89, 10.60, 9.85, 9.43, 2.12, -4.19 (br s), -6.81, -11.79, -26.25, -82.68 (br s). $\mu_{eff}$ (295 K,SQUID) 6.20 $\mu_B$. EPR (toluene, 4 K): $g_{eff}$ = 8.62, 5.35, 3.10. Zero-field $^{57}$Fe Mössbauer (200 K) (δ, $|\Delta E_Q|$ ($^{mm}/_s$)): 0.37, *0.00* ($\gamma$ = 0.50 $^{mm}/_s$). %CHN Calc. for $C_{76}H_{64}FeN_3$: C 84.90, H 6.00, N 3.91; Found: C 84.73, H 5.89, N 4.09. HRMS (ESI$^+$) *m/z* calcd $C_{66}H_{49}FeN_2^+$ [M$^+$]: 1074.4444, found: 1074.4421.

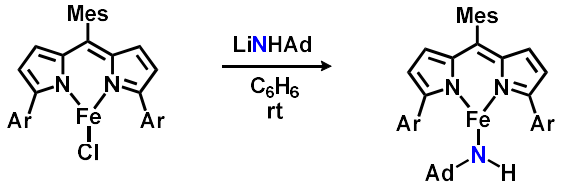


**($^{Ar}$L)Fe(HNAd) (6):** A solution of ($^{Ar}$L)FeCl (**1**) (25.8 mg, 26.8 μmol, 1.0 eq) in 5 mL benzene was added to a stirring slurry of lithium adamantyl amide (4.3 mg, 27.4 μmol, 1.02 eq) in 1 mL benzene. After stirring at room temperature for 8 hours, the reaction was filtered through celite and the filter cake washed with excess benzene until the eluent was nearly colorless. The solvent

was frozen and removed *in vacuo* to yield ($^{Ar}$L)Fe(HNAd) (**6**) as a purple powder (22.2 mg, 77 %) Crystals suitable for X-ray diffraction were grown from a concentrated solution of toluene layered with pentane at –40 °C. $^{1}$H NMR (400 MHz, $C_6D_6$) δ 71.27, 50.96, 49.63 (br), 47.26, 36.07, 25.61, 25.36, 17.53, 13.63, 11.69, 10.97, 9.96, 7.76, 2.26, -12.30, -22.49, -54.93 (br). Zero-field $^{57}$Fe Mössbauer (200 K) (δ, $|\Delta E_Q|$ ($^{mm}/_{s}$)): 0.61, *0.83* ($\gamma$ = 0.17 $^{mm}/_{s}$). %CHN Calc. for $C_{76}H_{65}FeN_3$: C 84.82, H 6.09, N 3.90; Found: C 84.68, H 5.96, N 3.76. HRMS (ESI$^+$) *m/z* calcd $C_{66}H_{49}FeN_2^+$ $[M+THF+MeOH+H]^+$: 1180.54435, found: 1180.5554. Note: ionization of this molecule was very poor, which contributed to the 9.3 ppm error.

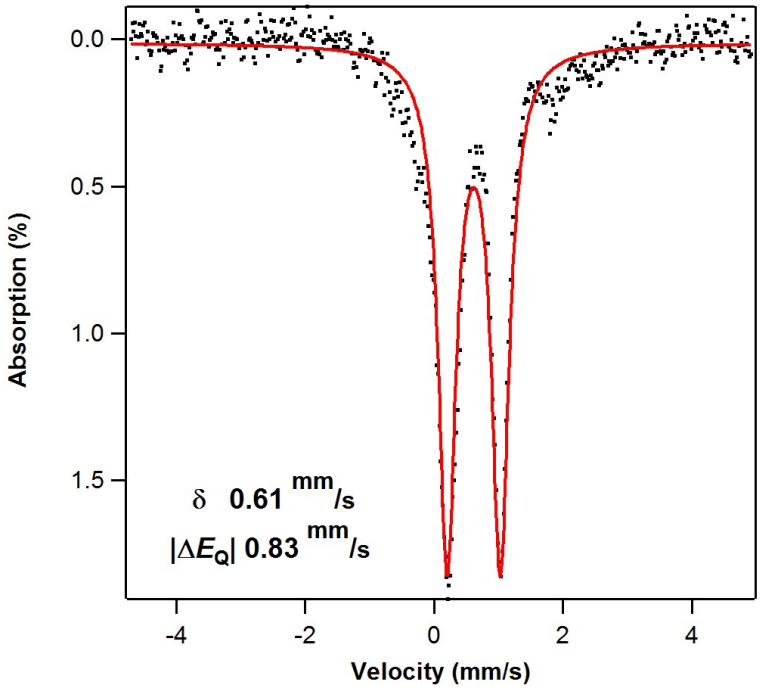


**Figure 2.20.** Zero-field $^{57}$Fe Mössbauer spectrum of ($^{Ar}$L)Fe(NHAd) **(6)**. Isomer shift and quadrupole splitting are reported relative to Fe foil at room temperature. Parameters calculated via single-point DFT: δ= 0.64 $^{mm}/_{s}$, $\Delta E_Q$= +0.98 $^{mm}/_{s}$

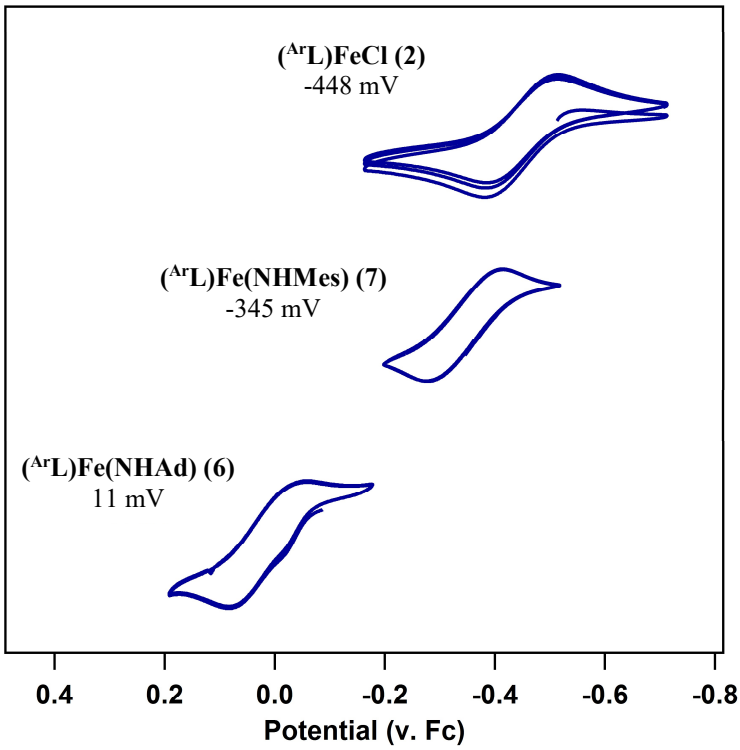


**Figure 2.21.** Comparison of cyclic voltammograms of **(ArL)FeX** obtained in $CH_2Cl_2$ at 25 °C, with 0.1 M ($nBu_4N$)($PF_6$) as supporting electrolyte and a scan rate of 100 mV/s showing a quasi-reversible oxidation event for each sample.

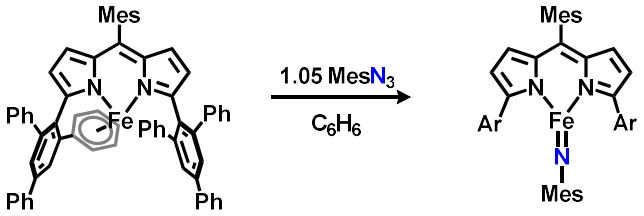


**($^{Ar}$L)Fe(NMes) (5):** A solution of mesityl azide (15 mg, 0.09 mmol, 1.05 equiv) in 1 mL benzene was added all at once to a solution of ($^{Ar}$L)Fe (**2**) (83 mg, 0.089 mmol, 1 equiv.) in 5 mL benzene, causing an immediate color change from purple to pink. The solvent was removed in vacuo and the resulting material recrystallized from a concentrated solution of toluene layered with pentane at -35 °C. The mother liquor was decanted the resulting crystals washed with pentane to yield the product ($^{Ar}$L)FeNMes as purple crystals (70 mg, 74 %). Crystals were suitable for X-ray diffraction prior to pentane washing. $^{1}$H NMR (400 MHz, $C_6D_6$) δ 60.95, 50.58, 38.18, 32.24, 17.51, 14.66, 12.57, 11.13, 5.61, -16.90, -22.01, -49.31. Zero-field $^{57}$Fe Mössbauer (200 K) (δ, $|\Delta E_Q|$ ($^{mm}/_{s}$)): 0.47, *0.00* ($\gamma = 0.82$ $^{mm}/_{s}$).

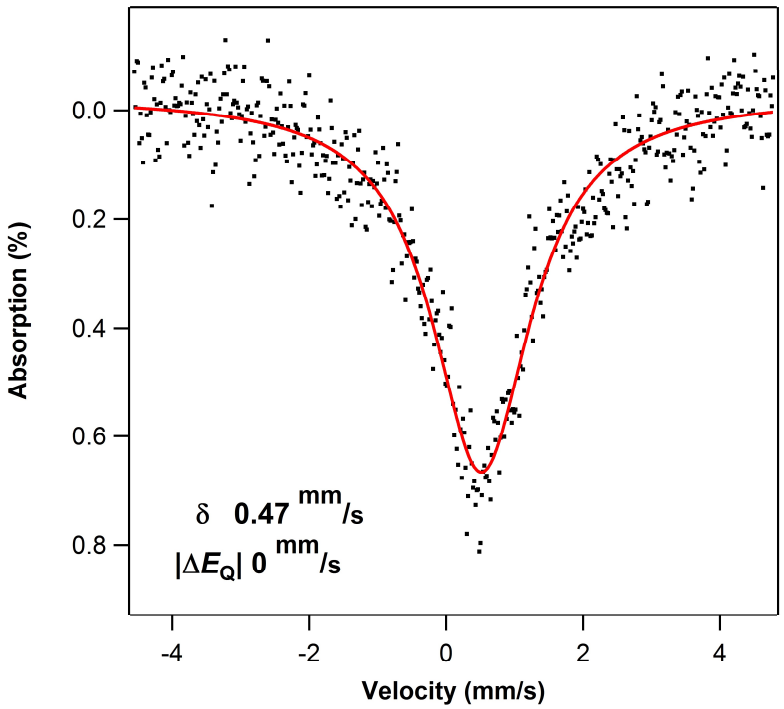


**Figure 2.22.** Zero-field $^{57}$Fe Mössbauer spectrum of ($^{Ar}$L)Fe(NMes) (**5**). Isomer shift and quadrupole splitting are reported relative to Fe foil at room temperature. $\Gamma = 0.82$ $^{mm}/_{s}$.

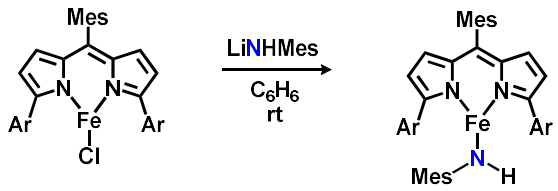


**($^{Ar}$L)Fe(HNMes), 7:** A solution of ($^{Ar}$L)FeCl (**1**) (100 mg, 0.089 mmol, 1.0 eq) in 5 mL benzene was added to a stirring slurry of lithium mesityl amide (14.7 mg, 0.1 mmol, 1.16 eq) in 1 mL benzene. After stirring at room temperature for 8 hours, the reaction was filtered through celite and the filter cake washed with excess benzene until the eluent was nearly colorless. The solvent was frozen and removed *in vacuo* to yield ($^{Ar}$L)Fe(HNMes) as a purple powder (105 mg, 95 %) $^{1}$H NMR (400 MHz, $C_6D_6$) δ 114.03, 93.91, 86.90, 79.20, 49.81, 38.01, 26.62, 14.47, 12.69, 11.62, 10.17, -18.90, -20.26, -34.42. Zero-field $^{57}$Fe Mössbauer (90 K) (δ, $|\Delta E_Q|$ ($^{mm}/_{s}$)): 0.66, *0.46*.

### *2.4.4 Reactivity Experiments*

**Reaction of ($^{Ar}$L)Fe(NAd) (4) with Dimethylphenylphospine.** A J. Young tube was charged with ($^{Ar}$L)Fe(NAd) (5.6 mg, 5.2 $\mu$mol, 1 equiv.) and 0.5 mL benzene-$d_6$. A solution of phosphine, $Me_2PhP$, in benzene-$d_6$ (73 mg, 1% *w/w*, 5.3 $\mu$mol, 1.01 equiv.) was added to the tube. The tube was placed in a thermostated oil bath at 80 °C and after 1 h, formation of the phosphinidine $Me_2PhP$=NAd was confirmed by $^{31}$P NMR (160 MHz, $C_6D_6$) which showed a single peak at −14.80 ppm and disappearance of phosphine at −45.45 ppm. Formation of product was verified by HRMS: (ESI$^+$) *m/z* Calc. $[C_{18}H_{26}NP+H]^+$ 288.1881, Found 288.1862 $[M+H]^+$. Frozen toluene EPR spectrum of the reaction mixture at 77K matched that observed for authentic ($^{Ar}$L)Fe even in the presence of excess (>100 eq) of $Me_2PhP$. The reaction proceeded at room temperature in the presence of excess phosphine.

**Reaction of ($^{Ar}$L)Fe(NAd) (4) with styrene.** A J. Young tube was charged with ($^{Ar}$L)Fe(NAd) (5.0 mg, 5.0 $\mu$mol, 1 equiv.) and styrene (101 mg, 1.0 mmol, 200 equiv.) in benzene-$d_6$. The tube was placed in a thermostated oil bath at 100 °C and monitored every 12 h by $^1$H NMR. After 24 h, all starting material was consumed, revealing a messy paramagnetic NMR. The desired aziridine product was not observed via $^1$H NMR, although a small amount was observed via GC-MS.

**Reaction of ($^{Ar}$L)Fe(NAd) (4) with styrene.** A J. Young tube was charged with ($^{Ar}$L)Fe(NAd) (5.4 mg, 4.7 $\mu$mol, 1 equiv.) and cyclohexene (98 mg, 1.2 mmol, 250 equiv.) in benzene-$d_6$. The tube was placed in a thermostated oil bath at 80 °C and monitored every 12 h by $^1$H NMR. After 72 h, all starting material was consumed, revealing $^{Ar}$LFeNHAd as the major species.

**Reaction of ($^{Ar}$L)Fe(NMes) (5) with 2, 4, 6- tris(*tert*-butyl)phenol.** A J. Young tube was charged with ($^{Ar}$L)Fe(NMes) (4.3 mg, 4.0 $\mu$mol, 1 equiv.), 2, 4, 6-tris(*tert*-butyl)phenol (1.4 mg, 5.3 $\mu$mol, 1.3 equiv.) and 0.7 g benzene-$d_6$. The tube was placed in a thermostated oil bath at 60 °C. After 6 h, paramagnetic peaks consistent with $^{Ar}$LFeNHMes were observed by $^1$H NMR. Further heating encouraged full consumption of $^{Ar}$LFeNMes, but also lead to the consumption of peaks corresponding to $^{Ar}$LFeNHMes and formation of a new set of paramagnetic peaks. The same paramagnetic peaks are observed when $^{Ar}$LFeNHMes and 2, 4, 6-tris(*tert*-butyl)phenoxyl radical are reacted at 60 °C overnight, and likely correspond to an adduct species.

**Reaction of ($^{Ar}$L)Fe(NMes) (5) with toluene.** A J. Young tube was charged with ($^{Ar}$L)Fe(NMes) (6.8 mg, 6.4 $\mu$mol, 1 equiv.) and 1 mL toluene. The tube was placed in a thermostated oil bath at

80 °C. After 24 hours, the tube was removed from the oil bath. Upon cooling to room temperature, the mixture was loaded onto an alumina plug and eluted with 20 mL DCM:MeOH (10:1) to afford a red solution. Trimethoxybenzene was added and the solvent removed *in vacuo*. $^1$H NMR analysis and integration of the benzylic methylene resonance (δ 4.17 ppm in CDCl3) against the trimethoxybenzene standard resulted in a yield of 29%. The product was confirmed via GC-MS.

**Determination of Intermolecular Primary Kinetic Isotope Effect for C–H Insertion Reactions via Intermolecular Competition Experiments.** A 150 μL portion of a solution of ($^{Ar}$L)Fe(NAd) (5.4 mg, 5.0 μmol) in 500 μL toluene was added to a J. Young NMR tube. An equimolar amount of toluene-$d_8$ (150 μL) was added, and the reaction sealed and placed in a thermomstated oil bath at 80 °C for 24 h. The reaction was cooled to room temperature and a 50 μL aliquot was diluted to 100 μL with MeOH and analyzed by LC-MS. Comparison of the area of the selected ion monitoring (SIM) of the formed proteo/duetero products ($A_H/A_D$) were equated to $k_H/k_D$ to give a value of 15.5(3). Three runs were performed to obtain the reported value and the calculated standard deviation. The following product distribution was obtained for proteo-products via GC-MS: N-benzyl-N-adamantylamine, 13.76(7) %; N-benzyl-N-adamantylimine, 2.790(4) %; adamantyl amine, 83.45(8) %. (A series of standard samples composed of a 1:1:2 molar ratio of $PhCH_2NHAd$:PhCHNAd:$AdNH_2$ with concentrations ranging from $3x10^{-8}$ to $1x10^{-4}$ M were run to establish a calibration curve based on absolute concentration.)

**Determination of Intramolecular Primary Kinetic Isotope Effect for C–H Insertion Reactions via Intramolecular Competition Experiments.** A 300 μL portion of a solution of ($^{Ar}$L)Fe(NAd) (6.8 mg, 6.3 μmol) in 1 mL toluene-α-$d_1$ was added to a J. Young NMR tube. The

reaction was sealed and placed in a thermomstated oil bath at 80 °C for 24 h. After cooling to room temperature, a 50 μL aliquot was diluted to 100 μL with MeOH and analyzed by LC-MS. Comparison of the area of the selected ion monitoring (SIM) of the formed proteo/duetero products ($A_H/A_D$) were equated to $k_H/k_D$ to give a value of 11(1). Three runs were performed to obtain the reported value and the calculated standard deviation. The cross-contribution of isotopomers (i.e. the natural isotope pattern of proteo-product has a non-zero contribution to the *m/z* value monitored for mono-deuterated product) was accounted for by utilizing the same LC-MS method for authentic proteo-products, obtaining the ratio of areas measured at each *m/*z value, and considering them in the final $A_H/A_D$ analysis.

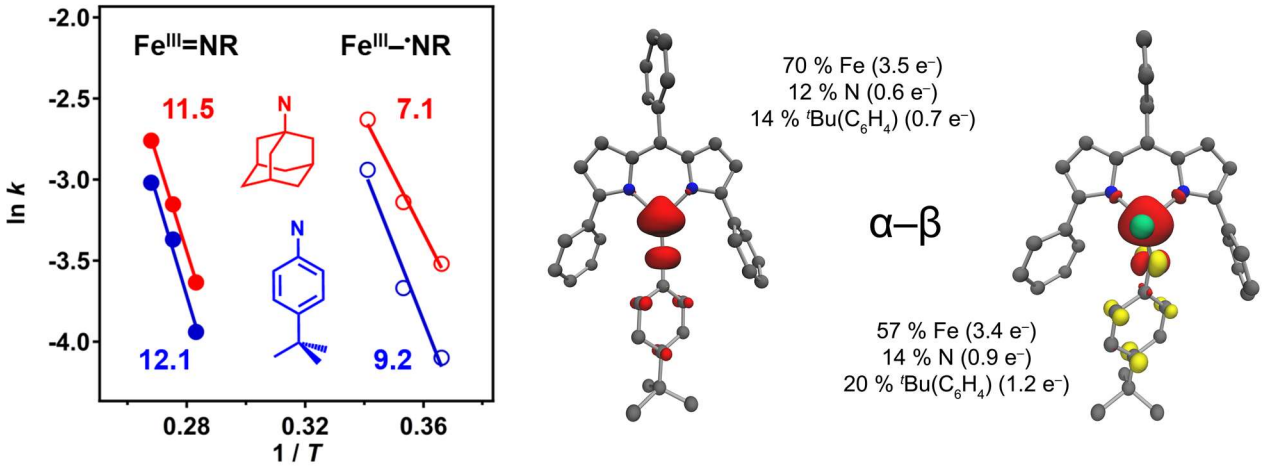


# Chapter 3: Direct comparison of C-H bond amination efficacy through manipulation of nitrogen-valence centered redox: imido versus iminyl[1]

## 3.1 Introduction

Late transition metal complexes featuring metal ligand multiple bonds have been investigated intensely for to probe their efficacy for functional group transfer to organic substrates.[2] Within this class of coordination complexes, iron complexes to which the nitrene functional group (R–N) is bound have now been characterized spanning a large range of oxidation states and electronic structures (Fe$^{II}$ $S$ = 0;

1. This work was conducted in collaboration with Sam MacMillan and Kyle Lancaster from Cornell University, who both collected XAS and EXAFS data with the Stanford Synchrotron Radiation Lightsource and provided analysis of the resulting data.
2. (a) Nugent, W. A.; Mayer, J. M. Metal-Ligand Multiple Bonds: The Chemistry of Transition Metal Complexes Containing Oxo, Nitrido, Imido, Alkylidene, or Alkylidyne Ligands; Wiley-Interscience: Georgetown, **1988**. (b) Saouma, C. T.; Peters, J. C. ME and ME complexes of iron and cobalt that emphasize three-fold symmetry (E=O, N, NR). Coordination Chemistry Reviews, 2011, 255, 920–937. (c) Berry, J. F. Comments Inorg. Chem. **2009**, 30, 28–66. (d) Zhang, L.; Deng, L. C-H bond amination by iron-imido/nitrene species. Chinese Science Bulletin, **2012**, 57, 2352–2360.

$Fe^{III}$ $S = {}^1/_2$, $S = {}^3/_2$, $S = {}^5/_2$; $Fe^{III}(^{\bullet}NR)$ $S = 2$; $Fe^{IV}$ $S = 0$, $S = 1$; $Fe^{V}$ $S = {}^1/_2$).[3] Of these examples, only the high-spin, ferric imido and iminyl complexes have been demonstrated to be competent for nitrene group transfer into aliphatic or olefinic substrates. The unique electronic configuration of the two amination agents warrants further investigation into how the electronic structure of the reactive intermediates impacts functional group transfer from complexes bearing metal ligand multiple bonds.

**Scheme 3.1.** Synthesis of imido (**3**, **5**) and iminyl (**2**, **6**) species.

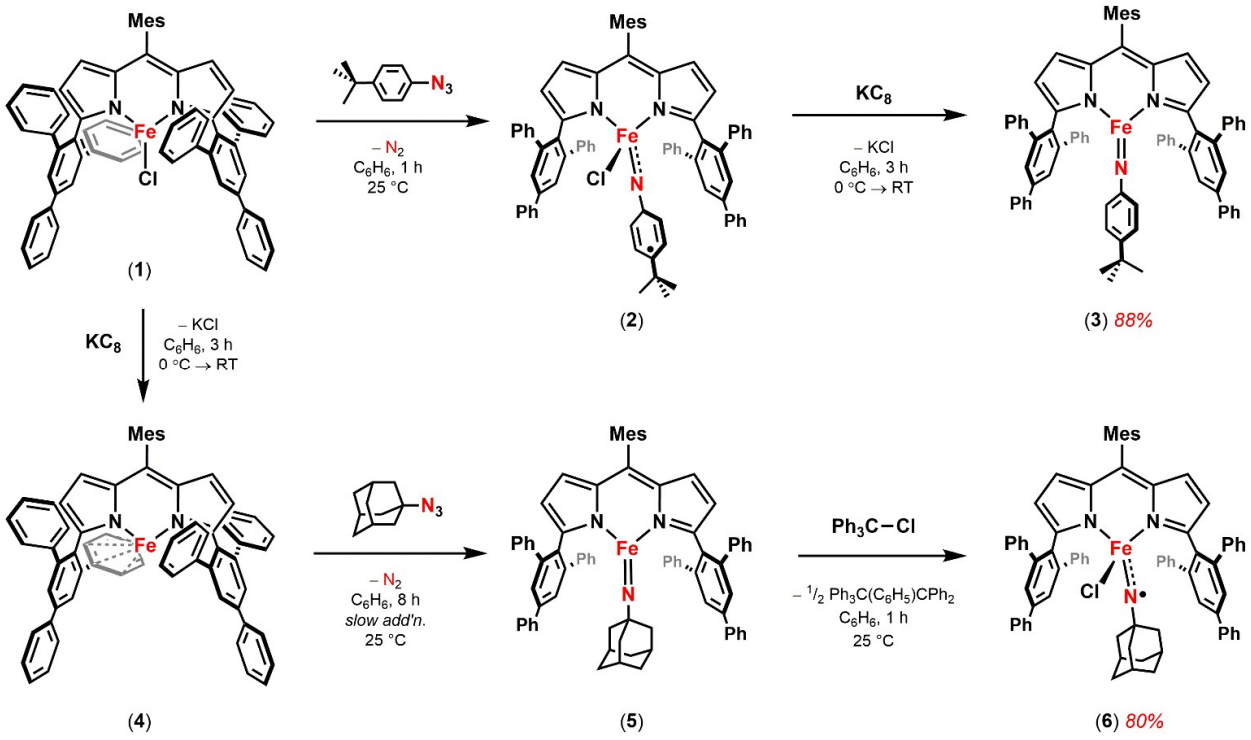


3. (a) Scepaniak, J. J.; Young, J. A.; Bontchev, R. P.; Smith, J. M. *Angew. Chem. Int. Ed. Engl.* **2009**, *48*, 3158–3160. (b) Betley, T. A.; Peters, J. C. *J. Am. Chem. Soc.* **2003**, *125*, 10782–10783. (c) Lu, C. C.; Saouma, C. T.; Day, M. W.; Peters, J. C. *J. Am. Chem. Soc.* **2007**, *129*, 4–5. (d) Cowley, R. E.; Holland, P. L. *Inorg. Chem.* **2012**, *51*, 8352–8361. (e) Brown, S. D.; Betley, T. A.; Peters, J. C. *J. Am. Chem. Soc.* **2003**, *125*, 322–323. (f) Bart, S. C.; Lobkovsky, E.; Bill, E.; Chirik, P. J. *J. Am. Chem. Soc.* **2006**, *128*, 5302–5303. (g) Cowley, R. E.; DeYonker, N. J.; Eckert, N. A.; Cundari, T. R.; DeBeer, S.; Bill, E.; Ottenwaelder, X.; Flaschenriem, C.; Holland, P. L. *Inorg. Chem.* **2010**, *49*, 6172–6187. (h) Brown, S. D.; Peters, J. C. *J. Am. Chem. Soc.* **2005**, *127*, 1913–1923. (i) Nieto, I.; Ding, F.; Bontchev, R. P.; Wang, H.; Smith, J. M. *J. Am. Chem. Soc.* **2008**, *130*, 2716–2717. (j) Verma, A. K.; Nazif, T. N.; Achim, C.; Lee, S. C. *J. Am. Chem. Soc.* **2000**, *122*, 11013–11014. (k) Thomas, C. M.; Mankad, N. P.; Peters, J. C. *J. Am. Chem. Soc.* **2006**, *128*, 4956–4957. (l) Searles, K.; Fortier, S.; Khusniyarov, M. M.; Carroll, P. J.; Sutter, J.; Meyer, K.; Mindiola, D. J.; Caulton, K. G. *Angew. Chemie Int. Ed.* **2014**, *53*, 14139–14143. (m) Searles, K.; Fortier, S.; Khusniyarov, M. M.; Carroll, P. J.; Sutter, J.; Meyer, K.; Mindiola, D. J.; Caulton, K. G.*Angew. Chemie Int. Ed.* **2014**, *53*, 14139–14143. (n) Wang, L.; Hu, L.; Zhang, H.; Chen, H.; Deng, L. *J. Am. Chem. Soc.* **2015**, *137*, 14196–14207. (o) Ni, C.; Fettinger, J. C.; Long, G. J.; Brynda, M.; Power, P. P. *Chem. Commun. (Camb).* **2008**, 6045–6047.

Key to the success of the two examples for which C–H bond amination is observed is the utilization of a weak-field ancillary ligand, [($^{Ar}$L)Fe] where $^{Ar}$L = 5-mesityl-1,9-(2,4,6-$Ph_3C_6H_2$)dipyrrin. We previously have shown that reaction of the ferrous chloride precursor ($^{Ar}$L)FeCl (**1**) with aryl azide $N_3(C_6H_4$-*p*-$^t$Bu) results in formation of the ferric iminyl complex ($^{Ar}$L)FeCl($^{\bullet}$N($C_6H_4$-*p*-$^t$Bu)) (**2**) (Scheme 1), where evidence of the iminyl radical can be seen in disruption of the iminyl aryl substituent. For example, reaction of **1** with $(C_6H_5)N_3$ results in bimolecular, radical coupling of the phenyl iminyl ligands to afford the diferric product [($^{Ar}$L)FeCl]$_2$(μ-N(Ph)($C_6H_5$)N), allowing for unambiguous spectroscopic assignment of the ferric state. A room temperature solution magnetic moment determination of **2** (5.3(1) $\mu_B$) in conjunction with agreement of the spectroscopic Mössbauer parameters between **2** and the bimolecularly-coupled product suggest the quintet **2** is comprised of a high-spin ferric center antiferromagnetically coupled to an iminyl radical [$S_{total} = (S_{ferric}\ ^5/_2) - (S_{iminyl}\ ^1/_2) = 2$].

**Scheme 3.2.** Previously reported iron-catalyzed C–H amination.

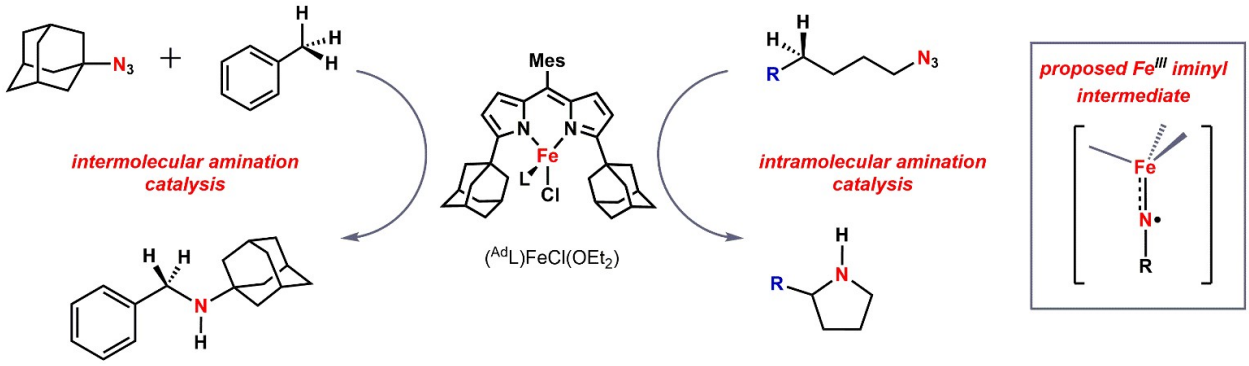


Although this electronic structure had been suggested previously,[4] **2** constitutes the first structurally and spectroscopically authenticated example of a transition metal stabilized iminyl complex. The isolated iminyl **2** was shown to be competent for both intermolecular amination of toluene as well as

4. (a) Shay, D. T.; Yap, G. P. A.; Zakharov, L. N.; Rheingold, A. L.; Theopold, K. H. *Angew. Chem., Int. Ed.* **2005**, 44, 1508. (b) Kogut, E.; Wiencko, H. L.; Zhang, L.; Cordeau, D. E.; Warren, T. H. *J. Am. Chem. Soc.* **2005**, 127, 11248. (c) Badiei, Y. M.; Dinescu, A.; Dai, X.; Palomino, R. M.; Heinemann, F. W.; Cundari, T. R.; Warren, T. H. *Angew. Chem., Int. Ed.* **2008**, 47, 9961. (d) Lu, C. C.; De Beer George, S.; Weyhermüller, T.; Bill, E.; Bothe, E.; Wieghardt, K. *Angew. Chem., Int. Ed.* **2008**, 47, 6384.

azirdination of styrene in stoichiometric reactions. Employing the less sterically demanding 1,9-adamantyl substituted dipyrrin ligand ($^{Ad}$L) allowed for the nitrene-transfer reaction to be run catalytically using 1-adamantylazide as an oxidant (Scheme 2). Although no reactive intermediate could be isolated or observed during the catalytic processes, the similarity between the kinetic isotope effects observed for both the stoichiometric and catalytic amination processes suggested a common ferric iminyl reactive intermediate was operative.

Oxidative group transfer with both alkyl ($AdN_3$) and aryl ($MesN_3$) azides to the monovalent iron complex ($^{Ar}$L)Fe (**4**) resulted in isolable ferric imido products ($^{Ar}$L)Fe(NAd) (**5**) and ($^{Ar}$L)Fe(NMes) (Scheme 1). The imido complexes were characterized and described as possessing genuine metal ligand multiple bond character with structural features similar to those reported for ferric imidos.[5] Unlike those literature precedents, the imido complexes were spectroscopically determined to be high-spin ($S = {}^5/_2$). Akin to their ferric iminyl congeners, the imido complexes were shown to be competent for both H-atom abstraction and nitrene transfer to benzylic C–H bond substrates.

Given the common core electronic structure ($S_{ferric} = {}^5/_2$) between the imido and iminyl molecular species, we sought to address the following questions through a comparative examination of two distinct molecular oxidation levels: (1) What are the redox stabilities of iminyl **2** and imido **5**? Are their respective imido and iminyl congeners electrochemically or chemically accessible? (2) We propose that the aryl-substituent in iminyl **2** is critical to stabilization of the iminyl functionality via delocalization of the radical throughout the aromatic ring. If chemical oxidation of the alkyl imido **5** is possible, would the oxidation of the complex be borne on the iron center resulting in a $Fe^{IV}$ oxidation state akin to the hydroxylating ferryl compound I in cytochrome P450? Or would a similar ferric-stabilized iminyl radical [e.g,

5. (a) Scepaniak, J. J.; Young, J. A.; Bontchev, R. P.; Smith, J. M. *Angew. Chem. Int. Ed. Engl.* **2009**, *48*, 3158–3160. (b) Betley, T. A.; Peters, J. C. *J. Am. Chem. Soc.* **2003**, *125*, 10782–10783. (c) Lu, C. C.; Saouma, C. T.; Day, M. W.; Peters, J. C. *J. Am. Chem. Soc.* **2007**, *129*, 4–5. (d) Cowley, R. E.; Holland, P. L. *Inorg. Chem.* **2012**, *51*, 8352–8361. (e) Brown, S. D.; Betley, T. A.; Peters, J. C. *J. Am. Chem. Soc.* **2003**, *125*, 322–323. (f) Bart, S. C.; Lobkovsky, E.; Bill, E.; Chirik, P. J. *J. Am. Chem. Soc.* **2006**, *128*, 5302–5303. (g) Cowley, R. E.; DeYonker, N. J.; Eckert, N. A.; Cundari, T. R.; DeBeer, S.; Bill, E.; Ottenwaelder, X.; Flaschenriem, C.; Holland, P. L. *Inorg. Chem.* **2010**, *49*, 6172–6187

$Fe^{III}(^{\bullet}NR)]$ be observed without the ability to delocalize the radical, as proposed for the intra- and intermolecular amination catalysts? Furthermore, can the two redox resonance forms be spectroscopically distinguished [$Fe^{IV}(NR) \leftrightarrow Fe^{III}(^{\bullet}NR)$]? (3) Lastly, if both the redox isomers are accessible for both alkyl and aryl imido/iminyl aryl moieties, how is the change in molecular oxidation level manifest in C–H bond amination efficacy? Herein we report our findings concerning the interconversion of the imido/iminyl redox forms, describe their comparative metal oxidation states using X-ray absorption spectroscopy, and provide a kinetic assessment of their reactivity in intermolecular amination.

## 3.2 Results and Discussion

### *3.2.1 Redox stability of imide/iminyl units*

To assess the redox stability of iminyl **2** and imido **5**, cyclic voltammetry (CV) was performed on both complexes (**Figure 3.1**). CV examination of iminyl **2** in dichloromethane show a quasi-reversible reduction event at –1.05 V versus $[Cp_2Fe]^{0/+}$ (**Figure 3.1a**). The anticipated imido complex may well dissociate the chloride ligand, akin to three-coordinate ($^{Ar}$L)Fe(NMes). The quasi-reversible couple

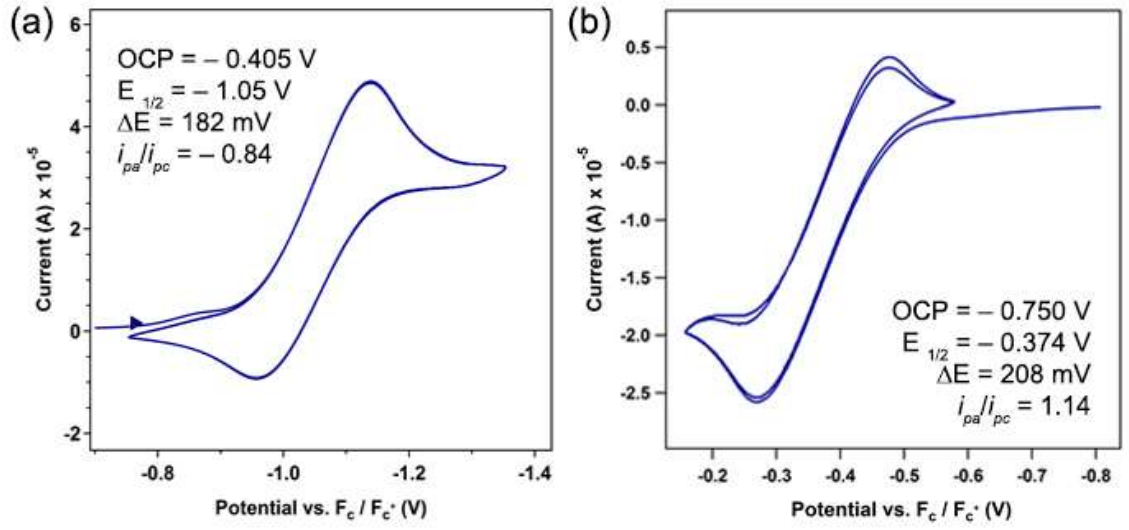


**Figure 3.1.** Cyclic voltammograms of **2** (a) and **5** (b) obtained in $CH_2Cl_2$ at 25 °C, with 0.1 M ($^n$Bu$_4$N)($PF_6$); 100 mV/s; referenced to $[Cp_2Fe]^{0/+}$ couple.

suggests a chemical process indeed occurs following reduction. The electrochemical behavior of imido **5** was also investigated and its cyclic voltammogram reveals a quasi-reversible oxidation event was observed at –374 mV versus versus $[Cp_2Fe]^{0/+}$ (**Figure 3.1b**). Given the reduction of 2 and oxidation of 5 constitute the same nominal redox couple, it is worth noting the large cathodic shift afforded by coordination of the chloride ligand and the aryl iminyl moiety (Δ = –0.676 V). The redox potential for adamantyl imido **5** is also mildly anodically shifted as compared with the more electron rich analogues ($E_{1/2}$ (vs. $[Cp_2Fe]^{0/+}$) for [{tris(carbeno)borate}Fe(NAd)]$^+$ –0.64 V,[2i] [{bis(phosphino)pyrazolylborate}Fe(NAd)]$^+$ –0.72 V[2k]), though the comparison is not straightforward given the coordination number change between species (3- vs. 4-coordinate).

### *3.2.2 Synthesis and spectroscopic characterization of imido Fe(N(C$_6$H$_4$-p-$^t$Bu) and iminyl FeCl(˙N(C$_6$H$_4$-p-$^t$Bu) pair*

While oxidative group transfer to the monovalent iron synthon **2** can afford imido complexes with sterically encumbered alkyl azides or o-substituted aryl azides, no terminal imido complexes could be obtained upon treatment of **2** with $N_3(C_6H_4$-*p*-$^t$Bu) and only the tetrazene adduct was obtained ($(^{Ar}L)Fe(N_4(C_6H_4$-*p*-$^t$Bu$)_2$). Given the mild reduction potential for **2**, chemical reduction was thus pursued as a means for generation of the terminal imido analogue. Accordingly, reduction of **2** with potassium graphite in thawing benzene-$d_6$ resulted the formation of a new paramagnetic complex via $^1$H NMR. The molecular structure of three coordinate iron imido ($^{Ar}$L)Fe(N(C$_6$H$_4$-*p*-$^t$Bu)) (**3**) was obtained by single crystal X-ray diffraction studies on single crystals grown from a concentrated toluene solution layered with pentane at –35 °C (**Figure 3.2a**). The molecular structure features a distorted trigonal planar iron(III) center supported by the dipyrrin ligand and the aryl imido. The Fe–N3 distance of 1.708(4) Å in **3** is longer than iron imido bond in **5** (1.674(11) Å), and nearly identical to that found in the mesityl imido ($^{Ar}$L)Fe(NMes) (1.708(2) Å), though far shorter than the corresponding distance in **2** (1.768(2) Å). The pertinent bond distances to compare **2** and **3** are presented in (**Figure 3.2**). Notably, all of the carbon-

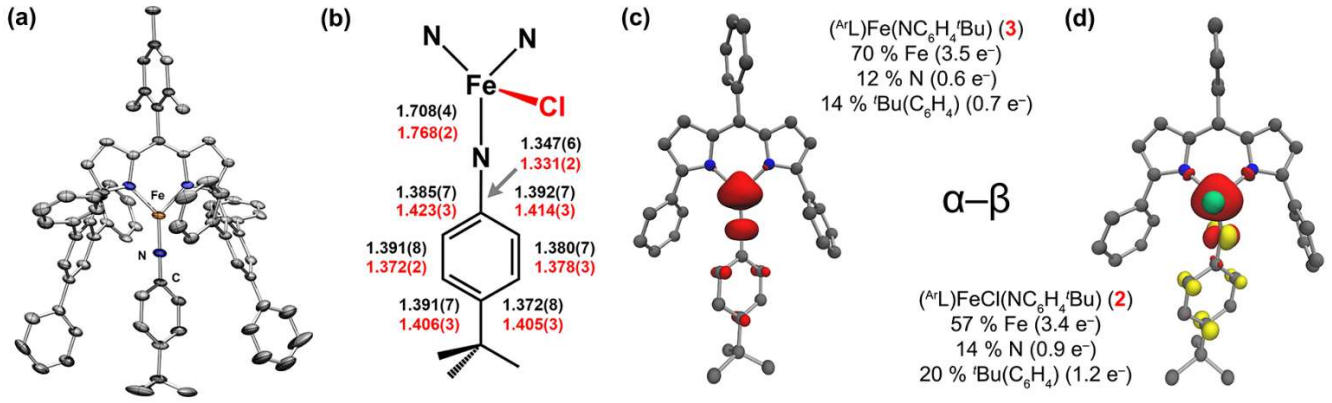


**Figure 3.2.** (a) Solid state molecular structure of **3** with thermal ellipsoids at the 35 % probability level. Positional disorder, solvent molecules, and H atoms are removed for clarity. Color scheme: Fe, orange; N, blue; C, gray. (b) Selected bond metrics (Å) for imido **3** in black with corresponding metrics for iminyl **2** in red. Mulliken spin density plots (*α–β*) and values calculated for **3** (c) and **2** (d).

carbon bonds within the imide aryl ring in **3** are equivalent within error, indicating the aromaticity of the imido aryl framework has been restored from the iminyl **2** upon reduction.

Further spectroscopic characterization of **3** reveals data in line with that observed for the alkyl imido **5**. The zero-field $^{57}$Fe Mössbauer spectrum displays a single broad transition (δ: 0.44 $^{mm}/_{s}$, $|\Delta E_Q|$: 0.00 $^{mm}/_{s}$) at 200 K that becomes broad and weakly absorbing at lower temperature (Figure 3a). In accordance with the observed temperature dependent phenomena (*vide supra*), **3** does not exhibit an EPR signal above ca. 50 K. The frozen toluene EPR spectrum of **3** obtained at 4 K displays a rhombic signal ($g_{eff}$ = 5.99, 4.43, 1.93), well reproduced by an $S = {}^5/_2$ simulation treating each intra-doublet transition as an effective $S = {}^1/_2$ system (in accordance with the weak-field limit) and including the effects of both rhombicity ($^E/_D$) and *D*-strain (simulation parameters: g = 1.95, $^E/_D$ = 0.05, linewidth = 15 G). The inclusion of *D*-strain is necessary to account for the randomness in spatial confirmation of the frozen solution and provide an effective powder pattern for a given *S* and $^E/_D$.[20] The data and corresponding simulation are shown in (**Figure 3.16**). Accordingly, solid-state magnetometry of **3** is consistent with a high spin state as evidenced by a $\mu_{eff}$ of 5.3 $\mu_B$ ($\chi_M T$ = 3.51 cm$^3$ K/mol) at 295 K (Figure S6). The value of $\chi_M T$ over the temperature range surveyed is consistent with an $S = {}^5/_2$ configuration (spin-only value

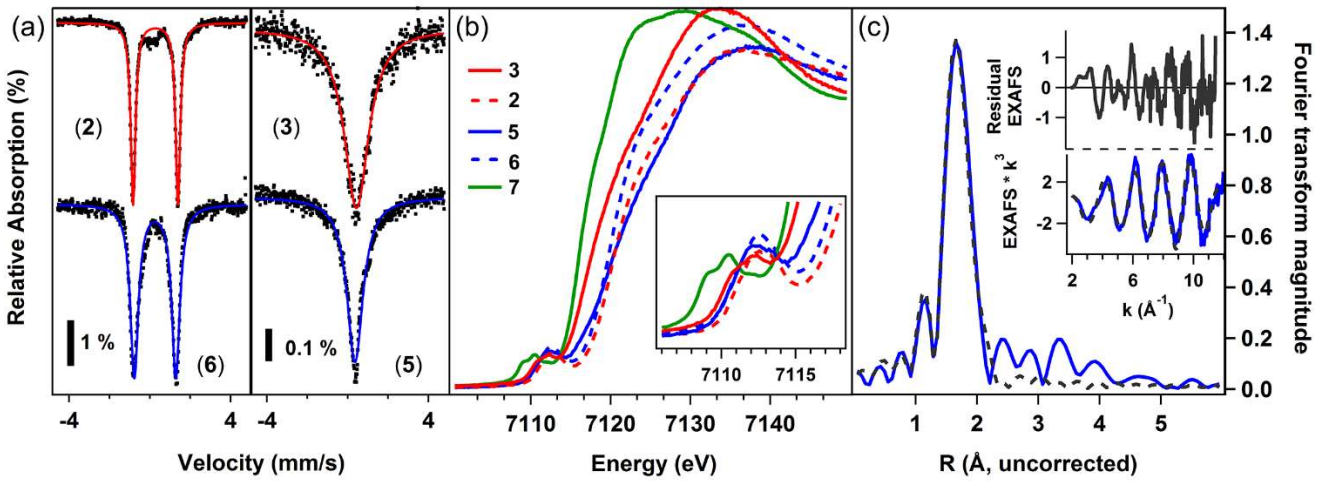


**Figure 3.3.** (a) Zero-field $^{57}$Fe Mossbauer spectra of iminyl **2** (top left, red trace: $\delta = 0.28$ $^{mm}/_{s}$, $|\Delta E_Q| = 2.22$ $^{mm}/_{s}$, $\Gamma = 0.14$ $^{mm}/_{s}$), iminyl **6** (bottom left, blue trace: $\delta = 0.26$ $^{mm}/_{s}$, $|\Delta E_Q| = 2.05$ $^{mm}/_{s}$, $\Gamma = 0.24$ $^{mm}/_{s}$); imido **3** (top right, red trace: $\delta = 0.44$ $^{mm}/_{s}$, $|\Delta E_Q| = 0.00$ $^{mm}/_{s}$, $\Gamma = 0.74$ $^{mm}/_{s}$), and **5** (bottom right, blue trace: $\delta = 0.37$ $^{mm}/_{s}$, $|\Delta E_Q| = 0.00$ $^{mm}/_{s}$, $\Gamma = 0.50$ $^{mm}/_{s}$). (b) Overlaid Fe K-edge XANES with inset Fe 1s → Fe 3d pre-edge features for **3** (solid red), **2** (dashed red), **5** (solid blue), **6** (dashed blue), **7** (solid green). (c) EXAFS for **6** with data shown in red and theoretical fit in black dashes.

anticipated is 4.38 cm$^3$ K/mol). The spin state suggested by the magnetic susceptibility data is further corroborated by variable-temperature, variable-field magnetization data collected on heating from 1.8 to 10 K and at increasing fields of 1–7 T (**Figure 3.12**). Magnetization saturation occurs at 2.6 $\mu_B$ at 1.8 K and 7 T. The lower than expected saturation (5 $\mu_B$ for an ideal $S = {}^5/_2$ with g = 2) and the observation of nonsuperimposable isofield curves indicates the presence of zero-field splitting and rhombicity, which was quantifed by fitting the date to the spin Hamiltonian $\hat{H} = D\hat{S}_z^2 + E(\hat{S}_x^2 - \hat{S}_y^2) + g_{iso}\mu_B$ **S•H**.[6] The fit parameters considering an $S = {}^5/_2$ that best reproduce the data are $g = 2.00$, D = 13.4.0 cm$^{-1}$, |E/D| = 0.29.

The original spin-state assignment for iminyl **2** was based on room temperature, solution magnetic moment determination. Thus we sought to probe the ground spin state electronic structure for this molecule to corroborate the quintet assignment. Solid-state magnetometry was collected on a sample of **2**, cleanly isolated following removal of H-atom sources via treatment of reaction glassware with trimethylsilylchloride, use of perdeuterated solvents, and immediate purification of azide prior to synthesis. The magnetic susceptibility reveals a well isolated ground state with no thermal transitions

6. Chilton, N. F.; Anderson, R. P.; Turner, L. D.; Soncini, A.; Murray, K. S. *J. Comput. Chem*. **2013**, 34, 1164.

apparent between 50 – 300K (**Figure 3.4**). Both the room temperature effective magnetic moment of 5.1 $\mu_B$ ($\chi_M T$ = 3.28 cm$^3$ K/mol) and reduced magnetization data can be well modeled as an $S = 2$ spin system (**Figure 3.4**). The spin state suggested by the magnetic susceptibility data is further corroborated by variable-temperature, variable-field magnetization data collected on heating from 1.8 to 10 K and at increasing fields of 1–7 T. Magnetization saturation occurs at 2.81 $\mu_B$ at 1.8 K and 7 T. The lower than expected saturation (4 $\mu_B$ for an ideal $S = 2$ with g = 2) and the observation of non-superimposable isofield curves indicates the presence of zero-field splitting and rhombicity, which was quantifed by fitting the date to the spin Hamiltonian $\hat{H} = D\hat{S}_z^2 + E(\hat{S}_x^2 - \hat{S}_y^2) + g_{iso}\mu_B$ **S•H**. The fit parameters considering an $S$ = 2 that best reproduce the data are $g$ = 2.12, D = –8.8 cm$^{-1}$, $|E/D|$ = 0.33.

As noted above, the magnetic susceptibility for **2** plateaus between 50 – 300 K without variation in the susceptibility. Thus, the strength of the antiferromagnetic coupling between the ferric site ($S_{Fe}$ = $^5/_2$) and iminyl moiety must exceed ca. 200 cm$^{-1}$, in line with the value predicted via DFT methods and supporting a broken-symmetry electronic structure of **2** ($J_{DFT}$ = –673 cm$^{-1}$).

Taking the data for the iminyl/imido pair of **2** and **3**, respectively, the data collectively support an assignment of **2** as a high-spin Fe$^{III}$ center antiferromagnetically coupled to an iminyl centered radical. Upon reduction of **2**, the added electron populates an orbital that is principally imide-based to restore aromaticity to the imide aryl π-system, maintaining the ferric oxidation state. The unusual stability of the ferric iminyl state could reasonably be attributed to the resonance stabilization afforded via π-delocalization within the iminyl aryl unit. To gain insight into the location of the redox, single-point DFT calculations on the iminyl **2** and imido **3** complexes was performed. The calculated spin density plots (α – β) for **2** and **3**, shown in Figure 2c-d, illustrate the contributions to the total spin contributed by iron (**2**: 57%; **3**: 70%) and the imido unit (**2**: 34%; **3**: 26%). The total spin contribution from the imido/iminyl aryl substituent is even more apparent in the oxidized iminyl structure where the contribution exceeds that of the iminyl N whereas the contributions are nearly equal in the imido (**2**: 12% N, 14% Ar; **3**: 14% N, 20% Ar). Successful preparation of the corresponding N-alkyl complex, where such delocalization is not

possible, would thus demonstrate that this electronic structure is not dictated by the imide substituent and, rather, is inherent to the system.

### *3.2.3 Synthesis and spectroscopic characterization of an alkyl iminyl ($^{Ar}$L)FeCl(•NAd)*

To synthesize the alkyl iminyl analogue to **2**, a solution of triphenylmethylchloride was added to a solution of imido **5** in thawing benzene-$d_6$ and allowed to stir for 1 h at room temperature. After 1 h elapsed and the reaction solution changed in color from pink to maroon, assessment of the reaction progress by $^1$H NMR revealed the consumption of **5** with concomitant formation of a new paramagnetic species and $Ph_3C(C_6H_5)CPh_2$. The reaction volatiles were removed in vacuo and the resultant precipitate

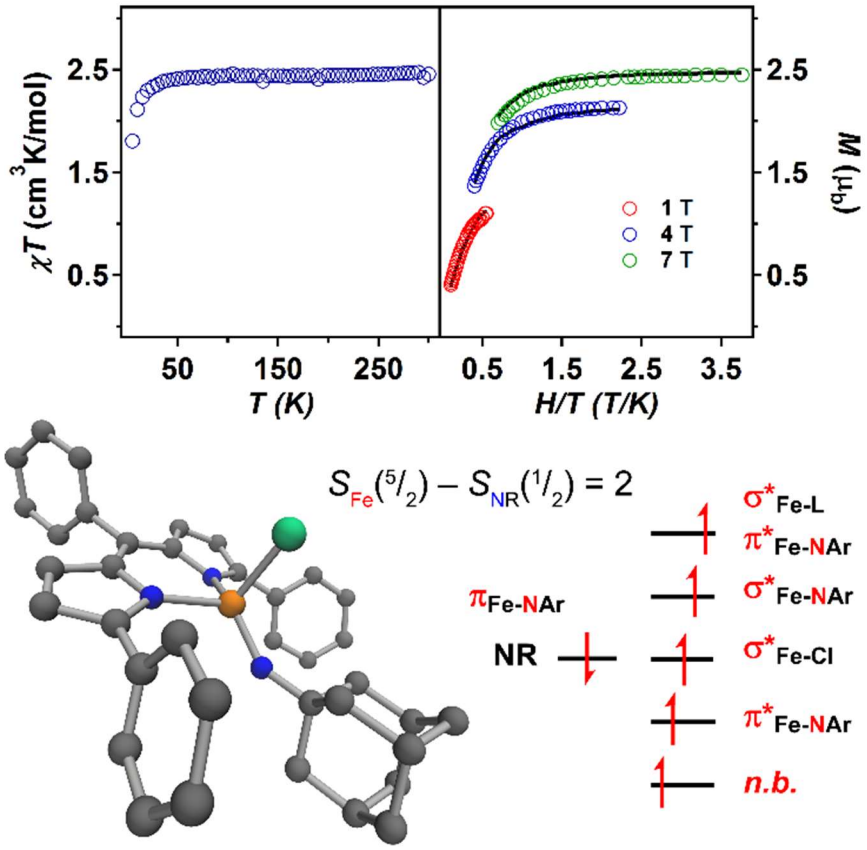


**Figure 3.4.** (top left) Variable-temperature susceptibility data of (ArL)FeCl(•NAd) (6) collected at 1.0 T, with χMT = 2.46 cm3K/mol at 295 K. (top right) Reduced magnetization data collected at 4 fields (1, 4, 7 T) over the temperature range 1.8 K–10 K. Magnetization fit parameters obtained with PHI: $S$ = 2, $g$ = 1.95, $D$ = 6.9 cm$^{-1}$, $|E/D|$= 0.33. (bottom) Geometry optimized structure (BP86) and qualitative molecular orbital diagram for **6**, illustrating the antiferromagnetic coupling between the high-spin Fe$^{III}$ and the iminyl radical.

was washed with pentane. Dissolution of the maroon solids in benzene followed by lyophilization yielded a maroon powder (80% yield). The zero-field $^{57}$Fe Mossbauer spectrum of the new material displayed a clean quadrupole doublet (δ: 0.26 $^{mm}/_{s}$, $|\Delta E_Q|$: 2.05 $^{mm}/_{s}$) with parameters very similar to those observed for **2** (δ: 0.26 $^{mm}/_{s}$, $|\Delta E_Q|$: 2.05 $^{mm}/_{s}$) (both shown in **Figure 3.3a**), suggesting a shared iron oxidation state, spin state, and geometric configuration, leading us to formulate the product as ($^{Ar}$L)FeCl($^{\bullet}$NAd) (**6**). The magnetic susceptibility of **6** is shown in **Figure 3.4** (top panel), revealing a magnetic susceptibility of 4.4 $\mu_B$ at 295 K ($\chi_M T$ = 2.46 cm$^3$ K/mol) consistent with an $S$ = 2 ground state electronic configuration. The spin state suggested by the magnetic susceptibility data is further corroborated by variable-temperature, variable-field magnetization data collected on heating from 1.8 to 10 K and at increasing fields of 1–7 T (**Figure 3.4**, top panel). Magnetization saturation occurs at 2.6 $\mu_B$ at 1.8 K and 7 T. The lower than expected saturation (4 $\mu_B$ for an ideal $S$ = 2 with g = 2) and the observation of non-superimposable isofield curves indicates the presence of zero- field splitting and rhombicity, which was quantifed by fitting the date to the spin Hamiltonian $\hat{H} = D\hat{S}_z^2 + E(\hat{S}_x^2 - \hat{S}_y^2) + g_{iso}\mu_B$ **S•H**. The fit parameters considering an $S$ = 2 that best reproduce the data are $g$ = 1.95, D = 6.9 cm$^{-1}$, and $|^E/_D|$ = 0.33. Thus, the data support a view of **6** as an Fe$^{III}$ iminyl complex even in the absence of an iminyl aromatic π–framework throughout which the nitrogen centered radical can delocalize.

### *3.2.4 Extended X-ray absorption fine structure analysis of iminyl 6*

The reactive nature of **6** made obtaining suitable single crystals for X-ray diffraction analysis very difficult. Thus, XAS and EXAFS analysis on a benzene solution of **6** was undertaken. The Fourier transform of the EXAFS region of the XAS spectrum for **6** to k = 10 Å$^{-1}$ (resolution = 0.15 Å) is well-modeled via a first shell simulation considering two pyrrole nitrogens, one chloride, and one iminyl nitrogen scattering paths (**Figure 3.3c**). The values are shown in **Table 3.1** and are nearly identical to the crystallographically determined bond lengths of **2** (Fe – $N_{pyrrole}$ 2.013(1) Å, 1.997(1) Å; Fe – Cl 2.210(1) Å; Fe – $N_{iminyl}$ 1.768(2) Å). The experimental bond lengths are reproduced well by theory. A geometry

optimized structure of **6** yields the following primary coordination sphere interatomic distances (Fe – $N_{pyrrole}$ 2.006 Å; Fe – Cl 2.246 Å; Fe – $N_{iminyl}$ 1.718 Å) and is presented in Figure 4. The resolution of the data is sufficient to differentiate the $N_{pyrrole}$ and $N_{iminyl}$ scattering paths, although it is not sufficient to detect asymmetry in the individual Fe–$N_{pyrrole}$ scattering paths. The structural corroboration of the composition of **6** as ($^{Ar}$L)FeCl($^{\bullet}$NAd) supports the assignment of **6** as a high-spin ($S = {}^5/_2$) $Fe^{III}$ center antiferromagnetically coupled to an iminyl radical ($S = -{}^1/_2$) (schematically depicted in Figure 3), in analogy to **2**. As such, we believe that oxidation of imido **5** affects the valence at the imido nitrogen, preserving the high-spin ferric electronic configuration at iron.

**Table 3.1.** EXAFS simulation of 4-Ad[a]

| path | CN | $R$ (Å) | $\sigma^2$ (Å) | $E_0$ |
|---|---|---|---|---|
| Fe–$N_{pyrrole}$ | 2 | 1.987 | 0.00034 | -7.6103 |
| Fe–Cl | 1 | 2.222 | 0.0011 | |
| Fe–$N_{iminyl}$ | 1 | 1.761 | 0.00036 | |

[a]EXAFS were fit in OPT using paths calculated by FEFF7. Coordination numbers (CN) were held constant while distances (R) and Debye-Waller factors ($\sigma^2$) were allowed to float. Errors in distances are estimated to be 0.02-0.03 Å and 25% for coordination numbers. Fits were performed over the entire (0 to 6.0 Å) Fourier transform window. Goodness of fit is measured by F, defined as $[(\sum_i^n [k_i^3(\mathrm{EXAFS}_{obs} - \mathrm{EXAFS}_{calc})_i])^2 / n]^{1/2}$.

### *3.2.5 X-ray absorption near edge spectroscopy on imidos 3 and 5; iminyls 2 and 6*

In light of the challenges associated with assignment of metal oxidation state in the presence of high-lying ligand-based molecular orbitals, samples of both imido/iminyl pairs (**3** and **2**; **5** and **6**) were investigated by X-ray absorption near edge spectroscopy and the results shown in **Figure 3.3b**. Note, given the coordination number change as well as potential change in iron-imido/iminyl covalency, comparison of the rising edge energy will not adequately reflect the respective metal oxidation levels for the three-coordinate imido and four coordinate iminyl complexes. Iron K-edge pre-edge absorption features are typically assigned to Fe 1s → 3d excitations, although in the present case appreciable ligand character can be expected in the acceptor molecular orbitals. Nevertheless, the maxima of the resolved

pre-edge features demonstrate that upon reduction of iminyl **2** (7111.5 eV) to imido **3** (7111.5 eV), or oxidation of imido **5** (7112.2 eV) to iminyl **6** (7112.4 eV), very little change in the physical oxidation state is seen. For comparison, the energy-weighted maximum of the resolved pre-edge bands of the ferrous product of **1** and adamantyl amine ($^{Ar}$L)FeCl($NH_2$Ad) (**7**) is shifted to lower energy (7110.3 eV), consistent with a more reduced iron center in this complex as compared to the other species studied. Comparison of the aryl and alkyl imido/iminyl pairs, the pre-edge absorption feature for the alkyl species (**5**, **6**) are shifted to higher energy compared with the aryl congeners (**2**, **3**) by 0.7 eV for the imido complexes and 0.9 eV for the iminyl complexes. The shift in energy is nearly as great as the difference between the ferrous complex examined (**7**) and the ferric imido (1.2 eV).

### *3.2.6 Comparative kinetic analysis for the imido/iminyl complexes undergoing C–H bond activation with toluene*

The isolation of iron imide/iminyl redox pairs provides a unique opportunity to investigate the effect of altering the valence of the transferred atom during a C–H functionalization reaction without affecting the transition metal oxidation state. Dissolution of iminyl complexes **2** or **6** in toluene results in immediate reaction, as demonstrated by the change in UV/Vis absorption over time (**Figure 3.5**). The change in absorbance at $\lambda_{max}$ can be fit as an exponential decay and the resulting observed rate constant is shown in **Table 3.2**. In contrast, the UV/Vis spectrum of the imido complexes **3** or **5** in toluene is identical to that observed in solvent benzene and does not change over the course of four hours at room temperature. In fact, a similar rate of reaction to those exhibited by the iminyl species are not achieved until the solution is heated to 80 °C, indicating a substantially higher barrier towards reactivity with toluene for the imidos **3** and **5**. Assuming a simple kinetic profile wherein the change in absorbance at $\lambda_{max}$ is directly related to the consumption of staring material (imido or iminyl) and the reaction course is not significantly altered by temperature, the activation energy can be extracted from these data for each complex and is presented in Table 2.

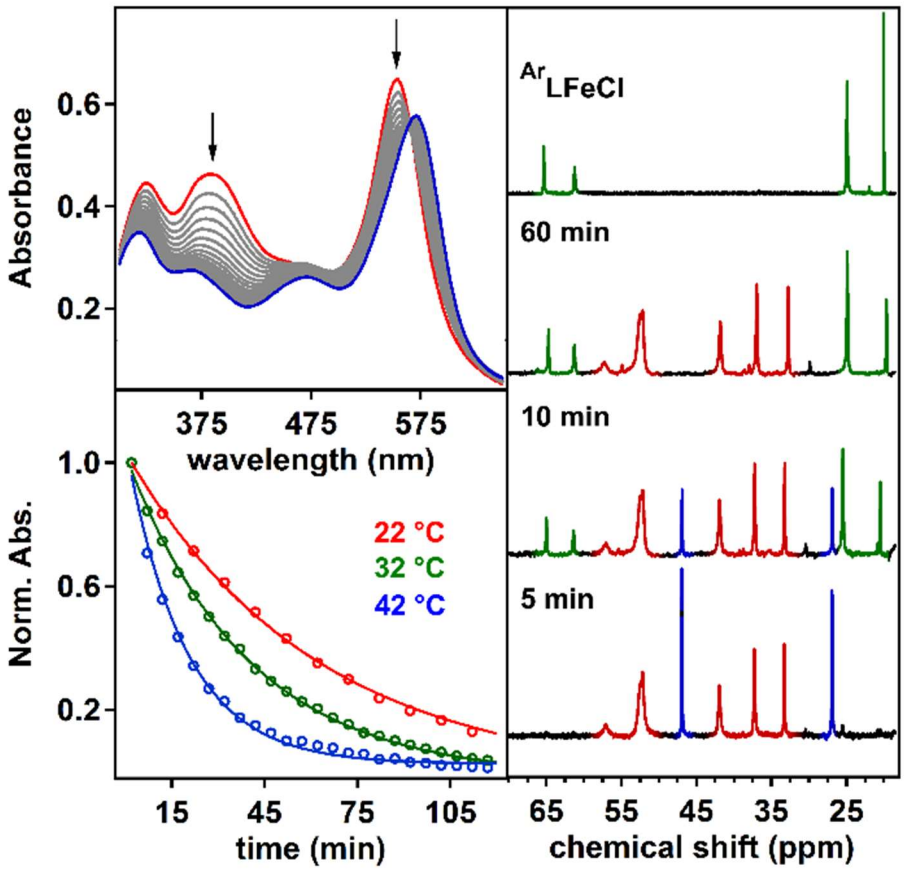


**Figure 3.5.** (Top left) UV/Vis traces of the reaction of **2** with toluene at 22 °C with spectra recorded every 10 minutes for 4 hours. (Bottom left) Normalized absorbance at $\lambda_{max}$ (554 nm) during the course of the reaction at various temperatures. (Right) $^{1}$H NMR spectra progression of a toluene solution of equimolar imido **5** and iminyl **6** at 60 °C at the time elapsed indicated. Chemical shifts corresponding to **5** are highlighted in red, **6** in blue, and ($^{Ar}$L)FeCl (**1**) in green.

Upon oxidation of the nitrogen atom from the imide to the iminyl state, the barrier for reaction with toluene is decreased by an average of 3.7 $^{kcal}/_{mol}$. The enhancement of reactivity can be rationalized by the additional radical density present on the nitrogen atom which more closely resembles the electronic structure at the transition state for hydrogen atom abstraction. This simple Hammond-type analysis is in line with the higher activation energy for the aryl imido and iminyl complexes **3** and **2**, respectively, which feature electron delocalization through the aromatic fragment as opposed to the localized spin density at the transferring nitrogen atom of **5** and **6**. Alternatively, the higher molecular oxidation state may also contribute to the increase in reactivity via an Bell-Evans'-Polyani-type correlation,[7] wherein the rate

7. Mayer, J. M. *Acc. Chem. Res.* **2011**, *44*, 36.

**Table 3.2.** Rate constants, half-lives, and activation energies for reaction of iron complexes with toluene[a].

| Complex | T (°C) | k ($s^{-1}$) | $t_{1/2}$ (min) | $E_a$ ($^{kcal}/_{mol}$) |
|---|---|---|---|---|
| **5** | 80 | 0.0264 | 26 | 11.5 |
| | 90 | 0.0427 | 16 | |
| | 100 | 0.0633 | 11 | |
| **3** | 80 | 0.0195 | 36 | 12.1 |
| | 90 | 0.0343 | 20 | |
| | 100 | 0.0745 | 9 | |
| **6** | 22 | 0.0299 | 23 | 7.1 |
| | 32 | 0.0433 | 16 | |
| | 42 | 0.0722 | 10 | |
| **2** | 22 | 0.0166 | 42 | 9.2 |
| | 32 | 0.0256 | 27 | |
| | 42 | 0.0528 | 13 | |

[a]Exponential decay of $\Delta(\lambda_{max})$ versus time was fit independently each temperature.

enhancement upon oxidation is attributable to the increased driving force of the reaction as a result of a higher oxidation potential or enhanced N–H bond strength of the resulting metal-amide product. Regardless, the activation parameters for reaction of these iron imide complexes with toluene demonstrate a higher enthalpic barrier upon oxidation or upon substitution with an aromatic imide substituent, suggesting that both a higher metal-imide bond order and delocalization through the aromatic π-system stabilize the iron imide with respect to hydrogen atom abstraction.

Comparison of the independent rates of reaction for **5** and **6** suggest that a rate enhancement of two orders of magnitude occurs upon oxidation. Indeed, heating an equimolar ratio of **5** and **6** to 60 °C in toluene results in selective consumption of the iminyl complex **6** and formation of a new set of paramagnetic resonances via $^{1}$H NMR. The appearance of these chemicals shifts can be attributed to the formation of ($^{Ar}$L)FeCl and occurs concomitantly with a peak at 3.72 *ppm* corresponding to N-benzyl-adamantylamine. The competition experiment validates the independent rate studies and demonstrates that the iminyl complex **6** is significantly more reactive towards C–H bonds than its imido congener **5**. The increased reactivity of **6** is not limited to C–H amination (**Scheme 3.3**): imido **5** is stable in neat

**Scheme 3.3.** Reactivity of iron imide and iminyl complexes.

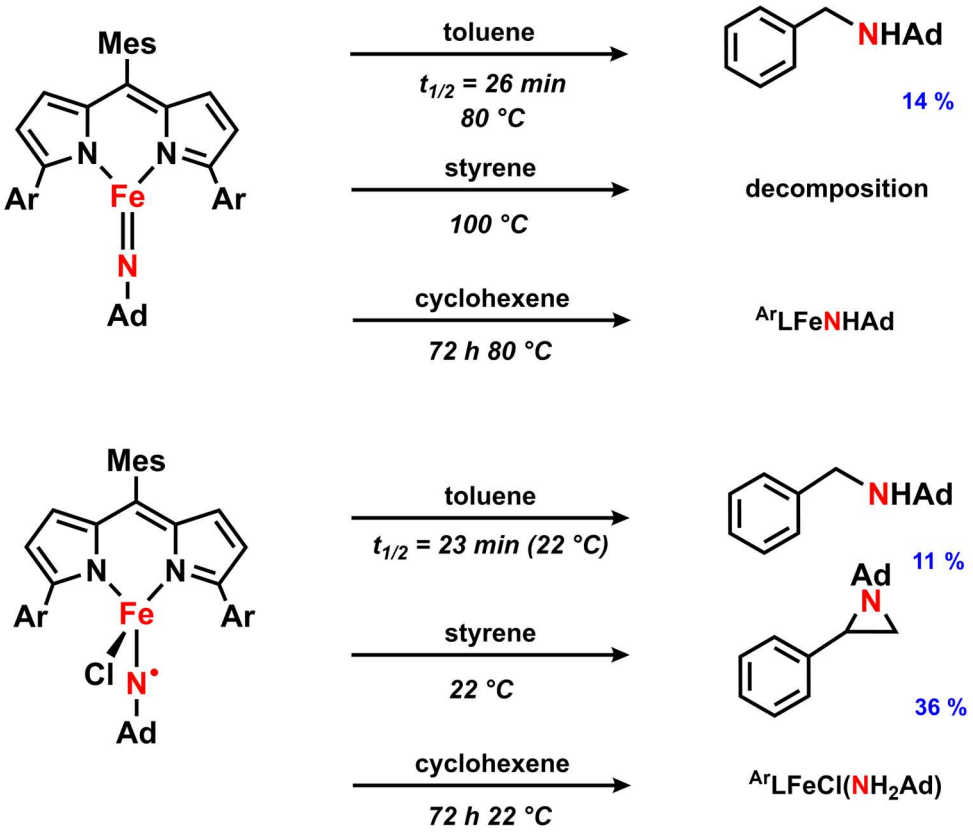


styrene up to 100 °C, whereas iminyl **6** reacts smoothly with 200 equiv. styrene at room temperature to yield the desired aziridine in 36 % yield. Further, hydrogen atom abstraction from cyclohexene occurs at room temperature with iminyl **6** whereas the imido congener **5** requires heating to 80 °C.

## 3.3 Reaction pathways and thermodynamic considerations

### *3.3.1 Frontier molecular orbital considerations*

The electronic structure of the imido and iminyl differ in the extent to which both *N* 2p orbitals engage in π-bonding with iron orbitals of appropriate symmetry. The imido complexes feature nearly linear Fe–N–C bond linkages, signifying maximal, though non-degenerate, π interactions: $\pi_x$ [$\sigma^*_{(dxz - L\sigma)} \pm Np_x$] which includes a Fe–$L_{dipyrrin}$ $\sigma^*$ component, and the orthogonal $\pi_y$ (Fe $d_{yz} \pm Np_y$). The high-spin imido complexes give rise to a $(\pi_x)^2(\pi_y)^2(\pi_y^*)^1(\pi_x^*)^1$ configuration. The iminyl complexes, however, lack

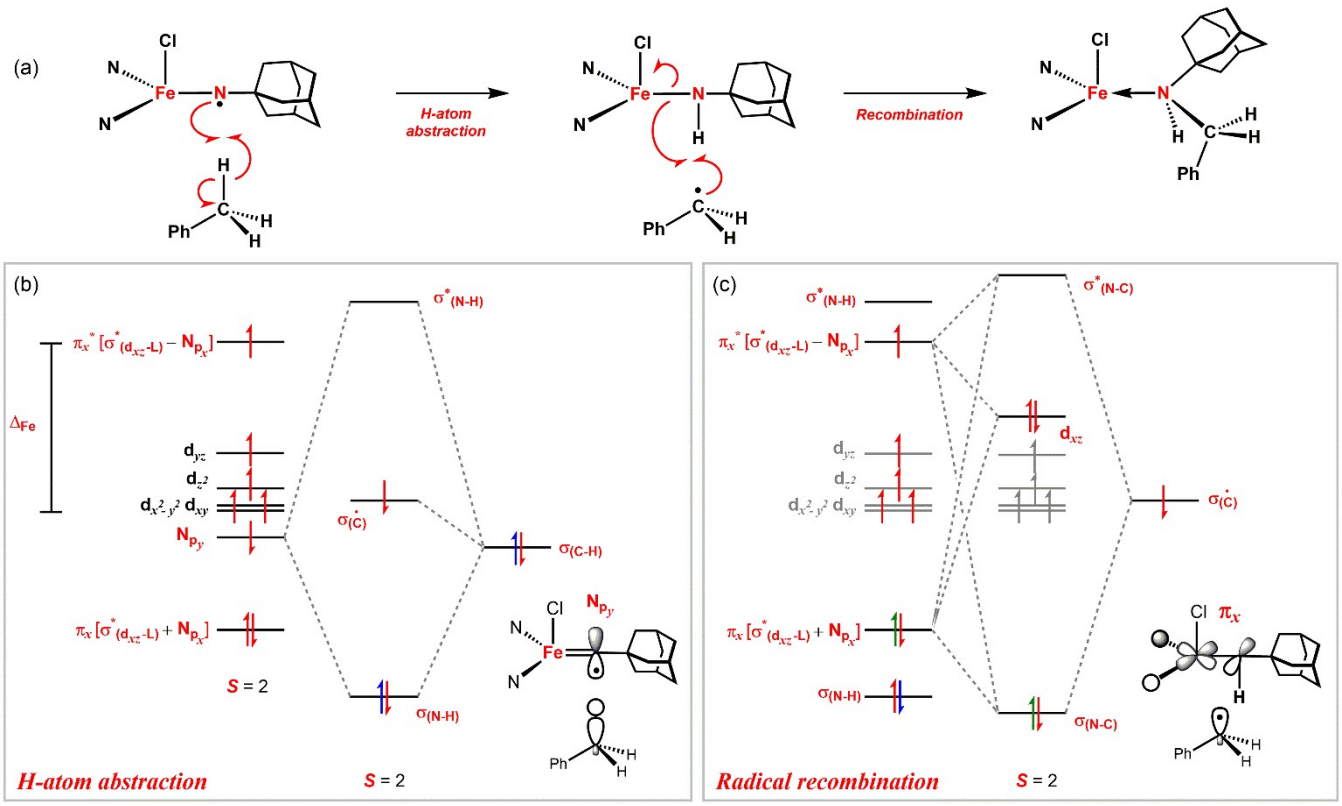


**Figure 3.6.** Frontier molecular orbital description of ($^{Ar}$L)FeCl(NAd) (**6**) reaction profile (a) for H-atom abstraction from $PhCH_3$ (b) and the subsequent radical rebound event (c).

conjugation of the two π manifolds. Indeed, a simple description for the iminyl consistent with the iron oxidation levels observed by $^{57}$Fe Mössbauer and XAS, consists of only the $\pi_x$ interaction, leaving a largely *N*-centered radical for **6**. While the iminyl radical lacks the enhanced stabilization afforded by delocalization in the aromatic ring of **2**, the radical is nonetheless stabilized by coupling antiferromagnetically to the five iron α spins (see Figure 6b). This electronic configuration is manifest in the larger Fe–N bond lengths observed, as well as the enhance reactivity of the iminyl with respect to the imido congener.

We have previously proposed a reaction sequence for intermolecular amination using imido **5**. We can amend that orbital description to describe qualitatively the reactivity differences observed between the imido and iminyl congeners. The large KIEs observed in the reactions of both imido (**3**, **5**) and iminyls (**4**, **6**) with toluene suggest that the C–H bond breaking event contributes significantly to the rate limiting step of the reaction sequence illustrated for **6** in **Figure 3.6**.

A consideration of the frontier molecular orbitals (FMOs) that complete this process include the Fe–N π interaction ($\pi_x$), the N 2py orbital containing the iminyl radical, and the toluene C–H σ bond (see Figure 6b). The N-radical $(2p_y)^1$ dictates the primary orbital interaction with the incoming toluene C–H substrate given its steric accessibility and more favorable energetic overlap. Thus the frontier orbital interaction with respect to the iron-iminyl is lower in energy than the analogous imido amination reaction which proceeds from the $(\pi_y^*)^1$ orbital. The H-atom abstraction step is highlighted in Figure 6b, where the homolyzed C–H orbital (yielding $PhC^{\bullet}H_2$ and H 1s) combine with N $2p_y$ to yield four orbital combinations: $(\sigma_{N-H})^2$ $(PhC^{\bullet}H_2)^1(\sigma^*_{N-H})^0$. Unlike the imido amination sequence where H-atom abstraction leads to metal reduction, the H-atom abstraction steps for the iminyl is completely *N*-centered, leaving the iron oxidation level unchanged. The H-atom abstraction step conserves total spin-angular momentum as the resulting radical pair complex remains in a quintet spin configuration. The recombination step (Fig. 6c) should proceed combining the benzylic radical with the remaining $\pi_x$ $[\sigma^*_{(dxz-L\sigma)} \pm Np_x]$ pair yielding three product orbitals: $(\sigma_{N-C})^2(Fe\ 3d_{xz})^2(\sigma^*_{N-C})^0$, constituting a net reduction of the iron center, yet again conserving the total spin-angular momentum for the entire reaction sequence.

That the iminyl complexes will activate the C–H bonds of toluene at lower temperatures than their respective imido congeners is a direct result of the diminished Fe–N bond order. Thus the oxidizing orbital $(N\ 2p_y)^1$ is lower in energy than the corresponding imido reaction partner ($\pi_y^*$), leading to a better energetic overlap between H-atom donor and acceptor orbitals. Furthermore, the entire amination sequence for the iminyls conserves the total spin angular momentum while the imido complexes must change their electronic configurations ($S = {}^5/_2 \rightarrow S = {}^3/_2$) concomitantly with iron reduction.

### *3.3.2 Thermodynamic Considerations*

In considering a stepwise mechanism for C–H amination, the initial hydrogen atom abstraction from substrate can be well-represented via a thermodynamic square scheme that partitions the driving force of the reaction into the constituent proton and electron transfer contributions, as shown in equation 1:

$$\Delta G_{HAT}\ (^{kcal}/_{mol}) = 23.06\ E^0 + 1.37\ pK_a + 59.5$$

where the final constant represents the standard potential for proton reduction in aprotic solvent. Electrochemical analysis of **2** revealed a quasi-reversible reduction potential of –1.05 V versus ferrocene/ferrocenium. Given this reduction potential, the productive activation of toluene (C–H BDE: 90 $^{kcal}/_{mol}$) by **2** would require a p$K_a$ of 40 in the resulting ($^{Ar}$L)FeCl(NH($C_6H_4$-*p*-$^t$Bu)) complex. This estimation is in line with both the experimentally determined p$K_a$ of Smith's iron(III)–amide (37(3)) and the calculated p$K_a$ of Borovik's manganese(II)–hydroxide ( ≥ 36) complexes, as well as others. The higher calculated p$K_a$ value for **2** as compared to Smith's cationic tris(carbeno)borate-supported iron(IV) imide can be rationalized via the difference in overall charge between these molecules, and permits the activation of the stronger C–H bond of toluene.

The ability of **2** to functionalize toluene allows a rough estimation of the Fe=N bond strength via equation 2:

$$DH^0_{(Fe=N)} = DH^0_{(N–H)} + DH^0_{(C–N)} – DH^0_{(C–H)} – 46.12\ E^0$$

where $E^0$ is the standard reduction potential of **2**. Although the appropriate bond dissociation energies have not been determined for *N*-benzyl-adamantyl amine, experimental values for *N*-methyl-benzyl amine are readily available and provide an Fe – N bond strength of approximately 94 $^{kcal}/_{mol}$. This value is similar to the experimentally determined $DH^0_{(Fe=O)}$ range of Nocera's pac-man iron(IV) oxo porphyrin system of 65 – 85 $^{kcal}/_{mol}$ which can promote two-electron oxidation of substrate, but not C–H hydroxylation chemistry.

A comparison of the activation energies for the imide/iminyl pairs demonstrated a lower barrier for reaction with toluene at the iminyl state. A Bell-Evans-Polyani correlation between the rate of reaction and thermodynamic driving force would suggest that hydrogen atom transfer is therefore less favorable at the lower valent state. The higher Fe – N bond order, coupled with the absence of electrochemical reduction of **5** under experimental conditions (to –2.3 V versus ferrocene/ferrocenium), indicate that the overall functionalization process is likewise less favorable at the imide state. These data

support that the enhancement of reactivity at the iminyl state is both kinetic and thermodynamic in nature, due to the higher radical density present at the *N*-atom and weaker iron–nitrogen interaction via the broken symmetry electron structure, respectively.

## 3.4 Conclusions

We have previously demonstrated that the (dipyrrin)iron platform is capable of stabilizing both high-spin ferric imido species, as well as the highly unusual ferric iminyl complex which features a high-spin iron center antiferromagnetically coupled to the iminyl radical. Both of the high-spin complexes are capable of effecting nitrene transfer to C–H bonds and olefinic substrates. The foregoing results demonstrate that the imido/iminyl redox isomers are chemically interchangeable. Furthermore, the elusive alkyl iminyl intermediate ($^{Ar}$L)FeCl(˙NAd), implicated in both inter- and intramolecular C–H bond functionalization catalytic processes, was isolated and spectroscopically characterized. Comparison of the Mössbauer spectroscopy, magnetometry, and bond lengths of the alkyl iminyl complex with the aryl iminyl congener revealed striking similarities, suggesting a common electronic structure and indicating the nitrene aryl component is not necessary to stabilize the iminyl oxidation level via radical delocalization. Furthermore, oxidation of the imido complexes to their iminyl redox isomers largely localizes the oxidation event to the NR fragment. Lastly, having access to both alkyl and aryl NR redox isomers, we were able to assess how is the change in molecular oxidation level manifests in changes to C–H bond amination efficacy. Oxidation of the imido complexes to their iminyl redox isomer results in a rate enhancement of two orders in magnitude. The rate enhancement is largely enthalpic (entropic barriers are nearly equal). The ability of the imido or iminyl component to delocalize the spin-density throughout an aryl substituent also results in a greater barrier towards functional group transfer. We infer this latter to mean that concentration of radical density upon the transferring group can play a large role in C–H bond functionalization processes.

## 3.5 Experimental Methods

### *3.5.1 General Considerations*

All manipulations of metal complexes were carried out in the absence of water and dioxygen using standard Schlenk techniques, or in an MBraun inert atmosphere drybox under a dinitrogen atmosphere. Ligand and ligand precursor syntheses were carried out in air, except where noted. All glassware was oven dried for a minimum of 1 h and cooled in an evacuated antechamber prior to use in the drybox. Benzene, *n*-hexane, and toluene were dried and deoxygenated on a Glass Contour System (SG Water USA, Nashua, NH) and stored over 4 Å molecular sieves (Strem) prior to use. Benzene-$d_6$ was purchased from Cambridge Isotope Labs, degassed, stored over 4 Å molecular sieves prior to use. Pentane was purchased from Sigma-Aldrich and stored over 4 Å molecular sieves prior to use. Iron(II) chloride was purchased from Strem and ground under inert atmosphere. The ligand $^{Ar}$LH and lithium salt ($^{Ar}$L)Li were synthesized as previously reported.[1] Potassium graphite was prepared by heating potassium with 8 equivalents of graphite powder at 80 °C in an evacuated flask for 4 h.[2] Toluene-α-$d_1$ was prepared with 95 % deuterium enrichment by treating a suspension of benzyl potassium in pentane with $D_2O$ dropwise. Celite® 545 (J. T. Baker) was dried in a Schlenk flask for 24 h under dynamic vacuum while heating to at least 150 °C prior to drybox use. Where noted, reaction equipment (including flasks, vials, pipets, and magnetic stir bars) were silanized by allowing a 10 % v/v solution of dichlorodimethylsilane in anhydrous hexanes to stand in contact with the surface for 30 minutes, washing the surface with

8. King, E. R.; Hennessy, E. T.; Betley, T. A. *J. Am. Chem. Soc.* **2011**, *133*, 4917-4923.
9. Bailey, P. J.; Coxall, R. A.; Dick, C. M.; Fabre, S.; Henderson, L. C.; Herber, C.; Liddle, S. T.; Loroño-González, D.; Parkin, A.; Parsons, S. *Chemistry* **2003**, *9*, 4820–4828.

additional hexanes, quenching with absolute ethanol, and allowing the equipment to dry overnight in a 220 °C oven.

### *3.5.2 Characterization and Physical Measurements*

$^{1}$H NMR spectra were recorded on Varian Mercury 400 MHz or Varian Unity/Inova 500 MHz spectrometers. $^{1}$H and $^{13}$C NMR chemical shifts are reported relative to $SiMe_4$ using the chemical shift of residual solvent peaks as reference.

Zero-field $^{57}$Fe Mössbauer spectra were measured with a constant acceleration spectrometer (SEE Co, Minneapolis, MN) at 90K. Isomer shifts are quoted relative to Fe foil at room temperature. Data was analyzed and simulated with Igor Pro 6 software (WaveMetrics, Portland, OR) using Lorentzian fitting functions. Samples were prepared by suspending 50-100 mg of compound in sufficient Paratone oil and immobilizing by rapid freezing in liquid nitrogen.

UV/Visible spectra were recorded on a Varian Cary 50 UV/Visible spectra using quartz cuvettes and a scan rate of 600 nm/min. Scanning kinetics data was obtained using an air-free cuvette equipped with a Teflon screw cap with a path length of 0.1 mm. The sample holder was preheated via a circulating water bath and the temperature monitored during the course of the reaction via an external thermocouple.

EPR spectra were obtained on a Bruker EleXsys E-500 CW-EPR spectrometer. Spectra were measured as frozen toluene glasses at a microwave power of 0.6325–2 mW. Effective g-values were obtained from spectral simulations of $S = {}^{1}/_{2}$ systems using the program Easyspin.[3] Spectral simulations incorporating spin state and rhombicity were performed using

10. Stoll, S.; Schweiger, A. *J. Magn. Reson.* **2006**, *178*, 42–55.

VisualRhombo.[4]

Magnetic data were collected using a Quantum Design MPMS-5S SQUID magnetometer. Measurements for were obtained for finely ground microcrystalline powders restrained in a frozen eicosane matrix within polycarbonate capsules. Samples were prepared under a dry nitrogen atmosphere by packing the powder in a gelcap and adding warm liquid eicosane, which formed a solid wax upon cooling. Dc susceptibility measurements were collected in the temperature range 5-300 K under a dc field of 5000 or 10000 Oe. Dc magnetization measurements were obtained in the temperature range 1.8-10 K under dc fields of 1, 2, 3, 4, 5, 6, and 7 T. The susceptibility data was corrected for contributions from the sample holder and eicosane, as well as the core diamagnetism of the sample using Pascal's constants. The reduced magnetization data were fit using PHI.[5]

### *3.5.3 XAS Measurements*

*Note: the compound labelling scheme in this section is distinct from the remainder of the work.*

Samples for XAS analysis were dissolved in $C_6H_6$, syringed into a 0.3 mL capacity Delrin XAS cell with a 9 x 2 mm slit and immediately flash frozen in a liquid $N_2$ bath. The slits were covered with 38 μm Kapton to make X-ray transparent windows. Solid samples of **5** were diluted in BN, finely ground in an agate mortar, pressed into 1 mm Al spacers, and sealed with 38 μm Kapton tape. Fe K-edge XAS spectra were collected at the Stanford Synchrotron Radiation Lightsource at beamline 7-3 under ring conditions of 3 GeV and 500 mA. A Si(220) double-crystal monochromator was used for energy selection and a Rh-coated mirror (set to an energy

11. Hagen, W. R. Mol. *Phys.* **2007**, *105*, 2031–2039.
12. Chilton, N. F.; Anderson, R. P.; Turner, L. D.; Soncini, A.; Murray, K. S. *J. Comput. Chem.* **2013**, *34*, 1164–1175.

cutoff of 9 keV) was used for harmonic rejection. Internal energy calibration was performed by assigning the first inflection point of a Fe foil spectrum to 7111.2 eV. Data were collected in fluorescence mode using a Canberra Ge 30-element array detector, with the sample maintained at 10 K in an Oxford liquid He flow cryostat. Elastic scatter into the detector was attenuated using a Soller slit with an upstream Co filter. Data were collected from 6784 to 7510 eV (k = 10 $Å^{-1}$) for **($^{Ar}$L)FeCl(NC$_6$H$_4$$^t$Bu)**, **($^{Ar}$L)Fe(NC$_6$H$_4$$^t$Bu)** and **($^{Ar}$L)Fe(NAd)**. Data were collected from 6784 to 7986 eV (k = 15 $Å^{-1}$) for **($^{Ar}$L)FeCl(NAd)**. Data were collected from 6782 to 8254 eV (k = 17 $Å^{-1}$) for **($^{Ar}$L)FeCl(H$_2$NAd)**. One to five scans were averaged and processed using the MAVE and PROCESS modules of the EXAFSPAK software package.[6] A smooth pre-edge background was removed from each averaged spectrum by fitting a second-order polynomial to the pre-edge region and subtracting this polynomial from the entire spectrum. A polynomial spline was subtracted above $E_0$ = 7130 eV and the data normalized in the post-edge absorption to 1.0. Pre-edge data were fit using Igor Pro 6.0. Background from the rising edge was modeled by fitting pseudo-Voigt lineshapes. Pre-edge peaks were fit with pseudo-Voigt lineshapes by the method of least-squares. Extended X-ray absorption fine structure (EXAFS) fitting was performed using the OPT module of the EXAFSPAK software package on k-smoothed data. Low-k amplitudes were minimized by optimizing the spline subtraction using PYSPLINE.[7] Coordinates from X-ray diffraction and DFT geometry optimizations were used to generate models for scattering path calculations by FEFF7.[8] Paths were optimized by least-squares fitting, where floated parameters included the interatomic scattering distances (R), and the Debye-Waller thermal factors ($\sigma^2$).

---


13. George, G.N. EXAFSPAK; Stanford Synchrotron Radiation Lightsource, Stanford Linear Accelerator Center, Stanford University, Stanford, CA, **2001**.
14. Tenderholt, A. *PySpline*, version 1.1; **2006**; http://sourceforge.net/projects/pyspline.
15. DeLeon, J.M.; Rehr, J.J.; Zabinsky, S.I.; Albers, R.C. *Phys. Rev. B* **1991**, *44*, 4146-4156. Rehr, J.J.; DeLeon, J.M.; Zabinsky, S.I.; Albers, R.C. *J. Am. Chem. Soc.* **1991**, *113*, 5135-5140.

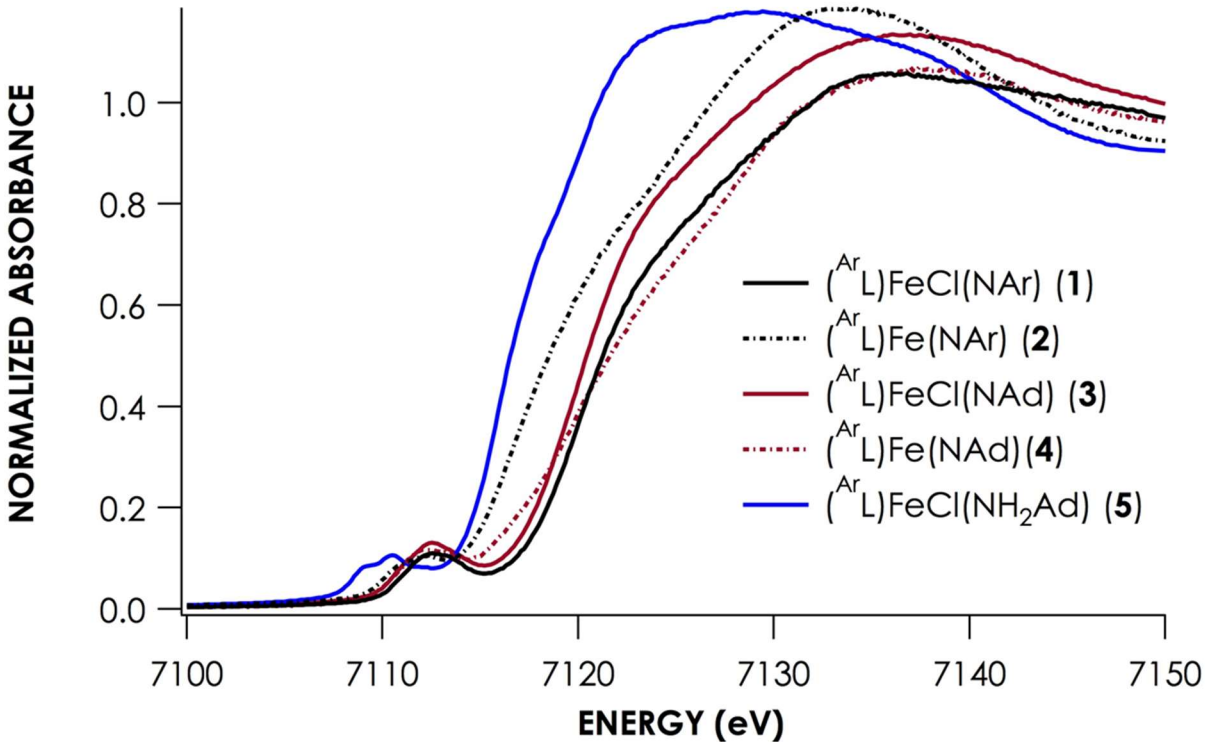


**Figure 3.7.** Overlaid Fe K-edge XAS spectra of dipyrrinato-iron compounds.

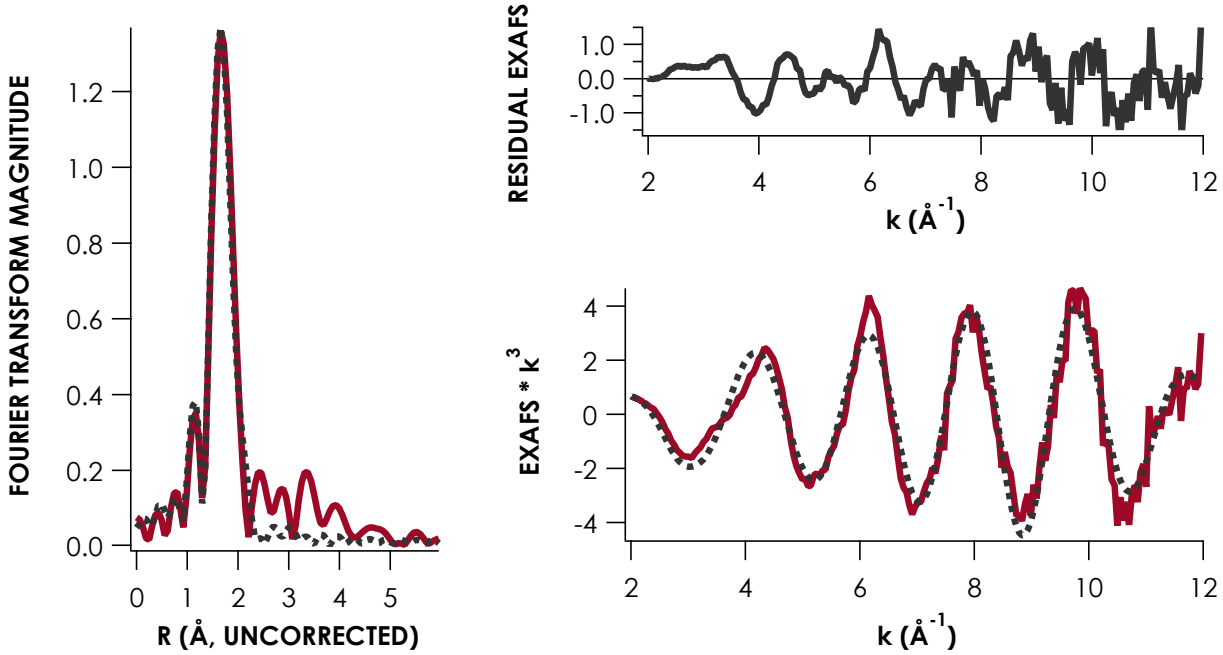


**Figure 3.8.** EXAFS of **$^{Ar}$LFeClNAd**. Red traces correspond to experimental data, while dashed black lines indicate simulated data from fits producing F factors.

**Table 3.3.** EXAFS Simulations of **$^{Ar}$LFeClNAd**.

| Fit | Path | CN | R (Å) | ΔR (Å) | σ² (Å) | Δσ² (Å) | $E_0$ | F |
|---|---|---|---|---|---|---|---|---|
| 1 | Fe–N (pyrole) | 2 | 2.081 | 0.003 | -0.001 | 0.0002 | 3.28302 | 46.75 |
| 2 | Fe–N (pyrole) | 2 | 2.06 | 0.005 | -0.000032 | 0.000332 | -0.5686 | 37.95 |
| | Fe–Cl | 1 | 2.245 | 0.01 | 0.0065 | 0.001 | | |
| 3 | Fe–N(pyrole) | 2 | 1.987 | 0.008 | 0.00034 | 0.00057 | -7.6103 | 29.52 |
| | Fe–Cl | 1 | 2.222 | 0.005 | 0.0011 | 0.00041 | | |
| | Fe–N (iminyl) | 1 | 1.761 | 0.006 | 0.00036 | 0.00067 | | |

EXAFS were fit in OPT using paths calculated by FEFF7. Coordination numbers (CN) were held constant while distances (R) and Debye-Waller factors ($\sigma^2$) were allowed to float. Errors in distances are estimated to be 0.02-0.03 Å and 25% for coordination numbers. Fits were performed over the entire (0 to 6.0 Å) Fourier transform window. Goodness of fit is measured by F, defined as $[(\sum_i^n [k_i^3(\mathrm{EXAFS_{obs}} - \mathrm{EXAFS_{calc}})_i])^2 / n]^{1/2}$.

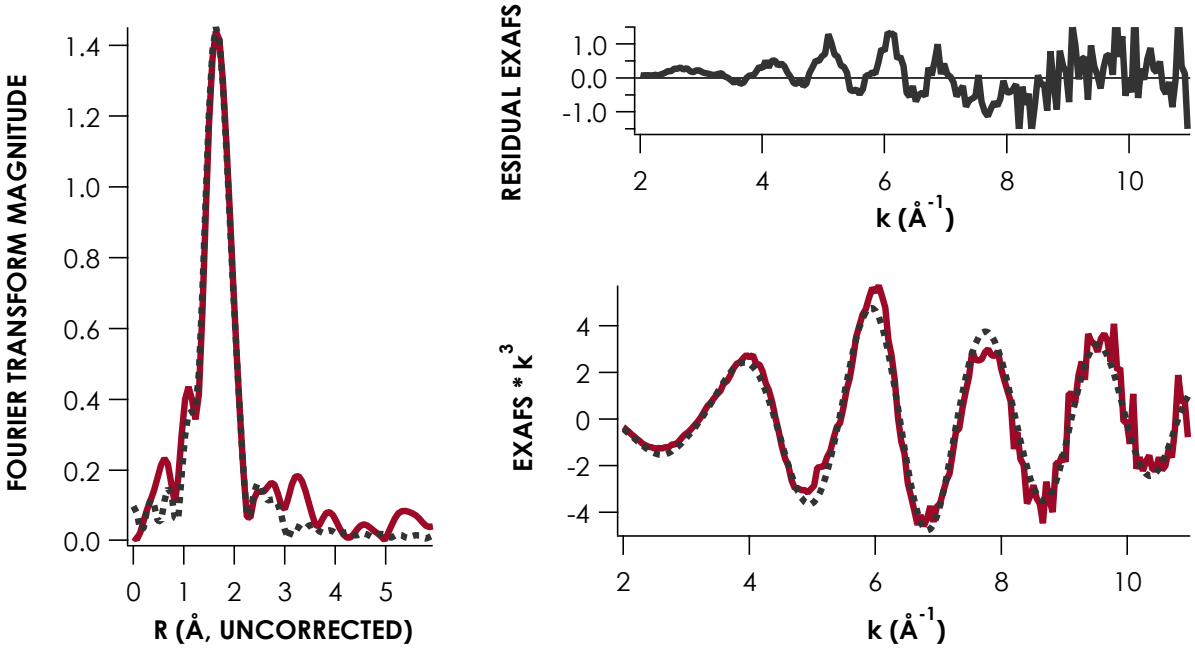


**Figure 3.9.** EXAFS of $^{Ar}$**LFeCl(H$_2$NAd)**. Red traces correspond to experimental data, while dashed black lines indicate simulated data from fits producing F factors.

**Table 3.4.** EXAFS Simulations of **5**.

| Fit | Path | CN | R (Å) | ΔR (Å) | σ² (Å) | Δσ² (Å) | E₀ | F |
|---|---|---|---|---|---|---|---|---|
| 1 | Fe–N | 3 | 2.112 | 0.004 | 0.000052 | 0.000265 | -2.59 | 42.24 |
| 2 | Fe–N | 3 | 2.059 | 0.007 | 0.00255 | 0.0005 | -8.95 | 28.32 |
| | Fe–Cl | 1 | 2.267 | 0.006 | 0.00215 | 0.00054 | | |
| 3 | Fe–N | 3 | 2.065 | 0.005 | 0.00184 | 0.00042 | -7.33 | 25.74 |
| | Fe–Cl | 1 | 2.281 | 0.006 | 0.00222 | 0.00052 | | |
| | Fe–C | 4 | 3.054 | 0.014 | 0.0102 | 0.0018 | | |
| 4 | Fe–N | 3 | 2.062 | 0.006 | 0.00198 | 0.00045 | -7.87 | 24.85 |
| | Fe–Cl | 1 | 2.278 | 0.007 | 0.00204 | 0.00053 | | |
| | Fe–C | 4 | 3.04 | 0.013 | 0.00815 | 0.00159 | | |
| | Fe–N–C (MS) | 8 | 3.106 | 0.036 | 0.00655 | 0.00613 | | |

EXAFS were fit in OPT using paths calculated by FEFF7. Coordination numbers (CN) were held constant while distances (R) and Debye-Waller factors ($\sigma^2$) were allowed to float. Errors in distances are estimated to be 0.02-0.03 Å and 25% for coordination numbers. Fits were performed over the entire (0 to 6.0 Å) Fourier transform window. Goodness of fit is measured by F, defined as $[(\sum_i^n [k_i^3(\mathrm{EXAFS_{obs}} - \mathrm{EXAFS_{calc}})_i])^2 / n]^{1/2}$.

To further support the trend in the pre-edge features in the XAS spectra, TD-DFT calculations were undertaken. All electronic structure and spectroscopic calculations were performed using version 3.03 of the ORCA computational chemistry package.[9] Geometry optimizations were performed using the BP86[10] functional, the zeroth-order regular approximation for relativistic effects (ZORA) as implemented by van Wüllen,[11] and the scalar-relativistically recontracted def2-TZVP(-f) basis set.[12] Structures were truncated by replacing the 1,3,5-triphenylaryl groups of the ligand with a single phenyl group. Solvation was modeled using the conductor-like screening model (COSMO[13]) using an infinite dielectric. Fe K-edge XAS was calculated using time-dependent DFT (TDDFT) on geometry optimized structures.[14] TDDFT calculations of Fe K-edge XAS were performed as described previously.[15] These calculations were initiated from spin-unrestricted single-point calculations that employed the B3LYP functional,[16] CP(PPP) basis on Fe,[17] def2-TZVP(-f) basis on all other atoms, ZORA, and COSMO with an infinite dielectric. A more dense integration grid (ORCA GRID7) was used on Fe.


16. Neese, F. *WIREs Comput. Mol. Sci.* **2012**, *2*, 73-78.
17. Becke, A. D. *Phys. Rev. A* **1988**, *38*, 3098-3100. Perdew, J. P. *Phys. Rev. B* **1986**, *33*, 8822-8824.
18. van Lenthe, E., van der Avoird, A., and Wormer, P. E. S. *J. Chem. Phys.* **1998**, *108*, 4783-4796. van Wüllen, C. *J. Chem. Phys.* **1998**, *109*, 392-399.
19. Pantazis, D. A., Chen, X. Y., Landis, C. R., and Neese, F. *J. Chem. Theory Comput.* **2008**, *4*, 908-919.
20. Klamt, A. and Schüürmann, G. *J. Chem. Soc., Perkin. Trans.* **1993**, *2*, 799-805.
21. DeBeer-George, S.; Petrenko, T.; Neese, F. *J. Phys. Chem. A* **2008**, *112*, 12936-12943.
22. DeBeer George, S.; Petrenko, T.; Neese, F., *J. Phys. Chem. A* **2008**, *112*, 12936–12943.
23. Stephens, P.; Devlin, F.; Chabalowski, C.; Frisch, M. J., *J. Phys. Chem.* **1994**, *98*, 11623–11627.
24. Neese, F. *Inorg. Chim. Acta* **2002**, *337*, 181–192.

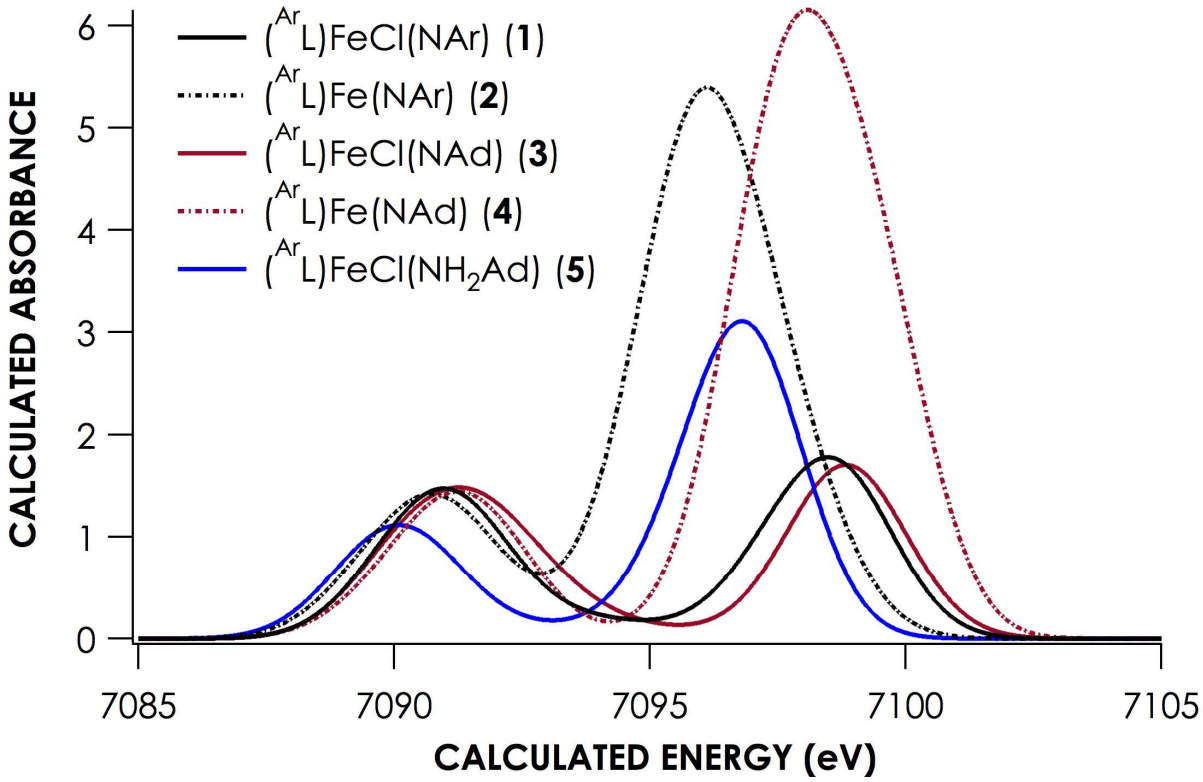


**Figure 3.10.** TDDFT-calculated Fe K-edge XAS for dipyrrinato-iron compounds.

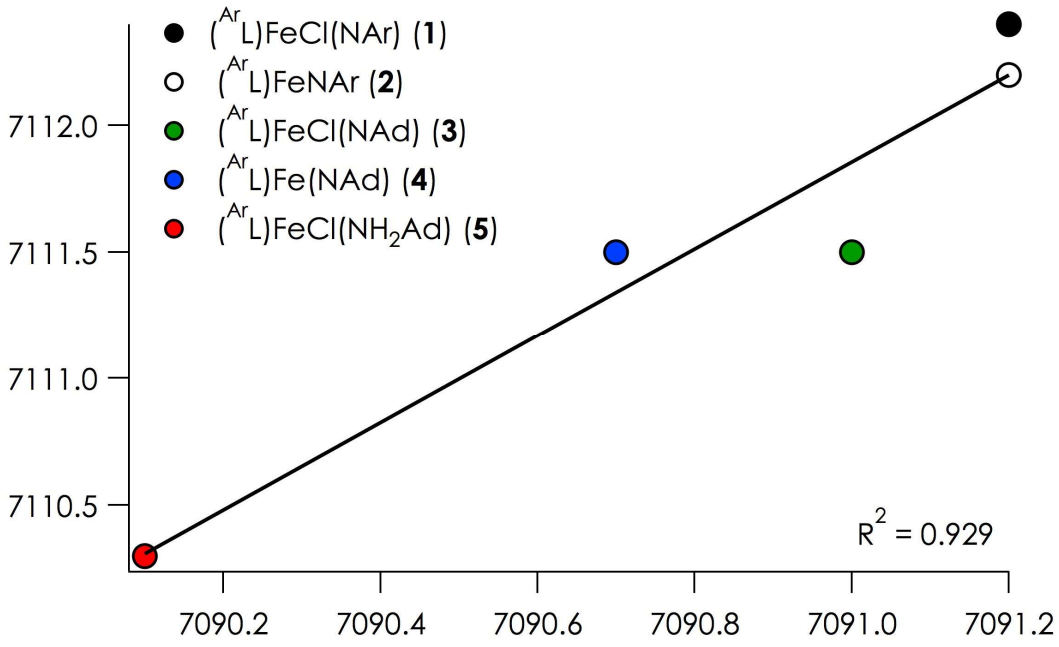


**Figure 3.11.** Calibration curve of TDDFT-calculated Fe K-edge XAS for dipyrrinato-iron compounds.

In general, the experimental bond lengths are reproduced well by theory, with a few exceptions. The average Fe-pyrole distances in **($^{Ar}$L)Fe(NC$_6$H$_4$$^t$Bu)** and **($^{Ar}$L)FeCl(NAd)** are overestimated, while in **($^{Ar}$L)FeCl(NC$_6$H$_4$$^t$Bu)** and **($^{Ar}$L)Fe(NAd)** they are underestimated. The Fe-imido distance of **($^{Ar}$L)Fe(NC$_6$H$_4$$^t$Bu)** is slightly overestimated, as is the Fe-Cl distance in **($^{Ar}$L)FeCl(NC$_6$H$_4$$^t$Bu)**. The Fe-iminyl distance in **($^{Ar}$L)FeCl(NAd)** is underestimated by DFT. The Fe–amine distance in **5** is not resolved from the Fe–pyrole distance by EXAFS, however the average distance determined by EXAFS is very close to the average of all Fe–N distances calculated by DFT (2.085 Å).

**Table 3.5.** Distances (Å) for all compounds.

| Bond | 1, DFT | 1, XRD | 2, DFT | 2, XRD | 3, DFT | 3, EXAFS | 4, DFT | 4, XRD | 5, DFT | 5, EXAFS |
|---|---|---|---|---|---|---|---|---|---|---|
| Fe-N (pyr, avg.) | 1.988 | 2.005 | 2.004 | 1.958 | 2.006 | 1.987 | 1.902 | 1.971 | 2.023 | 2.062 |
| Fe-N | 1.751 | 1.768 | 1.756 | 1.708 | 1.718 | 1.761 | 1.679 | 1.675 | 2.147 | 2.062 |
| Fe-Cl | 2.301 | 2.210 | -- | -- | 2.246 | 2.222 | -- | - | 2.255 | 2.278 |

**Note**: For compound **5**, the EXAFS were best modeled as having three Fe–N paths with an average distance of 2.062 Å. The pyrole nitrogen and amine nitrogen were not resolved from one another.

Optimized coordinates were used for TDDFT calculations of Fe K-edge XAS. The calculations reproduce the relative peak positions and intensities of the ca. 7110 eV pre-edge features. Calculated excitation energies were plotted against experimental energies extracted from least-squares fitting. We note that the absolute energies are not reproduced due to the inability of standard hybrid functionals (e.g. B3LYP) to properly model core (1s) potential energies. Errors in the calculated energies of frontier levels are considerably smaller than in the core orbital energies; consequently, the energies are well-reproduced following a scalar shift. Due to the limited energy range spanned by the features under investigation, we have not calculated this shift; fidelity to experiment is evident despite its absence.

### *3.5.4 Syntheses*

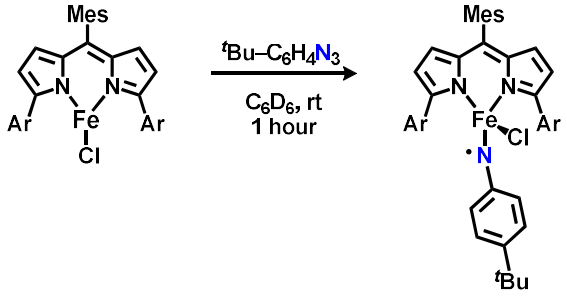


**($^{Ar}$L)FeCl($NC_6H_4{}^tBu$) (2)**: All manipulations performed with silanized reaction equipment. A solution of thawing ($^{Ar}$L)FeCl (**1**) (0.20 g, 0.21 mmol, 1 equiv.) in benzene-$d_6$ was added to a still frozen solution of $^t$Bu-$C_6H_4N_3$ (37 mg, 0.21 mmol, 1 equiv.) in benzene-$d_6$ and the reaction allowed to thaw and stir at room temperature for one hour, during which time the color changed from purple to maroon. The reaction was frozen and the solvent removed via lyophilization. The resulting powder was treated with pentane and the wash decanted to remove any unreacted azide or free ligand. After the residual pentane was removed *in vacuo*, the product was dissolved in minimal

benzene-$d_6$ and the solvent removed via lyophilization to yield the product as a maroon powder (0.22 g, 96 % yield), with physical data consistent with that previously reported. **Note**: Sufficient care must be taken to ensure the purity and stoichiometry of azide addition as unreacted metal complex cannot be removed from the mixture and unreacted azide enhances the solubility of the desired product such that pentane extraction (*vide supra*) will lower the reaction yield to an inhibitory level. Azide must therefore be purified via silica gel chromatography with hexanes eluent in the drybox immediately prior to reaction. In addition, performing the reaction in $C_6H_6$ will increase the formation of an impurity species, as assessed by $^{1}$H NMR and $^{57}$Fe Mössbauer spectroscopy. For this reason, only $C_6D_6$ should be utilized as reaction solvent.

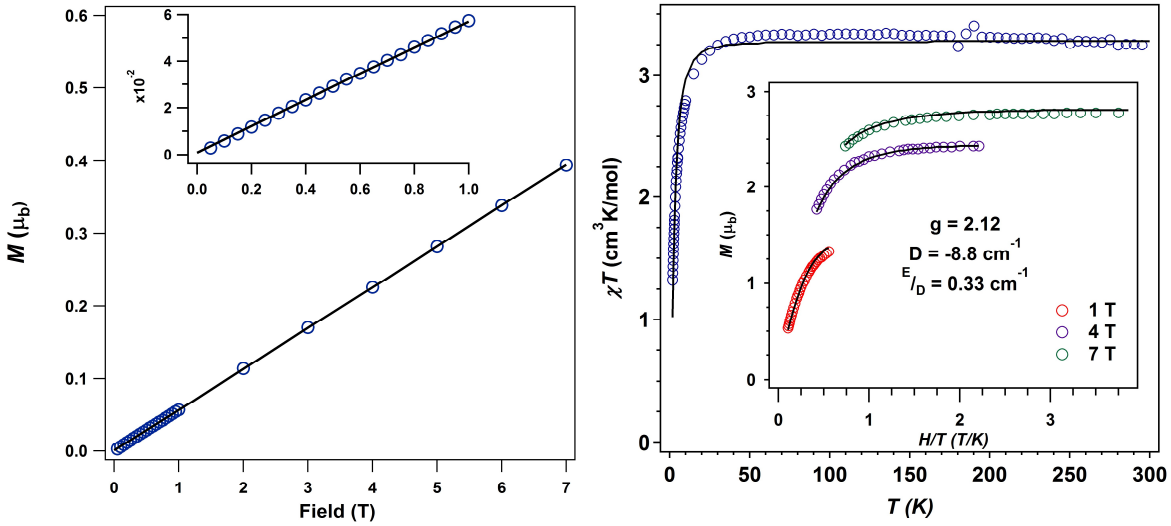


**Figure 3.12.** Magnetometry for ($^{Ar}$L)FeCl(NC$_6$H$_4$$^t$Bu) (**2**). **(left)** M vs. H at 100 K is linear, showing absence of ferromagnetic impurity even at low fields **(left, inset), (right)** $\chi_M$T vs. T at 1.0 T with fit parameters S = 2, g = 1.82, D = 6.6 cm$^{-1}$, and $^{E}/_{D}$ = 0.20, and **(right, inset)** reduced magnetization data (M vs. H/T) collected at 3 fields (1,4,7 T) over the temperature range (1.8 K – 10 K). Reduced magnetization fit parameters: S = 2, g = 2.12, D = -8.8 cm$^{-1}$, E/D = 0.33 from PHI.

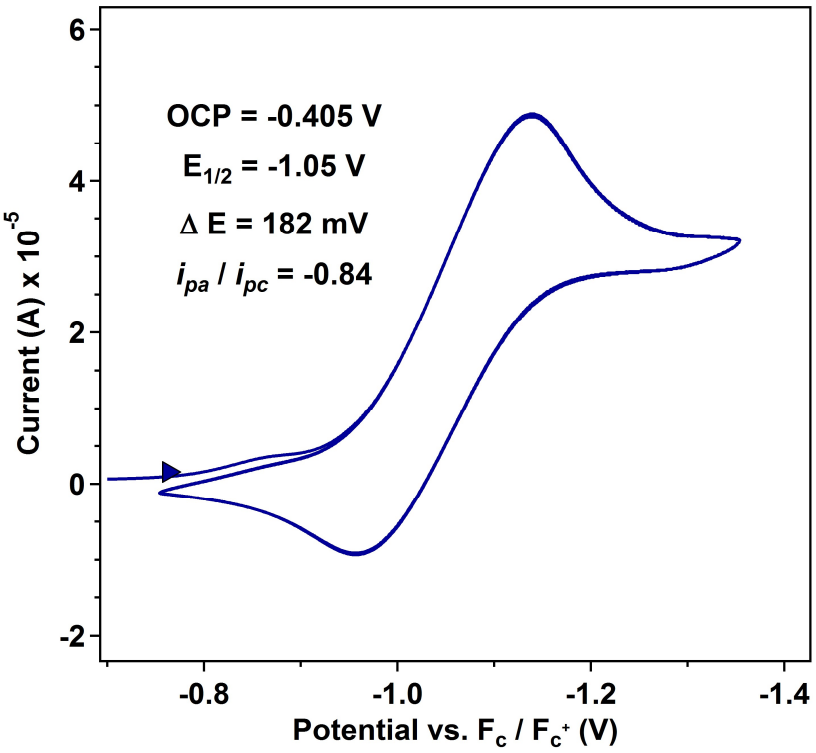


**Figure 3.13.** Cyclic voltammogram of ($^{Ar}$L)FeCl($NC_6H_4{}^tBu$) (**2**) obtained in $CH_2Cl_2$ at 25 °C, with 0.1 M ($nBu_4N$)($PF_6$) as supporting electrolyte and a scan rate of 100 mV/s showing a quasi-reversible reduction event at -1.05 V (OCP: -405 mV). Potentials are internally referenced versus the ferrocene/ferrocenium couple.

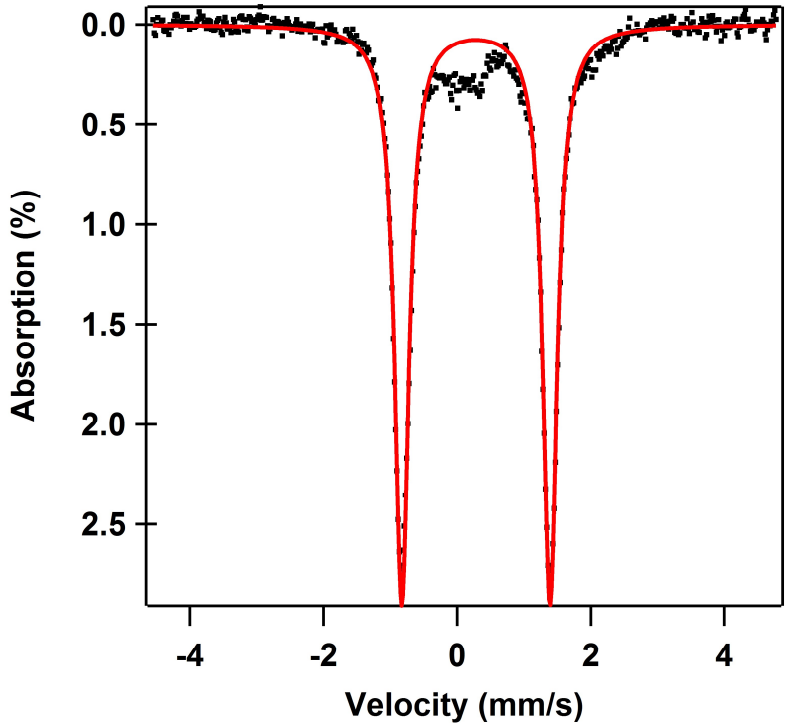


**Figure 3.14.** Zero-field $^{57}$Fe Mössbauer spectrum of ($^{Ar}$L)FeCl(NC$_6$H$_4$$^t$Bu) (**2**) in frozen benzene-$d_6$ solution at 90 K. Isomer shift and quadrupole splitting are reported relative to Fe foil at room temperature. δ ($^{mm}/_s$), $\Delta E_Q$ ($^{mm}/_s$), Γ($^{mm}/_s$) = 0.28, 2.22, 0.14.

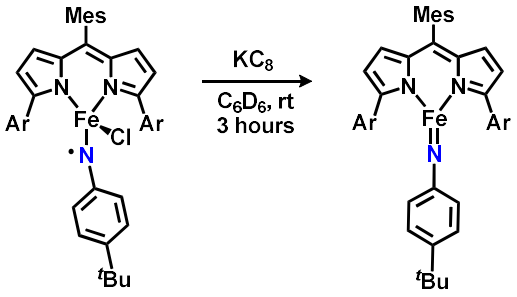


**($^{Ar}$L)Fe(NC$_6$H$_4$$^t$Bu) (3):** A solution of thawing ($^{Ar}$L)FeCl(NC$_6$H$_4$$^t$Bu) (**2**) (100 mg, 0.09 mmol, 1 equiv.) in benzene-$d_6$ was added to a frozen suspension of rigorously one equivalent of KC$_8$ (13 mg, 0.09 mmol) (which was evaluated by titrating each batch of reagent against ferrocenium hexfluorophosphate in order to suppress over-reduction to ($^{Ar}$L)Fe in benzene-$d_6$. The reaction was allowed to thaw and stir at room temperature for three hours, during which time a slow color change from maroon to pink occurred. The reaction was filtered through a pipet packed with celite,

and the filter cake washed until the eluent was colorless. The solvent was then frozen and removed *in vacuo* to yield the product (85 mg, 88 % yield) as a dark purple powder. Once synthesized, this material does not need to be handled in silanized equipment, although the lifetime at -40°C is approximately 2 weeks. Crystals suitable for X-ray diffraction were grown from a concentrated solution of toluene layered with pentane at -40 °C. $^{1}$H NMR (500 MHz, $C_6D_6$) δ 169.12 (br), 64.56, 55.21, 34.52, 23.20, 18.86, 15.06, 13.67, 12.97, 10.30, -3.31, -18.83, -28.88, -55.19. EPR (toluene, 2.8 K): $g_{eff}$ = 7.1, 5.9, 4.2, 1.2. Zero-field $^{57}$Fe Mössbauer (200 K) (δ, $|\Delta E_Q|$ ($^{mm}/_{s}$)): 0.44, *0.00* (γ = 0.74 $^{mm}/_{s}$). $\mu_{eff}$ (295 K, SQUID) 5.3 $\mu_B$.

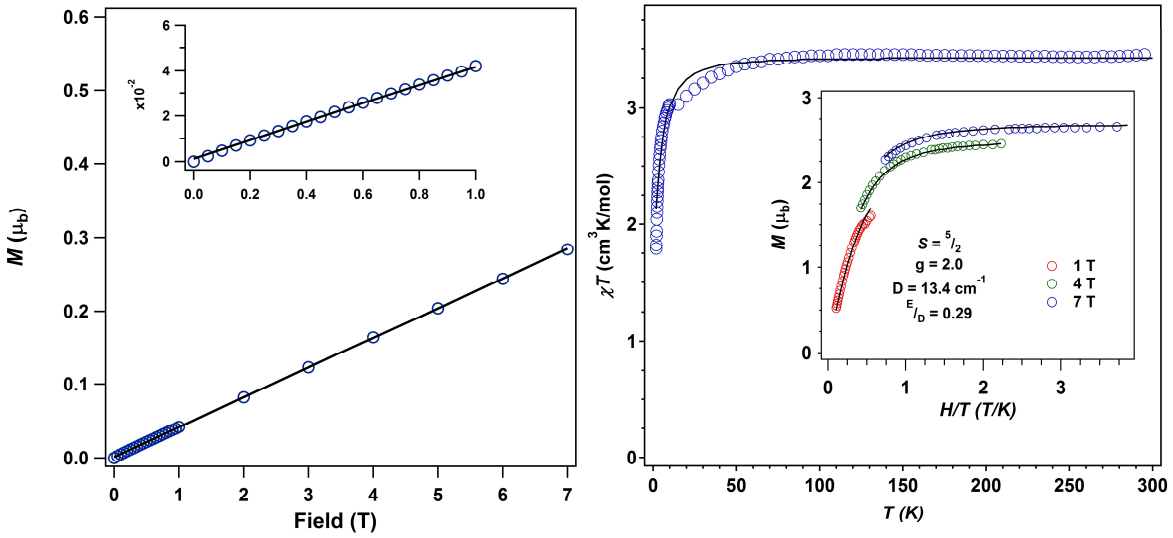


**Figure 3.15.** Magnetometry for ($^{Ar}$L)Fe(NC$_6$H$_4$$^t$Bu) (**3**). **(left)** M vs. H at 100 K is linear, showing absence of ferromagnetic impurity even at low fields **(left, inset), (right)** $\chi_M$T vs. T at 1 T with fit parameters S = $^5/_2$, g = 1.71, D = -1.6 cm$^{-1}$, and **(right, inset)** reduced magnetization data (M vs. H/T) collected at 4 fields (1,4,7 T) over the temperature range (1.8 K – 10 K). Reduced magnetization fit parameters: S = $^5/_2$, g = 2.0, D = 13.4 cm$^{-1}$, E/D = 0.29 from PHI.

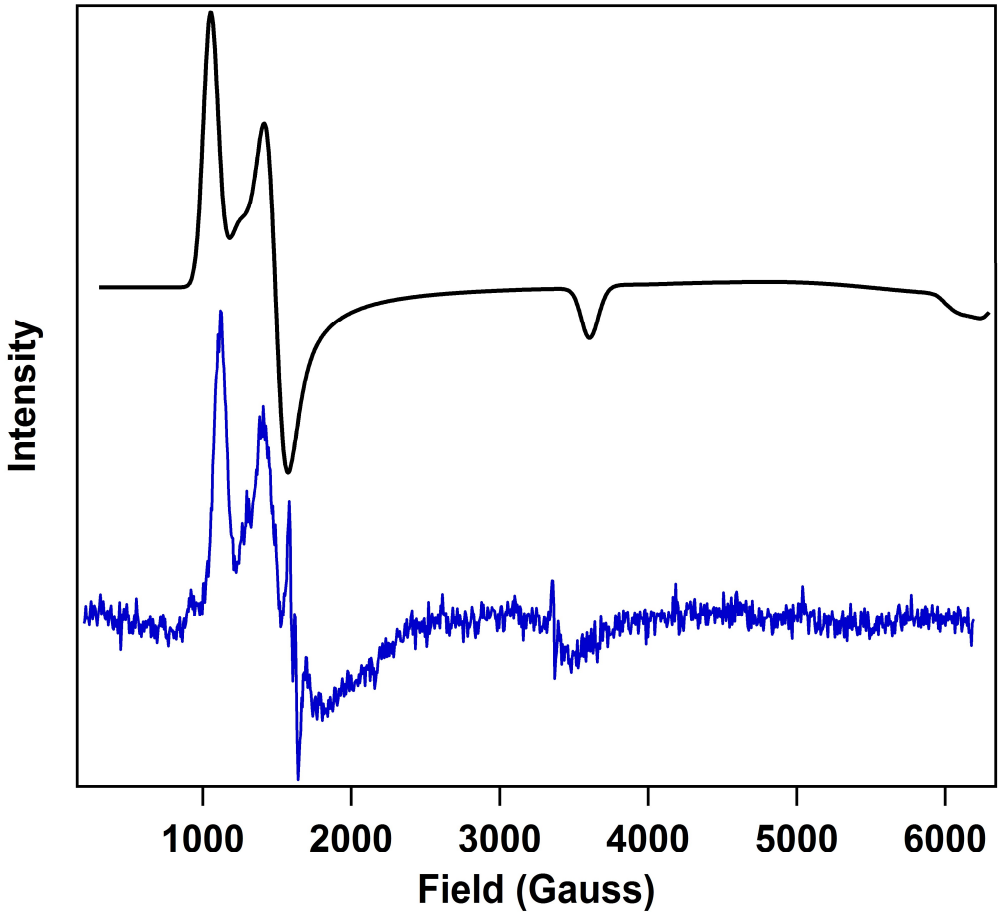


**Figure 3.16.** Frozen toluene EPR spectrum of ($^{Ar}$L)Fe(NC$_6$H$_4$$^t$Bu) (**3**) at 2.8 K. The black line represents a simulation with VisualRhombo corresponding to an S = $^5/_2$ system with $^E/_D$ = 0.05. The sharp features at 1625 G (g = 4.3) and 3375 G (g = 2.02) result from small amounts of unknown Fe$^{III}$ and organic radical impurity, respectively, and account for less than 0.4 % of the total spin of the sample as determined by double integration.

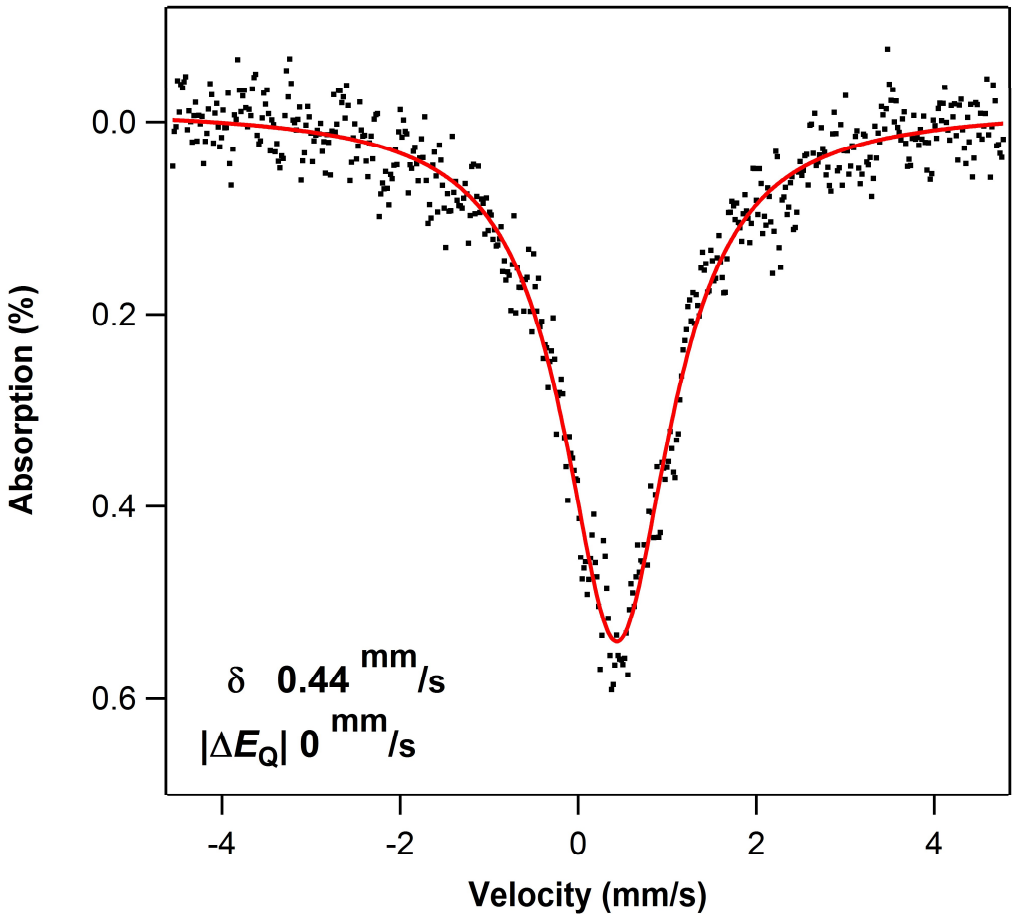


**Figure 3.17.** Zero-field $^{57}$Fe Mössbauer spectrum of ($^{Ar}$L)Fe(NC$_6$H$_4$$^t$Bu) (**3**) at 200 K. Isomer shift and quadrupole splitting are reported relative to Fe foil at room temperature. $\delta$ ($^{mm}/_{s}$), $\Delta E_Q$ ($^{mm}/_{s}$), $\Gamma$($^{mm}/_{s}$) = 0.44, 0.0, 0.74.

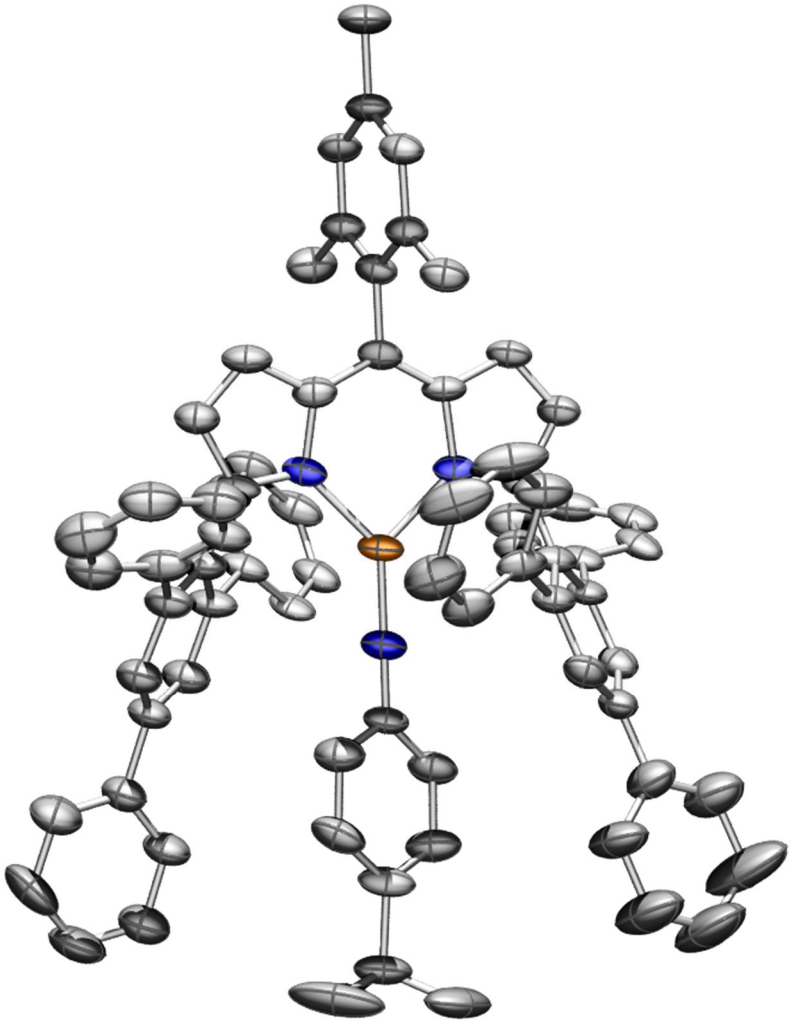

**Figure 3.18.** Solid-state molecular structure for ($^{Ar}$L)Fe(NC$_6$H$_4$$^t$Bu) (**3**) with thermal ellipsoids at 50% probability level. Hydrogen atoms not shown. Iron = orange, nitrogen = blue, carbon = gray.

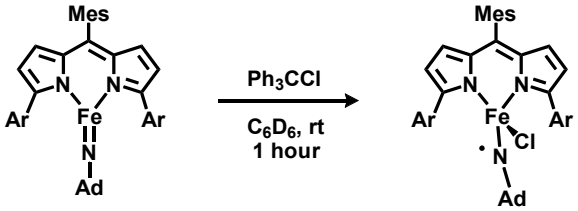


**($^{Ar}$L)FeCl(NAd) (6):** All manipulations performed with silanized equipment. A solution of ($^{Ar}$L)Fe(NAd) (**5**) (100 mg, 0.9 mmol, 1 equiv.) in benzene-$d_6$ was added to a frozen solution of trityl chloride (26 mg, 0.09 mmol, 1 equiv.) in benzene-$d_6$ and the reaction allowed to thaw and

stir at room temperature for an hour, during which time the color changed from pink to maroon. The reaction was frozen and the solvent removed via lyophilization. The residual sticky powder was treated with pentane, and the pentane wash decanted. Following removal of residual pentane *in vacuo*, the material was dissolved in minimal benzene-$d_6$ and the solvent frozen and removed via lyophilization to afford the product as a maroon powder (81 mg, 80 % yield). $^1$H NMR (500 MHz, $C_6D_6$) δ 47.11, 26.92, 10.50, 10.29, -0.98, -10.47, -16.09. $\mu_{eff}$ (295 K, SQUID) 4.5 $\mu_B$. Zero-field $^{57}$Fe Mössbauer (90 K) (δ, $|\Delta E_Q|$ ($^{mm}/_s$)): 0.26, *2.05* ($\gamma$ = 0.24 $^{mm}/_s$).

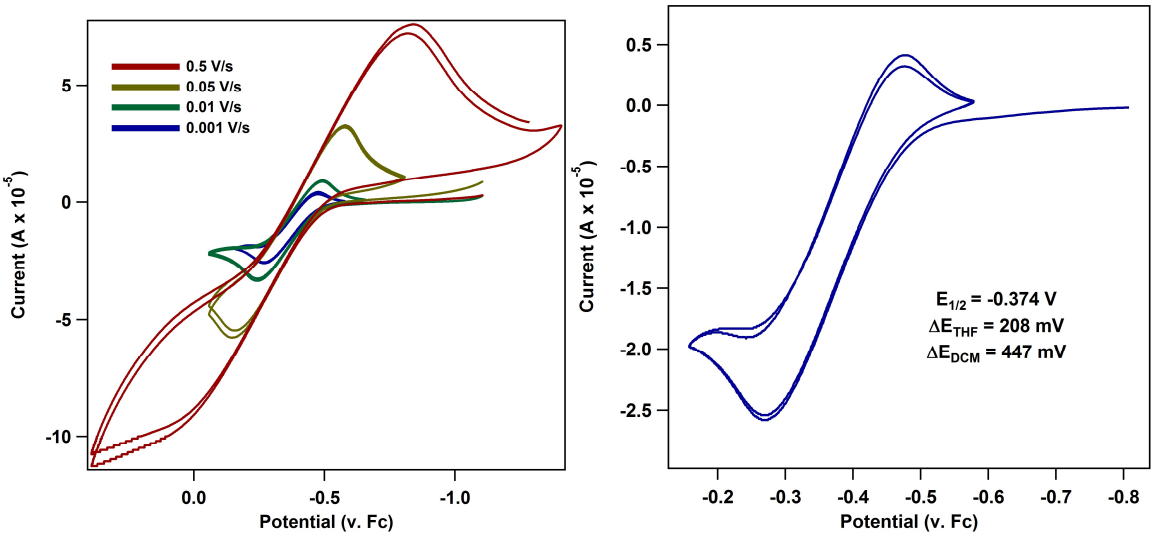


**Figure 3.19**. Cyclic voltammograms of ($^{Ar}$L)Fe(NAd) (**5**) obtained in $CH_2Cl_2$ at 25 °C, with 0.1 M ($nBu_4N$)($PF_6$) as supporting electrolyte. (**left**) Different scan rates in $CH_2Cl_2$ showing a strong dependence of scan rate on peak-to-peak separation of the oxidation event. (**right**) Cyclic voltammogram in THF at a scan rate of 10 mV/s showing a quasi-reversible oxidation event at -374 mV V (OCP: -1.07 mV, $i_{pa}$ / $i_{pc}$ = 1.15). Potentials are internally referenced versus the ferrocene/ferrocenium couple.

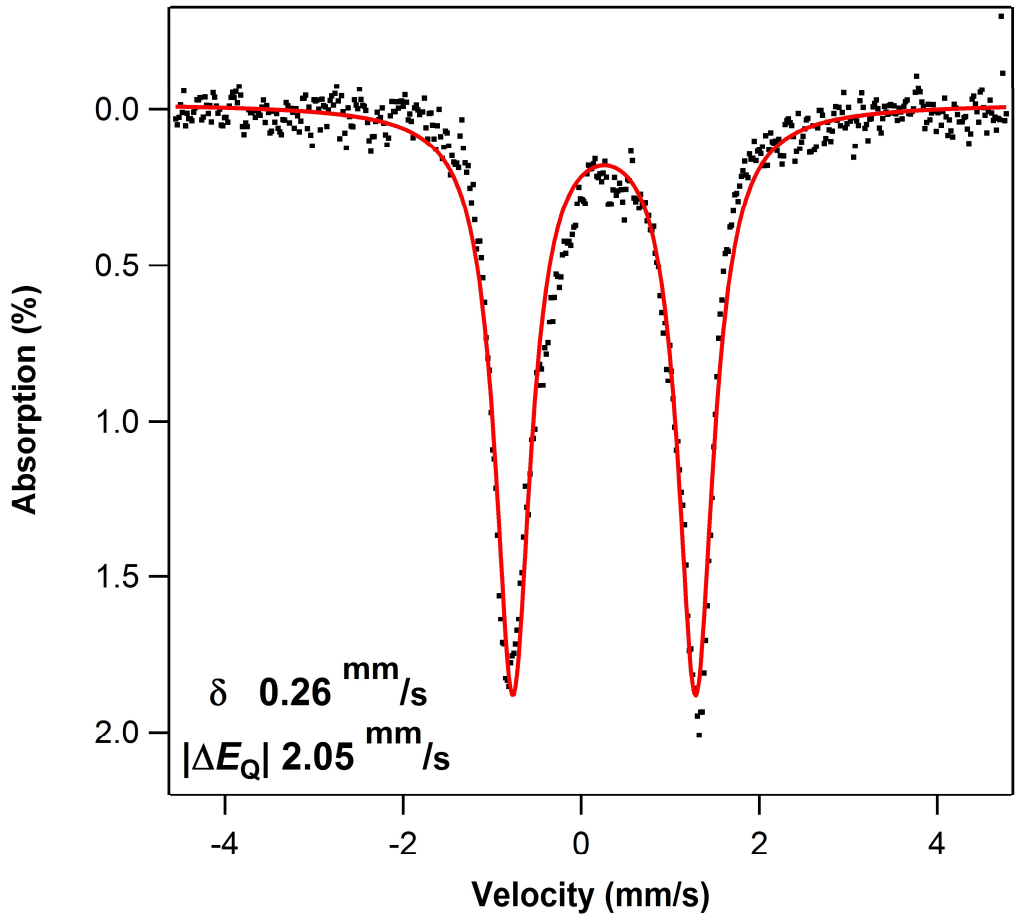


**Figure 3.20**. Zero-field $^{57}$Fe Mössbauer spectrum of ($^{Ar}$L)FeCl(NAd) (**6**) in frozen benzene-$d_6$ solution at 90 K. Isomer shift and quadrupole splitting are reported relative to Fe foil at room temperature. $\delta$ ($^{mm}/_{s}$), $\Delta E_Q$ ($^{mm}/_{s}$), $\Gamma$($^{mm}/_{s}$) = 0.26, 2.05, 0.24.

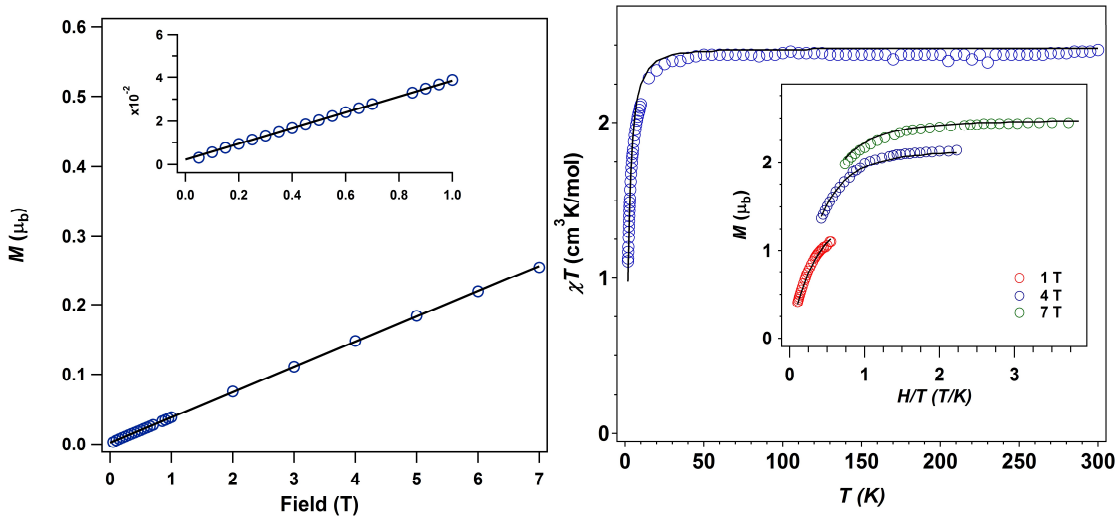


**Figure S-1:** Magnetometry for ($^{Ar}$L)FeCl(NAd) (**6**). **(left)** M vs. H at 100 K is linear, showing absence of ferromagnetic impurity even at low fields **(left, inset), (right)** $\chi_M$T vs. T at 1.0 T with fit parameters S = 2, g = 1.82, D = 6.6 cm$^{-1}$, $^{E}/_{D}$ = 0.19, and **(right, inset)** reduced magnetization data (M vs. H/T) collected at 3 fields (1, 4, 7 T) over the temperature range (1.8 K – 10 K). Reduced magnetization fit parameters: S = 2, g = 1.95, D = 6.9 cm$^{-1}$, E/D = 0.33 from PHI.

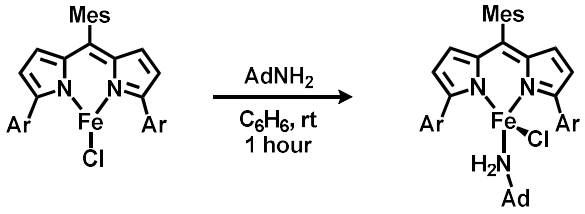


**($^{Ar}$L)FeCl(NH$_2$Ad) (7):** A solution of adamantyl amine (14 mg, 0.092 mmol, 1.03 equiv.) in 1 mL benzene was added all at once to a solution of ($^{Ar}$L)FeCl (**1**) (86 mg, 0.089 mmol, 1 equiv.) in 10 mL benzene, causing an immediate color change from purple to red. The reaction was allowed to stir at room temperature before the solvent was removed *in vacuo*. The residual powder was washed with 1 mL hexanes, the residual solvent removed *in vacuo*, and the product lyophilized from a solution of minimal benzene. The product was isolated as a red powder (98 mg, 98 % yield). $^1$H NMR (400 MHz, $C_6D_6$) δ 39.04, 18.61, 15.22, 14.88, 8.93, 8.15, 6.84, 6.41, 5.06, 4.41, 3.18, 0.91, -1.50, -1.93, -10.58, -11.52. Zero-field $^{57}$Fe Mössbauer (90 K) (δ, $|\Delta E_Q|$ ($^{mm}/_{s}$)): 0.91, *3.33* (γ = 0.18 $^{mm}/_{s}$).

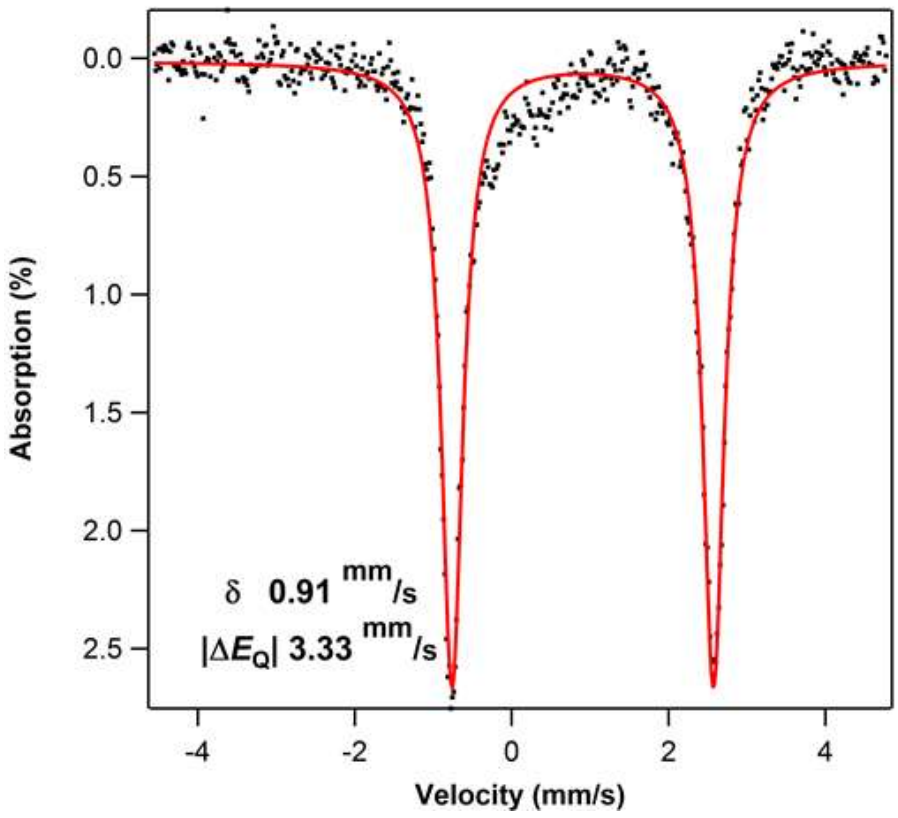


**Figure 3.21**. Zero-field $^{57}$Fe Mössbauer spectrum of ($^{Ar}$L)FeCl(NH$_2$Ad) (**7**). Isomer shift and quadrupole splitting are reported relative to Fe foil at room temperature. δ ($^{mm}/_{s}$), $\Delta E_Q$ ($^{mm}/_{s}$), Γ($^{mm}/_{s}$) = 0.91, 3.33, 0.17.

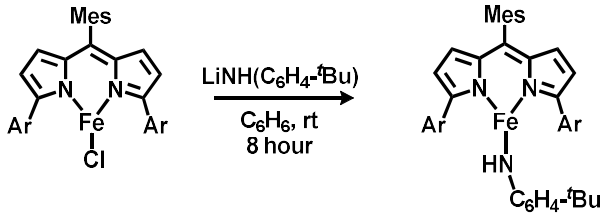


**($^{Ar}$L)Fe(NH(C$_6$H$_4$-$^t$Bu)):** ($^{Ar}$L)FeCl (**1**) (100 mg, 0.1 mmol, 1 equiv.) and lithium p-*tert*-butylanilide (16.2 mg, 0.1 mmol, 1 equiv.) were dissolved in 10 mL benzene and the solution allowed to stir at room temperature for eight hours. The reaction was then filtered through celite and the solvent removed via lyophilization to afford the product as a flocculent purple powder (102.7 mg, 92 % yield). Crystals suitable for X-ray diffraction were grown from a concentrated toluene solution layered with pentane at -35 °C. $^1$H NMR (400 MHz, C$_6$D$_6$) δ 78.37, 75.10, 52.43,

37.20, 25.90, 14.40, 13.97, 13.04, 11.91, 10.38, -18.36, -25.57, -37.85. Zero-field $^{57}$Fe Mössbauer (90 K) (δ, $|\Delta E_Q|$ ($^{mm}/_s$)): 0.63, *0.93* (γ = 0.19 $^{mm}/_s$).

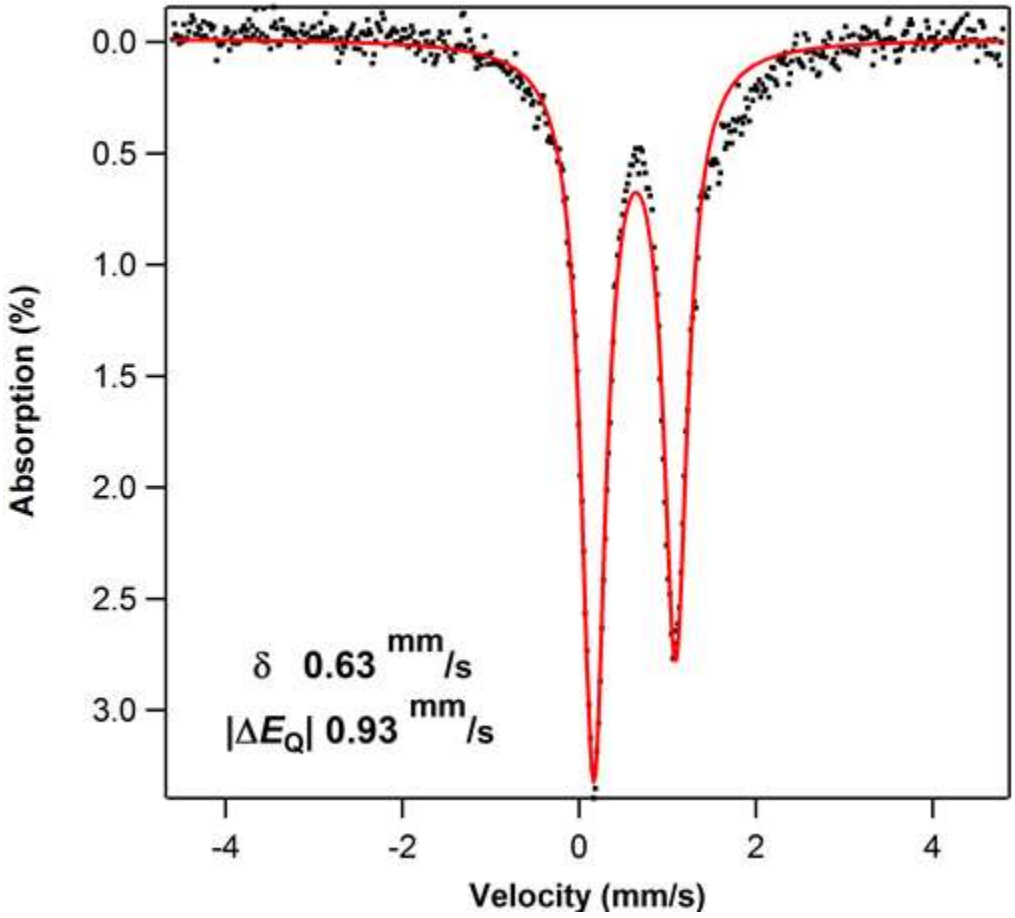


**Figure 3.22**. Zero-field $^{57}$Fe Mössbauer spectrum of ($^{Ar}$L)Fe(NHC$_6$H$_4$$^t$Bu). Isomer shift and quadrupole splitting are reported relative to Fe foil at room temperature. δ ($^{mm}/_s$), $\Delta E_Q$ ($^{mm}/_s$), Γ($^{mm}/_s$) = 0.63, 0.93, 0.17. Asymmetry of the quadrupole doublet was reproducible and fit with an asymmetry parameter of 0.547.

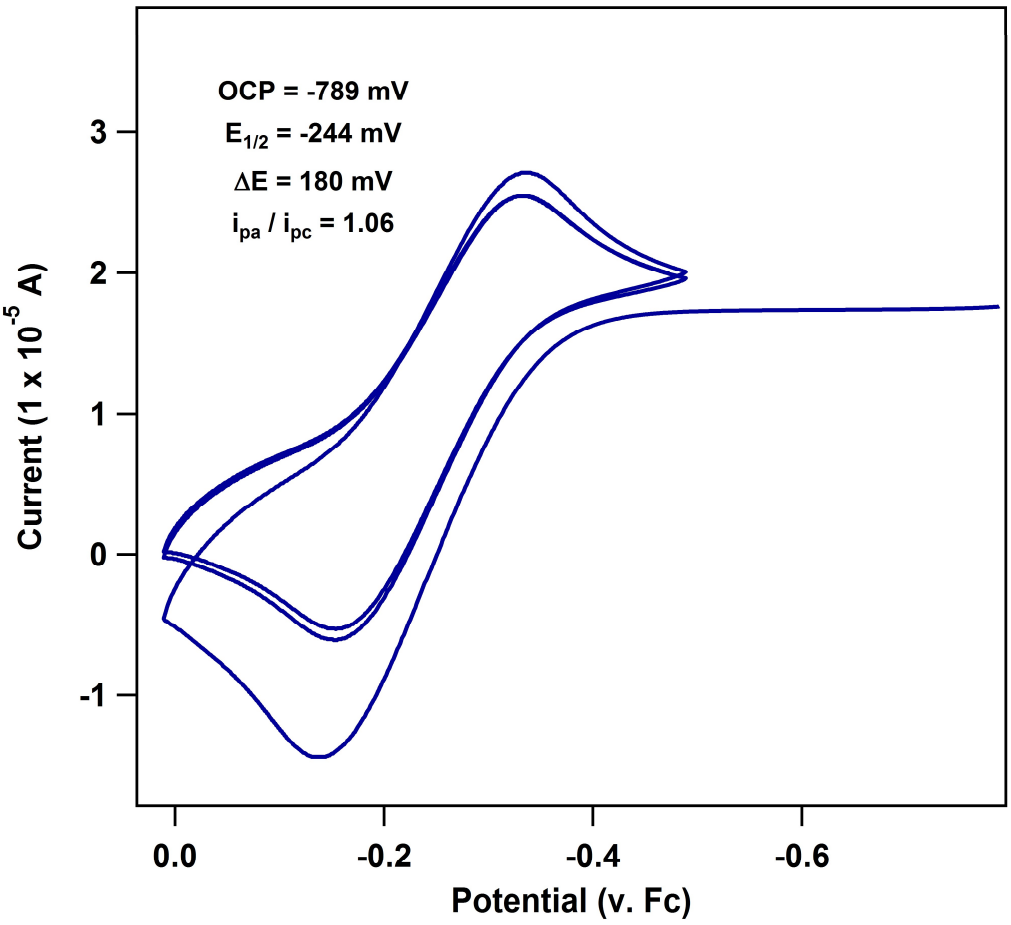


**Figure 3.23.** Cyclic voltammogram of ($^{Ar}$L)FeCl(NHC$_6$H$_4$$^t$Bu) obtained in $CH_2Cl_2$ at 25 °C, with 0.1 M ($nBu_4N$)($PF_6$) as supporting electrolyte and a scan rate of 50 mV/s showing a quasi-reversible oxidation event at -244 mV (OCP: -789 mV). Potentials are internally referenced versus the ferrocene/ferrocenium couple.

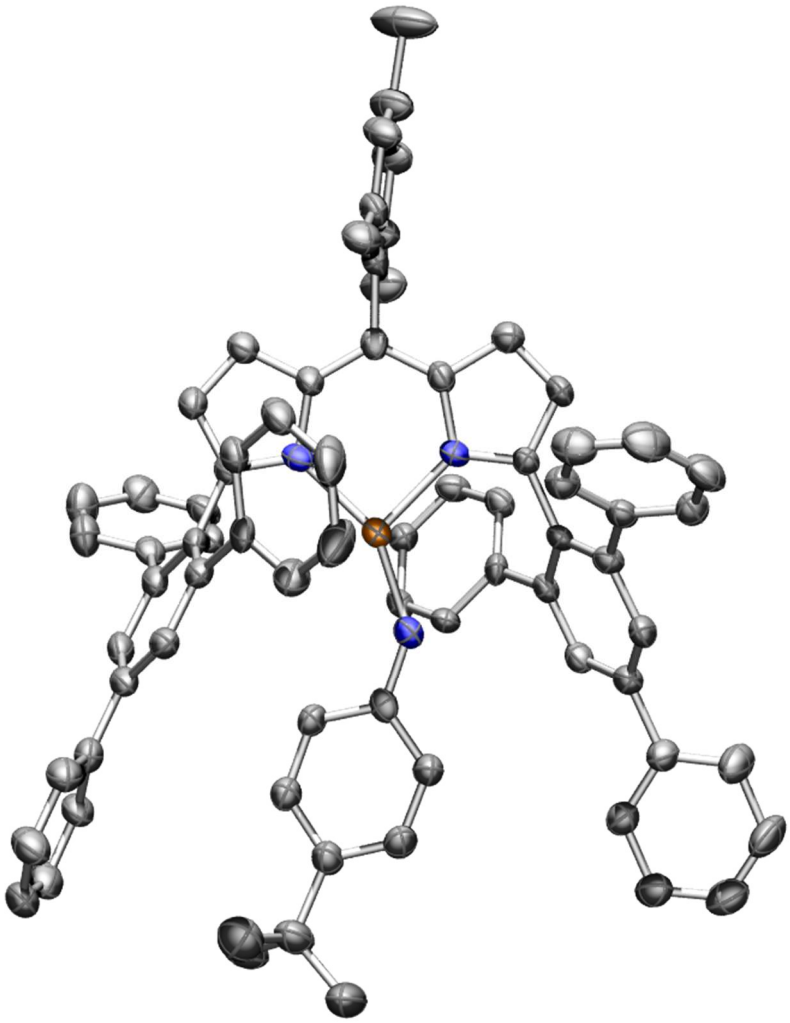

**Figure 3.24.** Solid-state molecular structure for ($^{Ar}$L)Fe(NHC$_6$H$_4$$^t$Bu) with thermal ellipsoids at 50% probability level. Hydrogen atoms not shown. Iron = orange, nitrogen = blue, carbon = gray.

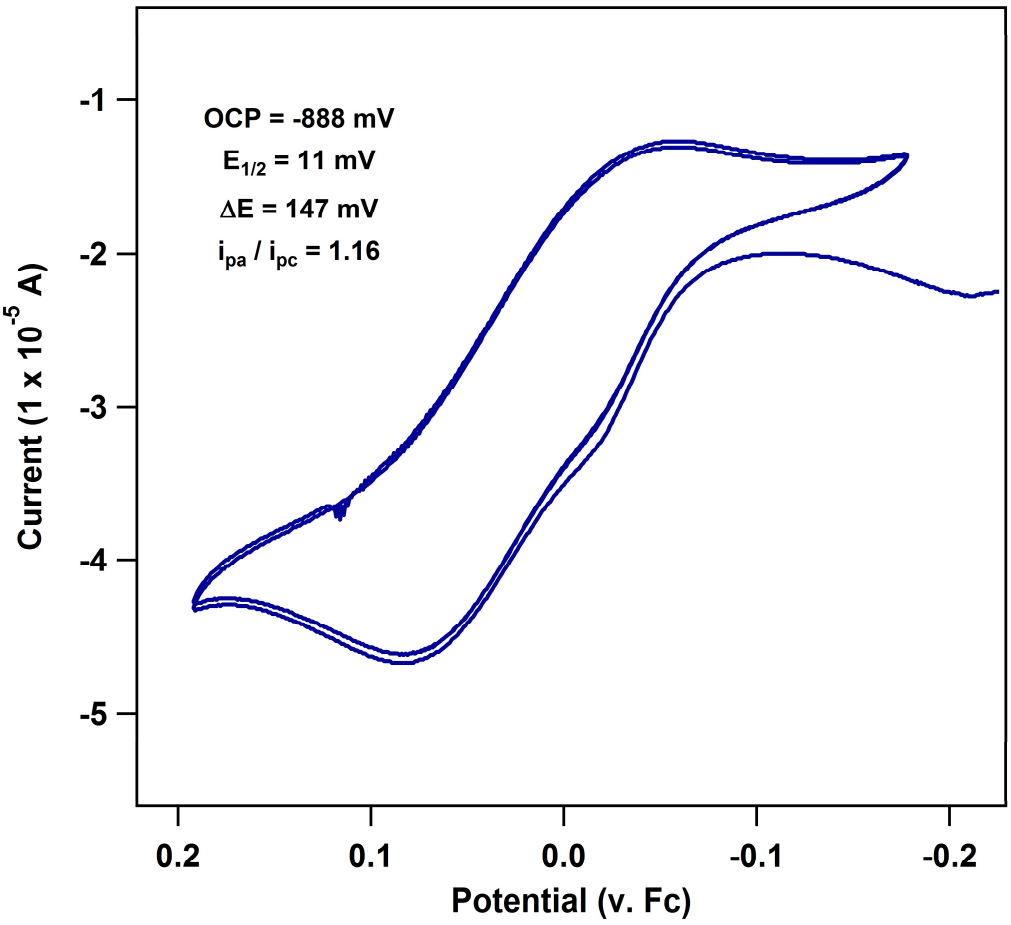


**Figure 3.25**. Cyclic voltammogram of ($^{Ar}$L)FeCl(NHAd) obtained in $CH_2Cl_2$ at 25 °C, with 0.1 M ($nBu_4N$)($PF_6$) as supporting electrolyte and a scan rate of 10 mV/s showing a quasi-reversible oxidation event at 11 mV (OCP: -888 mV). Potentials are internally referenced versus the ferrocene/ferrocenium couple.

### *3.5.5 Reactivity Experiments*

**Kinetic monitoring of reaction with toluene**. An air-tight quartz cuvette was charged with a solution of desired complex in $C_6D_6$ and appropriately diluted with toluene (M = ~ 40 μM, ϵ = ~30, 000 $M^{-1}cm^{-1}$). The cuvette was immediately sealed, removed from the drybox, and placed in the spectrometer sample holder, which was preheated by a circulating water bath for at least 15 minutes. Scans from 300-800 nm were recorded either every 5 or 10 minutes at a scan rate of 600

nm/min. The absorbance at $\lambda_{max}$ was then extracted, plotted as a function of time, and the data normalized. This data was fitted as an exponential decay according to $y = A * \exp(-Cx) + B$ to extract the reaction rate. The observed rates were utilized to construct both an Arrhenius plot and Eyring plot, from which the activation energy, enthalpy of activation, and entropy of activation could be determined.

**Table 3.6.** Kinetic activation parameters for dipyrrin-iron complexes.

| | *Temp (°C)* | *rate ($s^{-1}$)* | *half-life ($min^{-1}$)* | *$E_a$ ($^{kcal}/_{mol}$)* | *$\Delta H^{\ddagger}$ ($^{kcal}/_{mol}$)* | *$\Delta S^{\ddagger}$ ($^{kcal}/_{mol}$)* |
|---|---|---|---|---|---|---|
| **$^{Ar}$LFe(NAd)** | 80 | 0.0264 | 26 | | | |
| | 90 | 0.0427 | 16 | 11.5 | 8.22 | 0.037 |
| | 100 | 0.0633 | 11 | | | |
| **$^{Ar}$LFe(NAr)** | 80 | 0.0195 | 36 | | | |
| | 90 | 0.0344 | 20 | 12.1 | 8.80 | 0.036 |
| | 100 | 0.0748 | 9 | | | |
| **$^{Ar}$LFeCl(NAd)** | 22 | 0.0297 | 23 | | | |
| | 32 | 0.0432 | 16 | 7.1 | 1.84 | 0.051 |
| | 42 | 0.0722 | 10 | | | |
| **$^{Ar}$LFeCl(NAr)** | 22 | 0.0166 | 42 | | | |
| | 32 | 0.0256 | 27 | 9.2 | 3.84 | 0.045 |
| | 42 | 0.0528 | 13 | | | |

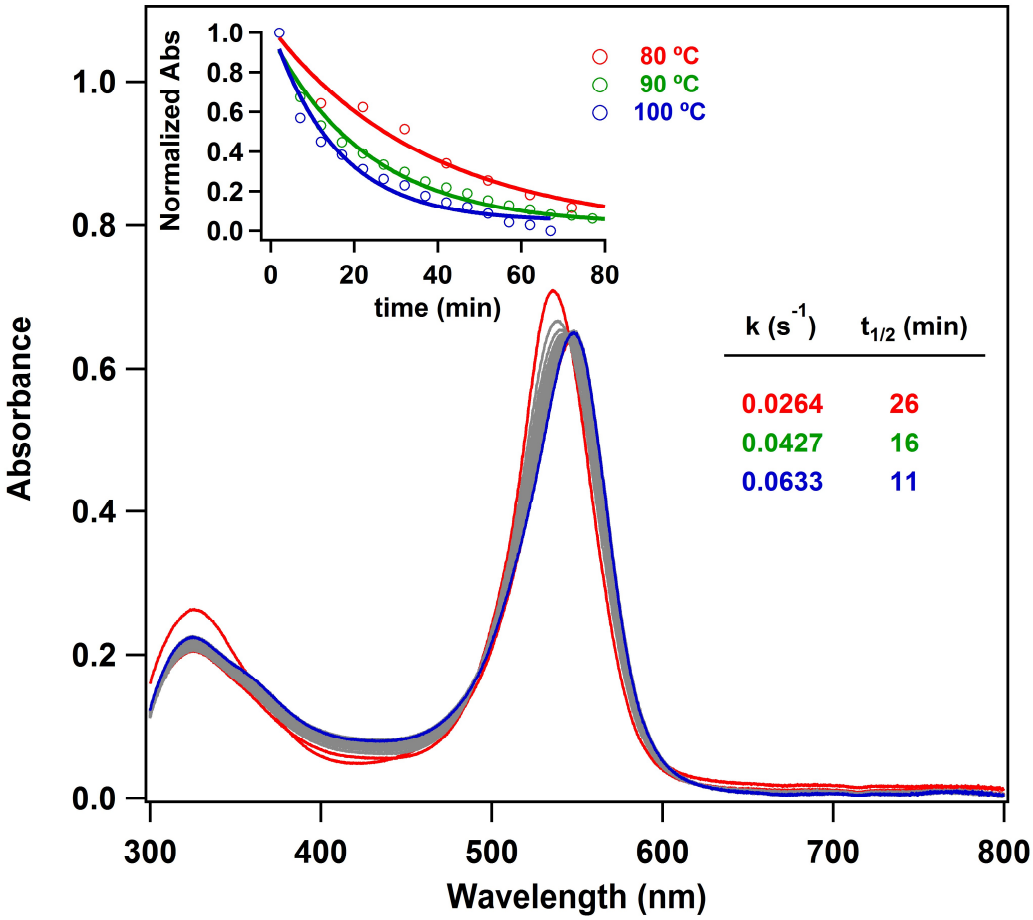


**Figure 3.26.** UV/Vis traces of ($^{Ar}$L)Fe(NAd) (**6**) in toluene as solvent taken at 5 minute intervals under inert atmosphere at 80 °C, with initial scan shown in red and final scan in blue. (**inset**) Normalized absorbance at $\lambda_{max}$ (536 nm) plotted as a function of time and fitted as an exponential decay, with the extracted rate constants and corresponding half-lives shown to the right.

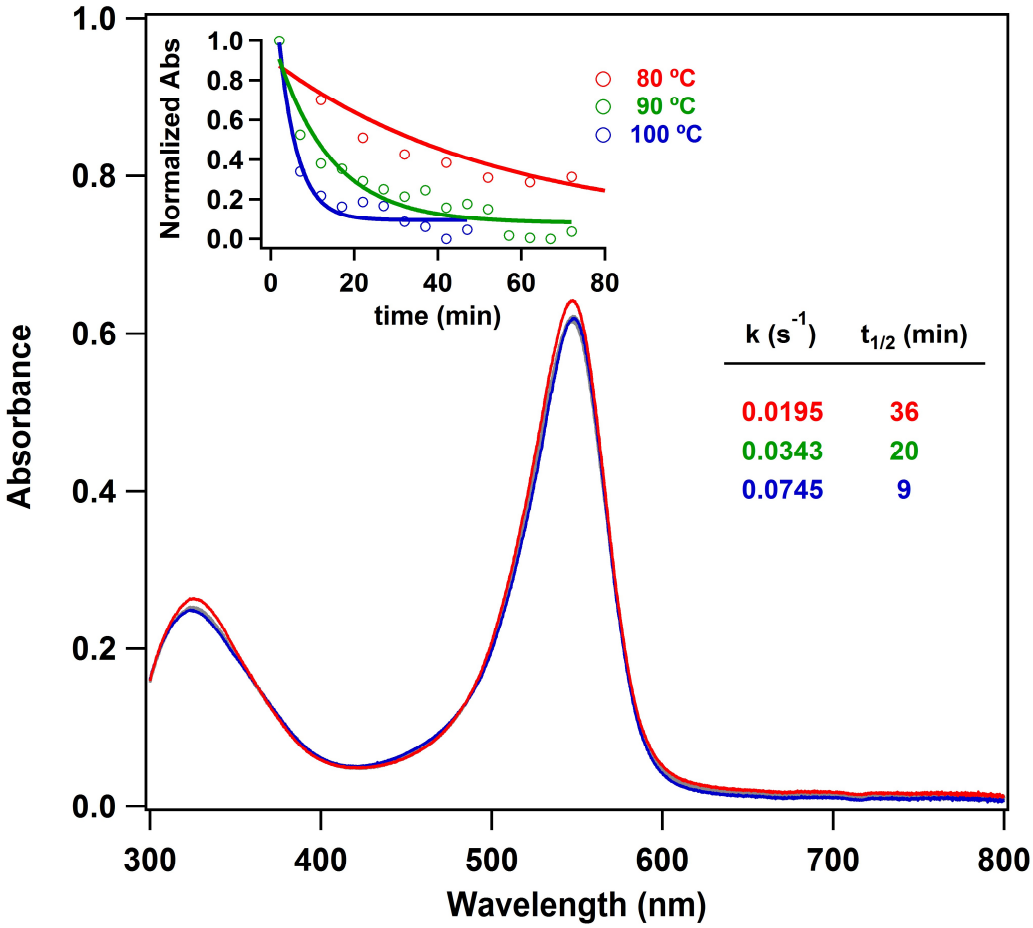


**Figure 3.27.** UV/Vis traces of **($^{Ar}$L)FeCl(NC$_6$H$_4$$^t$Bu)** (**2**) in toluene as solvent taken at 5 minute intervals under inert atmosphere at 100 °C, with initial scan shown in red and final scan in blue. (**inset**) Normalized absorbance at $\lambda_{max}$ (547 nm) plotted as a function of time and fitted as an exponential decay, with the extracted rate constants and corresponding half-lives shown to the right.

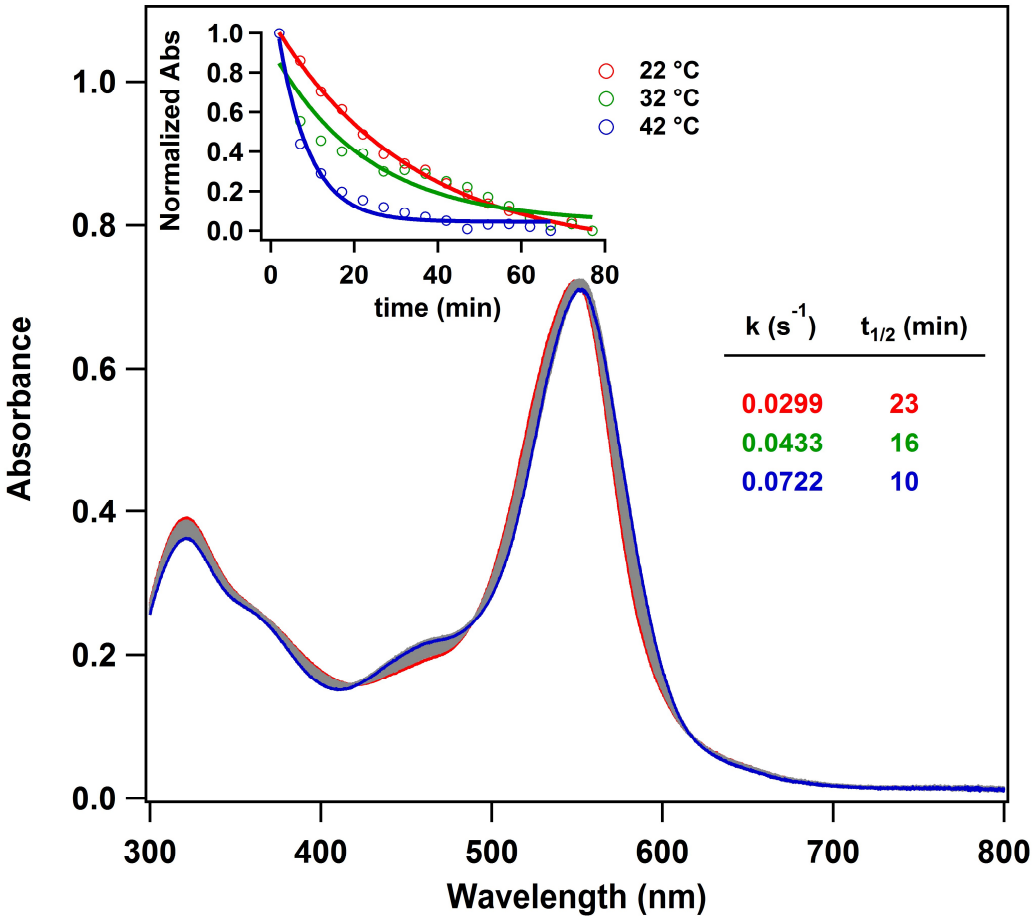


**Figure 3.28.** UV/Vis traces of ($^{Ar}$L)FeCl(NAd) (**6**) in toluene as solvent taken at 5 minute intervals under inert atmosphere at 22 °C, with initial scan shown in red and final scan in blue. (**inset**) Normalized absorbance at $\lambda_{max}$ (550 nm) plotted as a function of time and fitted as an exponential decay, with the extracted rate constants and corresponding half-lives shown to the right.

**Competitive reaction of ($^{Ar}$L)FeCl(NAd) (6) and ($^{Ar}$L)Fe(NAd) (5) with toluene.** A J. Young tube was charged with an equimolar mixture of ($^{Ar}$L)Fe(NAd) and ($^{Ar}$L)FeCl(NAd) and 1.0 mL (proteo)toluene. A zero-time $^{1}$H NMR was recorded (PRESAT solvent suppression, 1 db pulse power) before the tube was placed in a thermostated oil bath at 60 °C. By t = 60 min, the chemical shifts corresponding to ($^{Ar}$L)FeCl(NAd) were completely consumed and an additional set of paramagnetic resonances corresponding to ($^{Ar}$L)FeCl were observed. The resonances of ($^{Ar}$L)Fe(NAd) remained constant throughout the course of the reaction. The presence of N-

adamantylbenzylamine was confirmed by both $^{1}$H NMR ($\delta$ = 3.72 ppm) and GC-MS.

**Reaction of ($^{Ar}$L)Fe(NAd) with cyclohexene.** A J. Young tube was charged with ($^{Ar}$L)Fe(NAd) (5.0 mg, 4.7 $\mu$mol, 1 equiv.). A solution of cyclohexene in benzene-$d_6$ (98 mg, 1.2 mmol, 256 equiv. diluted to 1 mL) was added to the tube. A zero time $^{1}$H NMR was recorded. The tube was placed in a thermostated oil bath at 80 °C and monitored every 12 h by $^{1}$H NMR until formation of ($^{Ar}$L)FeNHAd was complete. Both aminated cyclohexene and radically couple cyclohexene dimer were observed via GC-MS. N-methylcyclohex-2-en-1-amine: (m/z) 233, 190, 176, 163, 149, 135, 121, 107, 94, 81, 67, 55. [1,1'-bi(cyclohexane)]-2,2'-diene: (m/z) 162, 148, 108, 93, 81, 67, 55. Reaction did not occur at temperatures lower than 80 °C.

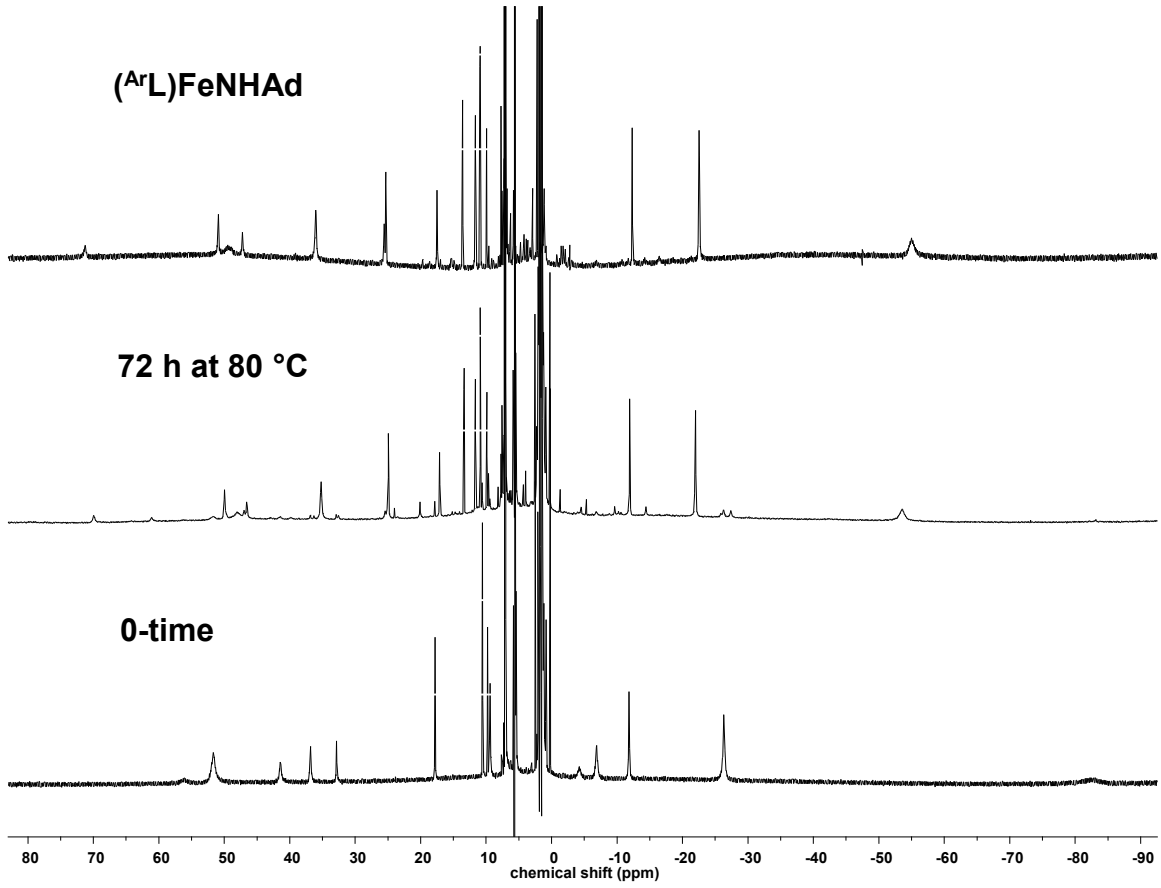


**Figure 3.29.** Stacked $^{1}$H NMR spectra for the reaction of ($^{Ar}$L)Fe(NAd) (5) with 200 equivalents

of cyclohexene with authentically prepared ($^{Ar}$L)FeNHAd, demonstrated productive H-atom abstraction from cyclohexene.

**Reaction of ($^{Ar}$L)Fe(NAd) (5) with styrene.** A J. Young tube was charged with ($^{Ar}$L)Fe(NAd) (7.1 mg, 6.6 μmol) and dissolved in 1 mL styrene. The reaction was placed in an oil bath thermostated at 100 °C. After 24 h, the $^{1}$H NMR (PRESAT solvent suppression, 10 db pulse power) indicated no remaining starting complex. A trace (> 5 %) of N-adamantyl-phenylaziridine was observed via $^{1}$H NMR and confirmed by GC-MS analysis. An accurate yield for this reaction could not be determined due to the insufficient yield.

**Reaction of ($^{Ar}$L)FeCl(NAd) (6) with cyclohexene.** A J. Young tube was charged with ($^{Ar}$L)FeCl(NAd) (4.7 mg, 4.2 μmol, 1 equiv.). A solution of cyclohexene (88 mg, 1.1 mmol, 253 equiv.) in 1 mL benzene-$d_6$ was added and the mixture allowed to reaction at room temperature for 24 hours. A small amount of ($^{Ar}$L)FeCl($NH_2$Ad) was observed via $^{1}$H NMR (PRESAT solvent suppression, 10 db pulse power), as well as aminated product and radically coupled cyclohexene with characterization data identical as that obtained from the analogous reaction with ($^{Ar}$L)Fe(NAd). An accurate yield for this reaction could not be determined due to the insufficient yield.

**Reaction of ($^{Ar}$L)FeCl(NAd) (6) with styrene.** A J. Young tube was charged with ($^{Ar}$L)FeCl(NAd) (6.8 mg, 6.1 μmol, 1 equiv.) and a solution of styrene (128 mg, 1.2 mmol, 200 equiv.) in 1 mL benzene-$d_6$. After 24 hours, $^{1}$H NMR analysis revealed only free ligand as the major species. The red solution was passed through an alumina plug, eluted with 20 mL DCM:MeOH (10:1), and the reaction yield of N-adamantyl-phenylaziridine (36 %) determined via

$^1$H NMR integration versus a trimethoxybenzene internal standard.

### *3.5.6 X-Ray Diffraction Techniques*

Structures of **2-5** were collected on a Bruker three-circle platform goniometer equipped with an Apex II CCD and an Oxford cryostream cooling device. Radiation was from a graphite fine focus sealed tube Mo Kα (0.71073 Å) source. Crystals were mounted on a cryoloop or glass fiber pin using Paratone N oil. Structures were collected at 100 K. Data was collected as a series of φ and/or ω scans. Data was integrated using SAINT and scaled with either a numerical or multi-scan absorption correction using SADABS. The structures were solved by direct methods or Patterson maps using SHELXS-97 and refined against $F^2$ on all data by full matrix least squares with SHELXL-97. All non-hydrogen atoms were refined anisotropically. Hydrogen atoms were placed at idealized positions and refined using a riding model. The isotropic displacement parameters of all hydrogen atoms were constrained to be 1.2 times the parameter of the atoms they were linked to (1.5 times for methyl groups). Further details on particular structures are noted below.

**($^{Ar}$L)Fe(NC$_6$H$_4$$^t$Bu) (3):** The structure was solved in the tetragonal space group I41/a with 1 molecules per unit cell. The toluene/pentane crystallization solvent yield a region of unresolved electron density which was treated via the solvent mask function in Olex2. One of the benzene rings of the dipyrrin ligand exhibited two rotational disorder.

**($^{Ar}$L)Fe(HNC$_6$H$_4$$^t$Bu):** The structure was solved in the triclinic space group $P\bar{1}$ with 1 molecule per unit cell.

**Table 3.7**. Table of experimental details for single crystal x-ray diffraction studies.

| | **($^{Ar}$L)Fe(NC$_6$H$_4$$^t$Bu) (3)** | **($^{Ar}$L)Fe(HNC$_6$H$_4$$^t$Bu)** |
|---|---|---|
| **Moiety Formula** | $C_{76}H_{62}FeN_3$ | $0.5(C_{76}H_{63}FeN_3)$ |
| **FW** | 1073.14 | 540 |
| **Crystal System Space Group** | Tetragonal, $I4_1/a$ | Triclinic, P-1 |
| ***T* (K)** | 100(2) | 100(2) |
| ***a* (Å)** | 42.4313(18) | 14.694(3) |
| ***b* (Å)** | 42.4313(18) | 15.145(3) |
| ***c* (Å)** | 15.8882(8) | 16.966(4) |
| ***α* (°)** | 90 | 68.051(3) |
| ***β* (°)** | 90 | 84.136(3) |
| ***γ* (°)** | 90 | 79.987(3) |
| **Volume (Å$^3$)** | 28605(2) | 3445.8(13) |
| **Z** | 16 | 4 |
| **Radiation Type** | Mo K$\alpha$ | Mo K$\alpha$ |
| ***μ* (mm$^{-1}$)** | 0.25 | 0.46 |
| **Crystal Size (mm)** | 0.35 × 0.33 × 0.15 | 0.61 × 0.30 × 0.20 |
| **Reflections** | 13709 | 21370 |
| **R1, *w*R2[a], *S* [$I > 2\sigma(I)$]** | 0.089, 0.280, 1.14 | 0.089, 0.280, 0.97 |

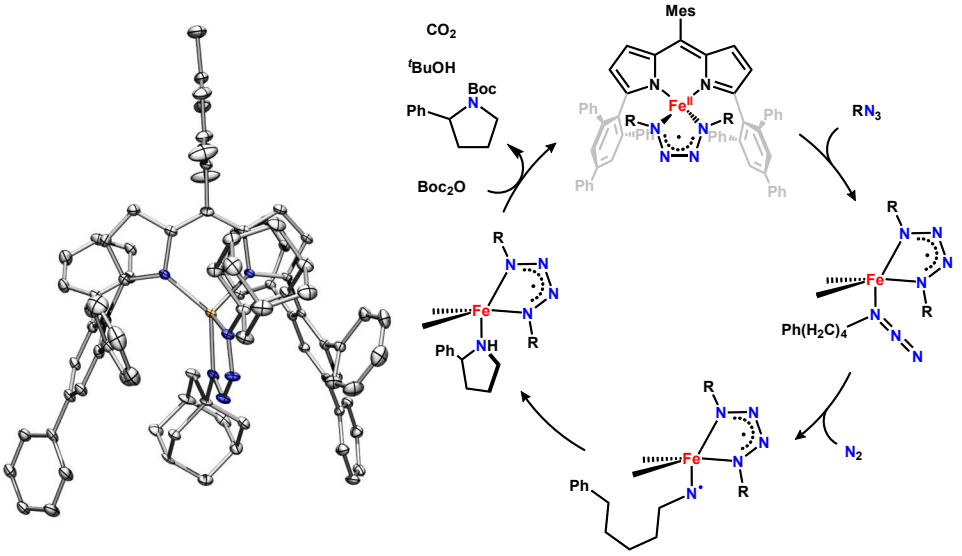


# Chapter 4: (Dipyrrinato)iron-tetrazene Complexes as Unexpected Catalysts for C–H Amination[1]

## 4.1 Introduction

Saturated cyclic amines are ubiquitous in biologically active natural products and pharmaceuticals;[2] however, their syntheses typically rely on functional group exchange, which leads to inefficient atom economy. By appending a C–H bond donor onto an azide moiety, direct C–H amination could provide these *N*-heterocycles in a single operation and would produce nitrogen as the only byproduct. Although C–H functionalization offers a more direct and atom-

1. This work was done in collaboration with Diana Iovan and Claire Lidston at Harvard University. My contributions included discovery and development of both the iron(I) catalytic system as well as the iron-tetrazene catalytic system. Kinetic investigations were performed jointly with Diana Iovan and further derivatization of iron tetrazene catalysts performed jointly with Claire Lidston.
2. Jugé, M.; Grimaud, N.; Biard, J. F.; Sauviat, M. P.; Nabil, M.; Verbist, J. F.; Petit, J. Y. *Toxicon* **2001**, *39*, 1231–1237. O'Hagan, D. *Nat. Prod. Rep.* **2000**, *17*, 435–446.

economic methodology for the construction of carbon-heteroatom bonds, current systems require directing groups, strong chemical oxidants, or preoxidation of substrate to overcome the relative chemical inertness of aliphatic C–H bonds, which have bond dissociation energies of 95 to 105 kcal/mol.[3] Further, the poor spatial and energetic accessibility of C–H bonding and antibonding orbitals hampers traditional organometallic oxidative addition.

**Scheme 4.1.** Iron-catalyzed C–H functionalization reactions conducted stoichiometrically or catalytically to furnish pyrrolidine products

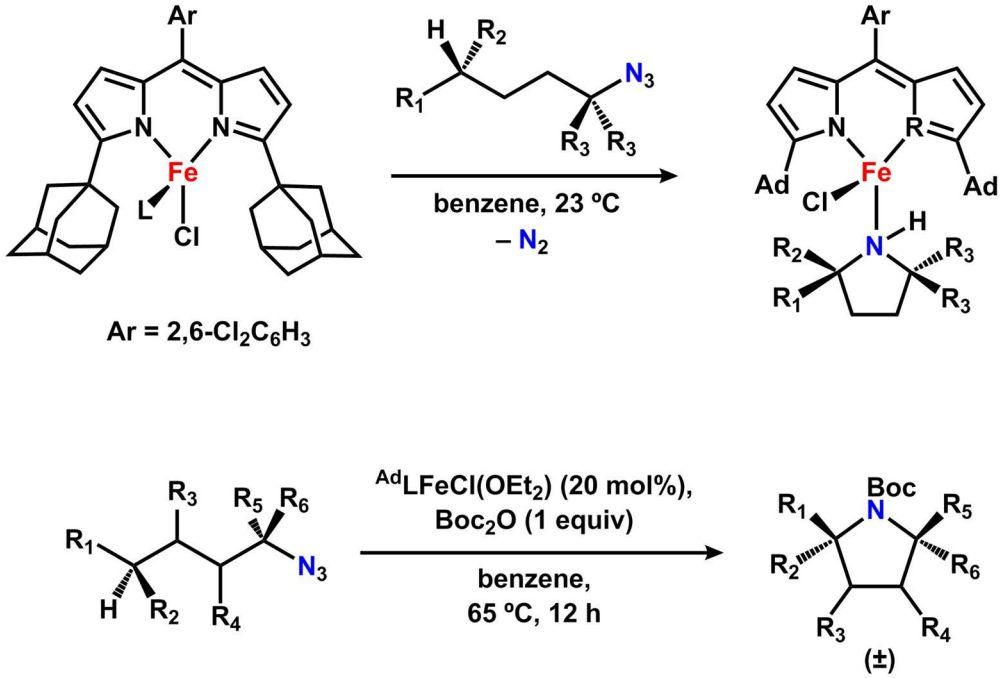


Our group has utilized high-spin metal-ligand multiple bonds to enable the direct C–H functionalization of a variety of hydrocarbon substrates (**Scheme 4.1**). For example, the previously reported catalytic system utilizing ($^{Ad}$L)FeCl(OEt$_2$) can cyclize 1-azido-4-phenylbutane in good

3. Zalatan, D. N.; Du Bois, J. *Top. Curr. Chem.* **2010**, *292*, 347–378. Ryabov, A. D. *Chem. Rev.* **1990**, *90*, 403–424. Dick, A. R.; Sanford, M. S. *Tetrahedron* **2006**, *62*, 2439–2463. Labinger, J. A.; Bercaw, J. E. *Nature* **2002**, *417*, 507–514.

yield with 10 mol % catalyst in the presence of stoichiometric di-*tert*-butyldicarbonate ($Boc_2O$).[4] The addition of protecting group is necessary to sequester the 2-phenylpyrrolidine product from the Lewis acidic iron center and enable catalytic turnover. Attempts to perform reactions with lower catalyst loadings were, however, unsuccessful, even with extended reaction times. Notably, the initially dark red reaction mixture became orange within 12 h, indicating protonolysis of the catalyst by the *in situ* generated *tert*-butanol.

We have recently reported on the effect of oxidation state in a series of dipyrrinato-iron imide complexes on productive intermolecular C–H functionalization.[5] Our findings indicated that the maximum population of the π* orbitals with respect to the iron imide bond is sufficient to engender the desired reactivity, even at the lower (ferric) oxidation state (**Scheme 4.2**). In addition, we observed that the radical content contained within the metal-ligand multiple bond vector directly influences the facility of the amination reaction, albeit at the expense of stability toward isolation and synthetic manipulation of the organometallic species. As such, the dipyrrinato-iron imide complexes in lower molecular oxidation states display significant resistance to decomposition both in the solid- and solution-phase while the higher-valent dipyrrinato-iron iminyl complexes decay over the course of 24 hours in solution. We hypothesized that the analogous intermediates formed *in situ* during C–H functionalization catalysis may be similarly stabilized given a reduction in their overall oxidation state from the current $Fe^{II}$ – $Fe^{III}$•NR catalytic cycle to a $Fe^{I}$ – $Fe^{III}$NR pathway.

4. Hennessy, E. T.; Betley, T. A. *Science* **2013**, *340*, 591.
5. Wilding, M. J. T.; Betley, T. A. Current work.

**Scheme 4.2.** Stoichiometric C–H amination of toluene by a ferric (dipyrrinato)iron complex

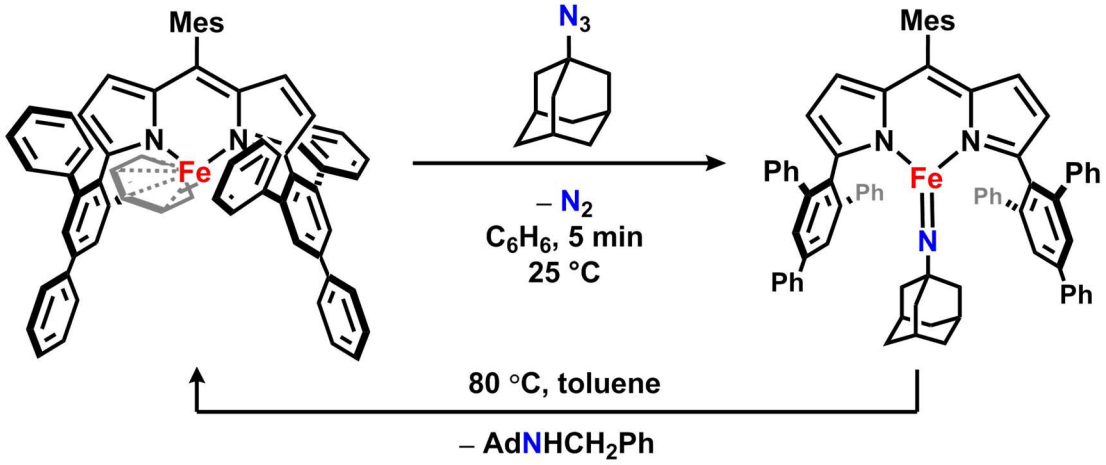


Herein, we report the performance of ($^{Ar}$L)Fe$^{I}$ as a precatalyst for intramolecular C–H amination to form *N*-Boc-pyrrolidine products, which allows for a reduction in catalyst loading of greater than two orders of magnitude while still preserving good reaction yields. We offer that the active catalyst is a dipyrrinato-iron tetrazene complex that forms *in situ* upon exposure of $^{Ar}$LFe$^{I}$ to excess azide. A family of iron complexes with varying *N*-substituents of the tetrazene ligand were prepared, surveyed for reactivity towards pyrrolidine formation, and determined to enable a highly tolerant catalytic protocol with as little as 1,000 ppm loading of catalyst. Kinetic analysis, $^{57}$Fe Mössbauer spectroscopy, and *in situ* infrared spectroscopy suggest that binding of an additional ligand to the catalyst is disfavored, and provide a rationale for the exceptional stability of the current catalytic system.

## 4.2 Results and Discussion

Exposure of ($^{Ar}$L)Fe$^{I}$ to a benzene-$d_6$ solution containing ten equivalents of 1-azido-4-phenylbutane resulted in a paramagnetically shifted $^{1}$H NMR spectrum that features resonances consistent with formation of the free (uncoordinated) *N*-heterocycle product. Consumption of

azide ceased after two hours (35 % yield), and neither longer reaction times nor heating furthered consumption of azide, suggesting inhibition by the Lewis basic 2-phenylpyrrolidine product. By conducting the reaction in the presence of stoichiometric $Boc_2O$, the desired *tert*-butyloxycarbonyl (Boc) – protected heterocycle was isolated in 63 % yield after 24 hours at 65 °C.

Prompted by this result and the notion that an *in situ* generated $Fe^{III}(NR)$ species may be more robust than the corresponding $Fe^{III}(^{\bullet}NR)$ under catalytic conditions, the reactivity of $(^{Ar}L)Fe^{I}$ was assayed for the synthesis of *N*-Boc-2-phenylpyrrolidine and the results shown in **Table 4.1**.

**Table 4.1.** Reactivity of dipyrrin-iron complexes for *N*-Boc-2-phenylpyrrolidine formation

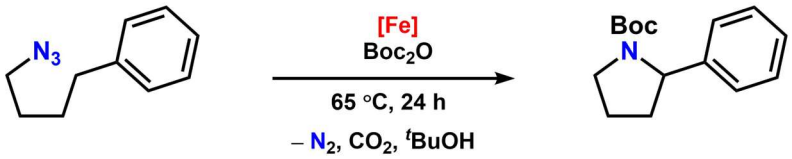


| | $[Fe]_0$ (mol %) | *n* $Boc_2O$ | isolated yield (%) | TON |
|---|---|---|---|---|
| 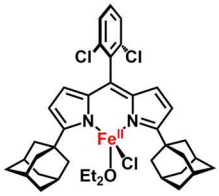 | 10 | 1 | 57 | 5.7 |
| | 0.1 | 1 | 1 | 1 |
| | | 3 | trace | N/A |
| 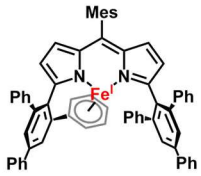 | 10 | 1 | 63 | 6.3 |
| | 1.0 | 1 | 64 | 64 |
| | 0.1 | 1 | 39 | 390 |
| | 1.0 | 3 | 70 | 70 |
| | 0.1 | 3 | 52 | 520 |
| | 0.01 | 3 | 12 | 1200 |

The yield of product was nearly identical with a ten-fold decrease in loading of $(^{Ar}L)Fe^{I}$, which is consistent with slow sequestration of 2-phenylpyrrolidine by $Boc_2O$ under reaction

conditions. Increasing the amount of $Boc_2O$ to three equivalents was sufficient to overcome the slow protection and raise the yield of protected heterocycle to 70 %. Formation of 1-imino-4-phenylbutane was competitive with the desired cyclization and incomplete conversion was also observed at loadings less than 0.1 mol % of catalyst. Nonetheless, the exceptional activity and stability of the system is highlighted by turnover numbers as high as 1200 with only 100 ppm of precatalyst, where the incident concentration of *t*-BuOH resulting from the protection step is three orders of magnitude higher than that of $(^{Ar}L)Fe^{I}$ and protonation of the highly basic dipyrrin ligand was not observed by $^{1}H$ NMR.

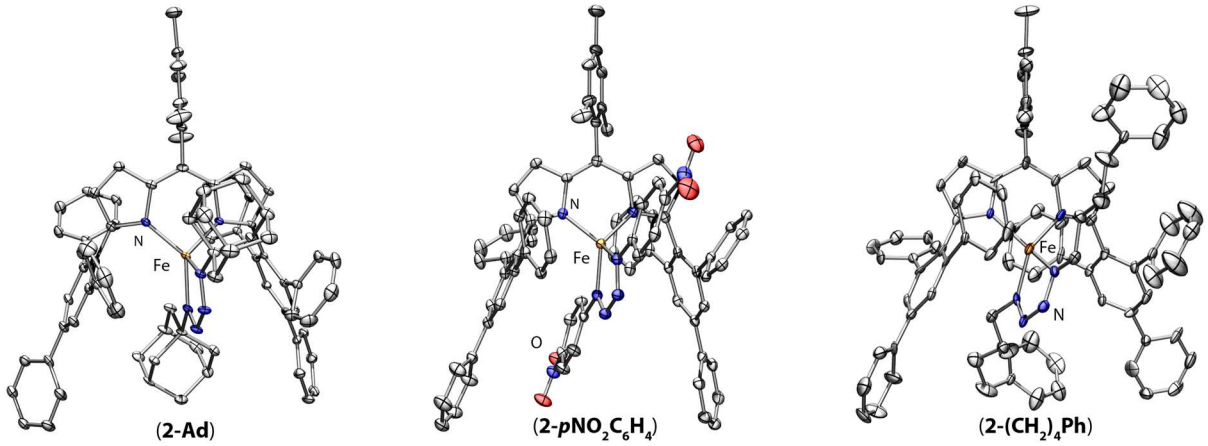


**Figure 4.1**. Solid state molecular structures for dipyrrin-iron tetrazene species with 35 % probability ellipsoids. H-atoms and solvent molecules omitted for clarity. The coloration is as follows: C gray, Fe orange, N blue, O red.

Encouraged by these findings, we sought to isolate and crystallographically characterize the putative $Fe^{III}NR$ intermediate in the C–H functionalization process. However, single crystal X-ray diffraction studies on the reaction product of $(^{Ar}L)Fe^{I}$ and stoichiometric 1-azido-4-phenylbutane instead revealed the formation of the dipyrrin-iron tetrazene complex $(^{Ar}L)Fe(\kappa^2\text{-}RN_4R)$ (R = $Ph(CH_2)_4$). This species possesses a zero-field $^{57}Fe$ Mössbauer spectrum consistent with that previously observed for $(^{Ar}L)Fe(\kappa^2\text{-}N_4Ad_2)$ and is likewise best described as an $Fe^{II}$ center ($S = 2$) center that is antiferromagnetically coupled to a tetrazene-centered radical ($S = -^1/_2$). The paramagnetic chemical shifts observed *in situ* during the cyclization reaction are consistent with

the $^{1}$H NMR spectrum of independently prepared material, which suggests that the majority of precatalyst ($^{Ar}$L)Fe$^{I}$ is effectively converted to the corresponding tetrazene complex during catalytic turnover. Accordingly, ($^{Ar}$L)Fe($\kappa^2$-RN$_4$R) (R = Ph(CH$_2$)$_4$) is catalytically competent to perform *N*-heterocycle formation under similar conditions, with similar yields to that observed with ($^{Ar}$L)Fe$^{I}$. However, these results are not sufficient to clarify if ($^{Ar}$L)Fe($\kappa^2$-RN$_4$R) (R = Ph(CH$_2$)$_4$) functions as a catalytic intermediate, a resting state that can re-enter the Fe$^{I}$/Fe$^{III}$ catalytic cycle, or decomposing to form a discrete species capable of catalyzing the transformation. To test if **2-(CH$_2$)$_4$Ph** could serve as a reactive intermediate, the complex was heated to 100 °C in benzene, which caused only slight decomposition after one week and no observable formation of 2-phenylpyrrolidine, the corresponding iron(III) imido, or ($^{Ar}$L)Fe$^{I}$ (**Scheme 4.3**). Further, cross-over experiments employing ($^{Ar}$L)Fe($\kappa^2$-RN$_4$R) (R = 4-F-C$_6$H$_4$(CH$_2$)$_4$) as a catalyst for the cyclization of 1-azido-4-phenylbutane or 1-azido-4-(3-fluorophenyl)butane showed no evidence for the formation of either *N*-Boc-2-(4-fluorophenyl)pyrrolidine or a separate iron tetrazene species (

**Scheme 4.4**).

**Scheme 4.3** Thermal stability of iron tetrazene complex

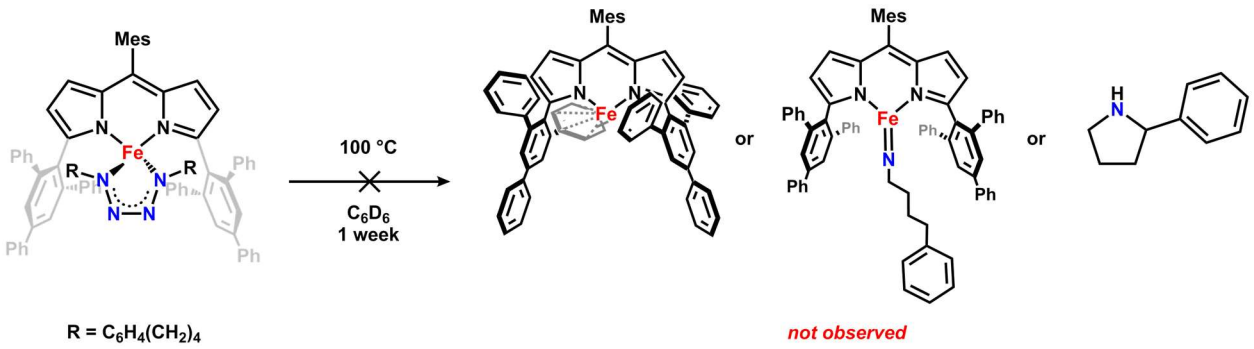


**Scheme 4.4** Cross-over experiment supporting integrity of iron tetrazene during catalysis

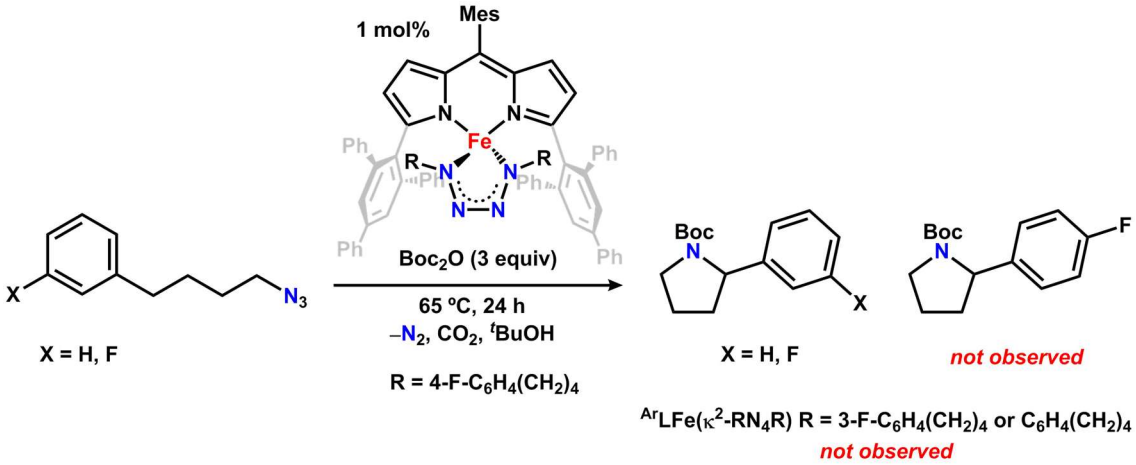


**Scheme 4.5.** Synthetic scheme for the preparation of (dipyrrinato)iron-tetrazene complexes.

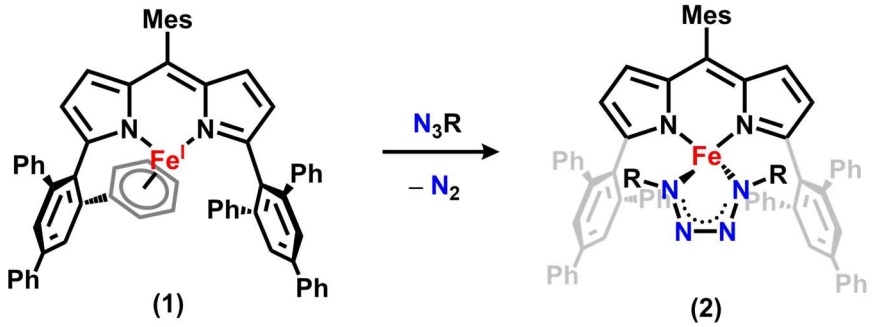


**Scheme 4.6.** Possible redox isomers for the iron-tetrazene fragment.

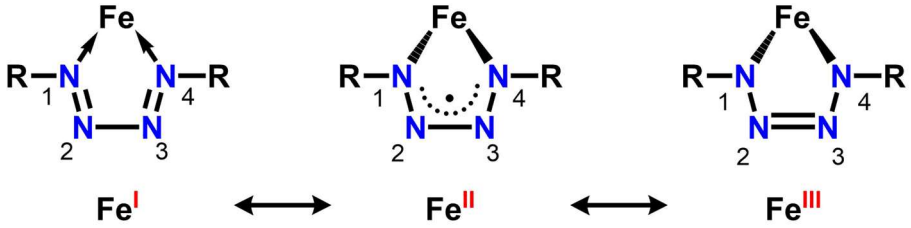


The observed ancillary behavior of the tetrazene ligand prompted the synthesis of a family of (dipyrrinato)iron tetrazene complexes differing in tetrazene *N*-substituents to study the effects of steric and electronic perturbations on catalytic performance (**Scheme 4.5**). Addition of excess alkyl or aryl azide to a purple solution of ($^{Ar}$L)Fe$^{I}$ resulted in immediate effervescence and a rapid color change to red. The solid state molecular structures are shown in **Figure 4.1** and reveal comparable four-coordinate iron centers in distorted trigonal pyramidal geometries for each class of *N*-substituent, although the N–N bond lengths within the tetrazene fragment do vary upon substitution. The $N_2$–$N_3$ bond length of 1.329(6) Å observed for **2-Ad** is reduced to 1.306(4) Å for **2-*p*NO$_2$C$_6$H$_4$** and 1.294(3) Å in **2-(CH$_2$)$_4$Ph**. The more localized double bond character suggests a more oxidized iron center in accordance with the rightmost redox isomer shown in

**Scheme 4.6**. Further support for this analysis comes from the zero-field $^{57}$Fe Mössbauer spectra of these complexes which shows a similar decrease in isomer shift (**2-Ad**: 0.70 $^{mm}/_{s}$, **2-*p*NO$_2$C$_6$H$_4$**: 0.61 $^{mm}/_{s}$, and **(CH$_2$)$_4$Ph**: 0.58 $^{mm}/_{s}$), consistent with a decrease in *d*-electron density. Formal determination of iron oxidation state in high-spin complexes supported by redox active ligands is limited; however, the variation in electronic structure in the current family of complexes emphasizes the breadth of possible configurations involved during catalytic turnover.

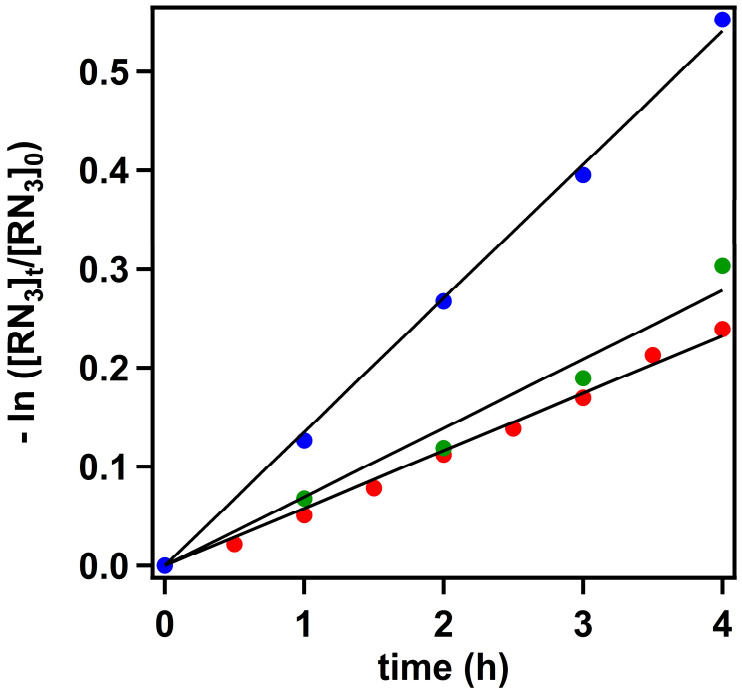


**Figure 4.2.** First-order kinetic plots for (dipyrrinato)iron tetrzene complexes in the cyclization of 1-azido-4-phenylbutane. The red data correspond to catalysis with **2-Ad** (5.81 x $10^{-2}$ $M^{-1}s^{-1}$), the green with **2-*n*Bu** (6.96 x $10^{-2}$ $M^{-1}s^{-1}$), and the blue with **2-(CH$_2$)$_4$Ph** (13.6 x $10^{-2}$ $M^{-1}s^{-1}$). [1-azido-4-phenylbutane]$_0$ = 57 mM, [Boc$_2$O]$_0$ = 172 mM, [Fe]$_0$ = 0.57 mM.

Initial rates of cyclization catalyzed by 1 mol % of complexes **2-(CH$_2$)$_4$Ph**, **2-*n*Bu**, and **2-Ad** respectively were measured over four hours and the results are summarized in **Figure 4.2**. The reaction was slowest for **2-Ad**, likely a consequence of the significant steric projection of the *N*-Ad group which hinders substrate access to the iron center. Reduction in steric bulk to a primary alkyl substituent yielded a 20 % rate enhancement for **2-*n*Bu**. Use of **2-(CH$_2$)$_4$Ph**, which most

closely represents the system when $^{Ar}LFe^{I}$ is employed as a precatalyst, resulted in a 2.3-fold increase in rate as compared to **2-Ad**. Although the initial rate of azide consumption by these catalysts varies highly, the isolated yield of pyrrolidine at 24 h is similar. Specifically, both **2-$(CH_2)_4$Ph** (70 %) and **2-$^n$Bu** (67 %) produced equivalent amounts of product while **2-Ad** (50 %) afforded a marginally lower yield. For all catalysts, no induction period was observable on the time-scale of the kinetic measurements, lending confidence to the notion that the iron tetrazene complexes do not decompose under catalytic conditions to afford slow release of catalytically active species, although additional kinetic investigation is required.

*In situ* investigation of the crude reaction mixture prior to isolation provides insight into the behavior of these catalysts. With the fastest initial rate of substrate consumption, only **2-$(CH_2)_4$Ph** yields complete consumption of azide by 24 h, with the remaining mass balance as the corresponding imine. While **2-$^n$Bu** and **2-Ad** do not fully consume the azide substrate, their higher selectivity for pyrrolidine formation effectively compensates for the slower reaction rate to produce similar yields to that observed with **2-$(CH_2)_4$Ph**. Additionally, the catalyst stability can be correlated to the amount of free dipyrrin ligand observed at completion of the reaction and tracks inversely with initial rate of substrate consumption. For this reason, all further mechanistic analysis was conducted with the *N*-adamantyl substituted catalyst **2-Ad**.

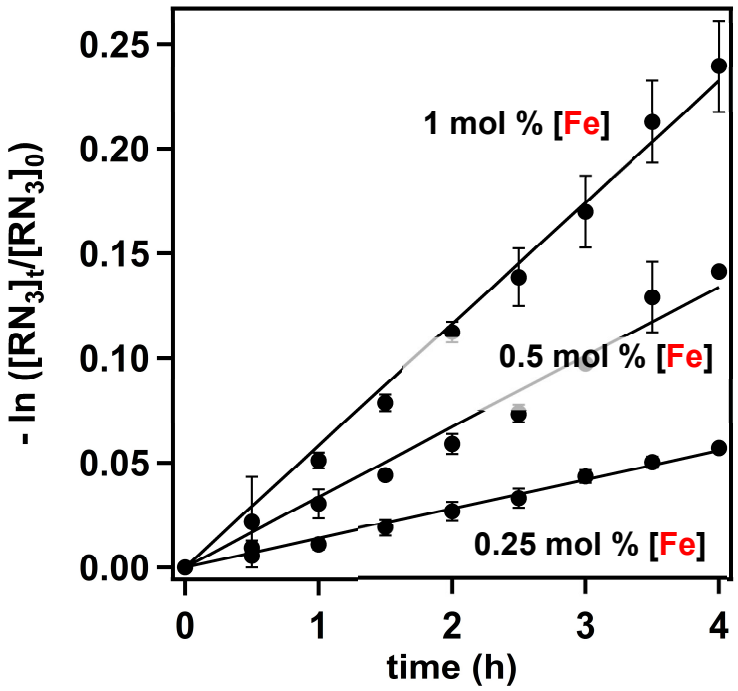


**Figure 4.3**. First-order kinetic plots for varying concentrations of **2-Ad** during the cyclization of 1-azido-4-phenylbutane. $[1\text{-azido-4-phenylbutane}]_0 = 57$ mM, $[Boc_2O]_0 = 172$ mM.

Kinetic analysis of the initial rates (t = 4h) of cyclization in the presence of varying concentration of catalyst produces an experimental reaction order of 1.02 with respect to **2-Ad** (**Figure 4.3**) and suggests that the reaction is first order in catalyst. First-order kinetic plots show strong linear correlation at all catalyst concentrations employed: no induction period is observable on the time scale of the measurement. Monitoring to full conversion produces data that can be well reproduced via least-squares regression to an integrated first-order rate equation (**Figure 4.4**). Overall, this implies that the reaction is first order in substrate as well as catalyst, although it cannot distinguish between the exact mechanistic pathway for substrate binding and activation (i.e. associative or dissociative pathway via dechelation of a single *N*-atom of the tetrazene ligand).

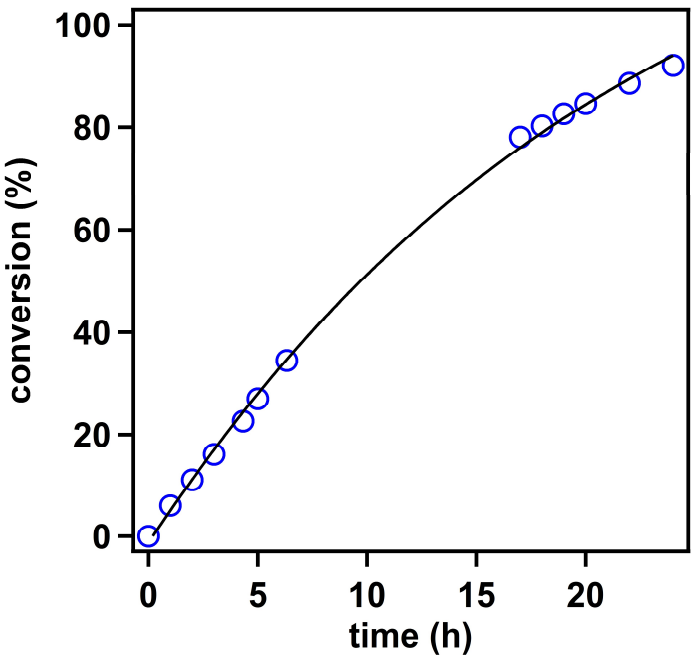


**Figure 4.4.** Plot of conversion versus time for the cyclization of 1-azido-4-phenylbutane by **2-Ad**. Data are shown as circles with the corresponding fit to the integrated first order equation. For details, see Supporting Information.

**Table 4.2** ($^{Ar}$L)Fe($\kappa^2$-$N_4Ad_2$) catalyst performance in the presence of additives

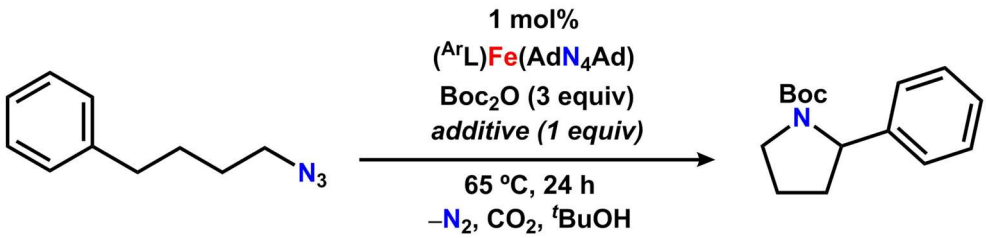


| Additive | Yield (%) |
|---|---|
| dichloromethane | 65 |
| 3,3-dimethyl-2-butanone | 64 |
| acetonitrile | 62 |
| tetrahydrofuran | 42 |
| pyridine | 26 |
| water | < 5 |
| oxygen | < 5 |

Given the higher tolerance of the current catalytic system to high concentrations of *tert*-butanol compared to ($^{Ad}$L)FeCl($OEt_2$) (as assessed via higher resistance to protonolysis of the catalyst under reaction conditions), we were interested to learn if the current system was likewise more stable to Lewis basic moieties under catalytic conditions. A variety of additives were separately combined with stoichiometric amounts of 1-azido-4-phenylbutane and the mixture subjected to cyclization conditions in the presence of 1 mol % of **2-Ad**. Dichloromethane, 3,3-dimethyl-2-butanone and acetonitrile did not impact the yield of the reaction at 24 h as determined via $^1$H NMR integration versus trimethoxybenzene as an internal standard (**Table 4.2**). As the Lewis basicity of the additive increases, the yield of product at 24 h is comparably lowered. For example, only 42 % of the desired pyrrolidine is observed in the presence of tetrahydrofuran while

the yield is even further affected in the presence of pyridine (26 %). Interestingly, although water (200 ppm) and ambient atmosphere strongly suppress catalysis, **2-Ad** does not decompose even upon heating to 65 °C for 24 h, highlighting the stability of the tetrazene-based catalytic system. In all cases, the remaining mass balance is composed predominately of unconsumed substrate, implicating competitive binding as a source of deactivation in the presence of Lewis basic additives.

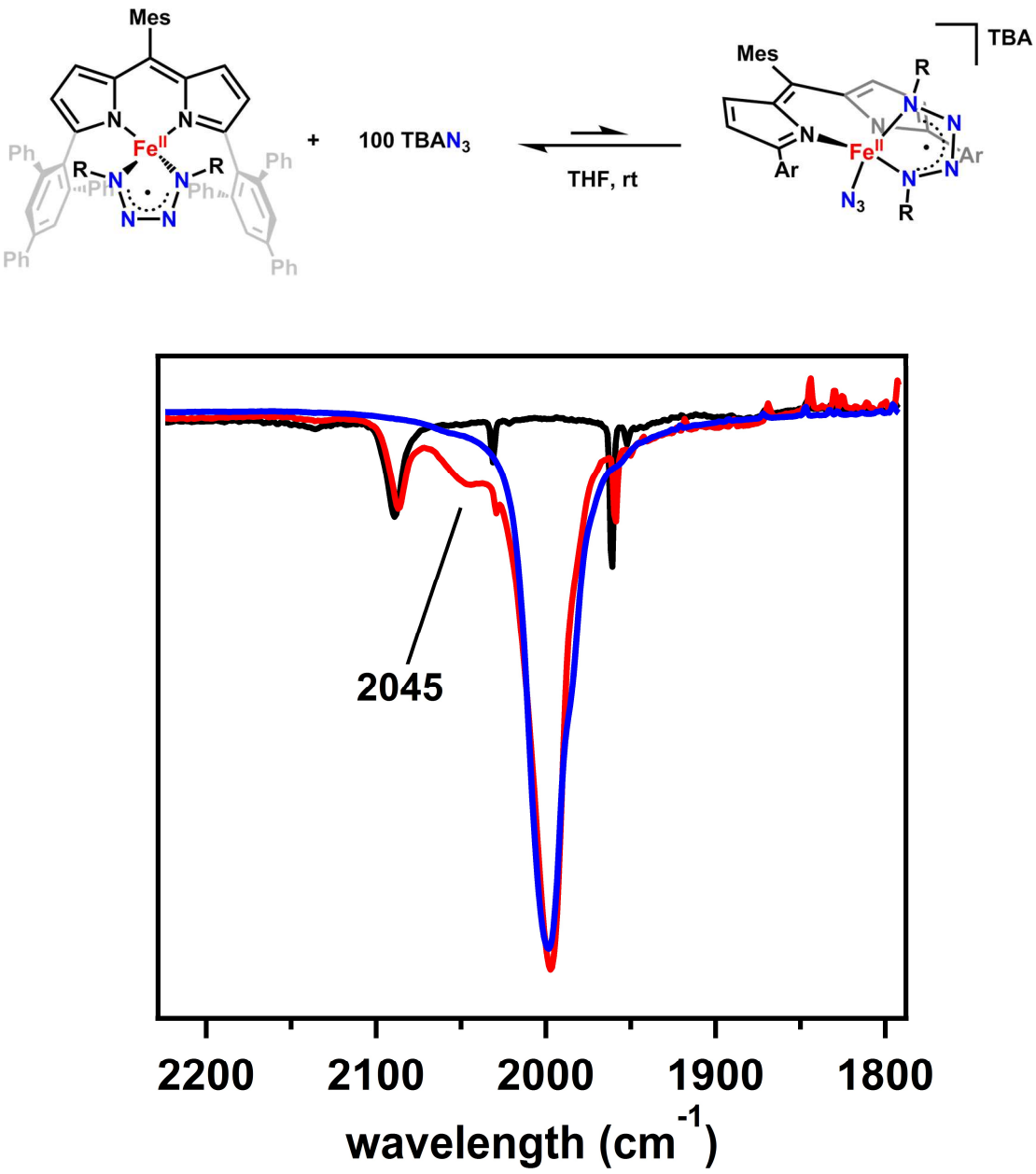


**Figure 4.5.** Stacked infrared spectra of **2-Ad** in black, tetrabutylammonium azide in blue, and a mixture of [**2-Ad**]:[$TBAN_3$] = 1:100 in tetrahydrofuran showing formation of an additional labelled peak consistent with the formation of an adduct complex.

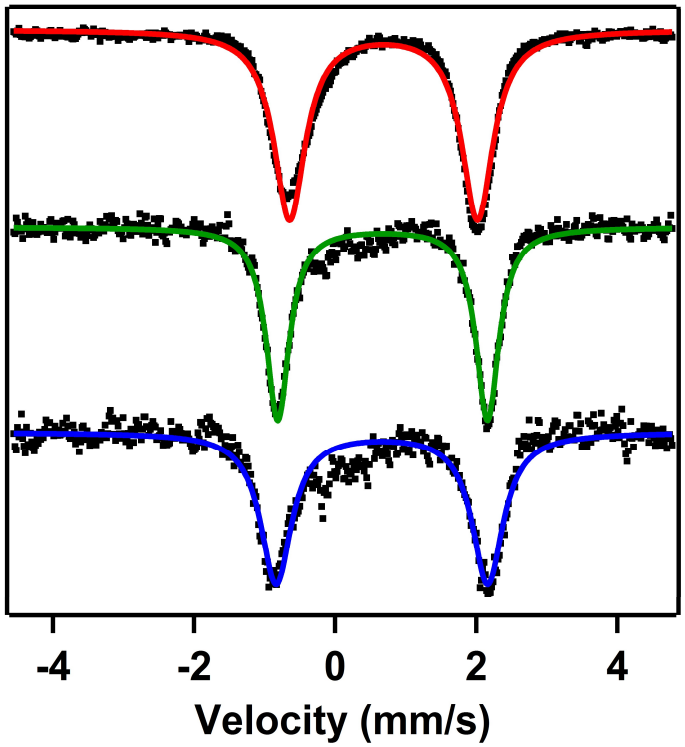


**Figure 4.6.** Stacked zero-field $^{57}$Fe Mössbauer spectra for **2-Ad** in red, *in situ* reaction mixture at t = 4 h in green, and *in situ* reaction mixture at t = 24 h showing preservation of **2-Ad** as the major species during catalytic turnover.

Despite the impact of competitive binding on catalyst performance, neither titration experiments nor variable temperature measurements via $^{1}$H NMR spectroscopy provide evidence for coordination of an additional ligand to **2-Ad**, either independently or *in situ* during catalytic turnover. Treatment of a tetrahydrofuran solution of **2-Ad** with 100 equivalents of tetrabutylammonium azide generates an infrared spectrum possessing an additional stretch at 2045 cm$^{-1}$ with 5 % relative area to the signal associated with uncoordinated tetrabutylammonium azide (**Figure 4.5**). While this peak is consistent with that observed for previous (dipyrrinato)iron chloride adducts with tetrabutylammonium azide, the relative amount of adduct formation is quite low, suggesting that binding is disfavored. *In situ* zero-field $^{57}$Fe Mössbauer spectroscopy supports this analysis as **2-Ad** is the major species observed during the reaction, although a small amount of catalyst decomposition does occur (**Figure 4.6**). Catalyst decomposition can also be inferred

from a same-excess kinetic experiment replicating reaction conditions at 50 % conversion which shows a reaction rate only marginally faster than that observed naturally at 50 % conversion (**Figure 4.7**). Combined with the lack of an observable induction period, the same-excess experiment intimates that **2-Ad** is the catalytically active species. A different-excess experiment replicating reaction conditions at 50 % conversion but excluding *tert*-butanol reveals significantly faster initial rates of cyclization, providing further support for the notion of competitive binding of Lewis basic functionalities to **2-Ad** to suppress the rate of catalytic turnover.

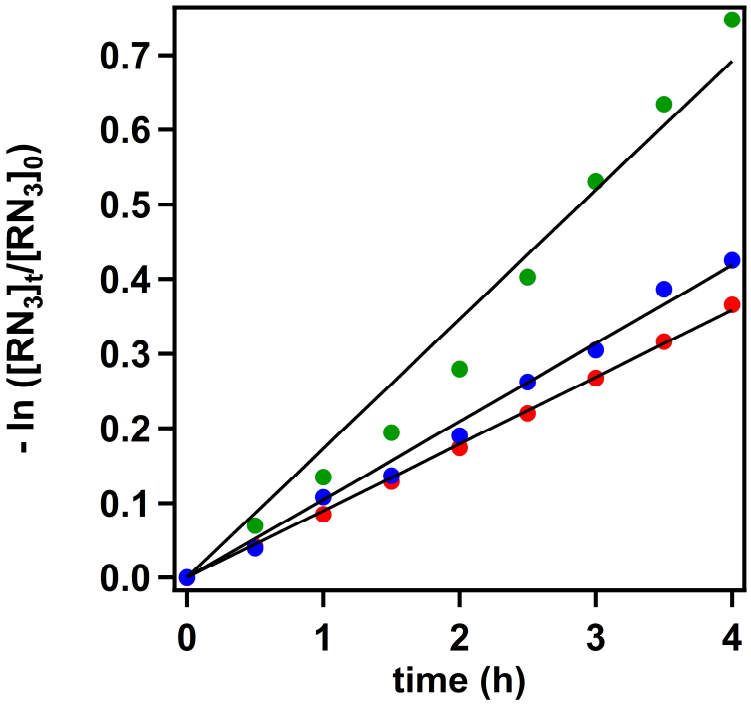


**Figure 4.7**. First-order plot of reaction progress kinetic analysis experiments. The data in red represent time-shifted reaction monitoring starting at 50 % conversion and the data in blue represent the same-excess experiment mimicking 50 % conversion conditions demonstrating slightly faster initial rate. The data in green represent a different-excess experiment mimicking 50 % conversion conditions excluding *t*-BuOH.

The higher functional group tolerance of this catalytic system can be leveraged to provide new classes of products for the cyclization reaction. Previously, we have demonstrated only hydrocarbon-based activating groups for the C–H amination process, i.e. cyclization at a benzylic, allylic, or tertiary C–H bond.[4] Preliminary studies indicate that the current catalytic system,

specifically **2-$^{n}$Bu**, is capable of performing C–H amination at the α-position of a variety of activating groups including boronic ester, nitrile, and ketone functionalities. Further, the standard catalyst loading for these transformations is 1 mol %, a ten-fold reduction from our previous system. For substrates that do not contain Lewis basic additives, the loading may be reduced a further ten-fold to 0.1 mol % while still maintaining good yields of product (61 % *N*-Boc-2-phenylpyrrolidine). Although reduction to 0.01 mol % results in impressive turn over numbers (1400 TON *N*-Boc-2-phenylpyrrolidine), optimization is required to improve the yield at these loadings.

**Scheme 4.7.** Proposed catalytic cycle for the formation of *N*-Boc-pyrrolidines from alkyl azides catalyzed by (dipyrrinato)iron tetrazenido complexes. Product formation may occur either (a) directly from the azide adduct, (b) via stepwise abstraction/recombination, or (c) via direct insertion pathways. Additional mechanistic information is required to favor one of these pathways.

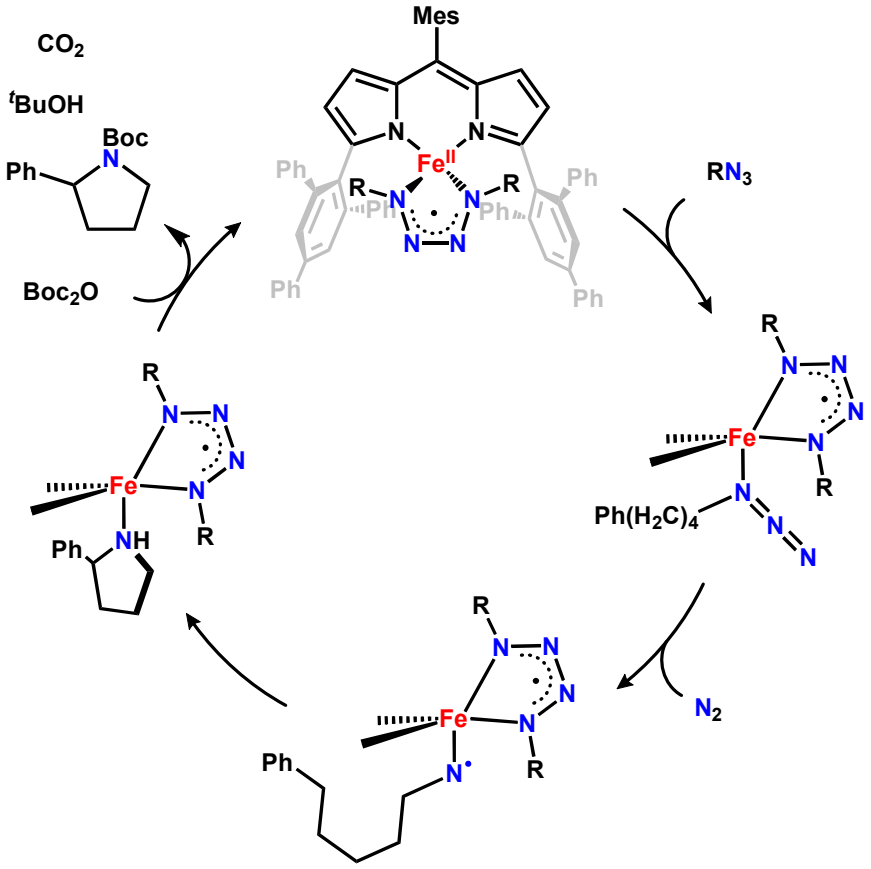

## 4.3 Conclusion

These results demonstrate that the cyclization of alkyl azides in the presence of Boc anhydride to form *N*-Boc-pyrrolidine products can be catalyzed by (dipyrrinato)iron-tetrazene complexes. Preliminary mechanistic analysis suggest that the (dipyrrinato)iron-tetrazene complex serves as the active catalyst via binding of azide, expulsion of dinitrogen, and intramolecular C–H amination to form the functionalized product (**Scheme 4.7**), rather than as an off-cycle species that is capable of forming a separate catalytically active species under reaction conditions. Although disfavored binding equilibria prevented the isolation and characterization of an adduct to the iron center, the addition of Lewis basic additives slowed the rate of catalysis, likely via competitive binding with substrate. *In situ* $^{57}$Fe Mössbauer spectroscopy shows (dipyrrinato)iron-tetrazene as the major iron-containing species during catalytic turnover, though some catalyst decomposition is noticeable, in line with same-excess kinetic experiments.

The catalyst loading required for these transformations may be reduced by two orders of magnitude from our previous catalytic system while still preserving good yields. The modular synthetic nature for tetrazene ligand assembly allows for rapid diversification in both the electronic and steric parameters of the catalyst. Oxidation state assignment for these molecules is challenging given the redox active nature of the tetrazene ligand. Kinetic analysis reveals a first-order rate dependence on both catalyst and substrate, the absence of an induction period, and the suppression of reaction rate in the presence of competitive binding ligands. The current system manifests a higher tolerance to Lewis basic moieties and therefore unlocks a new class of substrates based on activation by a variety of heteroatom functionalities.

## 4.4 Experimental Methods

### *4.4.1 General Considerations*

All manipulations of metal complexes were carried out in the absence of water and dioxygen using standard Schlenk techniques, or in an MBraun inert atmosphere drybox under a dinitrogen atmosphere. Ligand and ligand precursors were synthesized as previously reported.[6] ($^{Ar}$L)Fe (**1**) and ($^{Ar}$L)Fe($\kappa^2$-$N_4Ad_2$) (**2-Ad**) were prepared as previously reported.[7] All glassware was oven dried for a minimum of 1h and cooled in an evacuated antechamber prior to use in the drybox. Benzene, diethyl ether, dichloromethane, n-hexane and tetrahydrofuran were dried over 4 Å molecular sieves (Strem) prior to use. Chloroform-d was purchased from Cambridge Isotope Labs and used as received. Benzene-$d_6$ was purchased from Cambridge Isotope Labs and was degasses and stored over 4 Å molecular sieves prior to use. DDQ, triphenylphosphine, tetrabutylammonium azide, and 3-fluorophenylmagnesium bromide were purchased from Aldrich and used as received. 4-(4-fluorophenyl)butyric acid was purchased from Oakwood and used as received. Aryl azides were synthesized according to literature procedures.[8] Celite® 545 (J. T. Baker) was dried in a Schlenk flask for 24h under dynamic vacuum while heating to at least 150 °C prior to use in a drybox. Silica gel 32-63 μ (AIC, Framingham, MA) was used as received.

### *4.4.2 Characterization and Physical Measurements*

$^1$H and $^{13}$C NMR spectra were recorded on Varian Unity/Inova 400, 500 MHz- or Agilent DD2 600 MHz spectrometers. $^1$H and $^{13}$C NMR chemical shifts are reported relative to $SiMe_4$

6. King, E. K.; Hennessy, E. T.; Betley, T. A. *J. Am. Chem. Soc.* **2011**, *133*, 8293.
7. Wilding, M. J. T.; Betley, T. A. *J. Am. Chem .Soc.* Submitted
8. Smith, P. A.; Hall, J. H. *J. Am. Chem. Soc.* **1962**, *84*, 480.

using the chemical shift of residual solvent peaks as reference. Gas chromatography/mass spectrometry (GC/MS) was performed on an Agilent GC/MS 5975 Turbo system. UV/Visible spectra were recorded on a Varian Cary 50 UV/Visible spectra using a quartz cuvette and a scan rate of 600 nm/ min.

Zero-field $^{57}$Fe Mössbauer spectra were measured with a constant acceleration spectrometer (SEE Co, Minneapolis, MN) at 90K. Isomer shifts are quoted relative to Fe foil at room temperature. Data was analyzed and simulated with Igor Pro 6 software (WaveMetrics, Portland, OR) using Lorentzian fitting functions. Samples were prepared by suspending 25-50 mg of compound in sufficient Paratone oil and immobilizing by rapid freezing in liquid nitrogen.

### *4.4.3 Metal Complexes Syntheses*

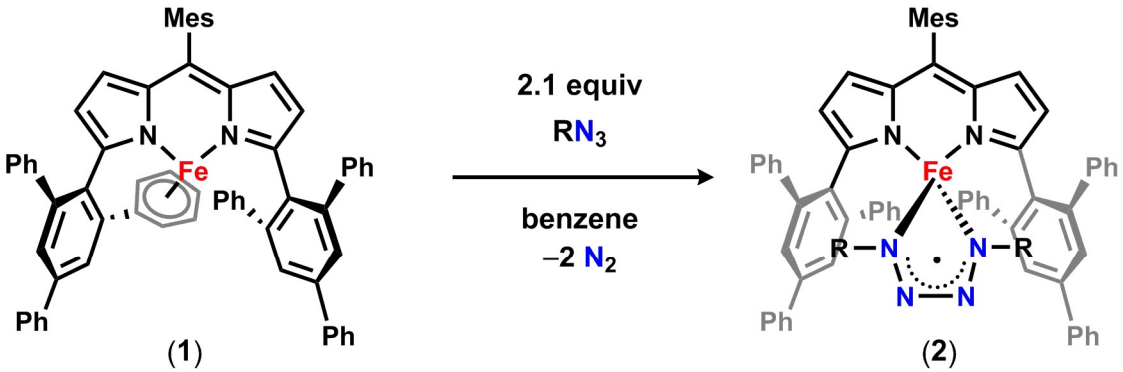


**R = Ad, $^{n}$Bu, $(CH_2)_4Ph$, $(CH_2)_4$(*p*F-Ph), $(CH_2)_4$(*m*F-Ph), *p*$NO_2C_6H_4$, *p*$BrC_6H_4$, *p*$FC_6H_4$, *p*$^{t}$$BuC_6H_4$, *p*$NMe_2C_6H_4$**

***General procedure*:** A solution of azide (2.1 equiv) in benzene was added to a stirring solution of (**$^{Ar}$L)Fe** (**1**) (1.0 equiv) in benzene to observe an immediate color change from dark purple to red/pink. After stirring for 3 hours at room temperatures, the reaction mixture concentrated under vacuum. The resulting solid was washed with hexanes to remove excess azide, dissolved in benzene and solvent lyophilized to afford the corresponding iron tetrazene complex.

**($^{Ar}$L)Fe(κ$^2$-N$_4$R$_2$), R = $^n$Bu), (2-$^n$Bu):** 47.3 mg, 80%. **$^1$H NMR** (500 MHz, $C_6D_6$): δ 21.43 (s), 9.82 (s), 9.69 (br. s), 8.83 (s), 8.36 (s), 6.52 (m), 6.37 (m), 5.80 (br. s), 5.27 (m), 4.40 (s), -10.22 (s), -13.93 (s), -20.71 (br. s).

**($^{Ar}$L)Fe(κ$^2$-N$_4$R$_2$), R = (CH$_2$)$_4$Ph, (2-(CH$_2$)$_4$Ph):** 62.5 mg, 93%. **$^1$H NMR** (500 MHz, $C_6D_6$): δ 21.25 (s), 10.08 (br. s), 9.51 (s), 9.05 (s), 8.51 (s), 6.46 (m), 6.34 (m), 5.78 (m), 5.58 (br. s), 5.48 (m), 5.17 (s), 4.21 (s), 3.38 (s), -6.77 (s), -12.91 (s), -18.25 (br. s). Zero-field $^{57}$Fe Mössbauer (90 K) δ = 0.58 mm/s, $|\Delta E_Q|$ = 3.49 mm/s. UV/Vis (benzene): $\lambda_{max}$ = 528 nm.

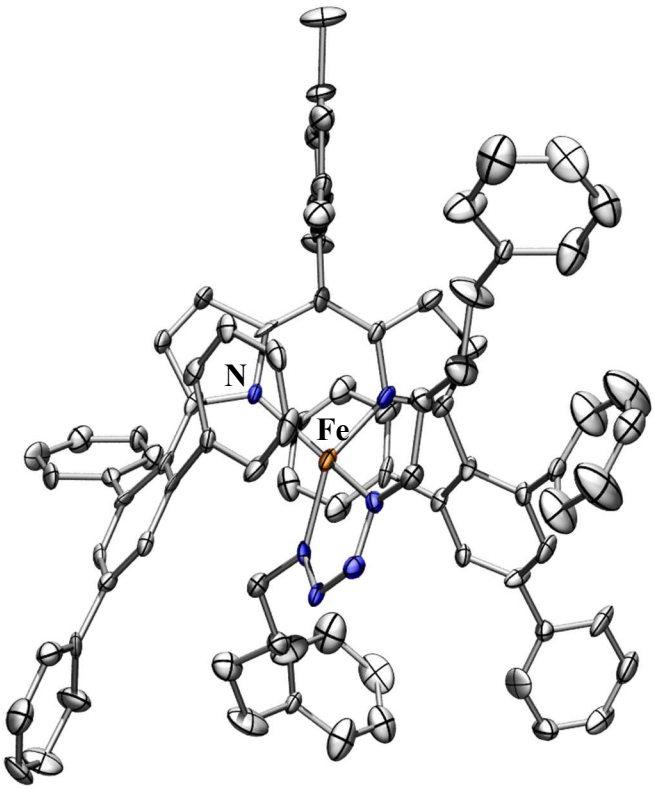


**Figure 4.8** Solid-state molecular structure for ($^{Ar}$L)Fe(κ$^2$-N$_4$R$_2$), R = (CH$_2$)$_4$Ph (**2-Ph(CH$_2$)$_4$**) with thermal ellipsoids at 50% probability level. Hydrogens and benzene solvent in the unit cell omitted for clarity.

**($^{Ar}$L)Fe(κ$^2$-N$_4$R$_2$), R = (CH$_2$)$_4$(*p*-F-Ph): (2-(CH$_2$)$_4$(*p*-F-Ph)): $^1$H NMR** (500 MHz, $C_6D_6$): δ 21.29 (s), 10.25 (br. s), 9.50 (s), 9.09 (s), 8.53 (s), 6.44 (m), 6.32 (m), 5.63 (br. s), 5.17 (m), 4.22 (s), 3.11 (s), -6.93 (s), -13.11 (s), -18.83 (br. s). **$^{19}$F NMR** (376 MHz, $C_6D_6$) δ -119 ppm.

**($^{Ar}$L)Fe(κ$^2$-N$_4$R$_2$), R = (CH$_2$)$_4$(*m*-F-Ph), (2-(CH$_2$)$_4$(*m*F-Ph)): $^1$H NMR** (500 MHz, $C_6D_6$): δ 21.18 (s), 10.07 (br. s), 9.47 (s), 9.01 (s), 8.48 (s), 6.37 (m), 5.48 (br. s), 5.26 (m), 4.20 (s), 3.19 (s), -6.69 (s), -12.80 (s), -18.44 (br. s). **$^{19}$F NMR** (376 MHz, $C_6D_6$) δ -115 ppm.

**($^{Ar}$L)Fe(κ$^2$-N$_4$R$_2$), R = *p*NO$_2$C$_6$H$_4$, (2-*p*NO$_2$C$_6$H$_4$):** 24 mg, 66%. **$^1$H NMR** (500 MHz, $C_6D_6$): δ 57.55 (br. s), 21.90 (s) 8.86 (s), 7.02 (s), 6.87 (s), 6.74 (br.s), 5.92 (s), 3.91 (s), -26.97 (s). Zero-field $^{57}$Fe Mössbauer (90 K) δ = 0.61 mm/s, $|\Delta E_Q|$ = 3.56 mm/s. Crystals suitable for X-ray diffraction were grown from a 1:2 benzene:hexane solution at -35 °C.

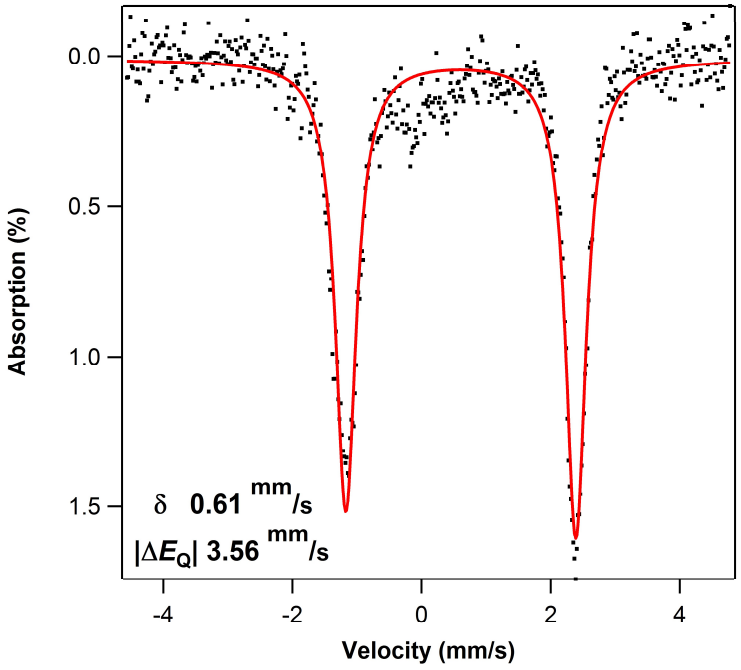


**Figure 4.9** Zero-field $^{57}$Fe Mössbauer of ($^{Ar}$L)Fe(κ$^2$-N$_4$R$_2$), R = *p*NO$_2$C$_6$H$_4$ (**2-*p*NO$_2$C$_6$H$_4$**) collected at 90 K. Isomer shift and quadrupole splitting are referenced to Fe foil at room temperature.

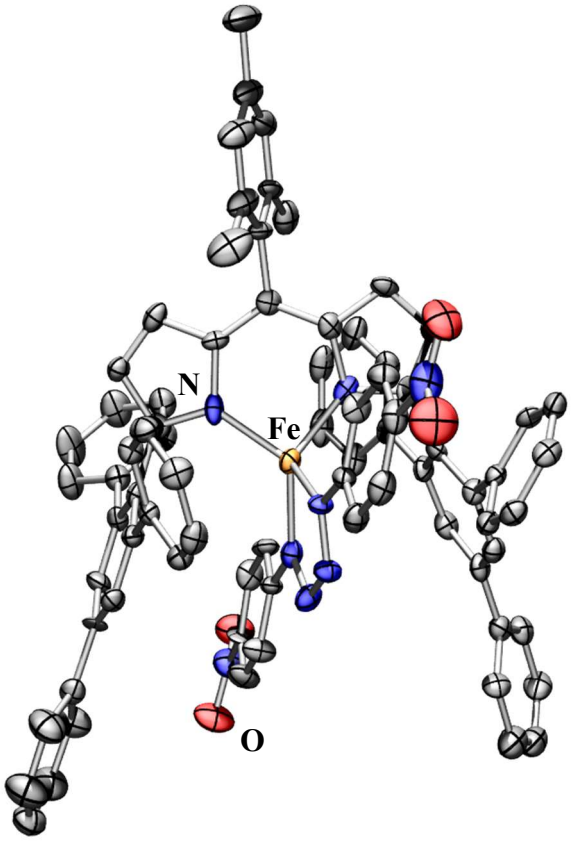


**Figure 4.10** Solid-state molecular structure for ($^{Ar}$L)Fe($\kappa^2$-$N_4R_2$), R = *p*$NO_2C_6H_4$ (**2-*p*$NO_2C_6H_4$**) with thermal ellipsoids at 50% probability level. Hydrogens and benzene solvent in the unit cell omitted for clarity.

**(ArL)Fe($\kappa^2$-$N_4R_2$), R = *p*$BrC_6H_4$, (2-*p*$BrC_6H_4$):** 30.1mg, 85%. **$^1$H NMR** (500 MHz, $C_6D_6$): δ 69.64 (br. s), 22.76 (s), 9.95 (s), 8.64 (br. s), 6.72 (br. s), 5.54 (br.s), 4.51 (s), -35.28 (br. s). Zero-field $^{57}$Fe Mössbauer (90 K) δ = 0.66 mm/s, $|\Delta E_Q|$ = 3.39 mm/s

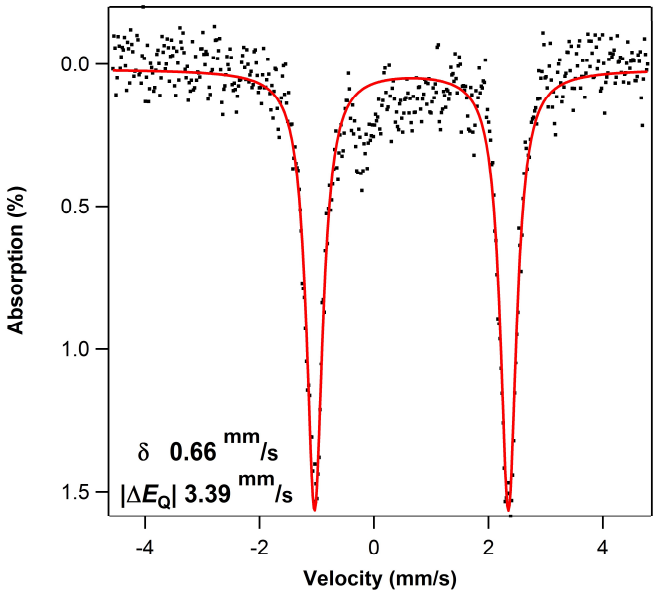


**Figure 4.11** Zero-field $^{57}$Fe Mössbauer of ($^{Ar}$L)Fe(κ$^2$-N$_4$R$_2$), R = *p*BrC$_6$H$_4$ (**2-*p*BrC$_6$H$_4$**) collected at 90 K. Isomer shift and quadrupole splitting are referenced to Fe foil at room temperature.

**($^{Ar}$L)Fe(κ$^2$-N$_4$R$_2$), R = *p*FC$_6$H$_4$, (2-*p*FC$_6$H$_4$):** 107.1 mg, 85%. **$^1$H NMR** (500 MHz, C$_6$D$_6$): δ 68.46 (br. s), 22.70 (s), 10.08 (s), 9.14 (br. s), 7.59 (s), 6.85 (br.s), 6.62 (m), 6.54 (m), 5.45 (br. s), 5.37 (s), 5.15 (s), 4.60 (s), -33.20 (s). Zero-field $^{57}$Fe Mössbauer (90 K) δ = 0.64 mm/s, $|\Delta E_Q|$ = 3.43 mm/s. Crystals suitable for X-ray diffraction were grown from a 1:2 benzene:hexane solution at -35 °C. UV/Vis (benzene): $\lambda_{max}$ = 540 nm.

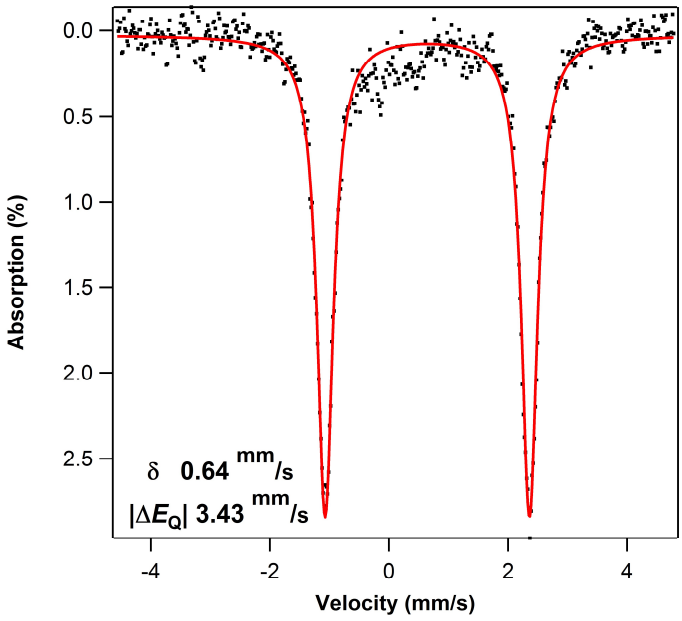


**Figure 4.12** Zero-field $^{57}$Fe Mössbauer of ($^{Ar}$L)Fe(κ$^2$-N$_4$R$_2$), R = *p*FC$_6$H$_4$ (**2-*p*FC$_6$H$_4$**) collected at 90 K. Isomer shift and quadrupole splitting are referenced to Fe foil at room temperature.

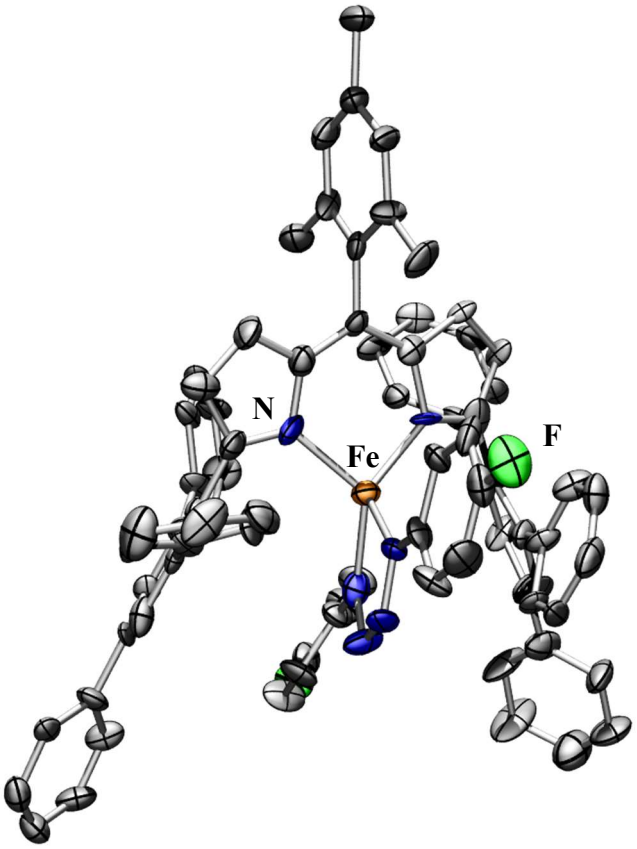


**Figure 4.13** Solid-state molecular structure for ($^{Ar}$L)Fe(κ$^2$-N$_4$R$_2$), R = *p*FC$_6$H$_4$ (**2-*p*FC$_6$H$_4$**) with thermal ellipsoids at 50% probability level. Hydrogens and benzene solvent in the unit cell omitted for clarity.

**($^{Ar}$L)Fe(κ$^2$-N$_4$R$_2$), R = *p*$^t$BuC$_6$H$_4$, (2-*p*$^t$BuC$_6$H$_4$):** 31.2 mg, 46%. **$^1$H NMR** (500 MHz, $C_6D_6$): δ 61.38 (br. s), 23.53 (s), 10.60 (s), 10.36 (s), 8.00 (s), 6.44 (s), 5.14 (m), 4.86 (s), 3.95 (s), -7.23 (s), -34.84 (s). Zero-field $^{57}$Fe Mössbauer (90 K) δ = 0.67 mm/s, $|\Delta E_Q|$ = 3.19 mm/s. UV/Vis (benzene): $\lambda_{max}$ = 540 nm.

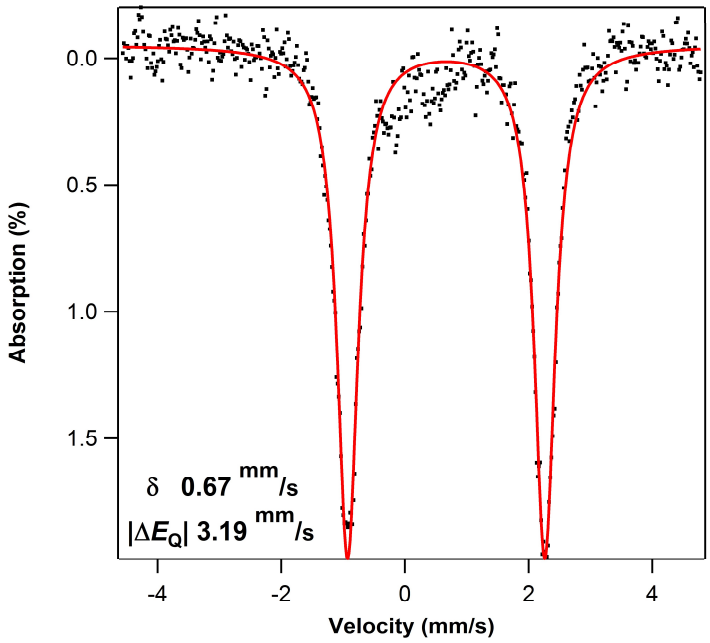


**Figure 4.14** Zero-field $^{57}$Fe Mössbauer of ($^{Ar}$L)Fe(κ$^2$-N$_4$R$_2$), R = *p*$^t$BuC$_6$H$_4$ (**2-*p*$^t$BuC$_6$H$_4$**) collected at 90 K. Isomer shift and quadrupole splitting are referenced to Fe foil at room temperature.

**($^{Ar}$L)Fe(κ$^2$-N$_4$R$_2$), R = *p*NMe$_2$C$_6$H$_4$, (2-*p*NMe$_2$C$_6$H$_4$):** 31.9 mg, 94%. **$^1$H NMR** (600 MHz, $C_6D_6$): δ 53.92 (br. s), 25.95 (s), 11.56 (br. s), 11.25 (s), 9.39 (br. s), 8.06 (s), 7.45 (s), 6.47 (s), 6.37 (s), 5.21 (s), 5.08 (s), 4.51 (br. s), 3.37 (s), 2.44 (s), -57.13 (s). Zero-field $^{57}$Fe Mössbauer (90 K) δ = 0.65 mm/s, $|\Delta E_Q|$ = 2.90 mm/s. Crystals suitable for X-ray diffraction were grown from a 1:2 benzene:hexane solution at -35 °C. UV/Vis (benzene): $\lambda_{max}$ = 540 nm.

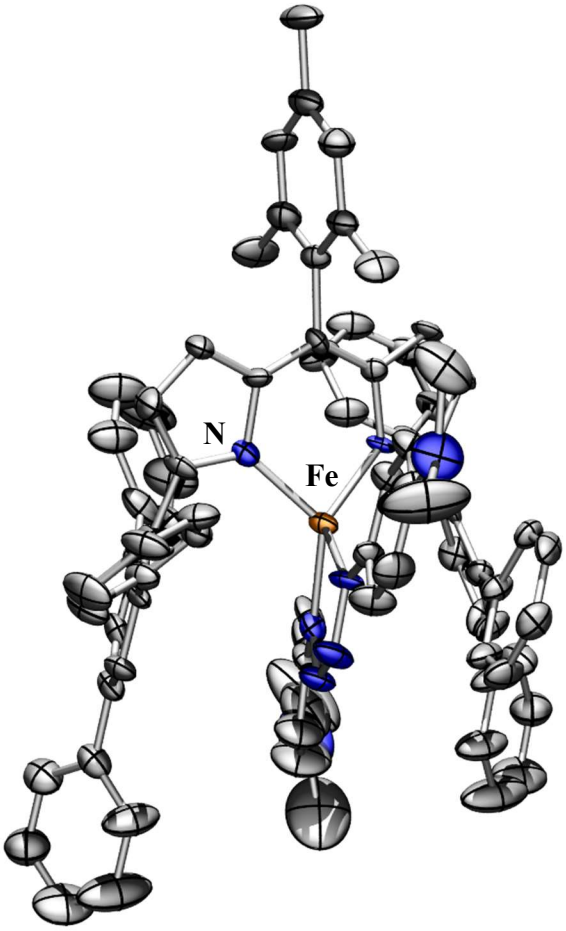


**Figure 4.15** Solid-state molecular structure for ($^{Ar}$L)Fe($\kappa^2$-$N_4R_2$), R = *p*$NMe_2C_6H_4$ (**2-*p*$NMe_2C_6H_4$**) with thermal ellipsoids at 50% probability level. Hydrogens, disordered aryl unit and benzene solvent in the unit cell omitted for clarity.

## *4.4.4 Substrate Syntheses.*

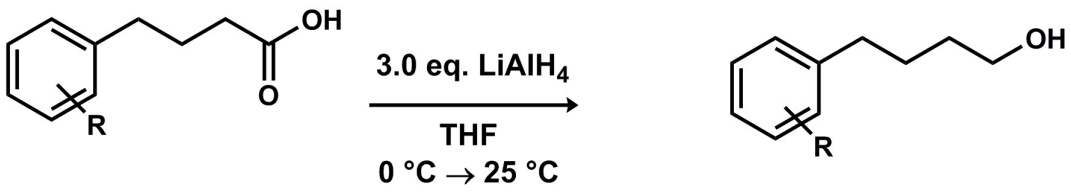

***Procedure A*** (adapted from literature procedure[9]): An oven-dried round-bottom flask was charged with lithium aluminum hydride (3.0 equiv) and THF under an $N_2$ atmosphere. The flask was cooled to 0 °C and a solution of carboxylic acid (1.0 equiv) in THF was added dropwise over 5 minutes. The resulting mixture was allowed to warm to room temperature and stir for 3 h. Excess lithium aluminum hydride was quenched by addition of water and 2M sodium hydroxide solution. The reaction mixture was diluted with ether, dried with $MgSO_4$, filtered and the solvent removed under vacuum to afford the alcohol as an oil. The materials were used without further purification.

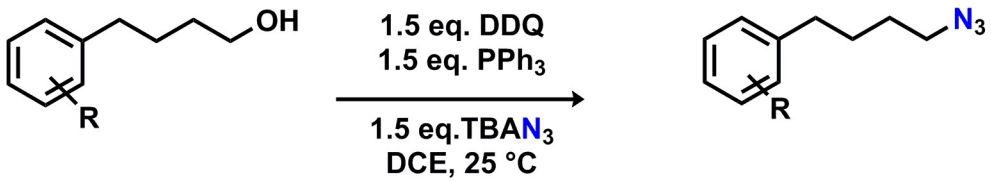


***Procedure B*** (adapted from literature procedure [10]): 2,3-Dichloro-5,6-dicyano-1,4-benzoquinone (1.5 equiv) was added portionwise to a stirring solution of $PPh_3$ (1.5 equiv) in dichloroethane. Two minutes following the addition, tetrabutylammonium azide and the alcohol substrate were added sequentially. The reaction was allowed to stir at room temperature for 12 hours (monitored by TLC). Upon completion, the solution was concentrated and loaded onto a silica column with minimal ethyl acetate and eluted with 100 % hexanes to 10:1 hexanes: ethyl acetate. The oil isolated was further purified via silica gel chromatography with 100% hexanes or pentane.

**4-(4-fluorophenyl)butan-1-ol** was synthesized following procedure A. Spectroscopic data matched previously reported characterization.[11]

---

9. Uyeda, C.; Jacobsen, E. N. *J. Am. Chem. Soc.* **2008**, *130*, 9228.
10. Iranpoor, N.; Firouzabadi, H.; Akhlaghinia, B.; Nowrouzi, N. *Tett. Lett.* **2004**, 3291.
11. Ganellin, C. R.; Leurquin, F.; Piripitsi, A.; Arrang, J.-M.; Garbarg, M.; Ligneau, X.; Schunack, W.; Schwartz, J.-C. *Arch. Pharm. Pharm. Med. Chem.***1998**, *331*, 395.

**1-(4-azidobutyl)-4-fluorobenzene** was synthesized following procedure B. 53%. **$^{1}$H NMR** (500 MHz, $C_6D_6$) δ 6.59 - 6.87 (m, 4 H), 2.62 (t, J=6.83 Hz, 2 H), 2.14 (t, J=7.57 Hz, 2 H), 1.00 - 1.26 (m, 4 H). **$^{13}$C NMR** (125 MHz, $C_6D_6$) δ: 137.0, 130.3 ($J_F$ = 7.66 Hz), 128.7, 115.7 ($J_F$ = 23.0 Hz), 51.4, 34.9, 28.9, 28.7. **$^{19}$F NMR** (376 MHz, $C_6D_6$) δ -117.4 ppm.

**4-(3-fluorophenyl)butyric acid methyl ester** (adapted from literature procedure[12]): In an oven dried 100 mL round bottom flask, solid titanocene dichloride (1.32 g, 5.3 mmol) and zinc dust (1.04 g, 15.9 mmol) were dissolved in 50 mL anhydrous THF in the glovebox. The suspension changed from orange to green within 10 minutes. The reaction was allowed to keep stirring at room temperature for 1 hour. Separately a 250 mL round bottom flask was flame dried and cooled under $N_2$. It was then charged with 3-fluorobenzyl bromide (0.5g, 2.65 mmol) and methyl acrylate (2.4 mL, 26.5 mmol) in 20 mL anhydrous THF. The titanocene solution was allowed to settle for 5 minutes before it was loaded into a 100 mL syringe. The solution was added, with stirring, at 20 mL / h using a syringe pump. Upon addition, the solution changed from green to brown/red. The reaction was allowed to continue stirring at room temperature for 1.5 h. Reaction was quenched via addition of 10 % $H_2SO_4$ in one portion at room temperature which caused a color change from dark red to a less intense orange-red. The solvent was removed *in vacuo* and the resulting oil extracted four times with ether. The extracts were combined, washed with water, then brine, and dried over $MgSO_4$. The ether solvent was removed *in vacuo*. The material was purified via silica gel chromatography eluting with 10:1 to 5:1 hexanes / ethyl acetate to isolate the product as a yellow oil (162.6 mg, 31 %). Spectroscopic characterization matched previously reported data.[13]

12. Mandal, S. K.; Jana, S.; Roy, S. C. *Tett. Lett.* **2005**, *46*, 6115,
13. Bi, H.; Feng, Z.; Wang, J.; Song, L. 05 Aug 2009, Faming Zhuanli Shenqing, 101497612.

**4-(3-fluorophenyl)butan-1-ol** was synthesized following procedure A. 82 %. Spectroscopic characterization matched previously reported data.[14]

**1-(4-azidobutyl)-3-fluorobenzene** was synthesized following procedure B. 74 %. **$^1$H NMR** (500 MHz, $C_6D_6$) δ 7.21 - 7.25 (m, 1 H), 6.86 - 6.98 (m, 2 H), 3.29 (t, *J*=6.60 Hz, 2 H), 2.64 (t, *J*=7.34 Hz, 2 H), 1.58 - 1.76 (m, 4 H). **$^{19}$F NMR** (376 MHz, $C_6D_6$) δ -113.8 ppm.

**5-azidopentanenitrile** was synthesized as previously reported.[15]

**2-(4'-Azidobutyl)-4,4,5,5-tetramethyl-1,3,2-dioxaborolane** was synthesized as previously reported. [16]

**5-azido-1-phenylpentan-1-one** was synthesized as previously reported. [17]

### *4.4.5 Catalytic Reactions*

Under an inert $N_2$ atmosphere, a 7-15 mM solution of ($^{Ar}$L)Fe($\kappa^2$-$N_4R_2$) **2-R** in $C_6D_6$ was freshly prepared. An appropriate amount of the catalyst solution was added to a solution of di-*tert*-butyl dicarbonate (3.0 equiv) and azide substrate (1.0 equiv) in 1 mL of $C_6D_6$ in a J Young NMR tube. The resultant solution was heated to 65 ºC for 24 hours. After cooling to room temperature, the crude reaction was purified via silica gel chromatography (hexanes/ethyl acetate, LC-MS detection of product) to obtain pure pyrrolidine product. All data reported is an average of at least two independent runs.

14. Evindar, G.; Deng, H; Bernier, S; Yao, G; Coffin, A; Yang, H. 07 Feb. 2008, PCT Int. Appl. 2008016692.
15. Li, C.; Han, K.; Li, J.; Zhang, J.; Chen, W.; Yu, Y.; Jia, X. *Chem. Eur. J.* **2013**, *19*, 11892.
16. Bagutski, V.; Elford, T. G.; Aggarwal, V. K. *Angew. Chem. Int. Ed.* **2011**, *50*, 1080.
17. Vaultier, M.; Lambert, P. H.; Carrie, R. *Bulletin de la Societe Chimique de France* **1986** , *1*, 83.

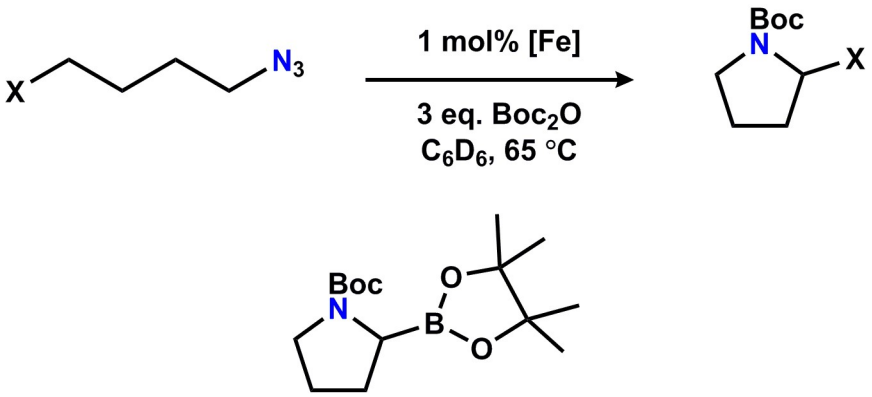


***tert*-butyl 2-(4,4,5,5-tetramethyl-1,3,2-dioxaborolan-2-yl)pyrrolidine-1-carboxylate**[18]

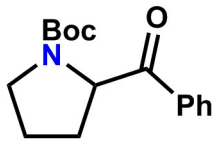


***tert*-butyl 2-benzoylpyrrolidine-1-carboxylate**[19]

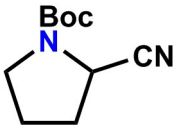


***tert*-butyl 2-cyanopyrrolidine-1-carboxylate**[20]

### *4.4.6 Iron tetrazene catalyst stability during catalysis*

#### *Cross-over experiments*

**A**: Under an inert $N_2$ atmosphere, a 7-15 mM solution of ($^{Ar}$L)Fe((4-(4-F-Ph)Bu)$N_4$(4-(4-F-Ph)Bu)) (**2-($CH_2$)$_4$(*p*F-Ph)**) in $C_6D_6$ was freshly prepared. An appropriate amount of the catalyst solution corresponding to 1 mol% loading was added to a solution of di-*tert*-butyl dicarbonate (3.0

18. Batsanov, A. S.; Grosjean, C.; Schuütz, T.; Whiting, A. *J. Org. Chem.* **2007**, *72*, 6276.
19. Kong, C.; Jana, N.; Driver, T. G. *Org. Lett.* **2013**, *15*, 824.
20. Lynch, K. R.; Macdonald, T. L.; Kharel, Y.; Mathews, T. P.; Wamhoff, B. R. 03 December 2009, WO2009/146112 A1.

equiv) and 1-azido-4-phenylbutane (1.0 equiv) in 1 mL of $C_6D_6$ in a J Young NMR tube. The resultant solution was heated to 65 ºC for 24 hours. After cooling to room temperature, the crude reaction was purified via silica gel chromatography (hexanes/ethyl acetate, LC-MS detection of product) to obtain pure pyrrolidine product, with matching characterization data to that previously reported.[21] The only isolated product was *tert*-butyl-2-phenylpyrrolidine-1-carboxylate and no *tert*-butyl-2-(4-fluorophenyl)pyrrolidine-1-carboxylate was detected by $^1H$ or $^{19}F$ NMR.

**B**: Under an inert $N_2$ atmosphere, a 7-15 mM solution of ($^{Ar}$L)Fe($\kappa^2$-$N_4R_2$)) R = $(CH_2)_4$(*p*-F-Ph) (**2-$(CH_2)_4$(*p*F-Ph**)) in $C_6D_6$ was freshly prepared. An appropriate amount of the catalyst solution corresponding to a 2 mol% loading was added to a solution of di-*tert*-butyl dicarbonate (3.0 equiv) and 1-(4-azidobutyl)-3-fluorobenzene (1.0 equiv) in 1 mL of $C_6D_6$ in a J Young NMR tube. The resultant solution was heated to 65 ºC for 24 hours. $^{19}F$ NMR analysis reveals persistence of the signal corresponding to the catalyst and no formation of the corresponding ($^{Ar}$L)Fe((4-(3-F-Ph)Bu)$N_4$(4-(3-F-Ph)Bu)) **2-$(CH_2)_4$(*m*-F-Ph**)) complex.

### *$^{57}$Fe Mössbauer reaction monitoring*

Under an inert $N_2$ atmosphere, ($^{Ar}$L)Fe($\kappa^2$-$N_4Ad_2$) (**2-Ad**) (25 mg, 5 mol%) was added to a solution of di-*tert*-butyl dicarbonate (3.0 equiv) and 1-azido-4-phenylbutane (1.0 equiv) in 7 mL of benzene in a pressure vessel. The resultant solution was heated to 65 ºC for 4 hours. After cooling to room temperature, the reaction mixture was brought back into the drybox and half of the solution removed and concentrated under vacuum. The residue was analyzed by $^{57}$Fe Mössbauer spectroscopy. The remaining solution was returned to the oil bath and heated up to 24 hours. The solution was then concentrated and residue analyzed by $^{57}$Fe Mössbauer spectroscopy.

21. Baekr, G.; O'Brien, P.; Campos, K. R. *Org. Lett.* **2010***, 12*, 4176.

### *4.4.7 Reaction of ($^{Ar}$L)Fe($\kappa^2$-N$_4$Ad$_2$) with tetrabutylammonium azide*

A solution of tetrabutylammonium azide (1.0 equiv) in THF was added to a solution of ($^{Ar}$L)Fe($\kappa^2$-N$_4$Ad$_2$) (**2-Ad**) in THF. An aliquant of the resulting solution was dropped onto salt plates and the IR spectrum was recorded.

### *4.4.8 Functional group tolerance via stoichiometric additives*

Under an inert $N_2$ atmosphere, a 7-15 mM solution of ($^{Ar}$L)Fe($\kappa^2$-N$_4$Ad$_2$) (**2-Ad**) in $C_6D_6$ was freshly prepared. An appropriate amount of the catalyst solution corresponding to 1 mol% loading was added to a solution of di-*tert*-butyl dicarbonate (3.0 equiv), 1-azido-4-phenylbutane (1.0 equiv) and additive (1.0 equiv) in 1 mL of $C_6D_6$ in a J Young NMR tube. The resultant solution was heated to 65 ºC for 24 hours. After cooling to room temperature, the reaction mixture was analyzed by $^1$H NMR to assess the faith of the catalyst and formation of pyrrolidine product. A solution of ferrocene was added and the amount of product was quantified via $^1$H NMR integration against the ferrocene internal standard.

### *4.4.9 Kinetic Measurements*

#### *Full-conversion kinetic run*

Under an inert $N_2$ atmosphere, a 7-15 mM solution of ($^{Ar}$L)Fe($\kappa^2$-N$_4$Ad$_2$) (**2-Ad**) in $C_6D_6$ was freshly prepared. An appropriate amount of the catalyst solution corresponding to 1 mol% loading was added to a solution of di-*tert*-butyl dicarbonate (37.4 mg, 3.0 equiv), 1-azido-4-phenylbutane (10 mg, 1.0 equiv) and trimethoxybenzene internal standard (0.1 equiv) in 1 mL of $C_6D_6$ in a J Young NMR tube. $^1$H NMR was recorded prior to heating the resultant solution to 65 °C. Time points were taken every hour for the first 6 hours and last 6 hours for a total of 24 hours.

A t1 relaxation of 15 s was used to ensure reproducible integration values. The resulting conversion versus time plot was fitted to a first-order integrated rate law: $y = a*(1-e^{-bt}) + c$, where a = 142.95 ± 8.64, b = 0.046 ± 0.005, c = -1.28 ± 0.94.

### *Determination of catalyst order*

Under an inert $N_2$ atmosphere, a 7-15 mM solution of ($^{Ar}$L)Fe($\kappa^2$-$N_4Ad_2$) (**2-Ad**) in $C_6D_6$ was freshly prepared. An appropriate amount of the catalyst solution corresponding to 1 mol%, 0.5 mol% and 0.25 mol% loading respectively was added to a solution of di-*tert*-butyl dicarbonate (37.4 mg, 3.0 equiv), 1-azido-4-phenylbutane (10 mg, 1.0 equiv) and trimethoxybenzene internal standard (0.1 equiv) in 1 mL of $C_6D_6$ in a J Young NMR tube. $^1$H NMR was recorded prior to heating the resultant solution to 65 °C. A t1 relaxation of 15 s was used to ensure reproducible integration values. Time points were taken every 30 min for a total of 4 hours. Each kinetic run was performed in duplicate and data averaged accordingly.

#### *Same-excess experiment*

Under an inert $N_2$ atmosphere, a 7-15 mM solution of ($^{Ar}$L)Fe($\kappa^2$-$N_4Ad_2$) (**2-Ad**) in $C_6D_6$ was freshly prepared. An appropriate amount of the catalyst solution corresponding to 1 mol% loading was added to a solution of di-*tert*-butyl dicarbonate (31.1 mg, 2.5 equiv), 1-azido-4-phenylbutane (5 mg, 0.5 equiv) and trimethoxybenzene internal standard (0.1 equiv) in 1 mL of $C_6D_6$ in a J Young NMR tube. $^1$H NMR was recorded prior to heating the resultant solution to 65 °C. Time points were taken every 30 min for a total of 4 hours. A t1 relaxation of 15 s was used to ensure reproducible integration values. The experiment was repeated in the presence of 0.5 equiv of *tert*-butanol (2.2 mg).

### *4.4.10X-Ray Diffraction Techniques.*

All structures were collected on a Bruker three-circle platform goniometer equipped with an Apex II CCD and an Oxford cryostream cooling device. Radiation was from a graphite fine focus sealed tube Mo Kα (0.71073 Å) source. Crystals were mounted on a cryoloop or glass fiber pin using Paratone N oil. Structures were collected at 100 K. Data was collected as a series of φ and/or ω scans. Data was integrated using SAINT[22] and scaled with either a numerical or multi-scan absorption correction using SADABS[22]. The structures were solved by direct methods or Patterson maps using SHELXS-97[23] and refined against $F^2$ on all data by full matrix least squares with SHELXL-97[23]. All non-hydrogen atoms were refined anisotropically. Hydrogen atoms were placed at idealized positions and refined using a riding model. The isotropic displacement parameters of all hydrogen atoms were fixed to 1.2 times the atoms they are linked to (1.5 times for methyl groups). Further details on particular structures are noted below.

**($^{Ar}$L)Fe(κ$^2$-N$_4$R$_2$)) R = *p*NO$_2$C$_6$H$_4$ (2-*p*NO$_2$C$_6$H$_4$).** The structure was solved in the triclinic space group $P\bar{1}$ with 2 molecules per unit cell.

**($^{Ar}$L)Fe(κ$^2$-N$_4$R$_2$)) R = *p*FC$_6$H$_4$ (2-*p*FC$_6$H$_4$).** The structure was solved in the monoclinic space group $P\bar{1}$ with 4 molecules per unit cell.

**($^{Ar}$L)Fe(κ$^2$-N$_4$R$_2$)) R = *p*NMe$_2$C$_6$H$_4$ (2-*p*NMe$_2$C$_6$H$_4$)** The structure was solved in the triclinic space group $P\bar{1}$ with 2 molecules per unit cell. One of the aryl substituents exhibited positional disorder and was refined using similarity constraints. A solvent mask was implemented

22. *APEX2 Software Suite*; Bruker AXS: Madison, WI, 2009.
23. Sheldrick, G. M. Acta Crystallogr., Sect. A: Found. Crystallogr. **2008**, 64, 112-122

in the Olex2 software due to disordered hexanes and benzene solvent molecules present in the unit cell.

**Table 4.3** X-ray diffraction experimental details[a,b]

| | **2-*p*NO$_2$C$_6$H$_4$** | **2-*p*FC$_6$H$_4$** | **2-*p*NMe$_2$C$_6$H$_4$** |
|---|---|---|---|
| **Moiety Formula** | $C_{78}H_{57}FeN_8O_4$; 0.5×($C_6H_6$) | 2×$C_{78}H_{57}F_2FeN_6$ 2×($C_6H_6$) | $C_{82}H_{68}FeN_8$ |
| **FW** | 1421.44 | 1250.75 | 1221.30 |
| **Crystal System** | triclinic | triclinic | triclinic |
| **Space Group (Z)** | $P\bar{1}$ (2)) | $P\bar{1}$ (4) | $P\bar{1}$ (2)) |
| **a (Å)** | 15.6343(4) | 15.9030(9) | 14.005(2) |
| **b (Å)** | 15.8721(3) | 30.6444(18) | 15.267(3) |
| **c (Å)** | 16.4976(4) | 34.0087(19) | 21.155(4) |
| **α (°)** | 76.934(1) | 63.282(4) | 84.180(4) |
| **β (°)** | 80.932(2) | 87.920(4) | 85.306(4) |
| **γ (°)** | 66.425(1) | 85.152(4) | 73.019(4) |
| **Volume (Å$^3$)** | 3644.67(15) | 14751.2(15) | 4297.3(13) |
| **Calc. $\rho$ (mg/m$^3$)** | 1.295 | 1.126 | 0.944 |
| **$\mu$ (mm$^{-1}$)** | 2.141 | 2.041 | 0.216 |
| **Crystal Size (mm)** | 0.19×0.065×0.05 | 0.17×0.035×0.021 | 0.2×0.07×0.03 |
| **Reflections** | 12935 | 49584 | 14958 |
| **Completeness (to 2θ)** | 95.8% 66.804° | 93.8% 67.268° | 99.9% 24.901° |
| **GOF on F$^2$** | 1.027 | 0.824 | 1.061 |
| **R1, wR2[c] [I>2σ(I)]** | 0.0548, 0.1460 | 0.0780, 0.2281 | 0.1041, 0.2969 |

[a] λ = 0.71073 Å; [b] T = 100(2) K; [c] R1 = $\Sigma||F_o|-|F_c||/\Sigma|F_o|$, wR2 = $\{\Sigma[w(F_o^2-F_c^2)^2]/\Sigma[w(F_o^2)^2]\}^{1/2}$

### *4.4.11 Computational Methods*

Computations were carried out utilizing the ORCA 2.9[24] program package. The B3LYP[25] functional was used with the def2-TZVP (Fe, N, Cl) and def2-SV(P) (C, H) basis sets[26]. For single point calculations and property calculations the def2-TZVP/J (Fe, N, Cl) and def2-SVP/J (C, H) auxiliary basis sets[27] were employed to utilize the RIJCOSX[28] approximation for accelerating the calculation. For the calculation of Mössbauer parameters the basis set at Fe was expanded to the CP(PPP) basis[29]. All geometries were taken from X-ray structures.

**Mössbauer.** Mössbauer parameters were obtained from additional single-point calculations, following methods described by F. Neese.[30] Quadrupole splittings ($\Delta E_Q$) were calculated from electric field gradient, Eq. S.2.

$$\Delta E_Q = \tfrac{1}{2} eQV_{zz}\sqrt{1+\tfrac{1}{3}\eta^2} \qquad \text{(S.2)}$$

The nuclear quadruple moment $Q(^{57}\text{Fe})$ was taken to be 0.16 barn.[30] The principal tensor components of the EFG are $V_{xx}$, $V_{yy}$, and $V_{zz}$, from which the asymmetry parameter $\eta = (V_{xx} - V_{yy})/V_{zz}$ can be defined.

Isomer shifts ($\delta$) were calculated from the electron density at the nucleus $\rho_0$, using a linear equation, Eq. S.3[30], with constants determined by fitting the calculated densities to experimental


24. Neese, F. ORCA - An ab initio, Density Functional and Semi-empirical Electronic Structure Package; Version 2.9-00 ed. ed. Universitat Bonn, Bonn, Germany, 2009.
25. (a) Becke, A. D. *J. Chem. Phys.* **98**, 5648 (1993); (b) Lee, C. T.; Yang, W. T.; Parr, R. G. *Phys Rev. B* **33**, 785 (1988).
26. (a) Schäfer, A.; Horn, H.; Ahlrichs, R. *J. Chem. Phys*. **1992**, *97*, 2571; b) Schäafer, A.; Huber, C.; Ahlrichs, R. *J. Chem. Phys.***1994**, *100*, 5829; (c) Weigend, F.; Ahlrichs, R. *Phys. Chem. Chem. Phys.* **2005**, *7*, 3297.
27. Weigand, F. Phys. Chem. Chem. Phys. **2006**, 8, 1057.
28. Neese, F.; Wennmohs, F.; Hansen, A.; Becker, U. *Chem. Phys.* **2009**, *356*, 98.
29. Neese, F. *Inorg. Chim. Acta* **2002**, *337*, 181.
30. (a) Ye, S.; Tuttle, T.; Bill, E.; Simkhovich, L.; Gross, Z.; Thiel, W.; Neese, F. *Chem. Eur. J.* **2008**, *14*, 10839; (b) Sinnecker, S.; Slep, L. P.; Bill, E.; Neese, F. *Inorg. Chem.* **2005**, *44*, 2245.

isomer shifts for a series of iron dipyrromethene complexes synthesized in the lab (with the 5-mesityl-1,9-di(2,4,6-triphenylphenyl)dipyrromethene ligand[6]). The basis sets and functional described above were used for all structures. X-ray coordinates were used, and spin-states were assigned based on experimental Mössbauer data.

$$\delta = a(\rho_0 - C) + b \tag{S.3}$$

For this series of compounds the parameters were determined to be $C$ = 11580 au$^{-3}$, $a$ = –0.355 au$^3$ mm s$^{-1}$, and $b$ = 1.418 mm.

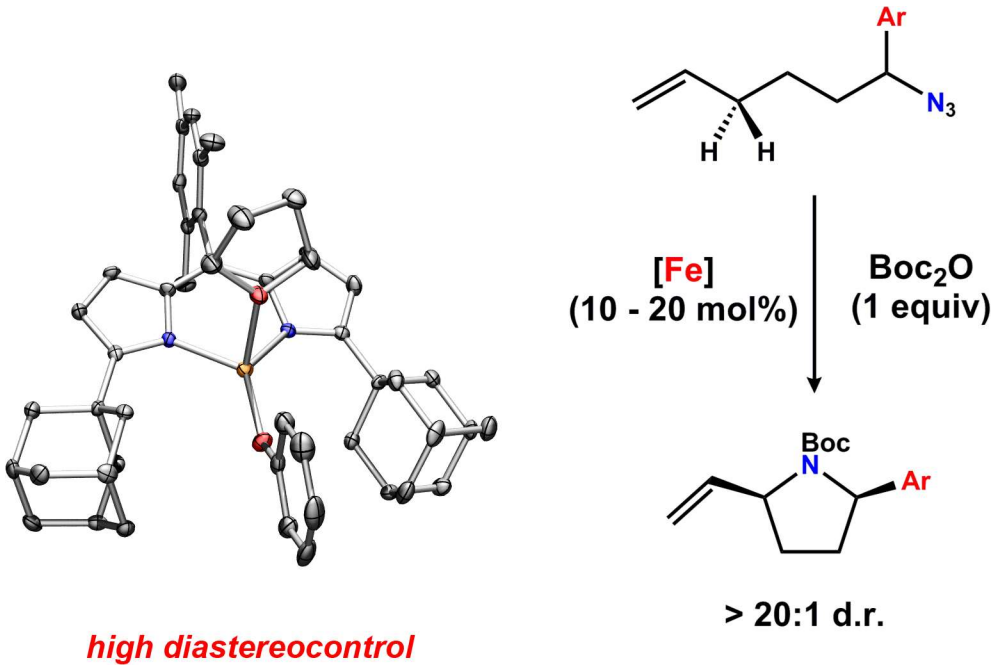


# Chapter 5: Diastereoselective C-H Bond Amination for Disubstituted Pyrrolidines[1]

## 5.1 Introduction

The prevalence of 2,5-disubstituted pyrrolidines in natural products[2], pharmaceuticals[3] as well as synthetic applications[4] has inspired the emergence of numerous stereoselective

1. This work was done in collaboration with Diana Iovan. My contributions included calculation of the reaction coordinate diagram, transition state analysis for the selectivity determining step, as well as intellectural contributions for the development of a proposed model for diastereoselective induction.
2. O'Hagan, D. *Nat. Prod. Rep.* **2000**, *17*, 435.
3. Juge, M.; Grimaud, N.; Biard, J. F.; Sauviat, M. P.; Nabil, M.; Verbist, J. F.; Petit, J. Y. *Toxicon.* **2001**, *39*, 1231.
4. a) Trost, B. M.; Stambuli, J. P.; Silverman, S. M.; Schwörer, U. *J. Am. Chem. Soc.* **2006**, *128*, 13328; (b) Franzen, J.; Marigo, M.; Fielenbach, D.; Wabnitz, T. C.; Kjærsgaard, A.; Jørgensen, A. *J. Am. Chem. Soc.* **2005**, *127*, 18296.

methodologies[5] for the synthesis of these *N*-heterocycles. However, more atom-economical, efficient and general protocols allowing access to complex architectures featured in many of these nitrogen-containing compounds are highly desirable. To this end, direct C–H bond amination methods could provide a more streamlined protocol and may serve to enhance the scope of current conventional syntheses.

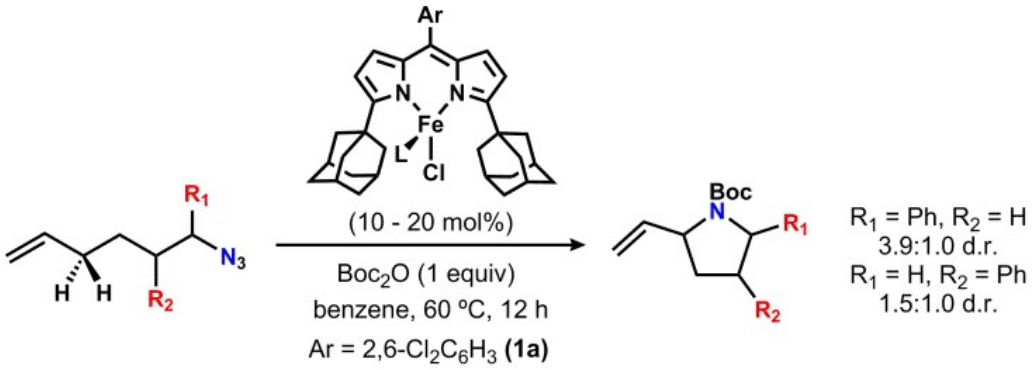


**Scheme 5.1** Diastereoselectivity of iron-catalyzed cyclization

Our group has recently reported a catalytic C–H amination process for the conversion of aliphatic azides to *N*-heterocycles using a high-spin iron dipyrrinato complex ($^{Ad}$L)FeCl(OEt$_2$)

5. (a) Pichon, M.; Figadere, B. *Tetrahedron: Asymmetry* **1996**, *7*, 927; (b) Katritzky, A. R.; Cui, Z.-L.; Yang, B.; Steel, P. J. *Tetrahedron Lett.* **1998**, *39*, 1697; (c) Shi, M.; Satoh, Y.; Masaki, Y. *J. Chem. Soc. Perkin Trans. I* **1998**, 2547; (d) Aggarwal, V. K.; Astle, C. J.; Rogers-Evans, M. *Org. Lett.* **2004**, *6*, 1329; (e) Sato, M.; Gunji, Y.; Ikeno, T.; Yamada, T. *Synthesis* **2004**, 1434; (f) Vasse, J. L.; Joosten, A.; Denhez, C.; Szymoniak, J. *Org. Lett.* **2005**, *7*, 4887; (g) Davis, F. A.; Song, M.; Augustine, A. *J. Org. Chem.* **2006**, *71*, 2779; (h) Gribkov, D. V.; Hultzsch, K. C.; Hampel, F. *J. Am. Chem. Soc.* **2006**, *128*, 3748; (i) Hussaini, S. R.; Moloney, M. G. *Org. Biomol. Chem.* **2006**, *4*, 2600; (j) Llamas, T.; Arrayas, R. G.; Carretero, J. C. *Org. Lett.* **2006**, *8*, 1795; (k) Sherman, E. S.; Fuller, P. H.; Kasi, D.; Chemler, S. R. *J. Org. Chem.* **2007**, *72*, 3896; (l) Sriramurthy, V.; Barcan, G. A.; Kwon, O. *J. Am. Chem. Soc.* **2007**, *129*, 12928; (m) Wang, P.-A.; Xu, Z. S.; Chen, C. F.; Gao, X. G.; Sun, X. L.; Zhang, S. Y. *Chirality* **2007**, *19*, 581; (n) Davis, F. A.; Zhang, J.; Qiu, H.; Wu, Y. *Org. Lett.* **2008**, *10*, 1433; (o) Kitulagoda, J. E.; Palmelund, A.; Aggarwal, V. K. *Tetrahedron* **2010**, *66*, 6293; (p) Lemen, G. S.; Wolfe, J. P. *Org. Lett.* **2010**, *12*, 2322; (q) Babij, N. R.; Wolfe, J. P. *Angew. Chem. Int. Ed.* **2012**, *51*, 4128; (r) Redford, J. E.; McDonald, R. I.; Rigsby, M. L.; Wiensch, J. D.; Stahl, S. S. *Org. Lett.* **2012**, *14*, 1242; (s) Ďuriš, A.; Barber, D. M.; Sanganee, H. J.; Dixon, D. J. *Chem. Commun.* **2013**, *49*, 2777; (t) Wang, P.-A.; Zhang, S.-Y.; Kagan, H. B. *Beilstein J. Org. Chem.* **2013**, *9*, 265; (u) Xu, F.; Chung, J. Y. L.; Moore, J. C.; Liu, Z.; Yoshikawa, N.; Hoerrner, R. S.; Lee, J.; Royzen, M.; Cleator, E.; Gibson, A. G.; Dunn, R.; Maloney, K. M.; Alam, M.; Goodyear, A.; Lynch, J.; Yasuda, N.; Devine, P. N. *Org. Lett.* **2013**, *15*, 1342; (v) Natori, Y.; Kikuchi, S.; Kondo, T.; Saito, Y.; Yoshimura, Y.; Takahata, H. *Org. Biomol. Chem.* **2014**, *12*, 1983; (w) Chen, C. F.; Rong, H.-J.; Yi, C.-B.; Y, J.-J.; Qu, J. *Org. Lett.* **2015**, *17*, 4758; (x) Jia, Y. Y.; Li, X.-Y.; Wang, P.-A.; Wen, A.-D. *Molecules* **2015**, *20*, 2922.

($^{Ad}$L = 1,9-adamantyl-5-Ar-dipyrrin, Ar = 2,6-$Cl_2C_6H_3$ (**1a**), mesityl (**1b**)).[6] During our studies, we found that exposure of 1-azido-1-phenyl-hex-5-ene to catalytic quantities of **1a** in the presence of stoichiometric di-*tert*-butyldicarbonate ($Boc_2O$) afforded Boc-protected 2-phenyl-5-vinylpyrrolidine as a 3.9:1 mixture of diastereomers (**Scheme 5.1**).[6] $^1$D NOESY experiments on the deprotected pyrrolidine product[7] revealed that the *syn* diastereomer is favored. This inherent stereocontrol of the iron-catalyzed cyclization, albeit modest, encouraged us to establish whether diastereoselectivity could be altered via catalyst tuning. Herein we present our findings of a phenoxide substituted iron dipyrrin complex that furnishes 2,5-disubstituted pyrrolidines with good *syn:anti* diastereoselectivity (d.r. > 20:1).

## 5.2 Scope of diastereoselectivity

To develop an understanding of the diastereocontrol, we began by investigating the scope of the diastereoselective cyclization with catalyst **1a**. A series of 1-azido-1-aryl-hex-5-ene substrates featuring aryl ring substitutions were examined to establish the influence of electronic and steric demands of the aryl-ring on the observed selectivity. Both electron-donating and withdrawing groups (Me, halides, $CF_3$) were amenable to cyclization (**Table 5.1**). *Para* (**3b-3f**) and *meta* (**3g-3i**) aryl functionality gave selectivities consistent with our initial findings (d.r. 3-4:1). However, *ortho*-substituted substrates (**3j-3n**) exhibited high stereocontrol, with only a single diastereomer detected. Additionally, increasing the steric bulk of the $R_1$ substituent (**3p**) or exchanging the positions of the phenyl and vinyl functionalities (**3q**) does not significantly affect

6. Hennessy, E. T.; Betley, T. A. *Science* **2013**, 591.
7. Trost, B. M.; Silverman, S. M.; Stambuli, J. P. *J. Am. Chem. Soc.* **2011**, *133*, 19483.

diastereoselectivity. However, the cyclization of 1-azido-2-phenyl-hex-5-ene (**2r**) yields the corresponding 2,4-disubstituted pyrrolidine (**3r**) with diminished diastereocontrol (d.r. 1.5:1).[6]

**Table 5.1** Diastereoselectivity for disubstituted pyrrolidines

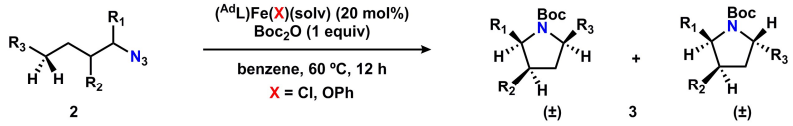


| Product | Yield (%)[a] | d.r.[b] | Product | Yield (%)[a] | d.r.[b] | Product | Yield (%)[a] | d.r.[b] |
|---|---|---|---|---|---|---|---|---|
| $R_3 = C_2H_3$ | | | $R_3 = C_2H_3$ | | | $R_3 = C_2H_3$ | | |
| 3a 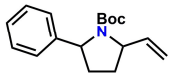 | (72)[c]<br>77 (72)[d] | 3.9:1[c]<br>>20:1[d] | 3f 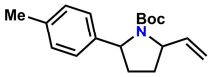 | 36(36)[c]<br>53(53)[d] | 4:1[c]<br>20:1[d] | 3k 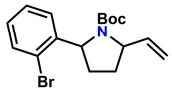 | 30 (30)[c,e]<br>52 (45)[d] | >20:1[c]<br>>20:1[d] |
| 3b 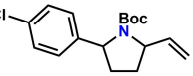 | (63)[c]<br>75 (67)[d] | 3:1[c]<br>>20:1[d] | 3g 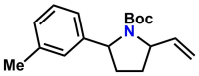 | (47)[c]<br>55 (49)[d] | 4:1[c]<br>>20:1[d] | 3l 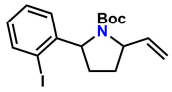 | 37 (36)[c]<br>58 (56)[d] | >20:1[c]<br>>20:1[d] |
| 3c 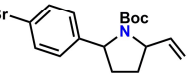 | 44 (41)[c]<br>67 (68)[d] | 4:1[c]<br>>20:1[d] | 3h 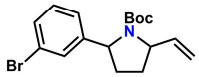 | 59 (55)[c]<br>79 (72)[d] | 4:1[c]<br>>20:1[d] | 3m 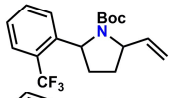 | 38 (31)[c]<br>58 (51)[d] | >20:1[c]<br>>20:1[d] |
| 3d 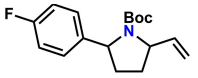 | (49)[c]<br>67 (66)[d] | 3:1[c]<br>>20:1[d] | 3i 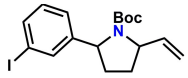 | 64 (48)[c]<br>74 (67)[d] | 4:1[c]<br>>20:1[d] | 3n 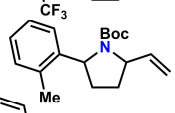 | 27 (30)[c]<br>50 (43)[d] | 4:1[c]<br>11:1[d] |
| 3e 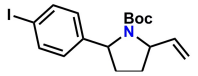 | 38(41)[c]<br>74 (71)[d] | 3:1<br>>20:1[d] | 3j 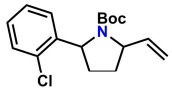 | 45 (38)[c]<br>69 (64)[d] | >20:1[c]<br>>20:1[d] | 3o 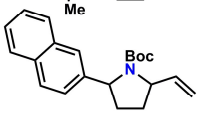 | 22 (16)[c]<br>20 (23)[d] | 3:1[c]<br>10:1[d] |
| $R_1 = Ph, R_3 = Ph$ | | | $R_1 = C_2H_3, R_3 = Ph$ | | | $R_1 = H, R_2 = Ph, R_3 = C_2H_3$ | | |
| 3p 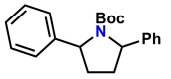 | 34 (37)[c]<br>43 (48)[d] | 5:1[c]<br>16:1[d] | 3q 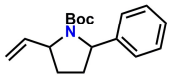 | N/A | 3.5:1[c]<br>7:1[d] | 3r 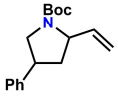 | (66)[c]<br>71 (72)[d] | 1.5:1[c]<br>2:1[d] |

[a] $^1$H NMR yield at 50 °C using ferrocene internal standard (isolated yields in parentheses). [b] d.r. (*syn*:*anti*) determined by GC/MS. [c] Reaction with catalyst **1a**. [d] Reaction with catalyst **8**. [e] Reaction with 10 mol% catalyst.

Regardless of the substitution pattern on the *N*-heterocycle formed, the major isomer was identified via $^1$D NOESY experiments as the *syn* configuration. The conformational assignment was further confirmed via X-ray diffraction on single crystals of the iron 2-(*o*-($F_3C$)$C_6H_4$)-5-vinylpyrrolidine adduct (**4**) (**Figure 5.1**).

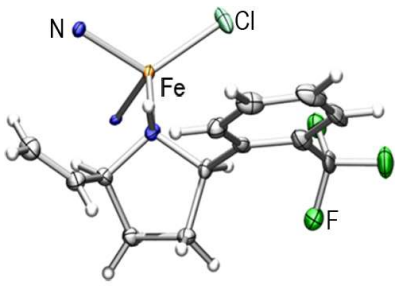


(**4**)

**Figure 5.1** Truncated solid-state structure of ($^{Ad}$L)FeCl[2-(*o*-($F_3C$)$C_6H_4$)-5-vinylpyrrolidine] (**4**) at 100 K with 50% probability ellipsoids. Colors: Fe, orange; C, gray; H, white; N, blue; O, red; F, green; Cl, aquamarine.

## 5.3 Diastereoselectivity model

Prompted by these results, DFT studies were undertaken to evaluate the factors leading to the diastereoselectivity manifest by **1a**. Geometry optimization of **1b** and product **4** accurately reproduced crystallographically determined bond metrics. The *ortho*-trifluoromethyl group utilized to crystallographically characterize the preferred isomer was removed in subsequent calculations to minimize computational effort. Mapping the reaction trajectory (**Figure 5.2a**), expulsion of dinitrogen from the azide substrate proceeds exothermically (39 kcal/mol) to afford an $Fe^{III}$ iminyl species. The Fe–$N_{im}$ bond distance of 1.765 Å and Fe–$N_{im}$–$C_1$ angle of 161 ° extracted from the optimized geometry of this $Fe^{III}$ intermediate are in good agreement with those found in previously reported dipyrrin iron iminyl species.[8] The ferric intermediate can effect activation of a pendant C–H bond with an energetic barrier of 12 kcal/mol, furnishing an $Fe^{III}$ amido species. The transition state (TS) identified displays an elongated Fe–$N_{im}$ bond (1.835 Å) and a nearly linear $N_{im}$–H–$C_4$ vector (155 °) in line with a hydrogen atom abstraction (HAA) mechanism.[9] Scanning the potential energy surface to locate a TS for the subsequent radical rebound step resulted in immediate convergence to the iron-pyrrolidine adduct, with an energy gain of 45 kcal/mol. This finding suggests a barrier-less recombination event, consistent with our experimental observations utilizing a radical-clock probe to establish a lifetime less than $10^{-11}$ s for

8. (a) King, E. R.; Hennessy, E. T.; Betley, T. A. *J. Am. Chem. Soc.* **2011**, *133*, 4917; (b) Iovan, D. A.; Betley, T. A. *J. Am. Chem. Soc.* **2016**, *138*, 1983.
9. Denisov, E. T.; Shestakov, A. F.; Denisova, T. G. *Russian Chem. Rev.* **2012**, *81*, 1117.

the putative carboradical intermediate.[6] A similar energetic profile was found for the allylic intramolecular C-H amination mediated by the di-ruthenium nitrene system reported by Du Bois.[10]

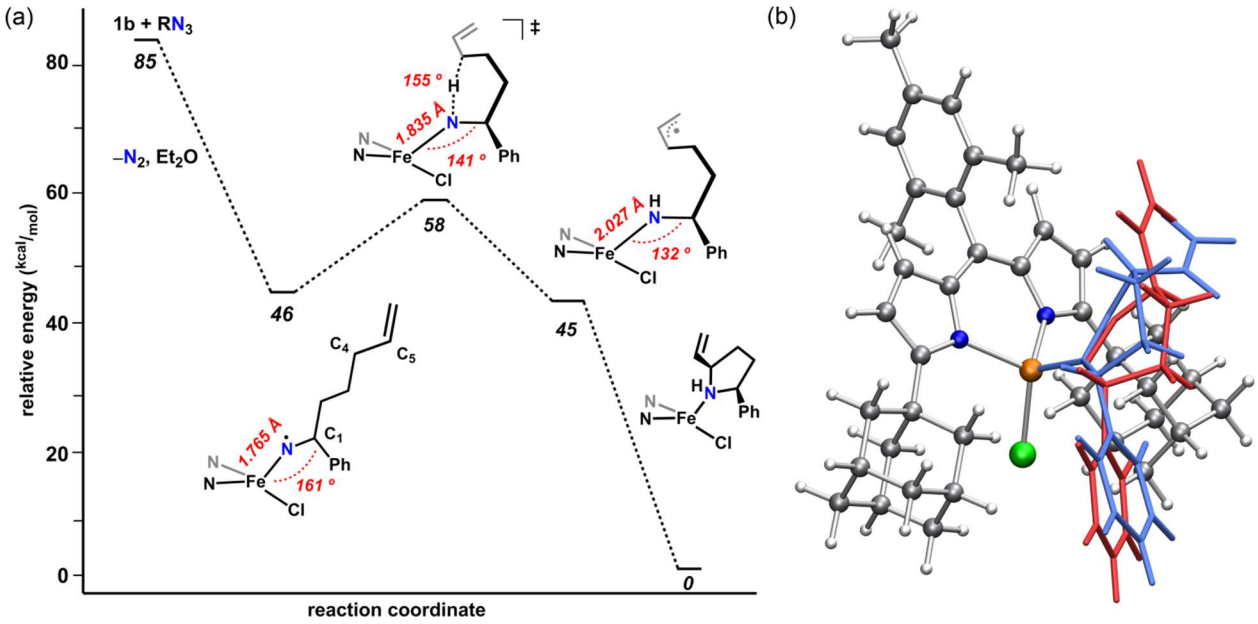


**Figure 5.2** (a) Calculated[11] reaction coordinate for cyclization of 1-azido-1-phenyl-hex-5-ene (**2a**) mediated by **1b**; (b) Geometry optimized transition states for the HAA step in the pro-*syn* (blue) and pro-*anti* (red) configuration.

The fast recombination rate identified both experimentally and theoretically indicates that HAA represents the selectivity determining step. As such, transition states corresponding to the HAA of each of the two diastereotopic H-atoms were investigated. Calculations revealed that formation of the *syn* pyrrolidine product is favored by 0.93 kcal/mol. The energy difference is subtle; however, the computed value predicts a 4.6:1 ratio of diastereomers, correlating well with the experimentally determined 3.9:1 d.r. (**Scheme 5.1**). Closer analysis of the optimized TS highlights a synergistic effect between different components of the iron coordination environment on the product selectivity. Orientation of the substrate in the pro-*syn* conformation minimizes unfavorable interactions with the dipyrrin bridgehead position as well as the cleft comprised of the

10. Harvey, M. E.; Musaev, D. G.; Du Bois, J. *J. Am. Chem. Soc.* **2011**, *133*, 17207.
11. Frisch, M. J. e. a.; Gaussian, Inc.: Wallingford, CT, USA, 2009.

adamantyl groups and the anionic ligand. Rotation about the $C_4$–$C_5$ bond induces steric interference between the vinyl substituent and the bridgehead mesityl group, destabilizing the pro-*anti* TS (**Figure 5.2b**). To release the steric pressure, an increase in the $C_{meso}$–Fe–$N_{im}$ angle from 106.9 ° (*syn)* to 112.1 ° (*anti*) pushes the iminyl fragment away from the bridgehead position and further into the cleft. However, the energetic penalty incurred from destabilizing interactions between the α-azido aryl substituent and the cleft components (**Figure 5.2b**) is significant, resulting in an overall higher energy pro-*anti* TS, in line with the experimentally observed minor *anti* diastereomer. Furthermore, introducing *ortho* functionality at $C_1$ induces additional strain, justifying the high selectivity for the *syn* product. Substitution at the *meta* or *para* positions is more remote and, thus, has no effect on the d.r. The modest diastereoselectivity found for substrates with modified functionalities at either $C_1$ or $C_4$ (**Table 5.1**, **3p-3q**) can also be explained: the planar phenyl ring interacts similarly with the benzylic mesityl position whereas a vinyl substituent does not project far enough into the cleft to effect higher diastereocontrol.

## 5.4 Ancillary ligand influence on diastereoselectivity

The insight gained from the DFT studies allowed us to systematically modulate our current system in an attempt to design a highly diastereoselective catalyst. Among the features proposed to dictate selectivity, the larger Taft steric parameter[12] of methyl versus chloride suggests that the bridgehead mesityl group is expected to have a larger effect than the 2,6-dichlorophenyl in **1a**. With respect to the cleft size, the adamantyl moieties provide a balance between productive reactivity and diastereoinduction and cannot be modified without compromising the desired

12. Hansch, C.; Leo, A. Substituent Constants for Correlation Analysis in Chemistry and Biology; Wiley-Interscience: NY, 1979.

chemistry. However, the ancillary anionic ligand could provide additional steric bulk. To this end, using the mesityl-substituted bridgehead, we sought to examine if anion metathesis of the Cl ligand in **1b** afforded superior catalysis and enhanced diastereoselectivities. We chose to investigate a series of alkoxide and aryloxide complexes, taking advantage of the electronic and steric flexibility of these ligands.

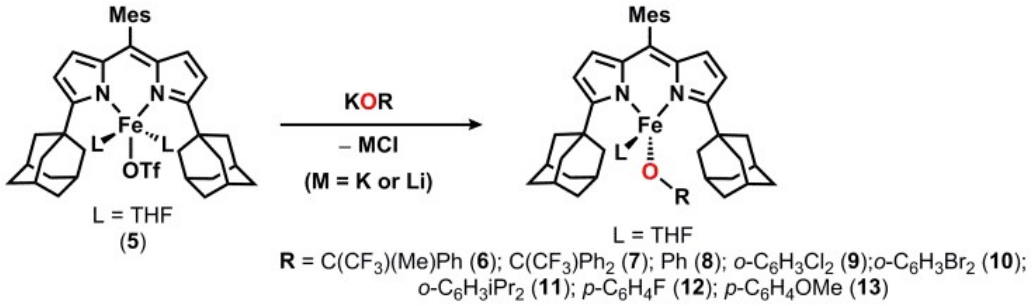


**Scheme 5.2** Synthesis of catalyst variants.

Direct metathesis of KOR reagents with **1b** did not cleanly produce mono-substituted complexes, rather, ate-complexes of the type ($^{Ad}$L)Fe(OR)$_2$($\mu^2$-K) were readily formed. Alternatively, metathesis from the triflate intermediate ($^{Ad}$L)Fe(OTf)(THF)$_2$ (**5**; synthesized via AgOTf addition to **1b**) provided the desired alkoxide or aryloxide adducts. In a typical reaction, room temperature addition of a THF solution of **5** to a THF solution of the corresponding Li- or K salt resulted in metathesis of the OTf anion to afford complexes of the type ($^{Ad}$L)Fe(OR)(THF) (**Scheme 5.2**, R: C(CF$_3$)(Me)Ph (**6**); C(CF$_3$)Ph$_2$ (**7**); Ph (**8**); *o*-C$_6$H$_3$Cl$_2$ (**9**); *o*-C$_6$H$_3$Br$_2$ (**10**); *o*-C$_6$H$_3$$^i$Pr$_2$ (**11**); *p*-C$_6$H$_4$F (**12**); *p*-C$_6$H$_4$OCH$_3$ (**13**)). Each of the paramagnetic complexes **5**–**13** was analyzed by $^1$H NMR and combustion analysis to assess purity and single crystal X-ray diffraction to establish the coordination geometry. Each complex is formed as the four-coordinate, THF solvated species and exhibits a coordination sphere typical of high-spin ferrous dipyrrin complexes (representative core structures are shown in **Figure 5.3**). While the individual bond metrics for the complexes are unremarkable, the size of the OR group does cause geometric distortion of the iron

center, ranging from trigonal monopyramidal for iron-phenoxide complexes **8**-**13** (**Figure 5.3b**) to distorted tetrahedral for the alkoxide variants **6**-**7** (**Figure 5.3a**), where the large alkoxide ligand resides outside the dipyrrin cleft created by the two adamantyl units.

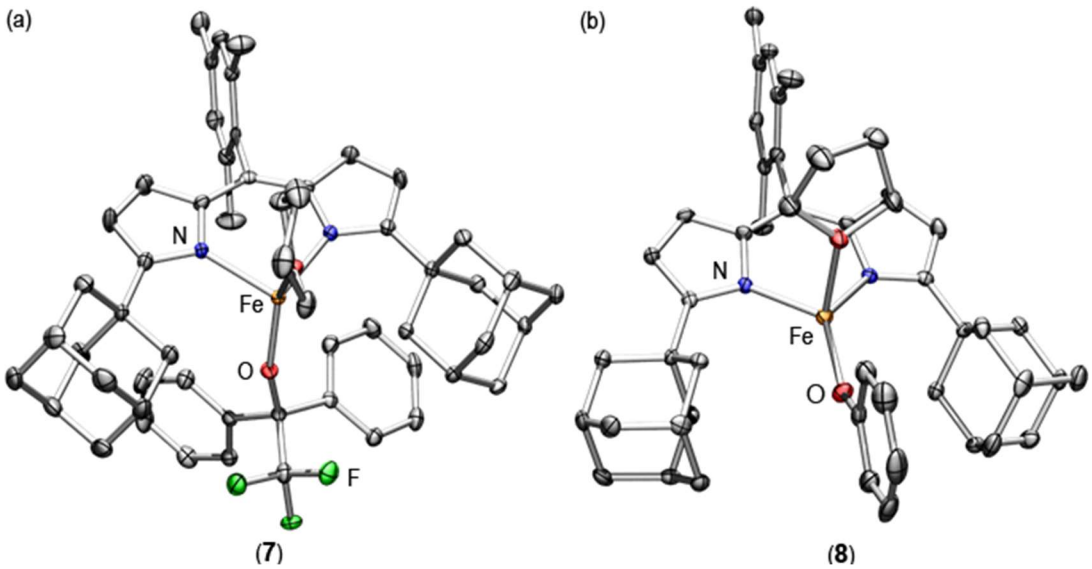


**Figure 5.3** Solid-state structure of (a) ($^{Ad}$L)FeOC($CF_3$)$Ph_2$ (**7**) and (b) ($^{Ad}$L)FeOPh (**8**)at 100 K with 50% probability ellipsoids. Colors: Fe, orange; C, gray; H, white; N, blue; O, red; F, green. Hydrogen atoms were omitted for clarity.

With catalyst variants **6**–**13** in hand, we began canvassing the respective performance for the cyclization of either azide **2b** (catalysts **6-8)** or **2a** (catalysts **9-13)** as test substrates. While **1a** yielded only modest d.r. (3:1), employing the larger alkoxide catalysts did enhance the d.r. Using the OC($CF_3$)(Me)Ph alkoxide variant in **6** improved the selectivity to 13:1; however, introduction of the more sterically encumbered alkoxide OC($CF_3$)$Ph_2$ (**7**) resulted in both diminished conversion and d.r. (**Table 5.2**, entries 2–3). In fact, paring back the steric demands of **6** to the parent phenoxide (**8**) provided the highest observed diastereoselectivity with the major *syn* diastereomer observed in > 20:1 d.r. (entry 4). *Ortho*-substitution on the aryl unit does not alter the observed d.r., but the yield does diminish with increased steric bulk of the *ortho* functionality (entries 5–7). Finally, substitution of the phenoxide ligand in the *para*-position preserves the observed d.r. relative to **8**, consistently offering the best overall yield of pyrrolidine product (66–82%; entries 8–9).

Given the high performance of catalyst **8** and the simplicity of the ligand, this complex was chosen to further explore the scope of stereoinduction. The results summarized in **Table 5.1** highlight the uniformly elevated isolated yields and the remarkable selectivity with the major diastereomer observed in greater than twenty-fold excess regardless of the aryl substitution for catalyst **8** compared to **1a**. We attribute this enhanced stereoinduction to the more directional phenoxide ligand projecting further into the cleft than the chloride or alkoxide variants, despite the reduced steric profile. The only exceptions for this class of substrates are entries **3n** (d.r. 11:1) and **3o** (d.r. 10:1) which feature a significantly reduced selectivity. In the former case, the presence of an accessible C–H bond proximal to the iminyl moiety may promote other activation pathways, decreasing both the d.r. and yield of pyrrolidine formation. The reason for the diminished selectivity of the naphthyl-containing substrate is at present unclear. Using a less sterically demanding α-azido functionality (**3q**) affords low d.r. (7:1), corroborating the proposed steric role of the anionic ligand. Similarly, in the absence of substantial interference with the cleft, cyclization of **2r** proceeds with poor selectivity (d.r. 2:1, **3r**).

**Table 5.2** Catalyst screening as a function of anionic ancillary ligand X.

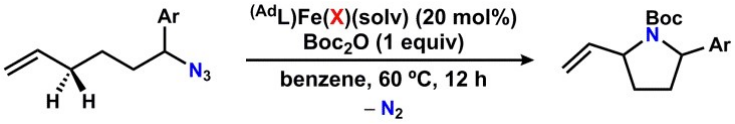


| | *X* | Complex | Yield (%) | d.r.[c] |
|---|---|---|---|---|
| 1 | Cl | **1a** | 63[a] | 3:1 |
| 2 | $OC(CF_3)(Me)Ph$ | **6** | 54[a] | 13:1 |
| 3 | $OC(CF_3)Ph_2$ | **7** | 26[a] | 6:1 |
| 4 | OPh | **8** | 67[a] | > 20:1 |
| 5 | $O(o\text{-}C_6H_3Cl_2)$ | **9** | 42[b] | 16:1 |

| | | | | |
|---|---|---|---|---|
| 6 | O(*o*-$C_6H_3Br_2$) | **10** | 42[b] | > 20:1 |
| 7 | O(*o*-$C_6H_3{}^iPr_2$) | **11** | 49[b] | > 20:1 |
| 8 | O(*p*-$C_6H_4F$) | **12** | 66[a] | > 20:1 |
| 9 | O(*p*-$C_6H_4OMe$) | **13** | 82[a] | > 20:1 |

Entries 1-4: reaction with 1-azido-1-(4-chlorophenyl)-hex-5-ene (**2b**); Entries 5-9: reaction with 1-azido-1-phenyl-hex-5-ene (2**a**); [a] Isolated yields. [b] $^1H$ NMR yields versus ferrocene internal standard. [c] d.r. (*syn*:*anti*) determined by GC/MS.

## 5.5 Conclusion

The foregoing results demonstrate the viability of rendering the catalytic *N*-heterocycle synthesis via direct C–H bond amination diastereoselective. DFT studies provided guidance towards a systematic catalyst design leading to an optimized diastereoselective cyclization via employment of a phenoxide ancillary ligand. This ligand likely creates a more directional steric profile than its chloride precursor without being as sterically inhibitive as the other anions examined. Furthermore, the accessible π orbital pathway between the iron center and the phenoxide ligand may serve to stabilize the reactive iron iminyl intermediate, leading to enhanced cyclization yields and highlighting an important feature to be considered for targeting more robust catalysts.

## 5.6 Experimental Methods

### *5.6.1 General Considerations.*

All manipulations of metal complexes were carried out in the absence of water and dioxygen using standard Schlenk techniques, or in an MBraun inert atmosphere drybox under a dinitrogen atmosphere. Ligand and ligand precursors were synthesized as previously reported.[6,8] All glassware was oven dried for a minimum of 1h and cooled in an evacuated antechamber prior to use in the drybox. Benzene, diethyl ether, dichloromethane, n-hexane and tetrahydrofuran were dried over 4 Å molecular sieves (Strem) prior to use. Chloroform-d was purchased from Cambridge Isotope Labs and used as received. Benzene-d6 was purchased from Cambridge Isotope Labs and was degasses and stored over 4 Å molecular sieves prior to use. DDQ, triphenylphosphine, tetrabutylammonium azide, sodium hypochlorite solution, 2-(4-bromophenyl)oxirane, 2-(4-chlorophenyl)oxirane, 2-(4-fluorophenyl)oxirane, 2-(trifluoromethyl)styrene, 2-chlorostyrene, 2-bromostyrene, 2-methylstyrene, 3-methylstyrene, 3-bromostyrene, 4-methylstyrene, 4-phenylbutan-1-ol, 3,3-dimethyl-1,2-epoxybutane, 3-chloroperbenzoic acid, silver trifluoromethanesulfonate, α-(trifluoromethyl)benzhydrol, trifluoroacetophenone, phenol, 2,6- dichlorophenol, 2,6-dibromophenol, 2,6-diisopropylphenol, 4-fluorophenol, 4-methoxyphenol, 5-bromo-1-pentene, 3-butenylmagnesium bromide and vinylmagnesium bromide were purchased from Aldrich and used as received. 2-vinylnaphthalene and 4-bromostyrene were purchased from Alfa Aesar and used as received. All the potassium alkoxide or aryloxide salts were prepared by treatment of the appropriate alcohol with potassium hydride in ether or THF. Lithium 1,1,1-trifluoro-2-phenylpropanol was prepared by addition of methyl lithium to trifluoroacetophenone. Celite® 545 (J. T. Baker) was dried in a Schlenk flask

for 24h under dynamic vacuum while heating to at least 150 °C prior to use in a drybox. Silica gel 32-63 μ (AIC, Framingham, MA) was used as received.

### *5.6.2 Characterization and Physical Measurements*

$^{1}H$ and $^{13}C$ NMR spectra were recorded on Varian Unity/Inova 500 MHz- or Agilent DD2 600 MHz spectrometers. $^{1}H$ and $^{13}C$ NMR chemical shifts are reported relative to $SiMe_4$ using the chemical shift of residual solvent peaks as reference. Gas chromatography/mass spectrometry (GC/MS) was performed on an Agilent GC/MS 5975 Turbo system. Mass spectrometry was performed on a Bruker microTOFII ESI LCMS for HRMS. Elemental analyses were carried out by Complete Analysis Laboratories, Inc. (Parsippany, NJ).

### *5.6.3 Metal Complexes Syntheses.*

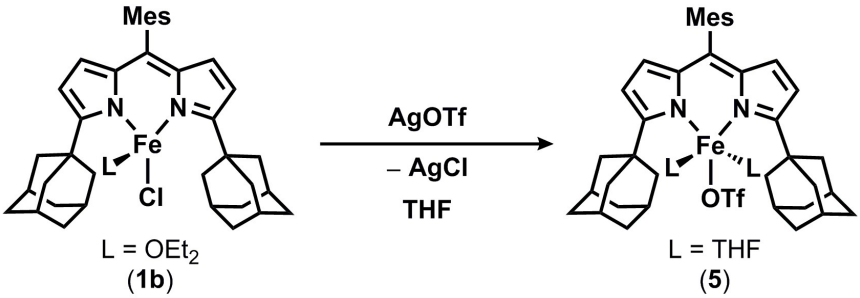


**($^{Ad}$L)Fe(OTf)(THF)$_2$ (5):** A solution of **($^{Ad}$L)FeCl(OEt$_2$)** (1.0 g, 1.44 mmol) in THF was added to a solution of silver trifluoromethanesulfonate (370 mg, 1.44 mmol) and the mixture was allowed to stir at room temperature for 2 hours. The reaction was filtered through Celite to remove the silver chloride precipitate. The Celite was washed with THF until filtrate was colorless. The solvent was removed *in vacuo* and the residue was dissolved in benzene and filtered through Celite to remove any additional insoluble materials. The dark red solution was lyophilized to afford

**($^{Ad}$L)Fe(OTf)(THF)$_2$** as a brown-red powder (1.07 g, 85%). **$^1$H NMR** (500 MHz, $C_6D_6$): δ 52.89 (br. s), 21.19 (br. s), 9.65 (s), 9.67 (br.s.), 6.61 (br. s.), 5.40 (br. s.), 4.19 (br. s.), 0.93 (br. s.), 0.65 (br. s.), -2.67 (br. s.), -6.73 (br. s.). Anal. Calc. for $C_{47}H_{58}F_3FeN_2O_5S$: C 64.23, H 7.00, N 3.19; Found: C 64.16, H 6.94, N 3.18. Crystals suitable for X-ray diffraction were grown from a *n*-hexane:THF solution at room temperature.

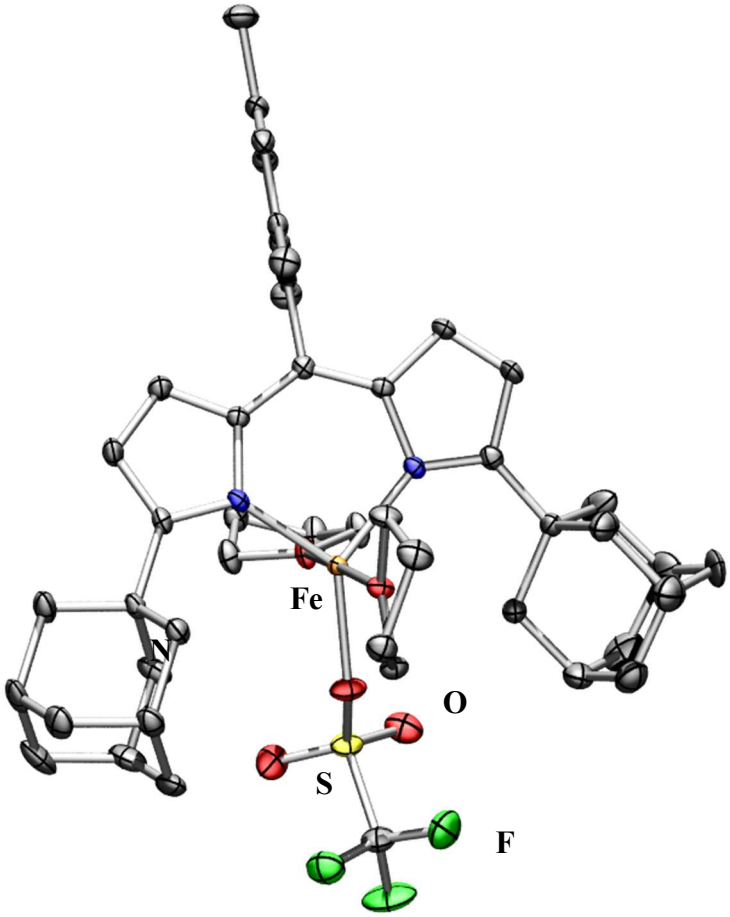


**Figure 5.4** Solid-state molecular structure for ($^{Ad}$L)Fe(OTf)(THF)$_2$ (**5**) with thermal ellipsoids at 50% probability level. Hydrogens and adamantyl group disorder omitted for clarity.

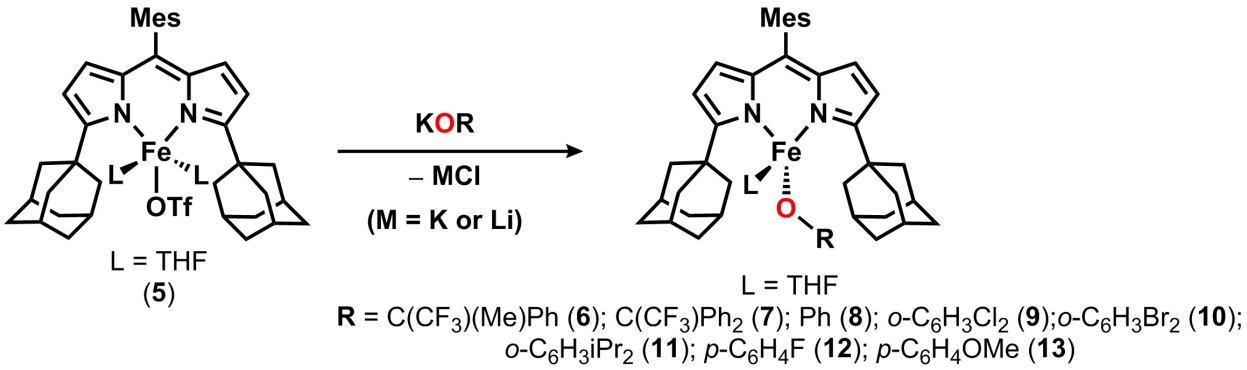


L = THF
(**5**)

L = THF
**R** = $C(CF_3)(Me)Ph$ (**6**); $C(CF_3)Ph_2$ (**7**); Ph (**8**); *o*-$C_6H_3Cl_2$ (**9**);*o*-$C_6H_3Br_2$ (**10**); *o*-$C_6H_3iPr_2$ (**11**); *p*-$C_6H_4F$ (**12**); *p*-$C_6H_4OMe$ (**13**)

***Procedure A*:** A solution of **($^{Ad}$L)Fe(OTf)(THF)$_2$** (1.0 equiv) in THF was added to a solution of the corresponding potassium alkoxide or aryloxide salt (1.0 equiv) in THF and the mixture was allowed to stir at room temperature for 2 hours. The reaction was filtered through Celite to remove the potassium trifluoromethanesulfonate precipitate. The Celite was washed with THF until filtrate was colorless. The solvent was removed *in vacuo* and the residue was dissolved in benzene and filtered through Celite to remove any additional insoluble materials. The dark red solution was lyophilized to afford the corresponding iron-phenoxide complex as a brown powder.

**($^{Ad}$L)Fe(OC(CF$_3$)(Me)Ph)(THF) (6):** Synthesized following procedure A (75.2 mg, 65%). **$^1$H NMR** (600 MHz, $C_6D_6$): δ: 62.05 (s), 61.22 (s), 45.30 (br. s), 35.61 (s), 14.98 (s), 13.52 (s), 5.14 (br.s.), 3.63 (s), 3.04 (s), -4.12 (s), -4.41(s), -7.50 (s), -21.19 (br.s.), -38.39 (s). Anal. Calc. for $C_{51}H_{61}F_3FeN_2O_2$: C 72.33, H 7.26, N 3.31; Found: C 72.19, H 6.99, N 3.36. Crystals suitable for X-ray diffraction were grown from a *n*-hexane:THF solution at room temperature.

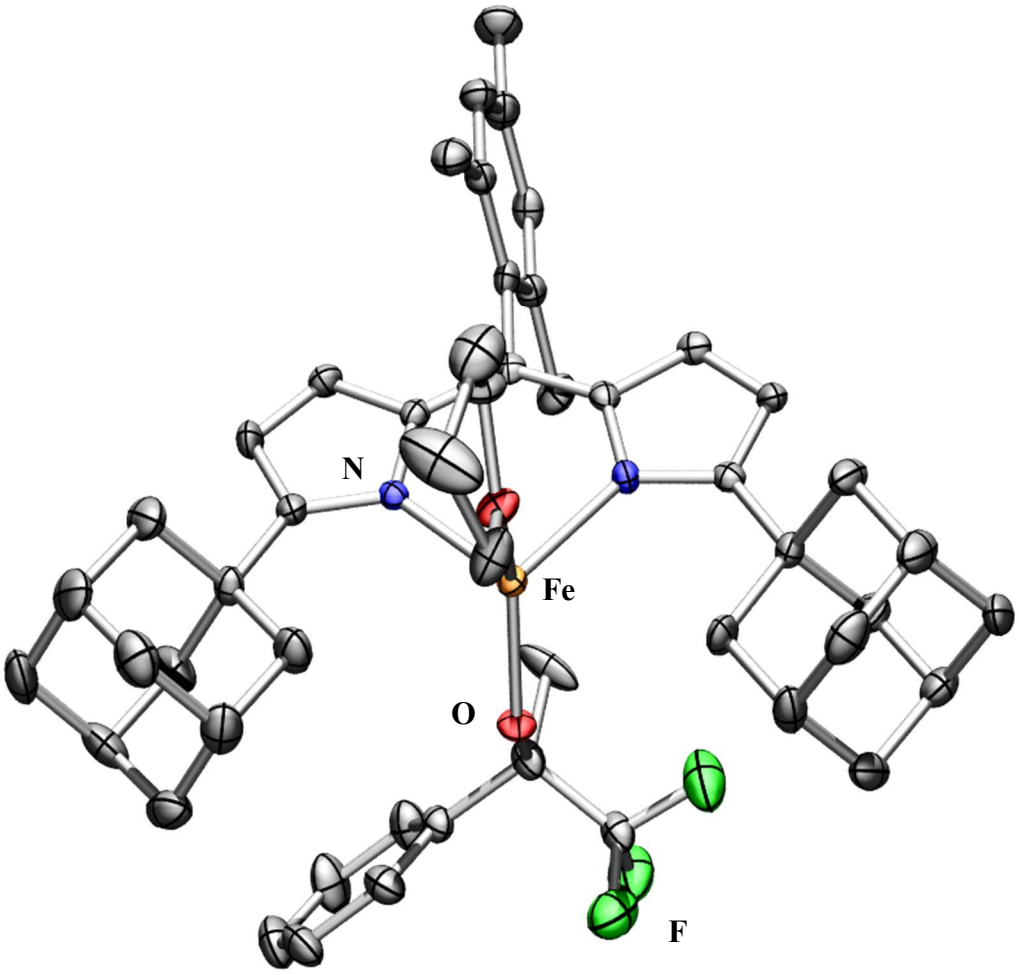


**Figure 5.5** Solid-state molecular structure for ($^{Ad}$L)Fe(OC($CF_3$)(Me)Ph)(THF) (**6**) with thermal ellipsoids at 50% probability level. Hydrogens omitted for clarity.

**($^{Ad}$L)Fe(OC(CF$_3$)Ph$_2$)(THF) (7):** Synthesized following procedure A (92.8 mg, 89%). **$^1$H NMR** (600 MHz, $C_6D_6$): δ: 61.68 (s), 35.30 (s), 32.35 (br. s), 35.61 (s), 13.33 (s), 8.01 (s), 6.67 (br.s.), 4.22 (s), 2.35 (s), 2.23 (s), -1.37 (s), -5.66 (s), -9.55(s), -23.71 (br.s.), -40.87 (s). Anal. Calc. for $C_{56}H_{63}F_3FeN_2O_2$: C 74.00, H 6.99, N 3.08; Found: C 73.88, H 6.76, N 3.13. Crystals suitable for X-ray diffraction were grown from a *n*-hexane:THF solution at room temperature.

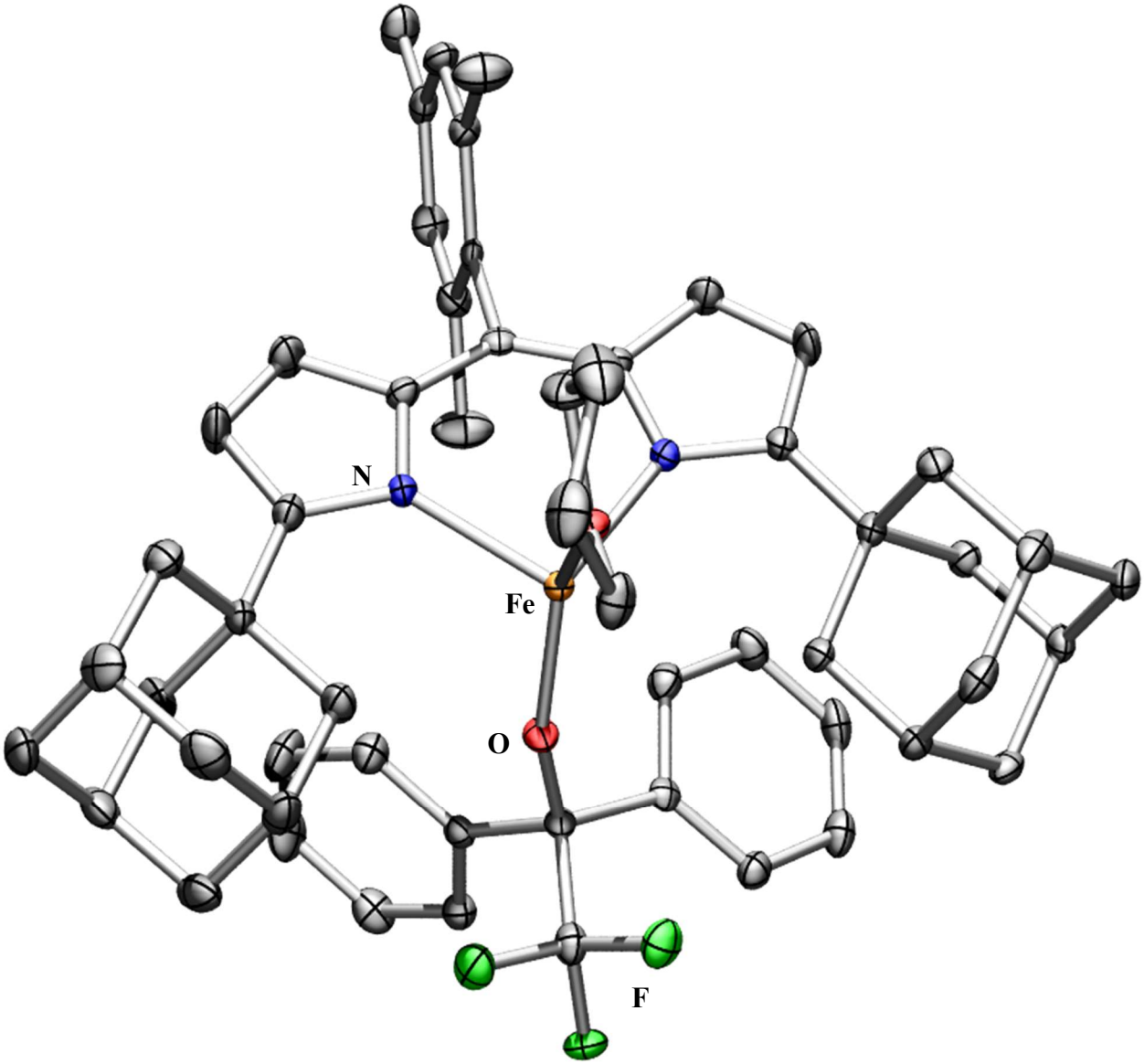


**Figure 5.6** Solid-state molecular structure for ($^{Ad}$L)Fe(OC(CF$_3$)Ph$_2$)(THF) (**7**) with thermal ellipsoids at 50% probability level. Hydrogens omitted for clarity

**($^{Ad}$L)Fe(OPh)(THF) (8):** Synthesized following procedure A (803 mg, 88%). **$^{1}$H NMR** (500 MHz, $C_6D_6$): δ: 55.93 (s), 51.29 (s), 28.70 (s), 11.84 (s), 11.29 (s), 9.93 (br.s.), 6.06 (s), 5.51 (s), 5.34 (s), 3.43 (s), -15.67 (br.s.), -30.46 (br.s.) Anal. Calc. for $C_{48}H_{58}FeN_2O_2$: C 76.78, H 7.79, N 3.73; Found: C 76.88, H 7.74, N 3.73. Crystals suitable for X-ray diffraction were grown from a *n*-hexane:THF solution at room temperature.

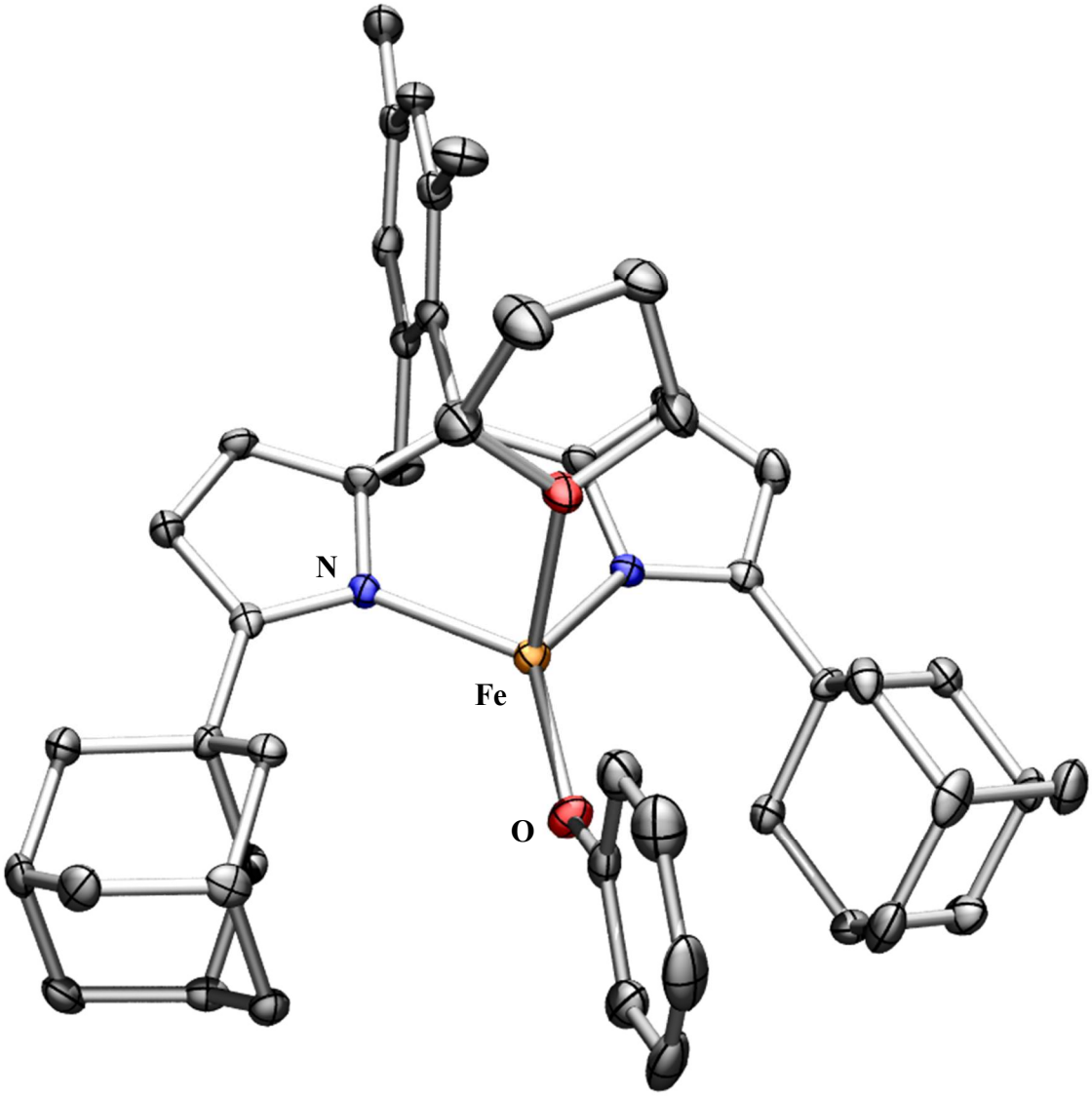


**Figure 5.7** Solid-state molecular structure for ($^{Ad}$L)Fe(OPh)(THF) (**8**) with thermal ellipsoids at 50% probability level. Hydrogens omitted for clarity.

**($^{Ad}$L)Fe($OC_6H_3Cl_2$)(THF) (9):** Synthesized following procedure A (84.4 mg, 90%). **$^1$H NMR** (500 MHz, $C_6D_6$) δ: 54.9 (br. s), 46.99 (s), 35.33 (s), 22.22 (br. s), 12.51 (br. s), 10.54 (s), 4.57 (s), -2.10 (s), -3.24 (s), -19.70 (s). Anal. Calc. for $C_{48}H_{56}Cl_2FeN_2O_2$: C 70.33, H 6.89, N 3.42; Found: C 70.29, H 6.78, N 3.39. Crystals suitable for X-ray diffraction were grown from a *n*-hexane:THF solution at room temperature.

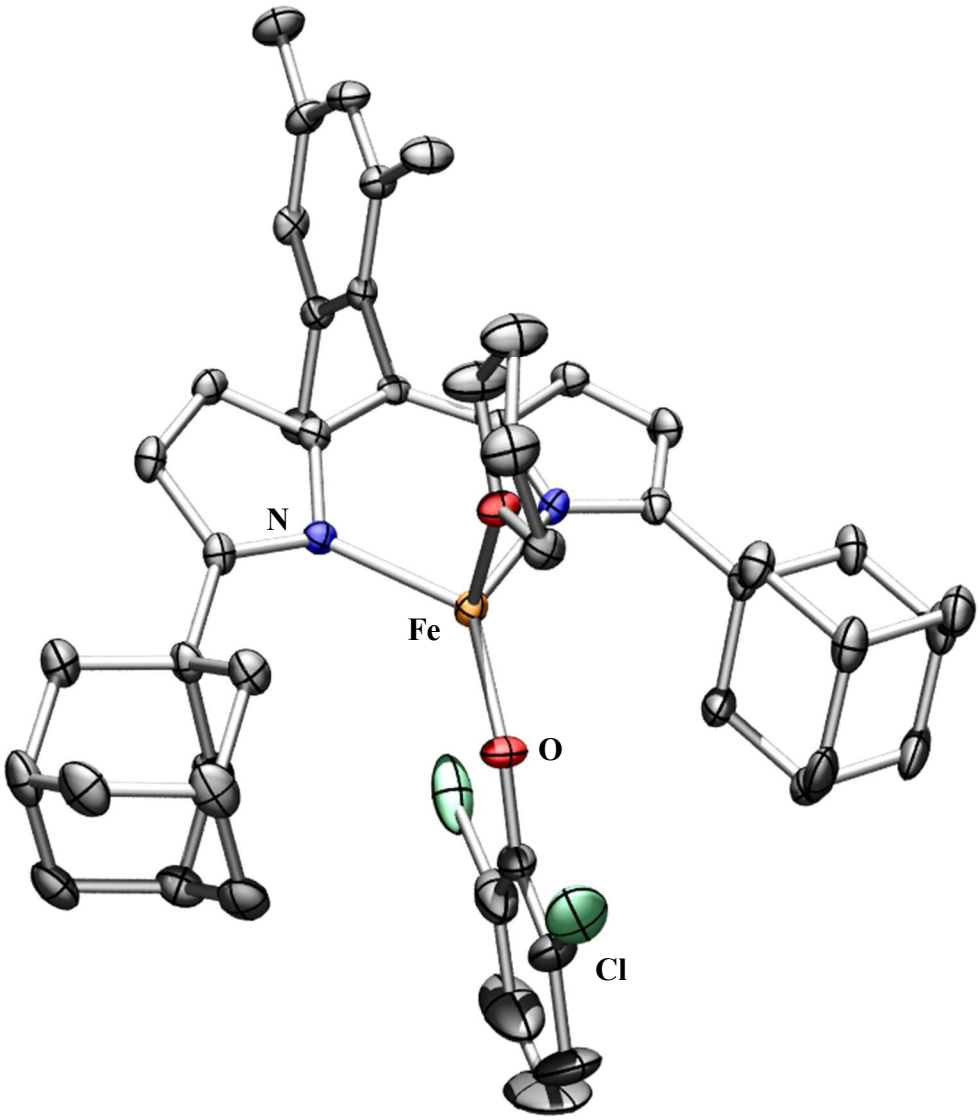


**Figure 5.8** Solid-state molecular structure for ($^{Ad}$L)Fe($OC_6H_3Cl_2$)(THF) (**9**) with thermal ellipsoids at 50% probability level. Hydrogens, aryl group disorder, THF and hexane solvents in the unit cell omitted for clarity.

**($^{Ad}$L)Fe($OC_6H_3Br_2$)(THF) (10):** Synthesized following procedure A (68.5 mg, 94%). **$^1$H NMR** (500 MHz, $C_6D_6$) δ: 57.29 (br. s), 47.41 (s), 34.82 (s), 22.14 (br. s), 12.48 (s), 10.78 (s), 4.71 (s), 3.56 (s), -2.81 (s), -3.98 (s), -20.23 (br. s). Anal. Calc. for $C_{48}H_{56}Br_2FeN_2O_2$: C 63.45, H 6.21, N 3.08; Found: C 63.52, H 6.16, N 2.99. Crystals suitable for X-ray diffraction were grown from a *n*-hexane:THF solution at room temperature.

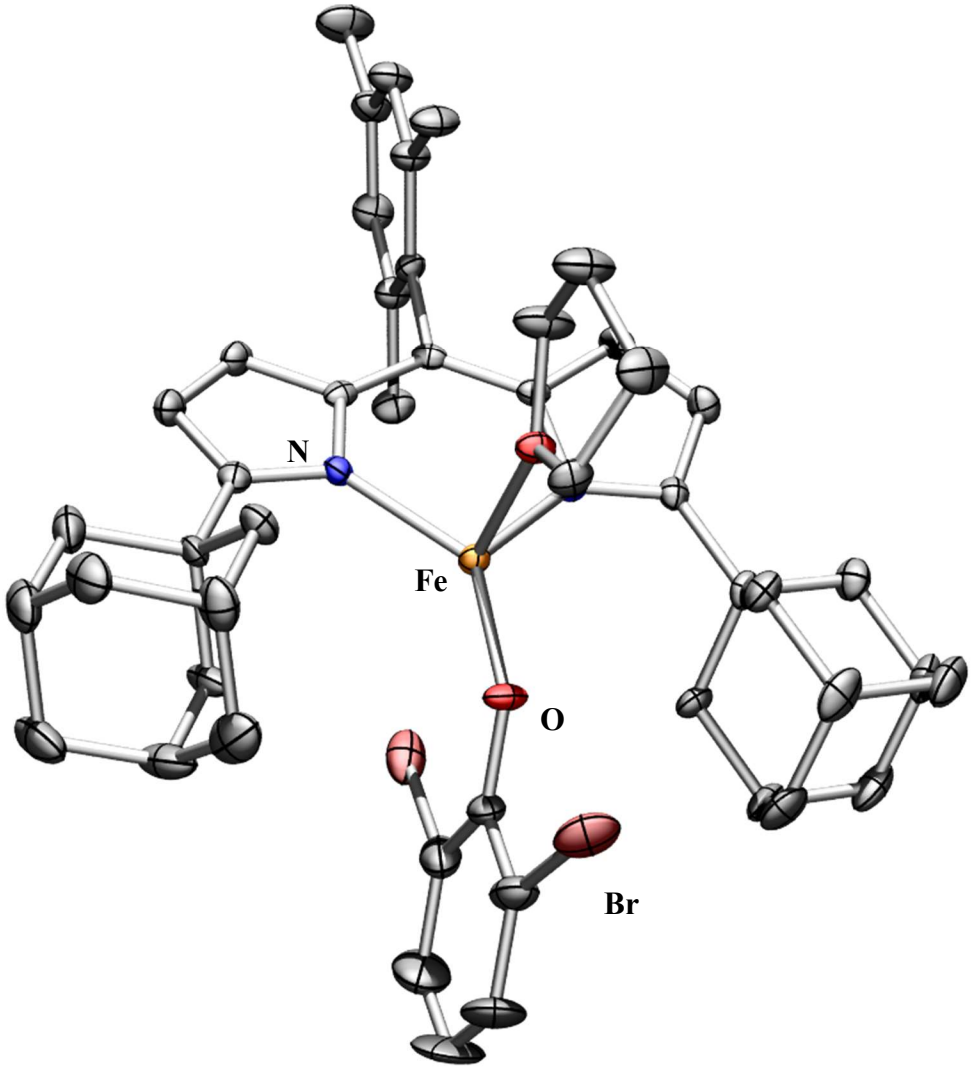


**Figure 5.9** Solid-state molecular structure for ($^{Ad}$L)Fe($OC_6H_3Br_2$)(THF) (**10**) with thermal ellipsoids at 50% probability level. Hydrogens, aryl group disorder, THF and hexane solvents in the unit cell omitted for clarity.

**($^{Ad}$L)Fe(OC$_6$H$_3$$^i$Pr$_2$)(THF) (11):** Synthesized following procedure A (63.7 mg, 94%). **$^1$H NMR** (500 MHz, $C_6D_6$) δ: 66.06 (s), 56.44 (s), 8.58 (s), 5.00 (br. s), 3.75 (s), -5.04 (s), -8.99 (s), -18.09 (br. s), -23.17 (s). Anal. Calc. for $C_{54}H_{70}FeN_2O_2$: C 77.67, H 8.45, N 3.35; Found: C 77.59, H 8.51, N 3.27. Crystals suitable for X-ray diffraction were grown from a *n*-hexane:THF solution at room temperature.

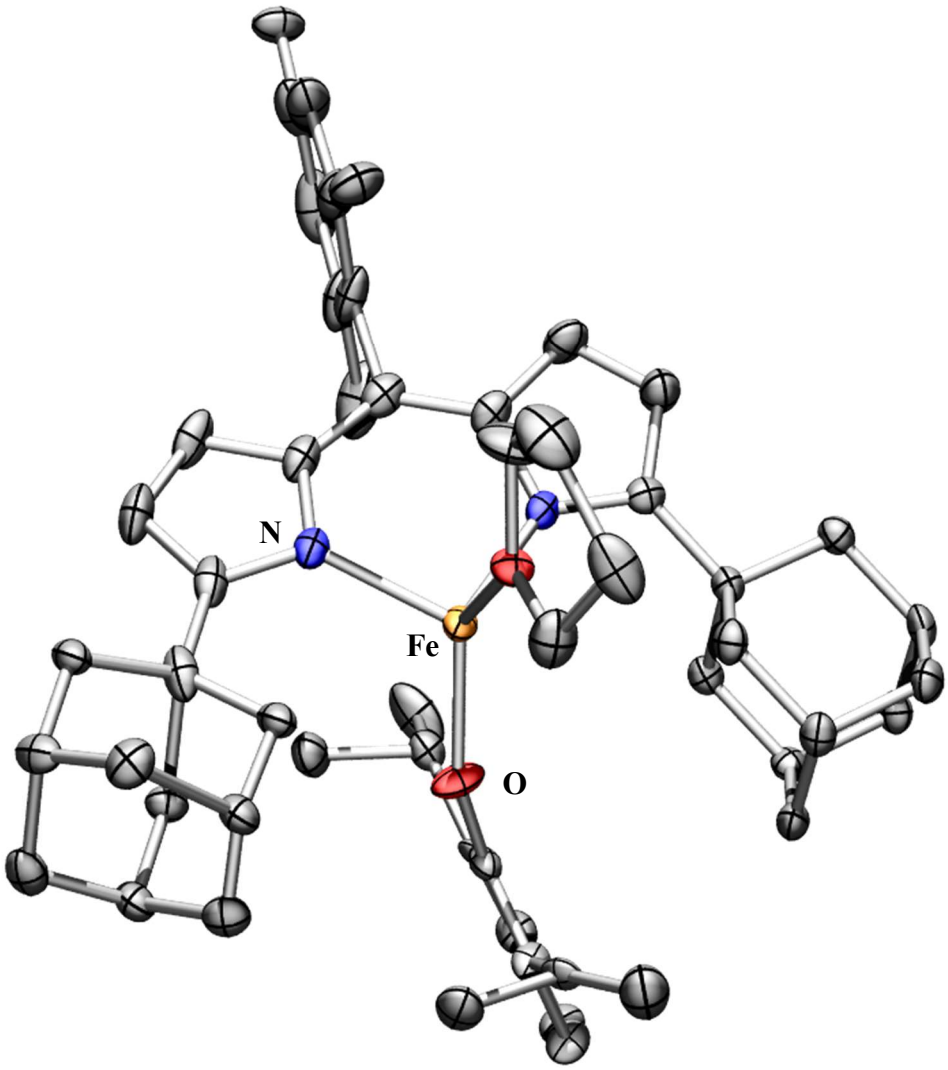


**Figure 5.10** Solid-state molecular structure for ($^{Ad}$L)Fe(OC$_6$H$_3$$^i$Pr$_2$)(THF) (**11**) with thermal ellipsoids at 50% probability level. Hydrogens, aryl group, adamantyl, mesityl and THF disorder, omitted for clarity.

**($^{Ad}$L)Fe(OC$_6$H$_4$F)(THF) (12):** Synthesized following procedure A (91 mg, 98 %). **$^1$H NMR** (500 MHz, $C_6D_6$): δ: 52.67 (s), 48.95 (s), 30.34 (s), 11.56 (br. s), 11.36 (s), 10.06 (br. s), 5.53 (s), 5.33 (s), 5.12 (s), -15.12 (br. s), -19.71 (br. s) Anal. Calc. for $C_{48}H_{57}FFeN_2O_2$: C 74.99, H 7.47, N 3.64; Found: C 74.87, H 7.34, N 3.62. Crystals suitable for X-ray diffraction were grown from a *n*-hexane:THF solution at room temperature. The complex crystallized as the bis-THF adduct **($^{Ad}$L)Fe(OC$_6$H$_4$F)(THF)$_2$.**

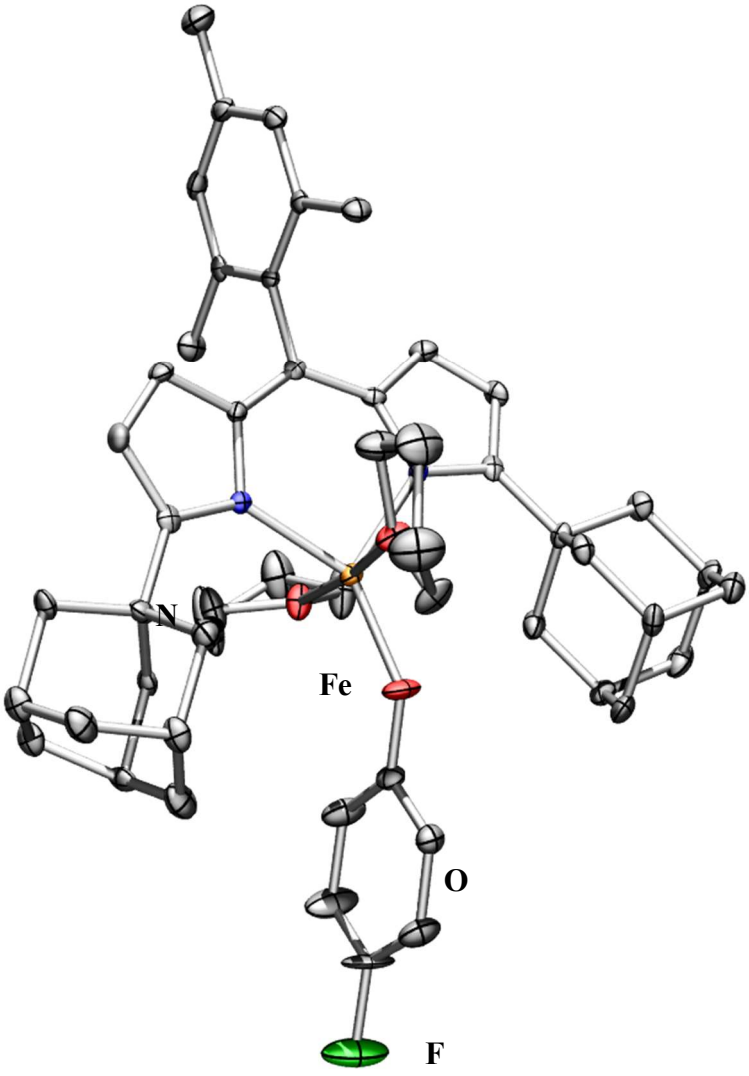


**Figure 5.11** Solid-state molecular structure for ($^{Ad}$L)Fe(OC$_6$H$_4$F)(THF)$_2$ (**12**) with thermal ellipsoids at 50% probability level. Hydrogens, adamantyl group disorder and THF solvent omitted for clarity.

**($^{Ad}$L)Fe(OC$_6$H$_4$OMe)(THF) (13):** Synthesized following procedure A (33.4 mg, 76 %). **$^1$H NMR** (500 MHz, $C_6D_6$): δ: 58.77 (s), 52.85 (s), 28.73 (s), 14.43 (s), 12.53 (s), 12.13 (br. s), 8.15 (br. s), 6.49 (s), 6.00 (s), 4.46 (s), -17.02 (br. s), -27.867 (br. s) Anal. Calc. for $C_{49}H_{60}FeN_2O_3$: C 75.37, H 7.75, N 3.59; Found: C 75.22, H 7.85, N 3.66. Crystals suitable for X-ray diffraction were grown from a *n*-hexane:THF solution at room temperature. The complex crystallized as the bis-THF adduct **($^{Ad}$L)Fe(OC$_6$H$_4$OMe)(THF)$_2$.**

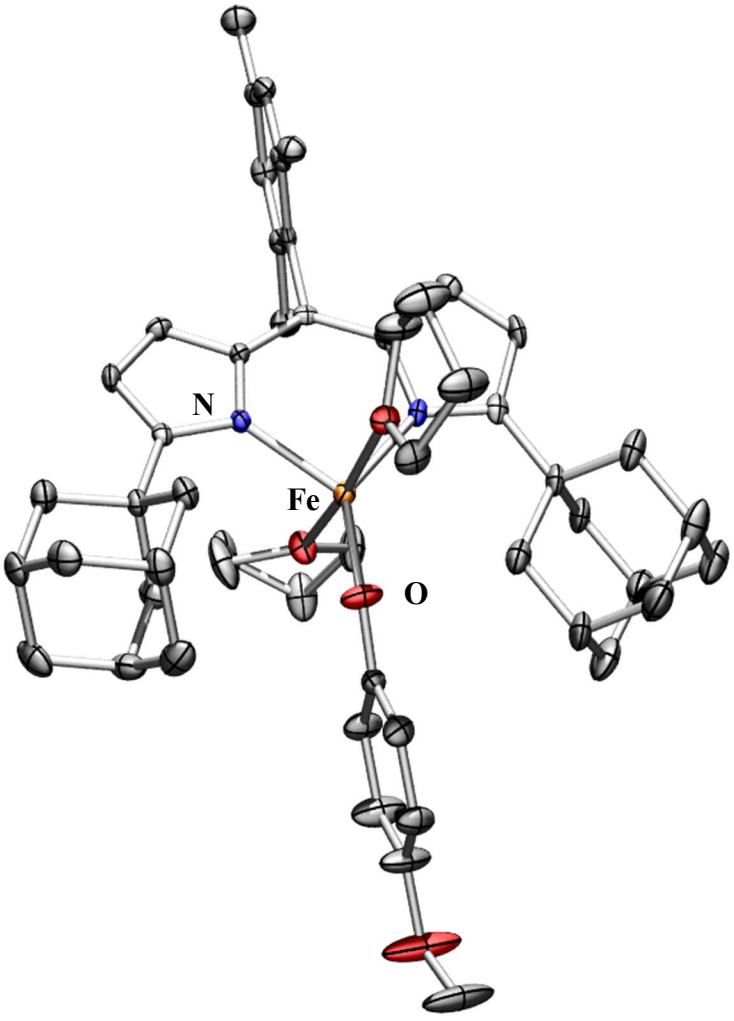


**Figure 5.12** Solid-state molecular structure for ($^{Ad}$L)Fe(OC$_6$H$_4$OMe)(THF)$_2$ (**13**) with thermal ellipsoids at 50% probability level. Hydrogens, adamantyl group disorder, bound THF disorder and THF solvent in the unit cell omitted for clarity.

### *5.6.4 Substrate Syntheses.*

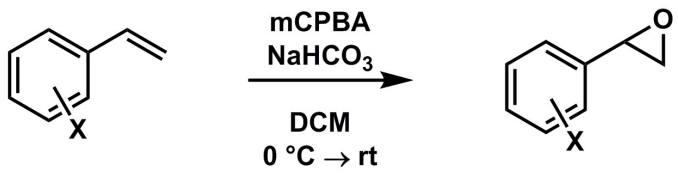


***Procedure B*** (modified from literature procedure[13]): A solution of mCPBA (2.0 equiv) in dichloromethane was added slowly over the course of 15 min to a stirring, 0 °C solution of the styrene substrate (1.0 equiv) and $NaHCO_3$ (3.0 equiv). The reaction was stirred at room temperature. Reaction was monitored by $^1H$ NMR to determine consumption of starting material (time varies depending on the styrene used, 3-8 hours). Upon completion, the reaction was quenched with a 10% solution of $Na_2SO_3$ and diluted with saturated $NaHCO_3$ solution, and the organic phase separated. The aqueous phase was extracted three times with dichloromethane, and the combined organic phases were washed five times with a saturated $Na_2CO_3$ solution, dried over $MgSO_4$, filtered and concentrated. The product was used without further purification.

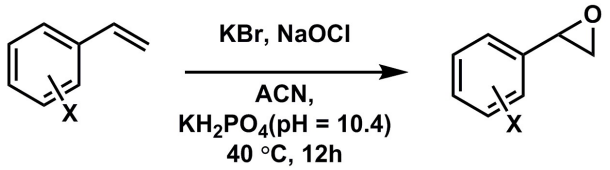


***Procedure C*** (adapted from literature procedure[14]): KBr (1.5 equiv), $KH_2PO_4$ buffer (pH = 10.4, 5 mL/mmol), acetonitrile (5 mL/mmol) and the styrene substrate (1.0 equiv) were added in a pressure vessel and the reaction mixture was heated to 40 °C in an oil bath. A solution of NaOCl (1.1 equiv, 10% aqueous solution) was added. The reaction mixture was stirred at 40 °C for 12

13. Mazimba, O.; Majinda, R. R.; Masesane, I. B. *Bull. Chem. Soc. Ethiop.* **2011**, *25*, 299.
14. Klawonn, M.; Bhor, S.; Mehltretter, G.; Döbler, C.; Fisher, C.; Beller, M. *Adv. Synth. Catal.* **2003**, *345*, 389.

hours. Upon completion, $Na_2SO_3$ (2.0 equiv) was added and the mixture was extracted three times with ethyl acetate, dried over $MgSO_4$ and concentrated.

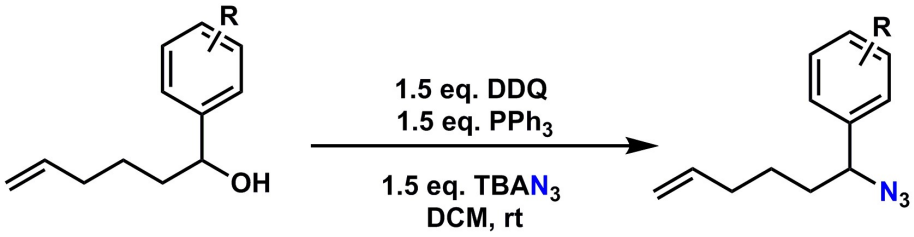


***Procedure D*** (adapted from literature procedure [15] )**:** 2,3-Dichloro-5,6-dicyano-1,4-benzoquinone (1.5 equiv) was added portionwise to a stirring solution of $PPh_3$ (1.5 equiv) in dichloromethane. Two minutes following the addition, tetrabutylammonium azide and the alcohol substrate were added sequentially. The reaction was allowed to stir at room temperature for 2-3 hours (monitored by TLC). Upon completion, the solution was concentrated and loaded onto a silica column with minimal dichloromethane and eluted with 10:1 hexanes: ethyl acetate. The oil isolated was further purified via silica gel chromatography with 100% hexanes or pentane.

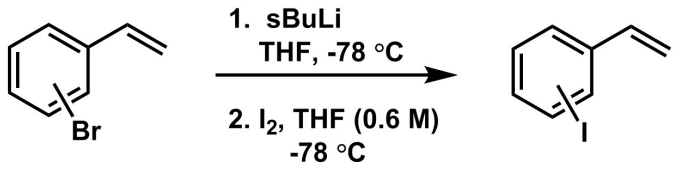


***Procedure E*** (modified from literature procedure[16])**:** An oven-dried RBF was charged with the corresponding bromo-styrene (2.0 g, 10.9 mmol, 1.0 equiv) and dissolved in 60 mL of THF inside a nitrogen atmosphere glove box. The flask was cooled inside a cold well with liquid nitrogen and a 1.4 M solution of *s*-BuLi in cyclohexane (12 g, 21.8 mmol, 2.0 equiv) was added slowly over 3 hours. The reaction mixture was stirred cold for 10 min and was then warmed to

15. Iranpoor, N.; Firouzabadi, H.; Akhlaghinia, B.; Nowrouzi, N. *Tett. Lett.* **2004**, 3291.
16. Tyson, E.; Ament, M.; Yoon, T. *J. Org. Chem.* **2013**, *78*, 2046.

room temperature. After 20 min, the flask was cooled to -78 °C under nitrogen and a solution of $I_2$ (0.6M in THF) was added slowly until the red color persisted. The mixture was warmed to room temperature, diluted with diethyl ether, washed with water, saturated aqueous $Na_2S_2O_3$, saturated aqueous $NaHCO_3$ and brine, dried over $MgSO_4$ and concentrated. The product was purified via silica gel chromatography with 100% pentane.

### *5.6.5 Stoichiometric Reactions*

Under an inert $N_2$ atmosphere, a solution of 1-azido-1-(2-trifluoromethylphenyl)-hex-5-en (**2m**) (1 equiv) in 2 mL of benzene was added to ($^{Ad}$L)FeCl($OEt_2$) (**1b**) (30.0 mg, 0.0432 mmol).The resultant inky, dark red solution was allowed to stir for 1 hour at room temperature. The reaction mixture was then lyophilized to a red/brown powder. The resultant solid was re-dissolved in hexanes, filtered to remove any insoluble material and left to crystallize at room temperature.

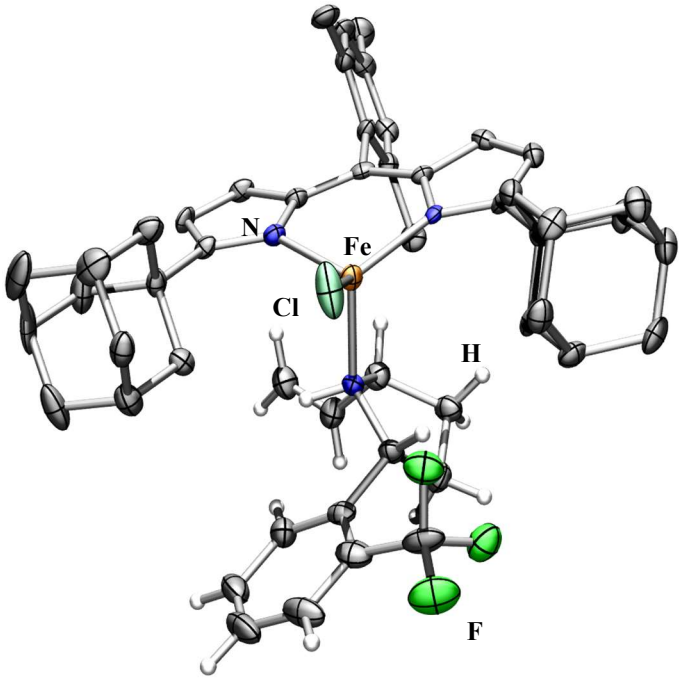

**Figure 5.13** Solid-state molecular structure for ($^{Ad}$L)Fe(2-(2-(trifluoromethyl)phenyl)-5-vinylpyrrolidine) (**4**) with thermal ellipsoids at 50% probability level. Hydrogens omitted for clarity.

### *5.6.6 Catalytic Reactions*

Under an inert $N_2$ atmosphere, solutions of the desired azide and di-*tert*-butyl-dicarbonate (5.0 equiv) in benzene (1 mL) were added to ($^{Ad}$L)FeCl($OEt_2$) (**1a**) (25.0 mg, 0.0346 mmol) or ($^{Ad}$L)Fe(OPh)(THF) (**5**) (25.0 mg, 0.0333 mmol) into a vial. The dark red solution was transferred to a pressure vessel and heated to 60 °C for 12 hours. The reaction mixture was run through a short pipette of silica gel eluting with a 10:1 mixture of dichloromethane and methanol to give a red-orange solution in order to remove paramagnetic materials. The internal standard ferrocene or 1,3,5-trimethoxybenzene was added and the solution concentrated. $^1$H NMR yields were determined by integration of product peaks against the internal standard. Products were purified and isolated via silica chromatography using mixtures of hexane and ethyl acetate or ether as eluents. Reactions were run in triplicate and the average yield of the three runs is reported. Deprotection of the pyrrolidine for $^1$D NOESY studies was achieved following a previously reported literature procedure.[7] Diastereomeric ratios were determined by GC-MS.

### *5.6.7 Catalyst screening*

Under an inert $N_2$ atmosphere, solutions of the desired azide and di-*tert*-butyl-dicarbonate (5.0 equiv) in benzene (1 mL) were added to the desired iron alkoxide (**3** or **4**) or aryloxide complex (**6** – **10**) into a vial. The dark red solution was transferred to a pressure vessel and heated to 60 °C for 12 hours. The reaction mixture was run through a short pipette of silica gel eluting with a 10:1 mixture of dichloromethane and methanol to give a red-orange solution in order to remove

paramagnetic materials. The internal standard ferrocene was added and the solution concentrated. $^{1}$H NMR yields were determined by integration of product peaks against the internal standard. Products were purified and isolated via silica chromatography using mixtures of hexane and ethyl acetate or ether as eluents. Diastereomeric ratios were determined by GC-MS.

### *5.6.8 Characterization of azide and pyrrolidine products*

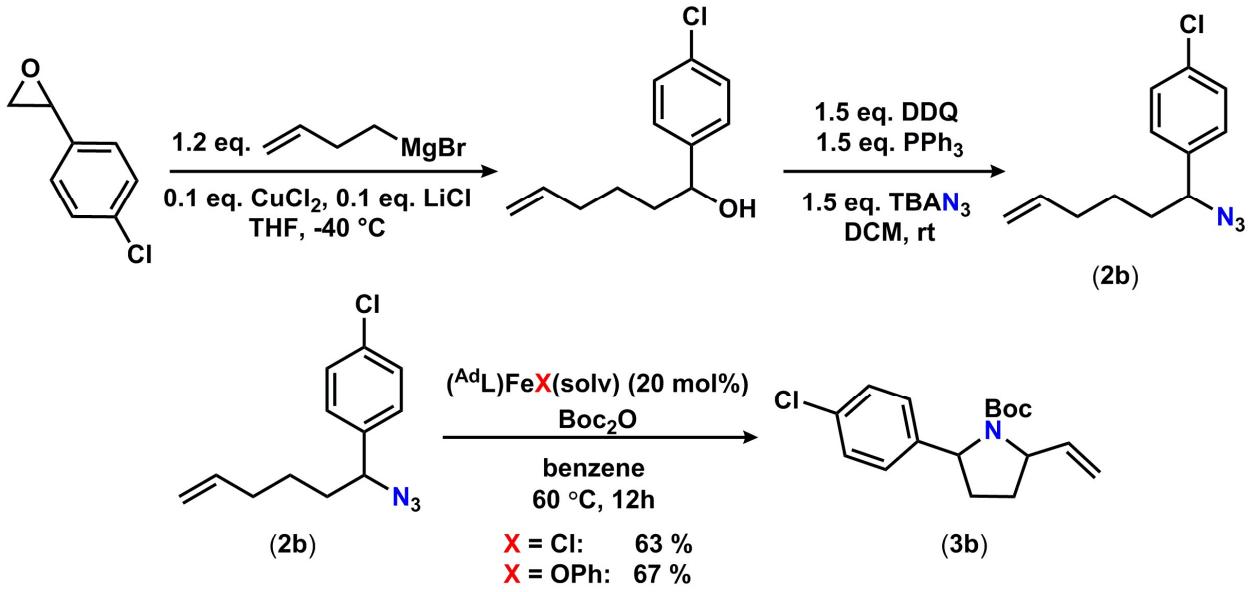


**1-(4-chlorophenyl)hex-5-en-1-ol:** Synthesized following previously reported procedure.[6] 78% (47% depicted regioisomer) **$^{1}$H NMR** (500 MHz, $CDCl_3$) δ: 7.21–7.36 (m, 4 H), 5.77 (ddt, *J* = 17.03, 10.32, 6.59, 6.59 Hz, 1 H), 4.93–5.05 (m, 2 H), 4.62–4.71 (m, 1 H), 2.01–2.14 (m, 2 H), 1.82–1.88 (br. s, 1H), 1.64–1.82 (m, 2 H), 1.44–1.55 (m, 1 H), 1.31–1.44 (m, 1 H). **$^{13}$C NMR** (125 MHz, $CDCl_3$) δ: 143.3, 138.5, 133.2, 128.7, 127.3, 114.9, 73.9, 38.6, 33.6, 25.0.

**1-azido-1-(4-chlorophenyl)-hex-5-en (2b):** Synthesized following procedure D. 69%. **$^{1}$H NMR** (600 MHz, $CDCl_3$) δ: 7.36 (dd, *J* = 8.2, 2.0 Hz, 5 H), 7.24 (dd, *J* = 8.5, 1.7 Hz, 2 H), 5.70–5.83 (m, 1 H), 5.01 (dt, *J* = 17.0, 1.7 Hz, 1 H), 4.97 (d, *J* = 10.2 Hz, 1 H), 4.41 (t, *J* = 7.2 Hz, 1 H), 2.07

(q, $J$ = 7.5 Hz, 2 H), 1.77–1.88 (m, 1 H), 1.68–1.77 (m, 1 H), 1.44–1.54 (m, 1 H), 1.30–1.42 (m, 1 H). **$^{13}$C NMR** (125 MHz, $CDCl_3$) δ: 138.3, 137.9, 133.9, 129.0, 128.2, 115.1, 65.5, 35.6, 33.2, 25.3. **GCMS (EI)** $t_R$ = 10.28 min *m/z*: 51, 64, 77, 91, 102, 113, 125, 141, 235.

***tert*-butyl 2-(4-chlorophenyl)-5-vinylpyrrolidine-1-carboxylate (3b): $^{1}$H NMR** (500 MHz, $C_6D_6$, 50 ºC) δ (major diastereomer): 7.10–7.14 (m, 3 H), 7.02–6.89 (m, 2 H), 5.54–5.97 (m, 1 H), 5.21 (d, $J$ = 16.9 Hz, 1 H), 4.86–5.10 (m, 1 H), 4.50–4.73 (m, 1 H), 4.20–4.47 (m, 1 H), 1.65–2.11 (m, 2 H), 1.36–1.61 (m, 2 H), 1.24–1.36 (m, 9 H). **$^{13}$C NMR** (125 MHz, $C_6D_6$, 50 ºC) δ(mixture of rotamers): 154.7, 143.5, 140.0, 132.5, 128.5, 127.8, 115.0, 79.2, 62.5, 61.0, 34.3, 30.3, 28.3. **HRMS** ($ESI^+$) *m/z* Calc. 308.1412 $[C_{17}H_{22}ClNO_2+H]^+$, Found. 308.1426 $[M+H]^+$.

**2-(4-chlorophenyl)-5-vinylpyrrolidine: $^{1}$H NMR** (600 MHz, $C_6D_6$) δ (3.4:1 mixture of diastereomers): 7.11–7.20 (m, 6.3 H), 7.06 (d, $J$ = 8.2 Hz, 0.6 H), 5.87 (ddd, $J$ = 17.0, 10.0, 7.0 Hz, 1 H), 5.69 (ddd, $J$ = 17.2, 10.4, 7.0 Hz, 0.3 H), 5.17 (d, $J$ = 15.3 Hz, 1 H), 5.03 (d, $J$ = 17.0 Hz, 0.3 H), 4.98 (dd, $J$ = 9.7, 1.5 Hz, 1 H), 4.92 (d, $J$ = 10.0 Hz, 0.3 H), 3.96 (t, $J$ = 7.6 Hz, 0.3 H), 3.71 (q, $J$ = 7.0 Hz, 1 H), 3.65–3.69 (m, 1 H), 3.29–3.37 (m, 1 H), 1.67–1.83 (m, 1.6 H), 1.57–1.67 (m, 1 H), 1.37–1.49 (m, 2 H), 1.25–1.37 (m, 0.6 H). **$^{13}$C NMR** (125 MHz, $CDCl_3$) δ (minor diastereomer in parentheses): 143.6, 141.6(140.5), 132.7(132.9), 128.5(128.7), 128.5(128.4), 114.3(114.6), 61.6, 61.2(60.9), 34.2(34.9), 31.4(32.5).

**1D NOESY** (600 MHz, $C_6D_6$)

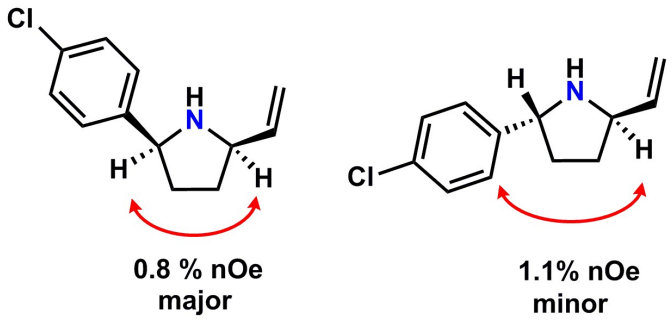

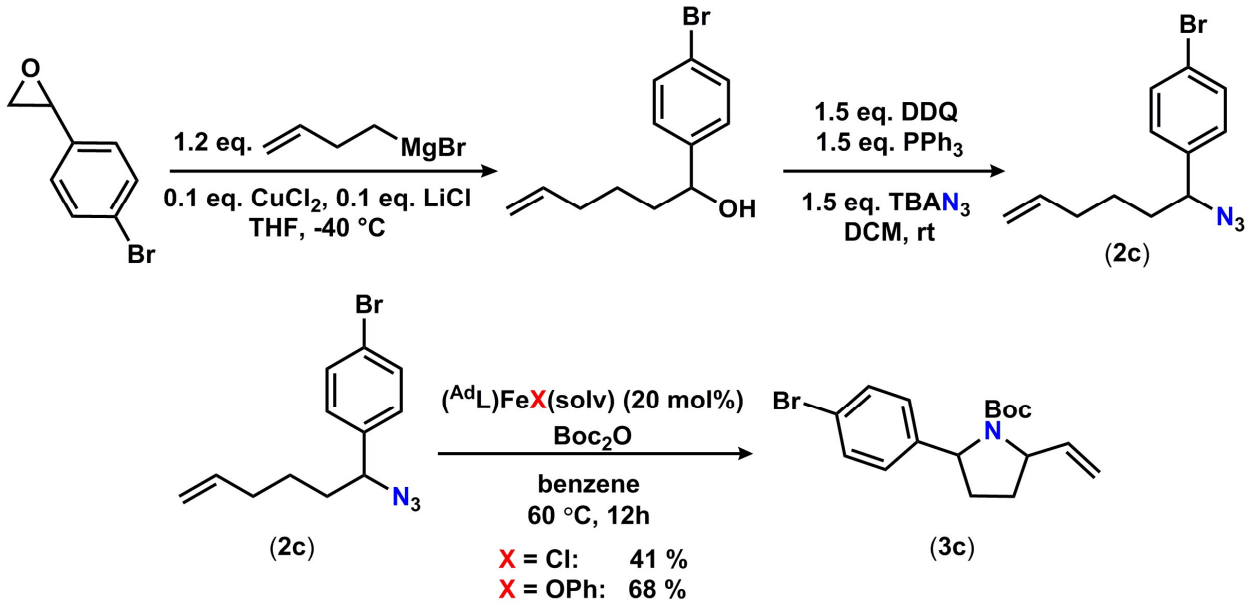


**1-(4-bromophenyl)hex-5-en-1-ol:** Synthesized following previously reported procedure.[6] 79% (42% depicted regioisomer). **$^1$H NMR** (600 MHz, $CDCl_3$) δ: 7.45–7.48 (m, 2 H), 7.20–7.23 (m, 2 H), 5.77 (ddt, *J* = 17.02, 10.27, 6.90, 6.90 Hz, 1 H), 4.92–5.02 (m, 2 H), 4.62–4.68 (m, 1 H), 2.05–2.10 (m, 2 H), 2.04 (s, 1 H), 1.74–1.80 (m, 1 H), 1.65–1.72 (m, 1 H), 1.50 (ddtd, *J* = 12.91, 10.49, 7.67, 7.67, 5.28 Hz, 1 H), 1.33–1.41 (m, 1 H). **$^{13}$C NMR** (125 MHz, $CDCl_3$) δ: 143.9, 138.5, 131.7, 127.8, 121.4, 115.0, 74.0, 38.6, 33.6, 25.1.

**1-azido-1-(4-bromophenyl)-hex-5-en (2c):** Synthesized following procedure D. 61%. **$^1$H NMR** (600 MHz, $CDCl_3$) δ: 7.48–7.60 (m, 2 H), 7.18 (d, *J* = 8.8 Hz, 2 H), 5.76 (ddt, *J* = 17.0, 10.1, 6.7, 6.7 Hz, 1 H), 4.94–5.09 (m, 2 H), 4.40 (t, *J* = 6.5 Hz, 1 H), 2.02–2.16 (m, 2 H), 1.68–1.90 (m, 2 H), 1.33–1.56 (m, 2 H). **$^{13}$C NMR** (125 MHz, $CDCl_3$) δ: 138.8, 137.9, 131.9, 128.5, 122.1, 115.1, 65.6, 35.5, 33.2, 25.3. **GCMS** (EI) $t_R$ = 11.00 min *m/z*: 55, 68, 81, 96, 115, 128, 144, 157, 172, 184, 197, 210, 223, 236, 251, 279.

***tert*-butyl 2-(4-bromophenyl)-5-vinylpyrrolidine-1-carboxylate (3c): $^1$H NMR** (500 MHz, $C_6D_6$, 50 °C) δ (major diastereomer): 7.21–7.43 (m, 2 H), 6.86–7.08 (m, 2 H), 5.82–5.96 (m, 1 H),

5.21 (d, $J$ = 16.94 Hz, 1 H), 5.05 (d, $J$ = 10.07 Hz, 1 H), 4.60 (br. s., 1 H), 4.37 (br. s., 1 H), 1.80–2.03 (m, 1 H), 1.60–1.79 (m, 1 H), 1.22–1.56 (m, 11 H). **$^{13}$C NMR** (125 MHz, $C_6D_6$, 50 °C) δ: 155.0, 144.4, 140.3, 131.9, 128.5, 127.8, 120.9, 115.4, 79.6, 62.9, 61.4, 34.6, 30.8, 28.8. **HRMS** (ESI$^+$) *m/z* Calc. 352.0907 $[C_{17}H_{22}BrNO_2+H]^+$, Found. 353.0905 $[M+H]^+$.

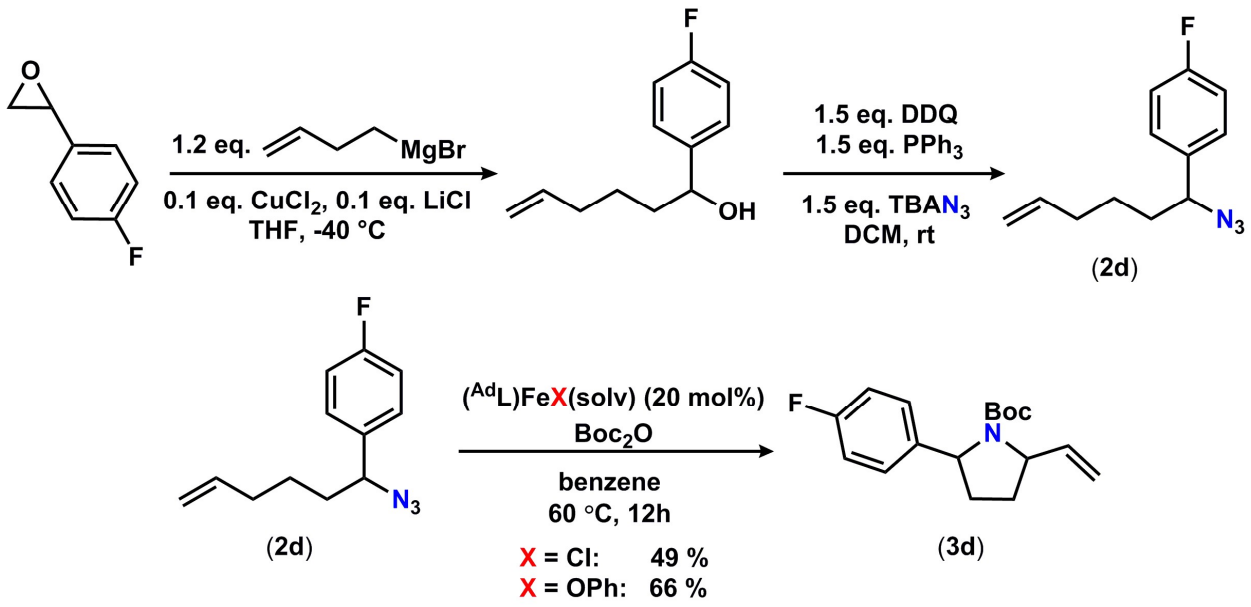


**1-(4-fluorophenyl)hex-5-en-1-ol:** Synthesized following previously reported procedure.[6] 78% (60% depicted regioisomer). **$^1$H NMR** (600 MHz, $CDCl_3$) δ: 7.29–7.33 (m, 2 H), 7.00–7.05 (m, 2 H), 5.77 (ddt, $J$ = 17.02, 10.27, 6.90, 6.90 Hz, 1 H), 4.92–5.02 (m, 2 H), 4.64–4.69 (m, 1 H), 2.07 (q, $J$ = 7.24 Hz, 2 H), 2.04 (s, 1 H), 1.77–1.84 (m, 2 H), 1.69 (ddt, $J$ = 13.79, 10.71, 5.36, 5.36 Hz, 1 H), 1.46–1.54 (m, 1 H). **$^{13}$C NMR** (125 MHz, $CDCl_3$) δ:140.7, 138.6, 127.6 (d), 115.5, 115.3, 114.9, 74.0, 38.7, 33.7, 25.1.

**1-azido-1-(4-fluorophenyl)-hex-5-en (2d):** Synthesized following procedure D. 56%. **$^1$H NMR** (600 MHz, $CDCl_3$) δ: 7.25–7.34 (m, 2 H), 7.04–7.14 (m, 2 H), 5.70–5.91 (m, 1 H), 4.91–5.13 (m, 2 H), 4.34–4.53 (m, 1 H), 2.01–2.19 (m, 2 H), 1.67–1.93 (m, 2 H), 1.32–1.55 (m, 2 H). **$^{13}$C NMR**

(125 MHz, $CDCl_3$) δ: 138.0, 135.6, 128.5, 128.3, 126.8, 115.6, 65.5, 35.6, 33.2, 25.3. **GCMS** (EI) $t_R$ = 11.05 min *m/z*: 55, 77, 91, 109, 122, 135, 148, 161, 178, 191, 207, 219.

***tert*-butyl 2-(4-fluorophenyl)-5-vinylpyrrolidine-1-carboxylate (3d): $^1$H NMR** (600 MHz, $C_6D_6$) δ(major diastereomer): 7.06 (br. s., 2 H), 6.72–6.91 (m, 3 H), 5.52–6.05 (m, 1 H), 4.90–5.38 (m, 2 H), 4.17–4.75 (m, 2 H), 1.612.06 (m, 2 H), 1.14–1.58 (m, 11 H). **$^{13}$C NMR** (125 MHz, $C_6D_6$) δ: 163.2, 161.3, 154.8, 140.8, 140.1, 127.9, 115.1 (d), 79.2, 62.5, 61.1, 34.4, 30.2, 28.4. **HRMS** ($ESI^+$) *m/z* Calc. 292.1713 $[C_{17}H_{22}FNO_2+H]^+$, Found. 292.1704 $[M+H]^+$.

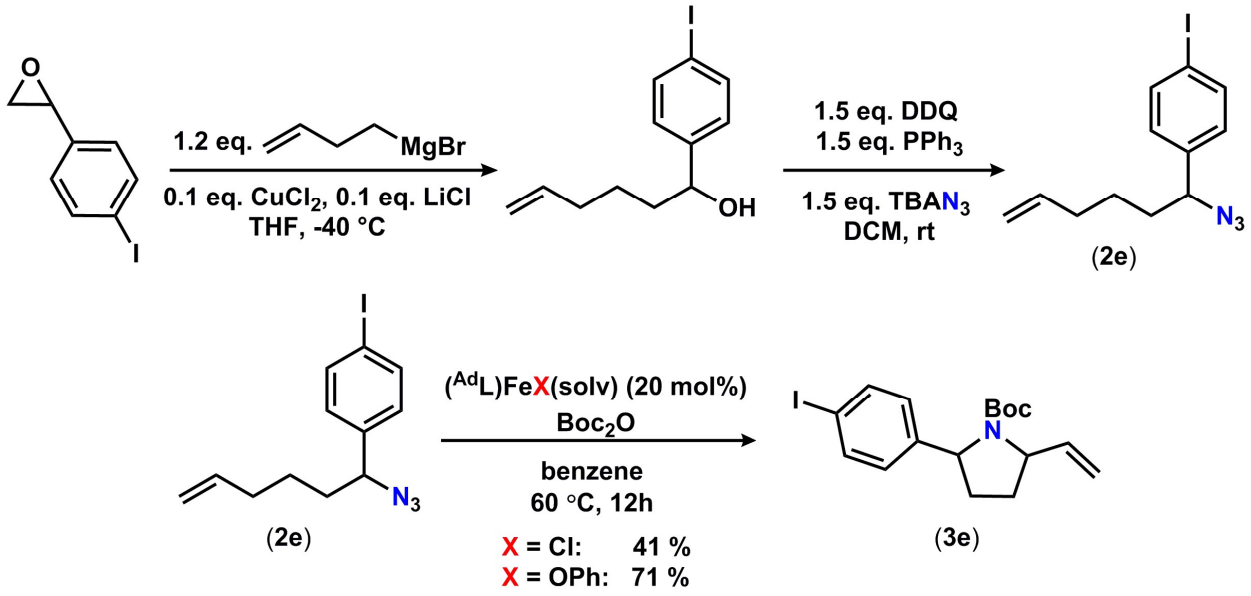


**4-iodostyrene:** Synthesized following procedure E. 73%. Spectroscopic data were consistent with reported values.[17]

**2-(4-iodophenyl)oxirane:** Synthesized following procedure C. Spectroscopic data were consistent with reported values.[18]

17. Kang, S.-K.; Lee, H.-W.; Kim, J.-S.; Choi, S.-C. *Tett. Lett.* **1996**, *37*, 3723.
18. Zu-yi Li, H. J.; Dong, X.-W. *Org. Biomol. Chem.* **2004**, *2*, 408.

**1-(4-iodophenyl)hex-5-en-1-ol:** Synthesized following previously reported procedure.[6] 49% (28% depicted regioisomer). **$^1$H NMR** (600 MHz, $CDCl_3$) δ: 7.67 (d, *J* = 7.63 Hz, 2 H), 7.09 (d, *J* = 8.22 Hz, 2 H), 5.77 (ddt, *J* = 16.95, 10.20, 6.68, 6.68 Hz, 1 H), 4.91–5.03 (m, 2 H), 4.61–4.66 (m, 1 H), 2.03–2.10 (m, 2 H), 1.79–1.82 (m, 1 H), 1.63–1.79 (m, 2 H), 1.45–1.54 (m, 1 H), 1.33–1.40 (m, 1 H). **$^{13}$C NMR** (125 MHz, $CDCl_3$) δ: 144.6, 138.5, 137.6, 128.0, 115.0, 92.9, 74.1, 38.6, 33.7, 25.1.

**1-azido-1-(4-iodophenyl)-hex-5-en (2e):** Synthesized following procedure D. 67%. **$^1$H NMR** (500 MHz, $C_6D_6$) δ: 7.37–7.42 (m, 2 H), 6.52 (d, *J* = 8.30 Hz, 2 H), 5.54–5.66 (m, 1 H), 4.90–4.98 (m, 2 H), 3.74–3.81 (m, 1 H), 1.79 (q, *J* = 7.00 Hz, 2 H), 1.41–1.51 (m, 1 H), 1.16–1.35 (m, 2 H), 1.00–1.12 (m, 1 H). **$^{13}$C NMR** (125 MHz, $C_6D_6$) δ: 139.7, 138.2, 138.1, 128.9, 127.9, 115.2, 65.7, 35.7, 33.5, 25.5. **GCMS** (EI) $t_R$ = 10.21 min *m/z*: 57, 77, 89, 103, 115, 128, 144, 172, 207, 230, 284, 299.

***tert*-butyl 2-(4-iodophenyl)-5-vinylpyrrolidine-1-carboxylate (3e): $^1$H NMR** (500 MHz, $C_6D_6$, 50 °C) δ (major diastereomer): 7.44–7.49 (m, 2 H), 6.83 (d, *J* = 8.30 Hz, 2 H), 5.80–5.94 (m, 1 H), 5.20 (d, *J* = 17.09 Hz, 1 H), 5.04 (d, *J* = 10.25 Hz, 1 H), 4.59 (br. s., 1 H), 4.36 (br. s., 1 H), 1.63–1.75 (m, 2 H), 1.23–1.58 (m, 11 H). **$^{13}$C NMR** (125 MHz, $C_6D_6$, 50 °C) δ: 154.7, 144.7, 140.0, 137.6, 129.8, 115.1, 91.8, 79.4, 62.6, 61.1, 34.4, 30.4, 28.4. **HRMS** ($ESI^+$) *m/z* Calc. 821.1283 $[(C_{17}H_{22}INO_2)_2+Na]^+$, Found. 821.1281 $[2M+Na]^+$.

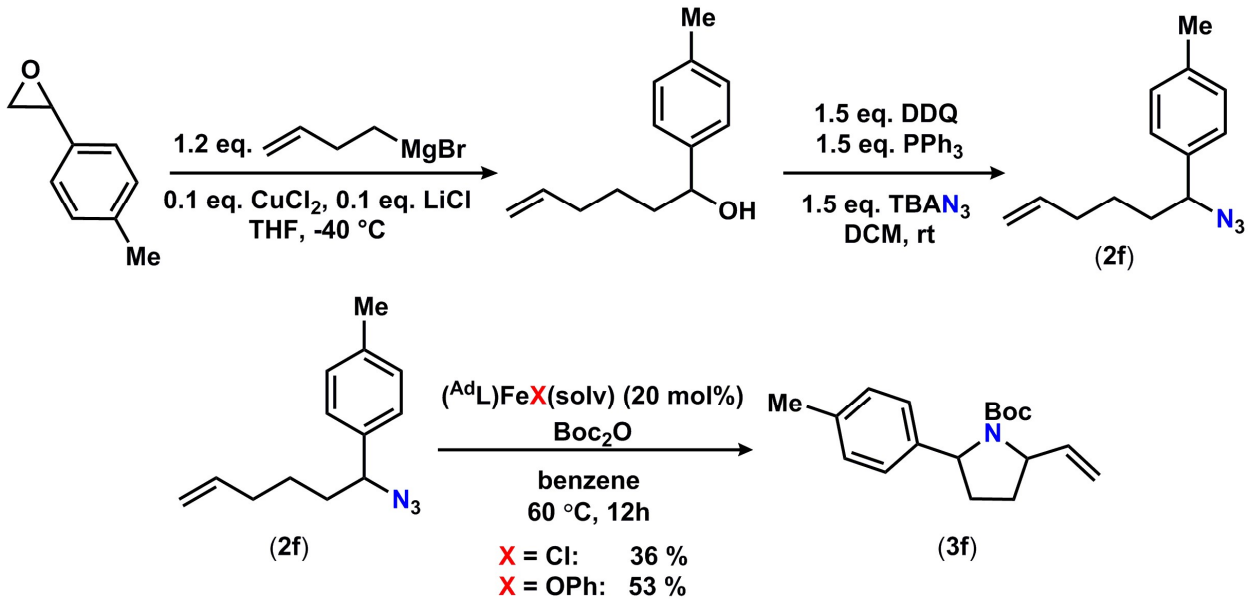


**2-(*p*-tolyl)oxirane:** Synthesized following procedure B. Spectroscopic data were consistent with reported values.[13]

**1-(*p*-tolyl)hex-5-en-1-ol:** Synthesized following previously reported procedure.[6] 52% (16% depicted regioisomer). **$^1$H NMR** (500 MHz, $CDCl_3$) δ: 7.21–7.25 (m, 2 H), 7.16 (d, *J* = 8.30 Hz, 2 H), 5.78 (ddt, *J* = 17.03, 10.19, 6.65, 6.65 Hz, 1 H), 4.90–5.02 (m, 2 H), 4.61–4.67 (m, 1 H), 2.34 (s, 3 H), 2.07 (q, *J* = 7.16 Hz, 2 H), 1.65–1.85 (m, 3 H), 1.46–1.55 (m, 1 H), 1.32–1.43 (m, 1 H). **$^{13}$C NMR** (125 MHz, $CDCl_3$) δ: 142.0, 138.7, 137.4, 129.3, 126.0, 114.8, 74.6, 38.6, 33.7, 25.3, 21.3.

**1-azido-1-(4-methylphenyl)-hex-5-en (2f):** Synthesized following procedure D. 49%. **$^1$H NMR** (600 MHz, $C_6D_6$) δ: 6.98–7.02 (m, 2 H), 6.94 (d, *J* = 7.63 Hz, 2 H), 5.58–5.67 (m, 1 H), 4.91–4.97 (m, 2 H), 4.02 (t, *J* = 7.34 Hz, 1 H), 2.06 (s, 3 H), 1.80–1.86 (m, 2 H), 1.61–1.70 (m, 1 H), 1.47–1.55 (m, 1 H), 1.28–1.37 (m, 1 H), 1.11–1.22 (m, 1 H). **$^{13}$C NMR** (125 MHz, $C_6D_6$) δ: 138.4, 137.9, 137.2, 129.7, 127.2, 115.1, 66.3, 35.9, 33.6, 25.8, 21.1. **GCMS** (EI) $t_R$ = 8.45 min *m/z*: 51, 65, 77, 91, 105, 118, 131, 144, 158, 172, 187.

***tert*-butyl 2-(*p*-tolyl)-5-vinylpyrrolidine-1-carboxylate (3f): $^{1}$H NMR** (500 MHz, $C_6D_6$, 50 °C) δ (major diastereomer): 7.21 (d, *J* = 7.81 Hz, 2 H), 7.01 (d, *J* = 7.81 Hz, 2 H), 5.96–6.08 (m, 1 H), 5.27 (d, *J* = 16.60 Hz, 1 H), 5.08 (d, *J* = 10.25 Hz, 1 H), 4.79 (br. s., 1 H), 4.45 (br. s., 1 H), 2.13 (s, 3 H), 1.76–1.86 (m, 1 H), 1.47–1.71 (m, 3 H), 1.29–1.38 (m, 9 H). **$^{13}$C NMR** (125 MHz, $C_6D_6$, 50 °C) δ: 154.9, 140.4, 136.0, 129.1, 128.3, 126.4, 114.8, 79.0, 63.0, 61.2, 34.5, 30.5, 28.5, 21.0. **HRMS** ($ESI^+$) *m/z* Calc. 597.3663 $[(C_{18}H_{25}NO_2)_2+Na]^+$, Found. 597.3650 $[2M+Na]^+$.

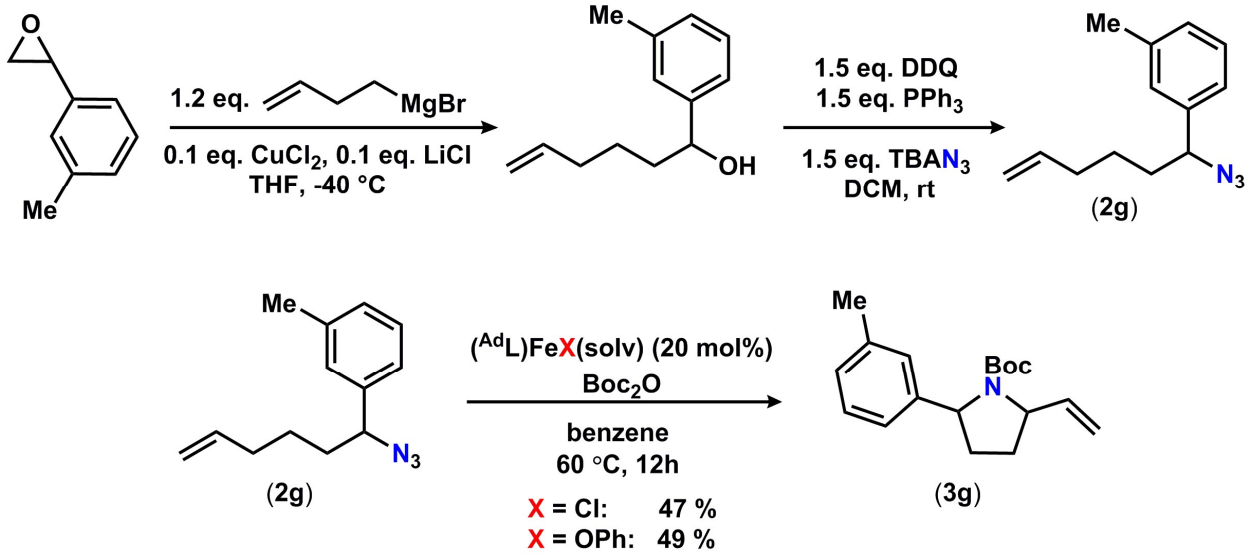


**2-(*m*-tolyl)oxirane:** Synthesized following procedure B. Spectroscopic data were consistent with reported values.[13]

**1-(*m*-tolyl)hex-5-en-1-ol:** Synthesized following previously reported procedure.[6] 51% (27% depicted regioisomer). **$^{1}$H NMR** (500 MHz, $CDCl_3$) δ: 7.24 (t, *J* = 7.57 Hz, 1 H), 7.06–7.19 (m, 3 H), 5.72–5.86 (m, 1 H), 4.91–5.04 (m, 2 H), 4.61–4.69 (m, 1 H), 2.36 (s, 3 H), 2.08 (q, *J* = 7.32 Hz, 2 H), 1.67–1.85 (m, 3 H), 1.48–1.58 (m, 1 H), 1.32–1.44 (m, 1 H). **$^{13}$C NMR** (125 MHz, $CDCl_3$) δ: 144.9, 138.7, 128.5, 128.4, 126.7, 125.1, 123.1, 114.8, 74.7, 38.6, 33.7, 25.3, 21.6.

**1-azido-1-(3-methylphenyl)-hex-5-en (2g):** Synthesized following previously reported procedure.**Error! Bookmark not defined.** 43%. **$^{1}$H NMR** (600 MHz, $C_6D_6$) δ: 7.06 (m, 1 H),

6.94 (m, 3 H), 5.57–5.66 (m, 1 H), 4.91–4.98 (m, 2 H), 3.99–4.05 (m, 1 H), 2.07 (s, 3 H), 1.83 (d, *J* = 7.63 Hz, 2 H), 1.60–1.71 (m, 1 H), 1.47–1.56 (m, 1 H), 1.14–1.39 (m, 2 H). **$^{13}$C NMR** (125 MHz, $C_6D_6$) δ: 140.3, 139.0, 138.7, 129.5, 129.2, 128.9, 128.1, 124.5, 66.9, 36.2, 33.9, 26.1, 22.0. **GCMS** (EI) $t_R$ = 8.37 min *m/z*: 51, 65, 77, 91, 105, 118, 131, 144, 158, 172, 187.

***tert*-butyl 2-(*m*-tolyl)-5-vinylpyrrolidine-1-carboxylate (3g): $^{1}$H NMR** (500 MHz, $C_6D_6$, 50°C) δ (mixture of rotamers): 7.17–7.22 (m, 1 H), 7.05–7.08 (m, 1 H), 7.03 (d, *J* = 7.6 Hz, 1.7 H), 6.95 (t, *J* = 6.5 Hz, 0.3 H), 5.79–6.11 (m, 1 H), 5.00–5.42 (m, 2 H), 4.64 –4.93 (m, 1 H), 4.29–4.58 (m, 1 H), 2.31–2.37 (m, 3 H), 2.25 (dd, *J* = 13.2, 6.2 Hz, 1 H), 2.02–2.11 (m, 1 H), 1.77–1.95 (m, 2 H), 1.08–1.35 (m, 9 H). **$^{13}$C NMR** (125 MHz, $C_6D_6$, 50°C) δ(mixture of rotamers and diastereomers): 155.0(154.0), 144.3(145.2), 139.5(138.9), 137.6(138.2), 128.1, 127.2, 126.7(125.9), 122.8(122.5), 115.0(113.9), 79.4(79.2), 62.9(61.7), 61.0(59.8), 34.5, 30.6, 28.2, 21.5. **HRMS** ($ESI^+$) *m/z* Calc. 597.3663 $[(C_{18}H_{25}NO_2)_2+Na]^+$, Found. 597.3642 $[2M+Na]^+$.

**1-methyl-2-(*m*-tolyl)-5-vinylpyrrolidine**: **$^{1}$H NMR** (500 MHz, $CDCl_3$) δ: 7.04–7.17 (m, 3 H), 6.96 (d, *J* = 7.3 Hz, 1 H), 5.67–5.79 (m, 1 H), 5.11 (dd, *J* = 17.1, 1.5 Hz, 1 H), 5.02 (dd, *J* = 10.0, 1.7 Hz, 1 H), 3.07 (t, *J* = 8.1 Hz, 1 H), 2.66 (q, *J* = 8.0 Hz, 1 H), 2.26 (s, 3 H), 1.80–2.12 (m, 5 H), 1.56–1.71 (m, 2 H). **$^{13}$C NMR** (125 MHz, $CDCl_3$) δ: 144.2, 137.9, 128.3, 128.2, 128.0, 127.7, 124.6, 116.0, 72.0, 70.9, 38.6, 33.4, 30.4, 21.4 **GCMS (EI)** (single diastereomer) $t_R$ = 9.76 min *m/z*: 55, 68, 82, 91, 110, 117, 132, 143, 158, 174, 186, 201.

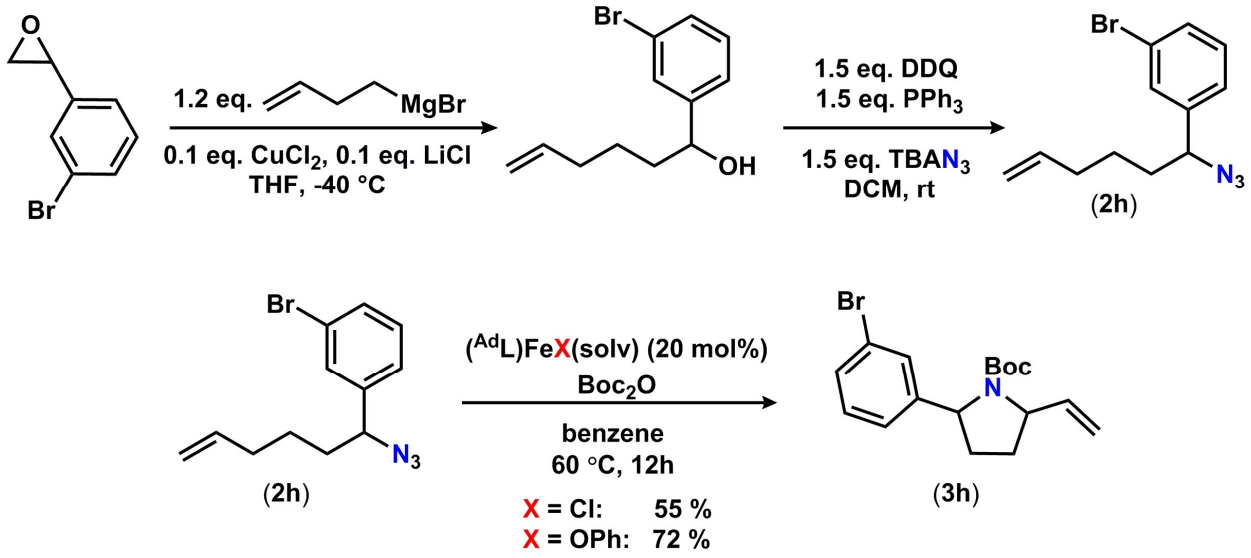


**2-(3-bromophenyl)oxirane:** Synthesized following procedure B. Spectroscopic data were consistent with reported values.[19]

**1-(3-bromophenyl)hex-5-en-1-ol:** Synthesized following previously reported procedure.[6] 50% (34% depicted regioisomer). **$^1$H NMR** (500 MHz, $CDCl_3$) δ: 7.50 (d, *J* = 1.83 Hz, 1 H), 7.40 (dt, *J* = 7.78, 1.60 Hz, 1 H), 7.24–7.28 (m, 1 H), 7.18–7.24 (m, 1 H), 5.78 (ddt, *J* = 17.06, 10.30, 6.70, 6.70 Hz, 1 H), 4.92–5.03 (m, 2 H), 4.62–4.69 (m, 1 H), 2.08 (q, *J* = 7.33 Hz, 2 H), 1.85 (d, *J* = 3.66 Hz, 1 H), 1.66–1.82 (m, 2 H), 1.47–1.56 (m, 1 H), 1.34–1.44 (m, 1 H). **$^{13}$C NMR** (125 MHz, $CDCl_3$) δ: 147.3, 138.5, 130.7, 130.2, 129.1, 124.6, 122.8, 115.0, 74.0, 38.7, 33.6, 25.1.

**1-azido-1-(3-bromophenyl)-hex-5-en (2h):** Synthesized following procedure D. 46%. **$^1$H NMR** (500 MHz, $C_6D_6$) δ: 7.24 (t, *J* = 1.71 Hz, 1 H), 7.02–7.19 (m, 1 H), 6.75–6.83 (m, 1 H), 6.63–6.71 (m, 1 H), 5.50–5.58 (m, 1 H), 4.86–4.95 (m, 2 H), 3.74 (dd, *J* = 7.81, 5.86 Hz, 1 H), 1.69–1.79 (m, 2 H), 1.35–1.45 (m, 1 H), 1.12–1.32 (m, 2 H), 0.97–1.08 (m, 1 H). **$^{13}$C NMR** (125

19. Huang, K.; Wang, H.; Stepanenko, V.; De Jesús, M.; Torruellas, C.; Correa, W.; Ortiz-Marciales, M. *J. Org. Chem.* **2011** *76* 1883

MHz, $C_6D_6$) δ: 143.1, 138.5, 131.7, 130.1, 130.6, 125.8, 123.5, 115.5, 66.0, 36.2, 33.8, 25.8. **GCMS** (EI) $t_R$ = 9.38 min *m/z*: 55, 67, 77, 89, 103, 115, 129, 144, 157, 172, 182/184, 192, 208/210, 222/224, 236/238, 249/250, 251/253.

***tert*-butyl 2-(3-bromophenyl)-5-vinylpyrrolidine-1-carboxylate (3h): $^1$H NMR** (500 MHz, $C_6D_6$, 50 °C) δ (major diastereomer): 7.47–7.49 (m, 1 H), 7.18 (m, 1 H), 7.07 (d, *J* = 7.32 Hz, 1 H), 6.79–6.83 (m, 1 H), 5.89 (br. s., 1 H), 5.21 (d, *J* = 17.58 Hz, 1 H), 5.04 (m, 1 H), 4.57 (br. s, 1 H), 4.37 (br. s., 1 H), 1.27–1.70 (m, 11 H). **$^{13}$C NMR** (125 MHz, $C_6D_6$, 50 °C) δ: 155.0, 148.0, 140.2, 130.4, 130.3, 130.2, 125.2, 123.1, 115.5, 79.7, 63.0, 61.4, 34.6, 30.6, 28.7. **HRMS** ($ESI^+$) *m/z* Calc. 352.0907 $[C_{17}H_{22}BrNO_2+H]^+$, Found. 352.0904 $[M+H]^+$; Calc. 374.0726 $[C_{17}H_{22}BrNO_2+Na]^+$, Found. 374.0723 $[M+Na]^+$.

**2-(3-bromophenyl)-5-vinylpyrrolidine: $^1$H NMR** (600 MHz, $C_6D_6$) δ: 7.55 (m, 1 H), 7.12–7.22 (m, 2 H), 6.72–6.77 (m, 1 H), 5.66–5.75 (m, 1 H), 5.00 (d, *J* = 17.09 Hz, 1 H), 4.83 (d, *J* = 10.25 Hz, 1 H), 3.79–3.86 (m, 1 H), 3.48 (d, *J* = 7.81 Hz, 1 H), 1.53–1.69 (m, 2 H), 1.31–1.42 (m, 2 H). **1D NOESY** (600 MHz, $C_6D_6$)

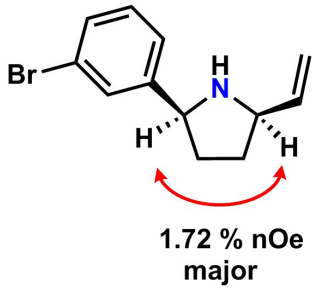

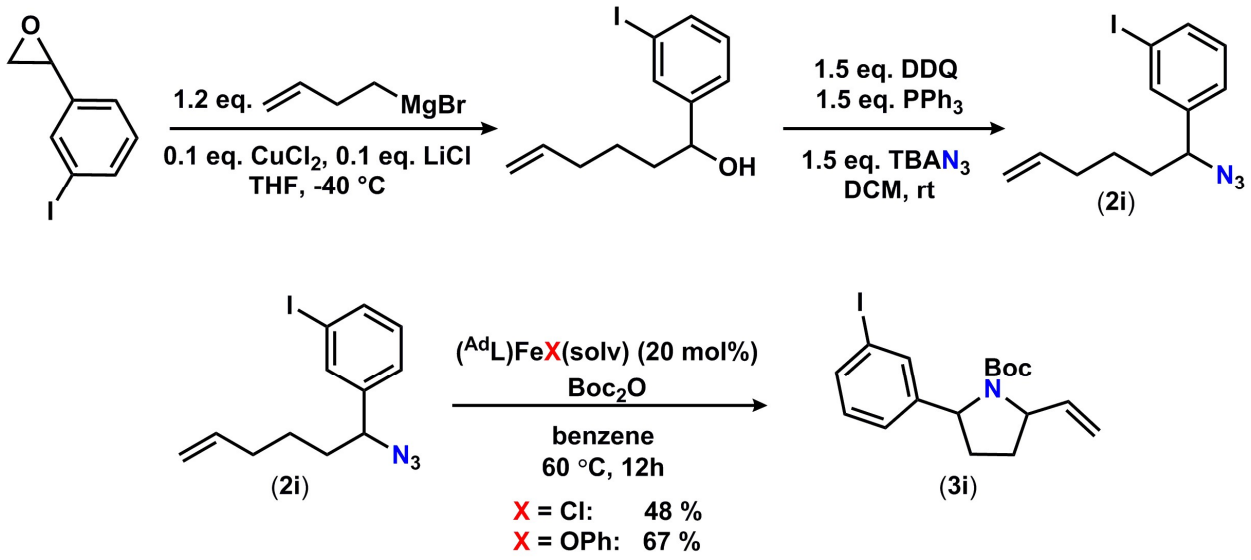


**3-iodostyrene:** Synthesized following procedure E. 67%. Spectroscopic data were consistent with reported values.[20]

**2-(3-iodophenyl)oxirane:** Synthesized following procedure C. 90%. **$^1$H NMR** (500 MHz, $CDCl_3$) δ: 7.60–7.66 (m, 2 H), 7.24 (d, *J* = 1.46 Hz, 1 H), 7.05–7.10 (m, 1 H), 3.79 (dd, *J* = 4.15, 2.69 Hz, 1 H), 3.14 (dd, *J* = 5.37, 3.91 Hz, 1 H), 2.75 (dd, *J* = 5.37, 2.44 Hz, 1 H). **$^{13}$C NMR** (125 MHz, $CDCl_3$) δ: 140.2, 137.4, 134.5, 130.3, 125.0, 94.5, 51.6, 51.4.

**1-(3-iodophenyl)hex-5-en-1-ol:** Synthesized following previously reported procedure.[6] 34% (25% depicted regioisomer). **$^1$H NMR** (500 MHz, $CDCl_3$) δ: 7.71 (t, *J* = 1.71 Hz, 1 H), 7.60 (dt, *J* = 7.81, 1.22 Hz, 1 H), 7.29 (d, *J* = 7.81 Hz, 1 H), 7.08 (t, *J* = 7.57 Hz, 1 H), 5.78 (dd, *J* = 17.09, 10.25 Hz, 1 H), 4.93–5.04 (m, 2 H), 4.59–4.65 (m, 1 H), 2.02–2.12 (m, 2 H), 1.82 (d, *J* = 3.42 Hz, 1 H), 1.65–1.80 (m, 2 H), 1.53 (dd, *J* = 7.57, 5.13 Hz, 1 H), 1.32–1.44 (m, 1 H). **$^{13}$C NMR** (125 MHz, $CDCl_3$) δ: 147.4, 138.7, 136.7, 135.1, 130.4, 125.3, 94.7, 115.0, 73.9, 38.7, 33.6, 25.1.

20. Hanagan, M. A.; Pasteris, R. J. 30 Jul 2009; Vol. 2009094407

**1-azido-1-(3-iodophenyl)-hex-5-en (2i):** Synthesized following procedure D. 54%. **$^1$H NMR** (600 MHz, $C_6D_6$) δ: 7.47–7.50 (m, 1 H), 7.32–7.38 (m, 1 H), 6.84 (d, *J* = 7.63 Hz, 1 H), 6.56 (t, *J* = 7.92 Hz, 1 H), 5.55 (s, 1 H), 4.89–4.96 (m, 2 H), 3.74 (dd, *J* = 7.92, 6.16 Hz, 1 H), 1.72 - 1.78 (m, 2 H), 1.38–1.46 (m, 1 H), 1.16–1.31 (m, 2 H), 1.00–1.09 (m, 1 H). **$^{13}$C NMR** (125 MHz, $C_6D_6$) δ: 142.8, 138.2, 137.4, 136.2, 130.6, 126.0, 115.2, 94.9, 65.5, 35.9, 33.4, 25.5. **GCMS** (EI) $t_R$ = 10.07 min *m/z*: 51, 63, 77, 89, 103, 115, 129, 144, 157, 172, 191, 207, 230, 245, 270, 284, 299, 327.

***tert*-butyl 2-(3-iodophenyl)-5-vinylpyrrolidine-1-carboxylate (3i): $^1$H NMR** (500 MHz, $C_6D_6$, 50 °C) δ (major diastereomer): 7.69 (s, 1 H), 7.38 (d, *J* = 7.81 Hz, 1 H), 7.11 (d, *J* = 7.81 Hz, 1 H), 6.68 (t, *J* = 7.57 Hz, 1 H), 5.82–5.95 (m, 1 H), 5.22 (d, *J* = 17.58 Hz, 1 H), 5.04 (d, *J* = 10.74 Hz, 1 H), 4.29–4.64 (m, 2 H), 1.61–1.72 (m, 1 H), 1.25–1.54 (m, 12H). **$^{13}$C NMR** (125 MHz, $C_6D_6$, 50 °C) δ: 154.6, 147.7, 139.9, 135.9, 130.2, 125.4, 115.1, 94.5, 79.4, 62.5, 61.0, 34.3, 30.3, 28.4. **HRMS** ($ESI^+$) *m/z* Calc. 422.0587 $[C_{17}H_{22}INO_2+Na]^+$, Found. 422.0605 $[M+Na]^+$.

**2-(3-iodophenyl)-5-vinylpyrrolidine: $^1$H NMR** (600 MHz, $C_6D_6$) δ (major diastereomer): 7.81 (br. s., 1 H), 7.36–7.40 (m, 1 H), 7.16 (d, *J* = 7.63 Hz, 1 H), 6.62–6.67 (m, 1 H), 5.75–5.83 (m, 1 H), 5.10 (d, *J* = 17.02 Hz, 1 H), 4.91 (d, *J* = 9.98 Hz, 1 H), 3.55 (t, *J* = 7.34 Hz, 1 H), 3.24 (q, *J* = 7.43 Hz, 1 H), 1.58–1.67 (m, 1 H), 1.49–1.57 (m, 1 H), 1.31–1.40 (m, 2 H).

**1D NOESY** (600 MHz, $C_6D_6$)

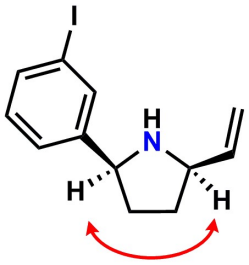


**4.37 % nOe**
**major**

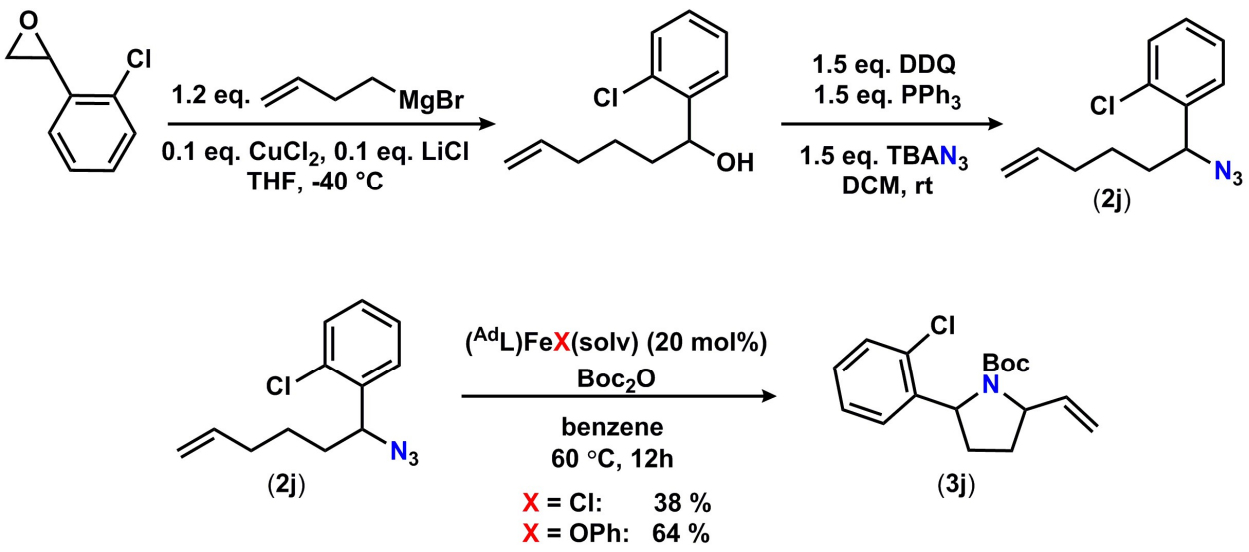


**2-(2-chlorophenyl)oxirane:** Synthesized following procedure B. Spectroscopic data were consistent with reported values.[21]

**1-(2-chlorophenyl)hex-5-en-1-ol:** Synthesized following previously reported procedure.[6] 52% (38% depicted regioisomer). **$^1$H NMR** (500 MHz, $C_6D_6$) δ: 7.55 (dd, *J* = 7.81, 1.46 Hz, 1 H), 7.27–7.34 (m, 2 H), 7.16–7.22 (m, 1 H), 5.81 (ddt, *J* = 16.85, 10.25, 6.71, 6.71 Hz, 1 H), 5.14 (dt, *J* = 8.06, 4.27 Hz, 1 H), 4.92–5.05 (m, 2 H), 2.07–2.14 (m, 2 H), 1.91 (d, *J* = 3.91 Hz, 1 H), 1.69–1.84 (m, 2 H), 1.57–1.66 (m, 1 H), 1.45–1.54 (m, 1 H). **$^{13}$C NMR** (125 MHz, $CDCl_3$) δ:142.3, 138.7, 132.0, 129.5, 128.5, 127.3, 127.2, 114.9, 70.8, 37.2, 33.7, 25.2.

**1-azido-1-(2-chlorophenyl)-hex-5-en (2j):** Synthesized following procedure D. 86%. **$^1$H NMR** (500 MHz, $C_6D_6$) δ: 7.18–7.23 (m, 1 H), 7.06–7.09 (m, 1 H), 6.82–6.87 (m, 1 H), 6.68–6.73 (m, 1 H), 5.56–5.66 (m, 1 H), 4.86–4.98 (m, 3 H), 1.79–1.86 (m, 2 H), 1.52–1.59 (m, 2 H), 1.32–1.44 (m, 1 H), 1.18–1.29 (m, 1 H). **$^{13}$C NMR** (125 MHz, $CDCl_3$) δ: 138.6, 138.5, 133.5, 130.3, 129.5,

21. Piccinini, A.; Kavanagh, S. A.; Connon, P. B.; Connon, S. J. *Org. Lett.* **2010**, *12*, 608.

127.8, 127.5, 115.5, 62.8, 35.4, 33.8, 25.8. **GCMS** (EI) $t_R$ = 8.68 min *m/z*: 51, 63, 77, 89, 103, 115, 125, 138/140, 144, 155, 172, 192, 207/209.

***tert*-butyl 2-(2-chlorophenyl)-5-vinylpyrrolidine-1-carboxylate (3j): $^1$H NMR** (500 MHz, $C_6D_6$, 50 °C) δ: 7.41–7.48 (m, 1 H), 7.14–7.21 (m, 1 H), 6.93–7.02 (m, 1 H), 6.74–6.84 (m, 1 H), 5.96–6.11 (m, 1 H), 5.20–5.41 (m, 2 H), 5.08 (dd, *J* = 10.25, 0.98 Hz, 1 H), 4.43 (br. s., 1 H), 1.99–2.13 (m, 2 H), 1.21–1.59 (m, 11 H). **$^{13}$C NMR** (125 MHz, $C_6D_6$, 50 °C) δ: 154.9, 143.1, 134.2, 132.9, 130.0, 127.4, 127.3, 115.5, 79.6, 61.5, 61.0, 33.1, 30.4, 28.7. **HRMS** ($ESI^+$) *m/z* Calc. 308.1412 $[C_{17}H_{22}ClNO_2+H]^+$, Found. 308.1423 $[M+H]^+$.

**2-(2-chlorophenyl)-5-vinylpyrrolidine: $^1$H NMR** (600 MHz, $C_6D_6$) δ: 7.91 (dd, *J* = 7.63, 1.76 Hz, 1 H), 7.20 (dd, *J* = 7.63, 1.17 Hz, 1 H), 6.99–7.04 (m, 1 H), 6.81 (td, *J* = 7.63, 1.76 Hz, 1 H), 5.90 (ddd, *J* = 17.31, 10.27, 7.04 Hz, 1 H), 5.15–5.20 (m, 1 H), 4.96–5.00 (m, 1 H), 4.39–4.44 (m, 1 H), 3.29–3.35 (m, 1 H), 2.09–2.17 (m, 1 H), 1.58–1.64 (m, 1 H), 1.39–1.50 (m, 2 H).

**1D NOESY** (600 MHz, $C_6D_6$)

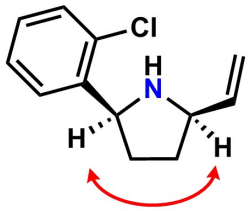


**0.53 % nOe**
**major**

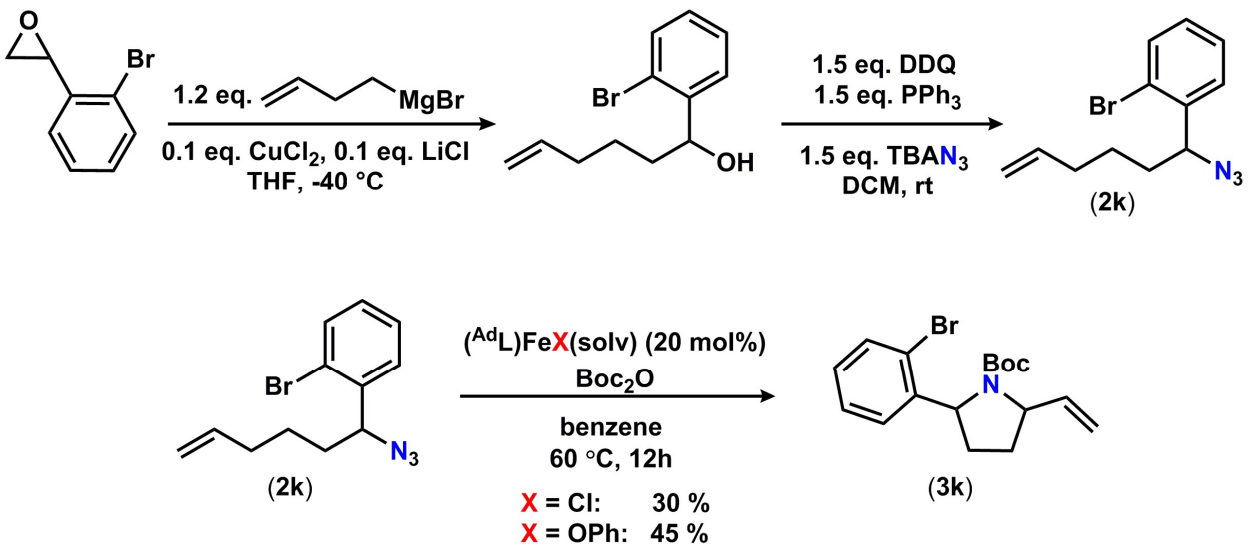


**2-(2-bromophenyl)oxirane:** Synthesized following procedure B. Spectroscopic data were consistent with reported values.[22]

**1-(2-bromophenyl)hex-5-en-1-ol:** Synthesized following previously reported procedure.[6] 53% (37% depicted regioisomer). **$^1$H NMR** (500 MHz, $C_6D_6$) δ: 7.48–7.57 (m, 2 H), 7.31–7.36 (m, 1 H), 7.12 (td, *J* = 7.78, 1.83 Hz, 1 H), 5.81 (ddt, *J* = 17.17, 10.30, 6.64, 6.64 Hz, 1 H), 5.08 (dd, *J* = 8.24, 4.12 Hz, 1 H), 4.93–5.05 (m, 2 H), 2.08–2.17 (m, 2 H), 2.02 (br. s., 1 H), 1.75–1.85 (m, 1 H), 1.58–1.75 (m, 2 H), 1.46–1.57 (m, 1 H). **$^{13}$C NMR** (125 MHz, $C_6D_6$) δ: 143.9, 138.7, 132.8, 128.9, 127.9, 127.4, 122.1, 114.8, 72.9, 37.3, 33.6, 25.2.

**1-azido-1-(2-bromophenyl)-hex-5-en (2k):** Synthesized following procedure D. 85%. **$^1$H NMR** (500 MHz, $C_6D_6$) δ: 7.25–7.29 (m, 1 H), 7.20 (dd, *J* = 7.78, 1.37 Hz, 1 H), 6.85–6.90 (m, 1 H), 6.59–6.65 (m, 1 H), 5.57–5.67 (m, 1 H), 4.87–4.98 (m, 3 H), 1.81–1.89 (m, 2 H), 1.51–1.59 (m, 2 H), 1.34–1.44 (m, 1 H), 1.22–1.33 (m, 1 H). **$^{13}$C NMR** (125 MHz, $C_6D_6$) δ: 140.1, 138.36 133.6,

22. Akgun, E.; Glinski, M. B.; Dhawan, K. L.; Durst, T. *J. Org. Chem.* **1981**, *46*, 2730

129.9, 128.5, 128.4, 123.9, 115.5, 65.2, 35.6, 33.8, 25.8. **GCMS** (EI) $t_R$ = 9.19 min *m/z*: 51, 63, 77, 89, 103, 115, 128/130, 144, 157, 172, 180/182, 194/196, 208/210, 222/224, 236/238, 251/253.

***tert*-butyl 2-(2-bromophenyl)-5-vinylpyrrolidine-1-carboxylate (3k): $^1$H NMR** (500 MHz, $C_6D_6$, 50 °C) δ(mixture of rotamers): 7.42 (d, *J* = 7.81 Hz, 1 H), 7.36 (dd, *J* = 8.30, 0.98 Hz, 1 H), 6.95–7.01 (m, 1 H), 6.67–6.72 (m, 1 H), 5.97–6.09 (m, 1 H), 5.25 (d, *J* = 15.63 Hz, 2 H), 5.08 (d, *J* = 10.25 Hz, 1 H), 4.42 (br. s., 1 H), 2.01–2.11 (m, 2 H), 1.21–1.56 (m, 11 H). **$^{13}$C NMR** (125 MHz, $C_6D_6$, 50 °C) δ (mixture of rotamers): 154.9, 144.9, 140.2, 133.3, 128.6, 127.9, 127.5, 123.1, 115.6, 79.6, 63.4, 61.6, 33.3, 30.3, 28.7. **GCMS** (EI) $t_R$ = 10.68 min (major diastereomer) *m/z*: 57, 68, 82, 96, 115, 128, 144, 156, 169/171, 182/184, 195, 216, 223/225, 235/237, 250/252, 295/297. **HRMS** (ESI$^+$) *m/z* Calc. 374.0726 $[C_{17}H_{22}BrNO_2+Na]^+$, Found. 374.0739 $[M+Na]^+$.

**2-(2-bromophenyl)-5-vinylpyrrolidine: $^1$H NMR** (600 MHz, $C_6D_6$) δ: 7.88 (dd, *J* = 7.63, 1.76 Hz, 1 H), 7.38 (d, *J* = 7.63 Hz, 1 H), 7.04 (t, *J* = 7.92 Hz, 1 H), 6.70–6.74 (m, 1 H), 5.90 (ddd, *J* = 17.31, 10.27, 7.04 Hz, 1 H), 5.14–5.19 (m, 1 H), 4.94–4.99 (m, 1 H), 4.38–4.43 (m, 1 H), 3.33 (q, *J* = 7.63 Hz, 1 H), 2.08–2.14 (m, 1 H), 1.55–1.61 (m, 1 H), 1.40–1.50 (m, 2 H).

**1D NOESY** (600 MHz, $C_6D_6$)

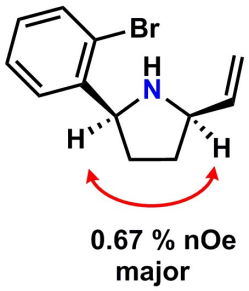

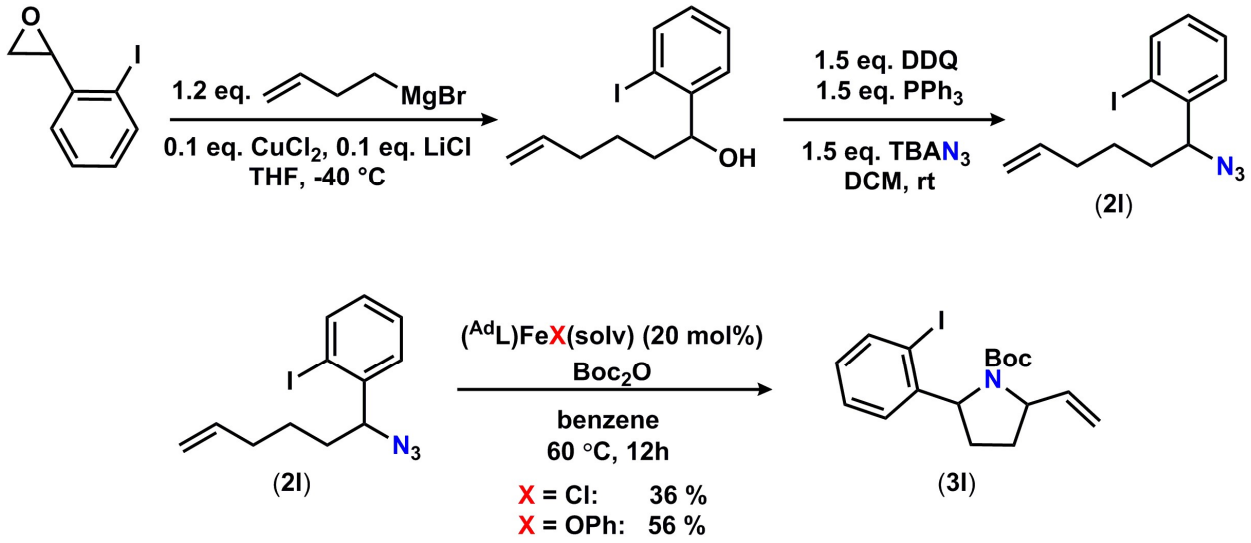


**2-iodostyrene:** Synthesized following procedure E. 43%. Spectroscopic data were consistent with reported values.[23]

**2-(2-iodophenyl)oxirane:** Synthesized following procedure C. Spectroscopic data were consistent with reported values.[24]

**1-(2-iodophenyl)hex-5-en-1-ol:** Synthesized following previously reported procedure.[6] 44% (20% depicted regioisomer). **$^1$H NMR** (500 MHz, $CDCl_3$) δ: 7.80 (d, *J* = 8.30 Hz, 1 H), 7.51 (dd, *J* = 7.57, 1.71 Hz, 1 H), 7.34–7.41 (m, 1 H), 6.97 (td, *J* = 7.57, 1.46 Hz, 1 H), 5.76–5.89 (m, 1 H), 4.84–5.08 (m, 4 H), 2.08–2.19 (m, 2 H), 1.96 (br. s., 1 H), 1.60–1.83 (m, 5 H), 1.48–1.57 (m, 5 H). **$^{13}$C NMR** (125 MHz, $CDCl_3$) δ: 146.8, 139.5, 138.7, 129.3, 128.7, 127.1, 114.9, 97.8, 75.7, 37.5, 33.7, 25.3.

**1-azido-1-(2-iodophenyl)-hex-5-en (2l):** Synthesized following procedure D. 53%. **$^1$H NMR** (500 MHz, $C_6D_6$) δ: 7.53–7.58 (m, 1 H), 7.14 (d, *J* = 1.76 Hz, 1 H), 6.91 (t, *J* = 7.63 Hz, 1 H),

23. Acheson, R. M.; Lee, G. C. M. *J. Chem. Soc. Perkin Trans. I* **1987**, 2321.
24. Eustache, J.; Van de Weghe, P.; Le Nouen, D.; Uyehara, H.; Kabuto, C.; Yamamoto, Y. *J. Org. Chem.* **2005**, *70*, 4043.

6.43–6.50 (m, 1 H), 5.63 (d, *J* = 7.04 Hz, 1 H), 4.92–5.00 (m, 2 H), 4.79 (dd, *J* = 7.92, 6.16 Hz, 1 H), 1.80–1.90 (m, 2 H), 1.49–1.57 (m, 2 H), 1.38–1.46 (m, 1 H), 1.21–1.34 (m, 1 H). **$^{13}$C NMR** (125 MHz, $C_6D_6$) δ: 142.8, 140.0, 138.3, 129.8, 128.9, 127.7, 115.2, 99.5, 69.5, 35.6, 33.5, 25.6. **GCMS** (EI) $t_R$ = 9.76 min *m/z*: 51, 77, 90, 103, 115, 129, 144, 157, 172, 217, 230, 256, 270, 299.

***tert*-butyl 2-(2-iodophenyl)-5-vinylpyrrolidine-1-carboxylate (3l): $^{1}$H NMR** (500 MHz, $C_6D_6$, 50 °C) δ: 7.65 (d, *J* = 7.81 Hz, 1 H), 7.38 (d, *J* = 7.81 Hz, 1 H), 7.02 (t, *J* = 7.57 Hz, 1 H), 6.54 (t, *J* = 7.32 Hz, 1 H), 5.97–6.10 (m, 1 H), 5.26 (d, *J* = 17.58 Hz, 1 H), 5.08 (d, *J* = 10.25 Hz, 2 H), 4.44 (br. s., 1 H), 2.04–2.12 (m, 1 H), 1.21–1.54 (m, 12 H). **$^{13}$C NMR** (125 MHz, $C_6D_6$) δ: 154.5, 147.2, 139.9, 139.6, 128.5, 127.6, 126.7, 115.2, 98.2, 79.2, 67.8, 61.4, 33.1, 30.2, 28.4. **HRMS** ($ESI^+$) *m/z* Calc. 821.1283 $[(C_{17}H_{22}INO_2)_2+Na]^+$, Found. 821.1270 $[2M+Na]^+$.

**2-(2-iodophenyl)-5-vinylpyrrolidine: $^{1}$H NMR** (500 MHz, $C_6D_6$) δ: 7.83 (dd, *J* = 7.92, 1.47 Hz, 1 H), 7.63–7.69 (m, 1 H), 7.04–7.10 (m, 1 H), 6.56 (td, *J* = 7.63, 1.76 Hz, 1 H), 5.89 (ddd, *J* = 17.17, 10.12, 7.34 Hz, 1 H), 5.11–5.19 (m, 1 H), 4.95 (dd, *J* = 9.98, 1.17 Hz, 1 H), 4.28 (t, *J* = 7.34 Hz, 1 H), 3.33 (d, *J* = 8.22 Hz, 1 H), 2.12 (d, *J* = 4.70 Hz, 1 H), 1.54–1.61 (m, 1 H), 1.37–1.48 (m, 2 H).

**1D NOESY** (600 MHz, $C_6D_6$)

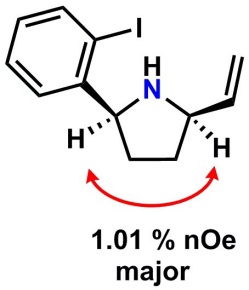

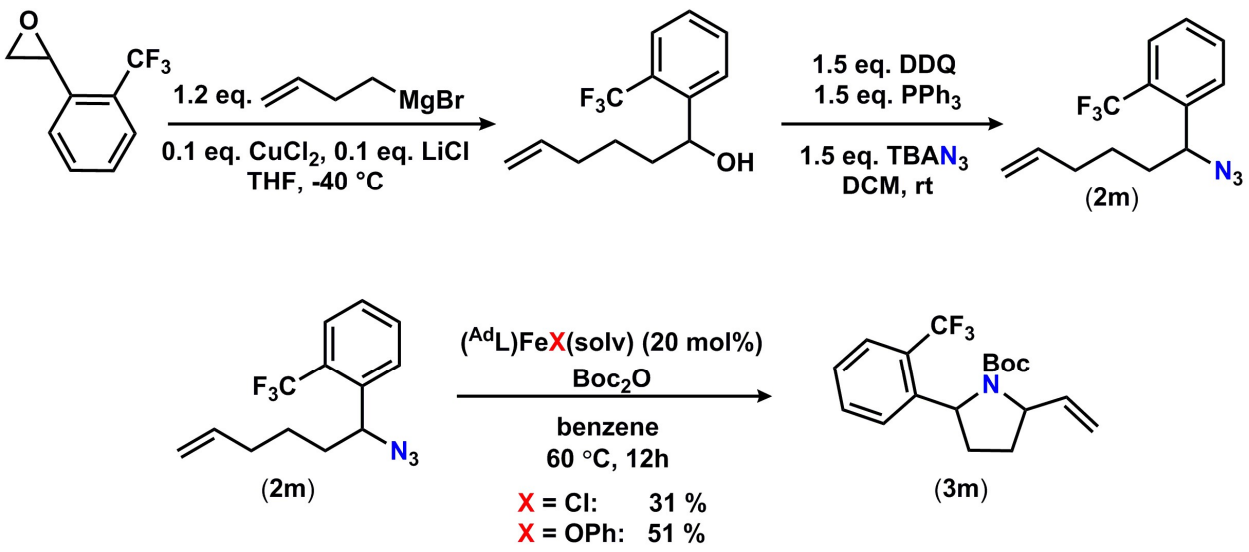


**2-(2-(trifluoromethyl)phenyl)oxirane:** Synthesized following procedure B. Spectroscopic data were consistent with reported values.[25]

**1-(2-(trifluoromethyl)phenyl)hex-5-en-1-ol:** Synthesized following previously reported procedure.[6] 44%. **$^1$H NMR** (500 MHz, $C_6D_6$) δ: 7.77 (d, *J* = 7.78 Hz, 1 H), 7.55–7.63 (m, 2 H), 7.37 (t, *J* = 7.78 Hz, 1 H), 5.80 (ddt, *J* = 17.11, 10.36, 6.64, 6.64 Hz, 1 H), 5.08–5.15 (m, 1 H), 4.91–5.04 (m, 2 H), 2.06–2.14 (m, 2 H), 1.95 (d, *J* = 2.29 Hz, 1 H), 1.62–1.81 (m, 3 H), 1.42–1.53 (m, 1 H). **$^{13}$C NMR** (125 MHz, $C_6D_6$) δ: 144.2, 138.6, 132.4, 127.7, 127.5, 127.0, 125.5 (q), 123.4, 114.9, 69.5, 38.8, 33.6, 25.5.

**1-azido-1-(2-trifluoromethylphenyl)-hex-5-en (2m):** Synthesized following procedure D. 58%. **$^1$H NMR** (500 MHz, $C_6D_6$) δ: 7.29 (d, *J* = 3.21 Hz, 2 H), 6.96–7.03 (m, 1 H), 6.72–6.79 (m, 1 H), 5.55–5.65 (m, 1 H), 4.85–4.98 (m, 3 H), 1.82 (m, 2 H), 1.34–1.61 (m, 2 H), 1.12–1.22 (m, 2 H). **$^{13}$C NMR** (125 MHz, $C_6D_6$) δ: 140.0, 138.5, 133.0, 128.8, 128.7, 128.5, 126.3, 126.1 (q, *J* = 5.5

25. Deregnaucourt, J.; Archelas, A.; Barbirato, F.; Paris, J. M.; Furstoss, R. *Adv. Synth. Catal.* **2007**, *349*, 1405.

Hz), 115.5, 61.9, 36.9, 33.8, 26.1. **GCMS** (EI) $t_R$ = 7.73 min *m/z*: 51, 68, 77, 87, 96, 107, 122, 135, 144, 159, 172, 186, 198, 212, 222, 241.

***tert*-butyl 2-(2-trifluoromethylphenyl)-5-vinylpyrrolidine-1-carboxylate (3m): $^1$H NMR** (500 MHz, $C_6D_6$, 50 °C) δ (mixture of rotamers): 7.60 (d, *J* = 7.81 Hz, 1 H), 7.43 (d, *J* = 7.81 Hz, 1 H), 7.12 (t, *J* = 7.57 Hz, 1 H), 6.86 (t, *J* = 7.32 Hz, 1 H), 6.02–6.12 (m, 1 H), 5.28 (d, *J* = 17.09 Hz, 1 H), 5.21 (br. s., 1 H), 5.07–5.13 (m, 1 H), 4.46 (br. s., 1 H), 1.98–2.06 (m, 2 H), 1.21–1.52 (m, 11 H). **$^{13}$C NMR** (125 MHz, $C_6D_6$, 50 °C) δ (mixture of rotamers): 154.7, 145.6, 139.8, 132.5, 128.7, 127.3, 126.9, 126.2 (m), 115.6, 79.7, 61.2, 60.2, 35.6, 30.1, 28.6. **GCMS** (EI) $t_R$ = 9.12 min (major diastereomer) *m/z*: 57, 68, 82, 96, 113, 134, 159, 163, 172, 192, 213, 226, 241, 268, 285, 341. **HRMS** (ESI$^+$) *m/z* Calc. 342.1675 $[C_{18}H_{22}F_3NO_2+H]^+$, Found. 342.1672 $[M+H]^+$.

**2-(2-trifluoromethylphenyl)-5-vinylpyrrolidine: $^1$H NMR** (600 MHz, $C_6D_6$) δ: 8.06 (d, *J* = 7.63 Hz, 1 H), 7.39 (d, *J* = 7.63 Hz, 1 H), 7.13–7.17 (m, 4 H), 6.84 (t, *J* = 7.63 Hz, 1 H), 5.89 (ddd, *J* = 17.02, 9.98, 7.04 Hz, 1 H), 5.13 (d, *J* = 17.02 Hz, 1 H), 4.93 (d, *J* = 9.98 Hz, 1 H), 4.53 (t, *J* = 7.34 Hz, 1 H), 3.31 (q, *J* = 7.63 Hz, 1 H), 1.93–2.00 (m, 1 H), 1.42–1.58 (m, 3 H).

**1D NOESY** (600 MHz, $C_6D_6$)

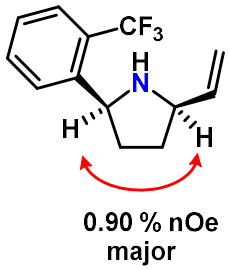


**0.90 % nOe**
**major**

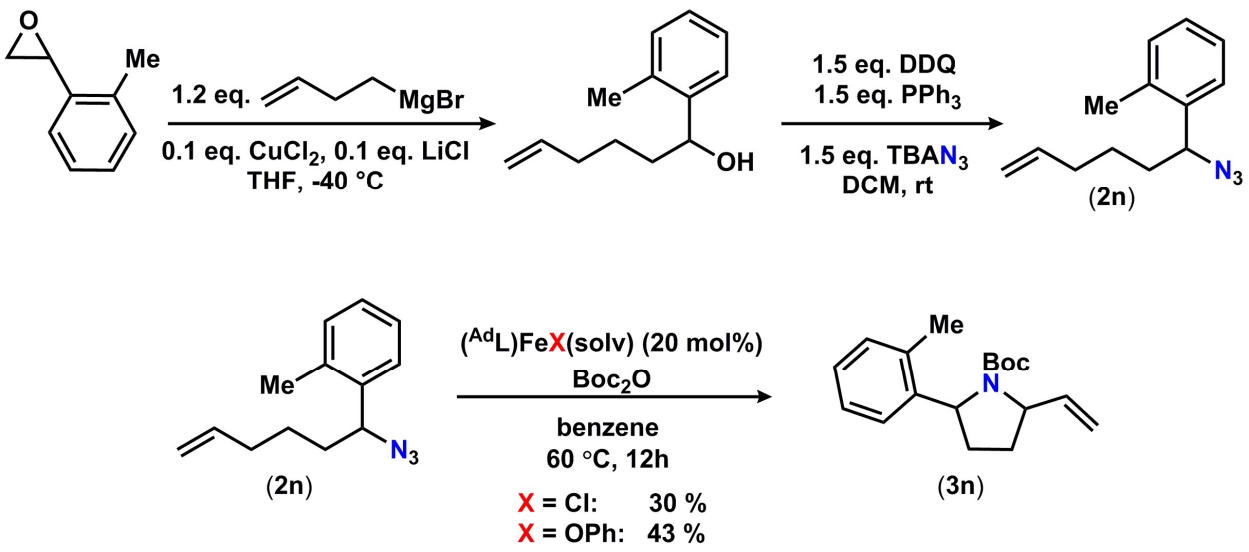


**2-(*o*-tolyl)oxirane:** Synthesized following procedure B. Spectroscopic data were consistent with reported values.[26]

**1-(*o*-tolyl)hex-5-en-1-ol:** Synthesized following previously reported procedure.[6] 42% (14% depicted regioisomer). **$^1$H NMR** (600 MHz, $CDCl_3$) δ: 7.47 (d, *J* = 7.63 Hz, 1 H), 7.23 (t, *J* = 7.34 Hz, 1 H), 7.17 (td, *J* = 7.34, 1.76 Hz, 1 H), 7.12–7.15 (m, 1 H), 5.76–5.85 (m, 1 H), 4.92–5.03 (m, 3 H), 2.34 (s, 3 H), 2.07–2.13 (m, 2 H), 1.69–1.79 (m, 2 H), 1.57–1.67 (m, 1 H), 1.42–1.51 (m, 1 H). **$^{13}$C NMR** (125 MHz, $CDCl_3$) δ: 143.1, 138.7, 134.6, 130.5, 127.3, 126.4, 125.2, 114.9, 70.7, 37.7, 33.8, 25.4, 19.2.

**1-azido-1-(2-methylphenyl)-hex-5-en (2n):** Synthesized following procedure D. 49%. **$^1$H NMR** (500 MHz, $C_6D_6$) δ: 7.26 (d, *J* = 7.81 Hz, 1 H), 6.98–7.07 (m, 2 H), 6.91–6.96 (m, 1 H), 5.56–5.69 (m, 1 H), 4.91–4.98 (m, 2 H), 4.36–4.42 (m, 1 H), 2.02 (s, 3 H), 1.80–1.86 (m, 2 H), 1.58–1.69 (m, 1 H), 1.44–1.54 (m, 1 H), 1.31–1.42 (m, 1 H), 1.15–1.27 (m, 1 H). **$^{13}$C NMR** (125

26. Bhor, S.; Anilkumar, G.; Tse, M. K.; Klawonn, M.; Dobler, C.; Bitterlich, B.; Grotevendt, A.; Beller, M. *Org. Lett.* **2005**, *7*, 3393

MHz, $C_6D_6$) δ: 138.7, 138.5, 135.9, 131.3, 128.7, 127.1, 126.9, 115.4, 62.9, 35.3, 33.9, 26.2, 19.5. **GCMS** (EI) $t_R$ = 8.45 min *m/z*: 51, 65, 77, 91, 103, 117, 130, 144, 158, 172, 186.

***tert*-butyl 2-(*o*-tolyl)-5-vinylpyrrolidine-1-carboxylate (3n): $^1$H NMR** (500 MHz, $C_6D_6$, 50 °C) δ (major diastereomer): 7.46 (d, *J* = 7.81 Hz, 1 H), 7.12 (t, *J* = 7.32 Hz, 1 H), 6.97–7.04 (m, 2 H), 6.12 (ddd, *J* = 17.34, 10.50, 6.35 Hz, 1 H), 5.29 (d, *J* = 17.58 Hz, 1 H), 5.11 (d, *J* = 10.25 Hz, 1 H), 4.96 (br. s., 1 H), 4.45 (br. s., 1 H), 2.18 (s, 3 H), 1.82 (dd, *J* = 12.45, 6.10 Hz, 1 H), 1.40–1.59 (m, 5 H), 1.28 (br. s., 9 H). **HRMS** ($ESI^+$) *m/z* Calc. 310.1778 $[C_{18}H_{25}NO_2+Na]^+$, Found. 310.1791 $[M+Na]^+$.

**2-(*o*-tolyl)-5-vinylpyrrolidine: $^1$H NMR** (500 MHz, $C_6D_6$) δ (major diastereomer): 7.76 (d, *J* = 7.63 Hz, 1 H), 7.12 (t, *J* = 7.34 Hz, 1 H), 7.00 (t, *J* = 7.63 Hz, 1 H), 6.92 (d, *J* = 7.63 Hz, 1 H), 5.85 (ddd, *J* = 17.46, 9.83, 7.92 Hz, 1 H), 5.07 (d, *J* = 17.02 Hz, 1 H), 4.78 (d, *J* = 9.98 Hz, 1 H), 4.23–4.31 (m, 1 H), 3.48 (q, *J* = 7.83 Hz, 1 H), 2.18 (s, 3 H), 1.61–1.71 (m, 3 H), 1.51 (dt, *J* = 13.21, 6.90 Hz, 1 H).

**1D NOESY** (600 MHz, $C_6D_6$)

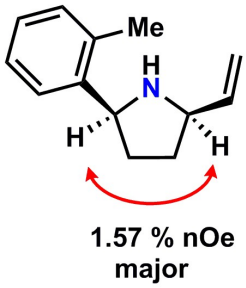

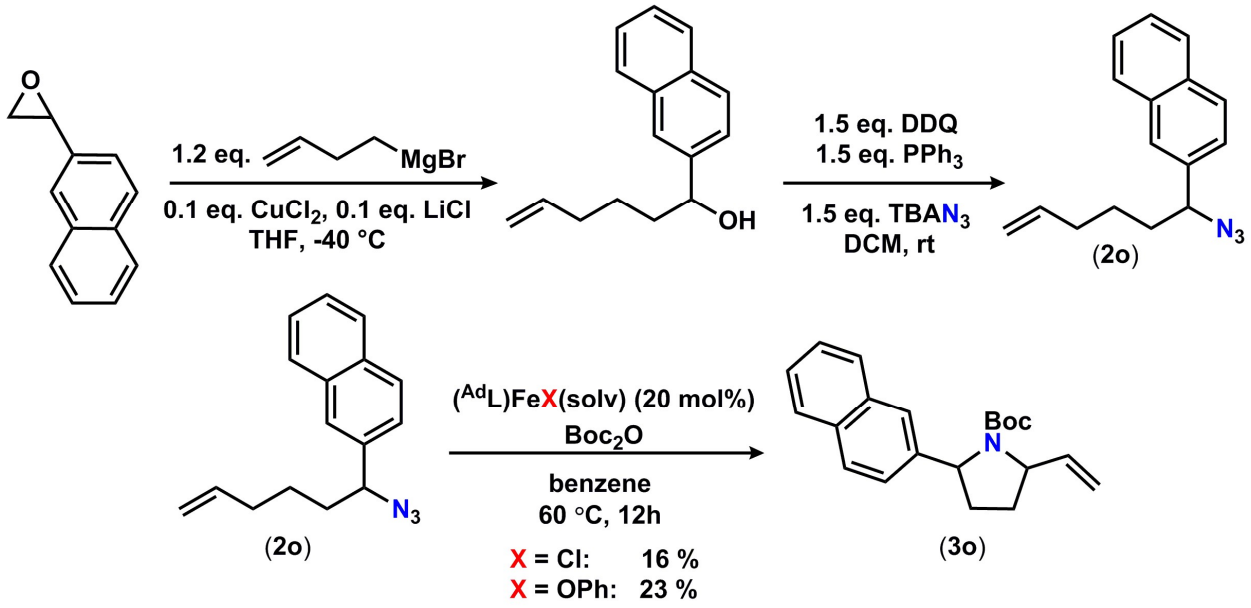


**2-(naphthalen-2-yl)oxirane:** Synthesized following procedure B. Spectroscopic data were consistent with reported values.[27]

**1-(naphthalen-2-yl)hex-5-en-1-ol:** Synthesized following previously reported procedure.[6] 24% (19% depicted regioisomer). **$^1$H NMR** (500 MHz, $CDCl_3$) δ: 7.80–7.87 (m, 3 H), 7.78 (s, 1 H), 7.45–7.52 (m, 3 H), 5.78 (ddt, *J* = 16.99, 10.25, 6.69, 6.69 Hz, 1 H), 4.91–5.05 (m, 2 H), 4.81–4.89 (m, 1 H), 2.09 (q, *J* = 7.42 Hz, 2 H), 1.76–1.97 (m, 2 H), 1.50–1.63 (m, 2 H), 1.34–1.47 (m, 1 H). **$^{13}$C NMR** (125 MHz, $CDCl_3$) δ: 142.3, 138.7, 133.4, 133.1, 128.5, 128.1, 127.8, 126.3, 126.0, 124.7, 124.2, 114.9, 74.8, 38.5, 33.8, 25.2.

**1-azido-1-(naphthalen-2-yl)-hex-5-en (2o):** Synthesized following procedure D. 46%. **$^1$H NMR** (500 MHz, $C_6D_6$) δ: 7.56–7.64 (m, 3 H), 7.49 (s, 1 H), 7.20–7.27 (m, 3 H), 5.58–5.67 (m, 1 H), 4.91– 4.98 (m, 2 H), 4.17 (t, *J* = 7.04 Hz, 1 H), 1.82–1.88 (m, 2 H), 1.66–1.75 (m, 1 H), 1.52–1.61 (m, 1 H), 1.30–1.39 (m, 1 H), 1.14–1.30 (m, 1 H). **$^{13}$C NMR** (125 MHz, $C_6D_6$) δ: 138.7, 137.9,

27. Robinson, M. W. C.; Davies, M.; Buckle, R.; Mabbett, I.; Taylor, S. H.; Graham, A. E. *Org. Biomol. Chem.* **2009**, *7*, 2559.

134.1, 134.0, 129.5, 128.7, 127.9, 127.0, 126.8, 126.7, 125.0, 115.5, 67.1, 36.2, 33.9, 26.1. **GCMS** (EI) $t_R$ = 11.25 min *m/z*: 51, 63, 76, 90, 115, 127, 141, 154, 165, 180, 194, 208, 223.

***tert*-butyl 2-(naphthalen-2-yl)-5-vinylpyrrolidine-1-carboxylate (3o): $^1$H NMR** (500 MHz, $C_6D_6$, 50 °C) δ (major diastereomer): 7.69 (s, 1 H), 7.57–7.66 (m, 3 H), 7.37 (d, *J* = 8.79 Hz, 1 H), 7.17–7.26 (m, 3 H), 5.98–6.10 (m, 1 H), 5.28 (d, *J* = 17.58 Hz, 1 H), 5.09 (d, *J* = 10.25 Hz, 1 H), 4.90 (br. s., 1 H), 4.46 (br. s., 1 H), 1.77–1.87 (m, 1 H), 1.64–1.72 (m, 1 H), 1.54–1.64 (m, 1 H), 1.46–1.54 (m, 1 H), 1.24 (br. s., 9 H). **$^{13}$C NMR** (125 MHz, $C_6D_6$, 50 °C) δ: 155.2, 142.8, 140.6, 134.4, 133.6, 128.7, 128.5, 128.3, 126.6, 126.0, 125.5, 125.2, 115.4, 79.5, 63.7, 61.6, 34.8, 30.8, 28.8. **HRMS** ($ESI^+$) *m/z* Calc. 324.1958 $[C_{21}H_{25}NO_2+H]^+$, Found. 324.1958 $[M+H]^+$; Calc. 346.1778 $[C_{21}H_{25}NO_2+Na]^+$, Found. 374.1772 $[M+Na]^+$.

**2-(naphthalen-2-yl)-5-vinylpyrrolidine: $^1$H NMR** (600 MHz, $C_6D_6$) δ (major diastereomer): 7.87 (s, 1 H), 7.71–7.74 (m, 1 H), 7.61 (t, *J* = 8.80 Hz, 2 H), 7.55 (dd, *J* = 8.51, 1.47 Hz, 1 H), 7.22–7.28 (m, 2 H), 5.75–5.86 (m, 1 H), 5.03 (d, *J* = 17.02 Hz, 1 H), 4.68 (br. s., 1 H), 4.04 (t, *J* = 8.51 Hz, 1 H), 3.43 (d, *J* = 7.63 Hz, 1 H), 1.73–1.80 (m, 2 H), 1.56–1.62 (m, 2 H).

**1D NOESY** (600 MHz, $C_6D_6$)

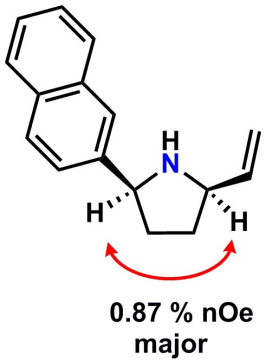

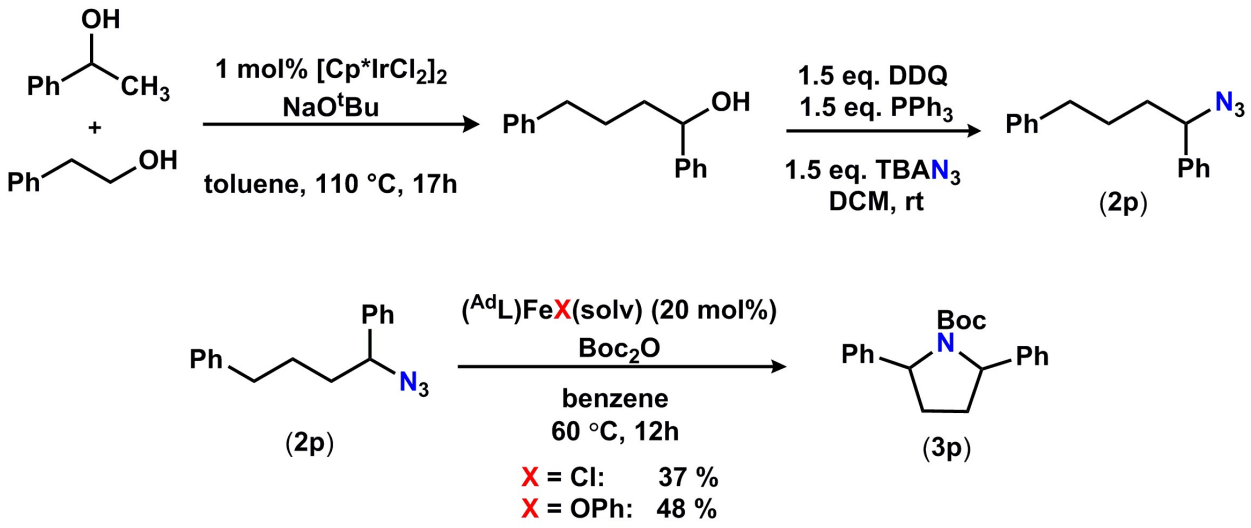


**1,4-diphenylbutan-1-ol:** Synthesized following literature procedure. Spectroscopic data were consistent with reported values.[28]

**(1-azidobutane-1,4-diyl)benzene (2p):** Synthesized following procedure D. 59%. **$^1$H NMR** (600 MHz, $C_6D_6$) δ: 7.12–7.15 (m, 2 H), 6.99–7.09 (m, 6 H), 6.95–6.98 (m, 2 H), 3.97 (dd, *J* = 7.63, 6.46 Hz, 1 H), 2.31–2.35 (m, 2 H), 1.59–1.66 (m, 1 H), 1.45–1.58 (m, 2 H), 1.3–1.41 (m, 1 H). **$^{13}$C NMR** (125 MHz, $C_6D_6$) δ: 142.4, 140.5, 129.3, 129.02, 129.0, 127.6, 127.5, 126.6, 66.8, 36.3, 36.0, 28.6. **GCMS** (EI) $t_R$ = 9.12 min *m/z*: 51, 65, 77, 91, 104, 119, 132, 146, 165, 178, 194, 208, 222, 234, 253,

***tert*-butyl 2,5-diphenylpyrrolidine-1-carboxylate**[29]**: $^1$H NMR** (500 MHz, $C_6D_6$, 50 °C) δ (major diastereomer): 7.40 (br. s., 4 H), 7.17–7.21 (m, 4 H), 7.04–7.09 (m, 2 H), 4.94 (br. s., 2 H), 1.74–1.88 (m, 4 H), 1.16–1.26 (m, 9 H). **$^{13}$C NMR** (125 MHz, $C_6D_6$, 50 °C) δ: 156.1, 144.9, 128.8, 127.4, 127.3, 79.6, 63.8, 34.0, 28.7. **GCMS** (EI) $t_R$ = 12.67 min *m/z*: 57, 77, 91, 104, 117,

28. Fujita, K. I.; Asai, C.; Yamaguchi, T.; Hanasaka, F.; Yamaguchi, R. *Org. Lett.* **2005**, 4017..
29. Durant, G. J.; Maillard, M.; Guo, J. Q. 1998; Vol. WO 9806401 A1 19980219.

129, 146, 163, 195, 207, 222, 250, 267. **HRMS** ($ESI^+$) *m/z* Calc. 324.1958 $[C_{18}H_{25}NO_2+H]^+$, Found. 324.1964 $[M+H]^+$.

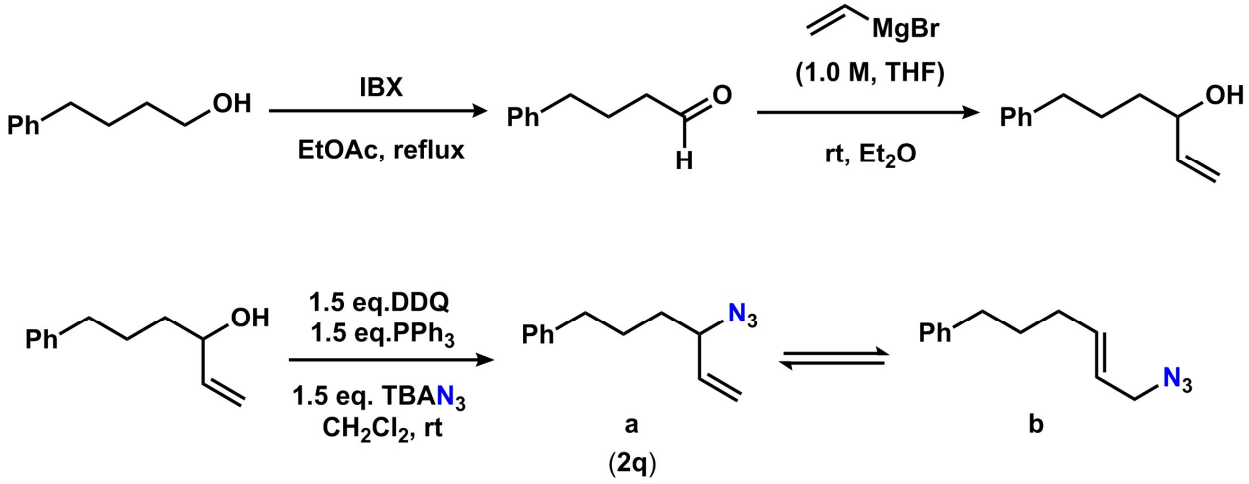


**4-phenylbutyraldehyde:** A solution of 4-phenylbutan-1-ol (1.0 equiv) and IBX (3.0 equiv) in ethyl acetate was heated to reflux for 4 hours. The reaction mixture was then allowed to cool to room temperature and the insoluble material was filtered through a medium porosity frit and the solvent was removed *in vacuo* to isolate a colorless oil. 100%. Spectroscopic data were consistent with reported values.[30]

**6-phenylhex-1-en-3-ol:** Synthesized following literature procedure.[31] The isolated product was further purified via silica gel chromatography with 15:1 hexanes:EtOAc. 41%. Spectroscopic data were consistent with reported values. [31]

**4-azido-1-phenyl-hex-5-en (2q):** Synthesized following procedure D. 79%. Note: allylic azides are known to quickly isomerize and exist as a mixture of regioisomers in equilibrium (Gagneux, A.; Winstein, S.; Young, W. G. *J. Am. Chem. Soc.* **1960**, *82*, 5956). Due to the presence of the two isomers and the complexity of the resulting reaction mixtures, no yield is reported for the

30. Colbon, P.; Ruan, J.; Purdie, M.; Mulholland, K.; Xiao, J. *Org. Lett.* **2011**, *13*, 5456.
31. De Greef, M.; Zard, S. Z. *Org. Lett.* **2007**, *9*, 1773.

cyclization to 2-phenyl-5-vinylpyrrolidine-1-carboxylate. The product was identified through comparison with the product formed upon reaction with (1-azidohex-5-en-1-y)benzene. **$^1$H NMR** (500 MHz, $CDCl_3$) δ: 7.26–7.31 (m, 4 H, **a** and **b**), 7.15–7.24 (m, 6 H, **a** and **b**), 5.67–5.82 (m, 2 H, **b**), 5.50–5.58 (m, 1 H, **a**), 5.22–5.29 (m, 2 H, **a**), 3.83 (q, *J* = 7.04 Hz, 1 H, **a**), 3.71 (d, *J* = 7.04 Hz, 2 H, **b**), 2.63 (m, 4 H, **a** and **b**), 2.13 (q, *J* = 7.04 Hz, 2 H, **a**), 1.71–1.78 (m, 3 H, **a** and **b**), 1.56–1.71 (m, 3 H, **a** and **b**). **$^{13}$C NMR** (125 MHz, $CDCl_3$) δ (**a** and **b**): 142.3, 142.0, 136.8, 135.9, 128.6, 128.5, 128.4, 126.0, 125.9, 123.4, 118.3, 65.2, 53.0, 35.6, 35.4, 34.0, 31.9, 30.9, 27.7. **GCMS** (EI) $t_R$ = 8.36 min *m/z*: 51, 65, 69, 77, 82, 91, 104, 117, 130, 144, 158, 172.

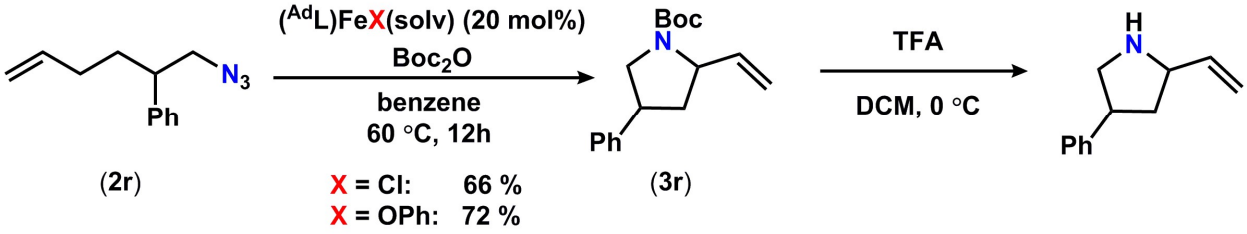


**4-phenyl-2-vinylpyrrolidine**: **$^1$H NMR** (600 MHz, $C_6D_6$) δ (mixture of diastereomers): 7.08–7.15 (m, 4.6 H), 7.00–7.07 (m, 3.0 H), 6.59 (br. s., 0.5 H), 6.33 (br. s., 1 H), 6.01 (dddd, *J* = 17.2, 10.2, 7.5, 5.0 Hz, 1 H), 5.88 (dddd, *J* = 17.1, 10.3, 6.9, 5.6 Hz, 0.5 H), 5.14–5.24 (m, 1.5 H), 4.97–5.04 (m, 1.5 H), 3.78–3.86 (m, 0.5 H), 3.63–3.72 (m, 1 H), 3.36 (td, *J* = 11.0, 7.9 Hz, 0.5 H), 3.23–3.31 (m, 1 H), 3.19 (dq, *J* = 17.2, 8.4 Hz, 0.5 H), 3.05–3.11 (m, 1 H), 2.94–3.05 (m, 1 H), 2.88 (dt, *J* = 10.6, 8.8 Hz, 0.5 H), 1.85–1.93 (m, 1 H), 1.83 (q, *J* = 8.0 Hz, 1 H), 1.62–1.71 (m, 1 H). **$^{13}$C NMR** (125 MHz, $CDCl_3$) δ (minor diastereomer in parentheses): 141.9(143.0), 136.9(138.4), 128.9(128.8), 127.5(127.5), 127.0(126.8), 117.8(116.4), 62.5(61.3), 52.2(53.4), 44.7(43.7), 40.7(39.8). **GCMS** (EI) $t_R$ = 7.80 min *m/z*: 51, 68, 78, 91, 104, 115, 129, 146, 160, 173.

**1D NOESY** (600 MHz, $C_6D_6$)

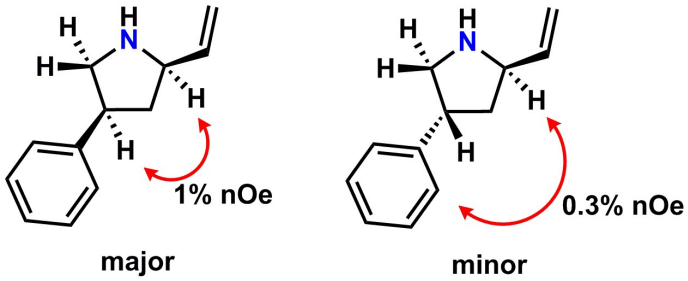


### *5.6.9 X-Ray Diffraction Techniques.*

All structures were collected on a Bruker three-circle platform goniometer equipped with an Apex II CCD and an Oxford cryostream cooling device. Radiation was from a graphite fine focus sealed tube Mo Kα (0.71073 Å) source. Crystals were mounted on a cryoloop or glass fiber pin using Paratone N oil. Structures were collected at 100 K. Data was collected as a series of φ and/or ω scans. Data was integrated using SAINT[32] and scaled with either a numerical or multi-scan absorption correction using SADABS[32]. The structures were solved by direct methods or Patterson maps using SHELXS-97[33] and refined against $F^2$ on all data by full matrix least squares with SHELXL-97[33]. All non-hydrogen atoms were refined anisotropically. Hydrogen atoms were placed at idealized positions and refined using a riding model. The isotropic displacement parameters of all hydrogen atoms were fixed to 1.2 times the atoms they are linked to (1.5 times for methyl groups). Further details on particular structures are noted below.

**($^{Ad}$L)Fe(2-(2-(trifluoromethyl)phenyl)-5-vinylpyrrolidine) (4).** The structure was solved in the monoclinic space group $P2_1/n$ with 4 molecules per unit cell.

32. *APEX2 Software Suite*; Bruker AXS: Madison, WI, 2009.
33. Sheldrick, G. M. Acta Crystallogr., Sect. A: Found. Crystallogr. **2008**, 64, 112-122

**($^{Ad}$L)Fe(OTf)(THF)$_2$ (5)** The structure was solved in the triclinic space group $P\bar{1}$ with 2 molecules per unit cell. One of the adamantyl substituents exhibited positional disorder and was refined using similarity constraints.

**($^{Ad}$L)Fe(OCCF$_3$MePh)(THF) (6).** The structure was solved in the monoclinic space group $P2_1/n$ with 4 molecules per unit cell.

**($^{Ad}$L)Fe(OCCF$_3$Ph$_2$)(THF) (7).** The structure was solved in the monoclinic space group $P2_1/n$ with 4 molecules per unit cell. One of the THF solvent molecule exhibited positional disorder and was refined using similarity constraints.

**($^{Ad}$L)Fe(OPh)(THF) (8).** The structure was solved in the orthorhombic space group *Pbca* with 8 molecules per unit cell.

**($^{Ad}$L)Fe(OC$_6$H$_3$Cl$_2$)(THF) (9).** The structure was solved in the triclinic space group $P\bar{1}$ with 2 molecules per unit cell. The aryl ring exhibited positional disorder and was refined using similarity constraints. One THF and one hexane solvent molecules lie on special positions and were refined with half occupancy for the asymmetric unit.

**($^{Ad}$L)Fe(OC$_6$H$_3$Br$_2$)(THF) (10).** The structure was solved in the triclinic space group $P\bar{1}$ with 2 molecules per unit cell. The aryl ring exhibited positional disorder and was refined using similarity constraints. Due to high disorder of the hexane and THF solvent molecules, an acceptable model could not be refined. Instead, a solvent mask was implemented in the Olex2 software which did not seriously affect the chemically significant features of the structure.

**($^{Ad}$L)Fe(OC$_6$H$_3$$^{i}$Pr$_2$)(THF) (11).** The structure was solved in the monoclinic space group $P2_1/n$ with 4 molecules per unit cell. The aryl ring, one of the adamantyl substituents, the mesityl group and the bound THF solvent molecule exhibited positional disorder and were refined using similarity constraints.

**($^{Ad}$L)Fe(OC$_6$H$_4$F)(THF) (12).** The structure was solved in the triclinic space group $P\bar{1}$ with 2 molecules per unit cell. One of the adamantyl substituents exhibited positional disorder and was refined using similarity constraints. A THF solvent molecule lies on a special position and was refined with half occupancy for the asymmetric unit.

**($^{Ad}$L)Fe(OC$_6$H$_4$OMe)(THF) (13).** The structure was solved in the triclinic space group $P\bar{1}$ with 2 molecules per unit cell. One of the adamantyl substituents and the bound THF solvent exhibited positional disorder and were refined using similarity constraints. A THF solvent molecule lies on a special position and was refined with half occupancy for the asymmetric unit. Due to significant disorder associated with this solvent molecule, it was not possible to model the THF moiety with multiple positions, but it was improved by refining the O atom with 0.25 occupancy.

**Table 5.3** X-ray diffraction experimental details[a,b]

| | **(1b)[2-(*o*-($CF_3$)-$C_6H_4$)-5-vinylpyrrolidine] (4)** | **$^{Ad}$LFe(OTf)(THF)$_2$ (5)** | **$^{Ad}$LFe(OCCF$_3$ MePh)(THF) (6)** | **$^{Ad}$LFe(OCCF$_3$ Ph$_2$)(THF) (7)** | **$^{Ad}$LFe(OPh)(THF) (8)** |
|---|---|---|---|---|---|
| **Moiety Formula** | $C_{51}H_{59}ClF_3FeN_3$ | $C_{41}H_{52}F_3FeN_2O_5S$ | $C_{51}H_{61}F_3FeN_2O_2$; 0.5×($C_6H_{14}$) | $C_{56}H_{63}F_3FeN_2O_2$; $C_4H_8O$ | $C_{48}H_{58}FeN_2O2$ |
| **FW** | 862.31 | 878.90 | 889.95 | 981.04 | 750.81 |
| **Crystal System** | monoclinic | triclinic | monoclinic | monoclinic | orthorhombic |
| **Space Group (Z)** | $P2_1/n$ (4) | $P\bar{1}$ (2) | $P2_1/n$ (4) | $P2_1/n$ | *Pbca* (8) |
| **a (Å)** | 16.593(2) | 9.6284(4) | 16.909(3) | 15.0070(6) | 15.9524(17) |
| **b (Å)** | 16.688(2) | 11.5848(5) | 14.693(2) | 15.9770(7) | 17.9261(19) |
| **c (Å)** | 16.898(2) | 20.0161(9) | 19.125(3) | 21.0611(9) | 27.481(3) |
| **α (°)** | 90 | 102.192(1) | 90 | 90 | 90 |
| **β (°)** | 112.486(2) | 95.052(1) | 106.151(3) | 98.864(1) | 90 |
| **γ (°)** | 90 | 98.218(1) | 90 | 90 | 90 |
| **Volume (Å$^3$)** | 4323.5(10) | 2143.70(16) | 4564.2(12) | 4989.4(4) | 7858.7(14) |
| **Calc. $\rho$ (mg/m$^3$)** | 1.325 | 1.362 | 1.295 | 1.305 | 1.269 |
| **$\mu$ (mm$^{-1}$)** | 0.463 | 0.462 | 0.387 | 0.362 | 0.426 |
| **Crystal Size (mm)** | 0.37×0.13×0.10 | 0.31×0.22×0.08 | 0.35×0.23×0.04 | 0.24×0.23×0.11 | 0.16×0.16×0.12 |
| **Reflections** | 7483 | 7995 | 8690 | 8869 | 6952 |
| **Completeness (to 2θ)** | 97.6% 25.07° | 98.9% 25.63° | 99.9% 25.71° | 99.6% 25.12° | 99.8% 25.05° |

| | | | | | |
|---|---|---|---|---|---|
| **GOF on $F^2$** | 0.982 | 0.826 | 0.867 | 1.027 | 1.013 |
| **R1, wR2[c] [I>2σ(I)]** | 0.0593, 0.1494 | 0.0378, 0.1007 | 0.0562, 0.1421 | 0.0403, 0.0961 | 0.0512, 0.1250 |

[a] λ = 0.71073 Å; [b] T = 100(2) K; [c] $R1 = \Sigma||F_o|-|F_c||/\Sigma|F_o|$, $wR2 = \{\Sigma[w(F_o^2-F_c^2)^2]/\Sigma[w(F_o^2)^2]\}^{1/2}$

| | **$^{Ad}$LFe($OC_6H_3Cl_2$)(THF) (9)** | **$^{Ad}$LFe($OC_6H_3Br_2$)(THF) (10)** | **$^{Ad}$LFe($OC_6H_3{}^iPr_2$)(THF) (11)** | **$^{Ad}$LFe($OC_6H_4F$)(THF) (12)** | **$^{Ad}$LFe($OC_6H_4OMe$)(THF) (13)** |
|---|---|---|---|---|---|
| **Moiety Formula** | $C_{48}H_{56}Cl_2FeN_2O_2$; 0.5×($C_6H_{14}$); 0.5×($C_4H_8O$) | $C_{48}H_{56}Br_2FeN_2O_2$ | $C_{54}H_{70}FeN_2O_2$ | $C_{52}H_{65}FFeN_2O_3$ ; 0.5×($C_4H_8O$) | $C_{53}H_{68}FeN_2O_4$; 0.5×($C_4H_8O_{0.5}$) |
| **FW** | 898.84 | 908.60 | 834.97 | 876.96 | 885.00 |
| **Crystal System** | triclinic | triclinic | monoclinic | triclinic | triclinic |
| **Space Group (Z)** | $P\bar{1}$ (2) | $P\bar{1}$ (2) | $P2_1/n$ (4) | $P\bar{1}$ (2) | $P\bar{1}$ (2) |
| **a (Å)** | 10.4968(12) | 10.5179(12) | 9.8765(7) | 10.0677(7) | 10.2472(5) |
| **b (Å)** | 11.0850(12) | 11.1427(13) | 22.8307(17) | 11.2545(8) | 11.1204(5) |
| **c (Å)** | 21.083(2) | 20.962(3) | 20.7312(14) | 21.0949(16) | 21.6205(10) |
| **α (°)** | 102.775(2) | 102.443(2) | 90 | 75.4820(14) | 77.168(1) |

| | | | | | |
|---|---|---|---|---|---|
| **β (°)** | 100.577(2) | 100.222(2) | 102.286(1) | 82.1410(15) | 79.978(1) |
| **γ (°)** | 99.818(2) | 99.605(2) | 90 | 80.2050(15) | 80.313(1) |
| **Volume (Å$^3$)** | 2294.0(4) | 2306.5(5) | 4567.6(6) | 2269.0(3) | 2343.88(19) |
| **Calc. $\rho$ (mg/m$^3$)** | 1.301 | 1.308 | 1.214 | 1.284 | 1.254 |
| **$\mu$ (mm$^{-1}$)** | 0.490 | 2.097 | 0.373 | 0.384 | 0.371 |
| **Crystal Size (mm)** | 0.31×0.20×0.04 | 0.34×0.23×0.14 | 0.23×0.21×0.17 | 0.23×0.15×0.13 | 0.70×0.22×0.15 |
| **Reflections** | 8170 | 8284 | 8509 | 8111 | 8317 |
| **Completeness (to 2θ)** | 99.5% 25.13° | 99.6% 25.20° | 97.9% 25.71° | 99.5% 25.151° | 98.6% 25.18° |
| **GOF on F$^2$** | 0.969 | 0.929 | 0.995 | 0.823 | 0.848 |
| **R1, wR2[c] [I>2σ(I)]** | 0.0492, 0.1220 | 0.0361, 0.0829 | 0.0571, 0.1343 | 0.0472, 0.0981 | 0.0410, 0.0857 |

### *5.6.10 Computational Methods.*

Computations were carried out utilizing the Gaussian 09[34] program package. The B3LYP[35] functional was used with the def2-TZVP (Fe, N, Cl), def2-SV(P) (C, H) basis sets and the W06

34. Frisch, M. J.; Trucks, G. W.; Schlegel, H. B.; Scuseria, G. E.; Robb, M. A.; Cheeseman, J. R.; Scalmani, G.; Barone, V.; Mennucci, B.; Petersson, G. A.; Nakatsuji, H.; Caricato, M.; Li, X.; Hratchian, H. P.; Izmaylov, A. F.; Bloino, J.; Zheng, G.; Sonnenberg, J. L.; Hada, M.; Ehara, M.; Toyota, K.; Fukuda, R.; Hasegawa, J.; Ishida, M.; Nakajima, T.; Honda, Y.; Kitao, O.; Nakai, H.; Vreven, T.; Montgomery Jr., J. A.; Peralta, J. E.; Ogliaro, F.; Bearpark, M. J.; Heyd, J.; Brothers, E. N.; Kudin, K. N.; Staroverov, V. N.; Kobayashi, R.; Normand, J.; Raghavachari, K.; Rendell, A. P.; Burant, J. C.; Iyengar, S. S.; Tomasi, J.; Cossi, M.; Rega, N.; Millam, N. J.; Klene, M.; Knox, J. E.; Cross, J. B.; Bakken, V.; Adamo, C.; Jaramillo, J.; Gomperts, R.; Stratmann, R. E.; Yazyev, O.; Austin, A. J.; Cammi, R.; Pomelli, C.; Ochterski, J. W.; Martin, R. L.; Morokuma, K.; Zakrzewski, V. G.; Voth, G. A.; Salvador, P.; Dannenberg, J. J.; Dapprich, S.; Daniels, A. D.; Farkas, Ö.; Foresman, J. B.; Ortiz, J. V.; Cioslowski, J.; Fox, D. J.; Gaussian, Inc.: Wallingford, CT, USA, 2009.
35. (a) Becke, A. D. *J. Chem. Phys.* **98**, 5648 (1993); (b) Lee, C. T.; Yang, W. T.; Parr, R. G. *Phys Rev. B* **33**, 785 (1988).

density fitting basis set of Ahlrichs and coworkers[36]. For the reaction trajectory, the geometry optimization of complex **1b** was started using crystallographically determined coordinates. For the ether molecule, coordinates from the X-ray structure of **1b** were used as initial input.

The crystallographic coordinates for the characterized iron-pyrrolidine adduct (**1b**)[2-(*o*-($F_3C$)$C_6H_4$)-5-vinylpyrrolidine] were used as a starting point for the transition state calculation, removing the *ortho*-trifluoromethyl group to minimize computational effort. An initial relaxed potential energy surface scan was conducted over the $C_4$–N bond range of 1.6 – 3.5 Å in 20 steps to find a plateau at 2.7 Å. Using the geometry optimized structure for the $C_4$–N bond length of 2.7 Å, the proton was moved from the N atom onto the $C_4$ atom and the H-atom positions were re-optimized. These coordinates were then used as input for geometry optimization of the $Fe^{III}$ iminyl intermediate preceding the transition state for hydrogen atom abstraction. To prevent the transfer of H-atom during the optimization cycle, the dihedral angle formed by H, $C_4$ and vinyl group was constrained, forcing the C atom to remain $sp^3$ hybridized. The geometry optimized structure was used as input for the potential energy surface scan conducted to identify a transition state corresponding to H-transfer. The N–H bond distance was varied 1.46 – 1.23 Å to identify the maximum energy structure corresponding to an N–H distance of 1.3 Å. The coordinates found were used as input for geometry optimization of the transition state. A frequency calculation on the final geometry identified a single negative frequency along the N–H–$C_4$ vector. To determine the energy for the pro-*anti* transition state, the vinyl group in the optimized iron iminyl structure was rotated in the *anti* configuration and the potential energy surface scan was repeated as above. Geometry optimized coordinates and final energies for each intermediate along the reaction trajectory are provided below.

---

36. (a) Schäfer, A.; Horn, H.; Ahlrichs, R. *J. Chem. Phys*. **1992**, *97***,** 2571; (b) Schäafer, A.; Huber, C.; Ahlrichs, R. *J. Chem. Phys.***1994**, *100*, 5829; (c) Weigend, F.; Ahlrichs, R. *Phys. Chem. Chem. Phys.* **2005**, *7*, 3297; (d) Weigend, F. *Phys. Chem. Chem. Phys.* **2006**, *8*, 1057.

### *5.6.11 Geometry optimized structures along the reaction **trajectory:***

**Table 5.4** Optimized geometry coordinates for $^{Ad}$LFeCl(OEt$_2$) (**1b**)

| | | | |
|---|---|---|---|
| 26 | -0.093713000 | -0.798304000 | -0.095103000 |
| 17 | -0.403452000 | -2.708778000 | -1.287507000 |
| 8 | -0.204332000 | -1.231882000 | 2.042410000 |
| 7 | 1.627774000 | 0.302574000 | -0.201080000 |
| 7 | -1.503557000 | 0.718721000 | -0.220387000 |
| 6 | -2.851274000 | 0.788080000 | -0.269433000 |
| 6 | -3.274295000 | 2.153279000 | -0.263273000 |
| 6 | -2.138844000 | 2.931434000 | -0.214591000 |
| 6 | -1.021582000 | 2.040494000 | -0.193942000 |
| 6 | 0.322044000 | 2.464461000 | -0.157413000 |
| 6 | 1.513244000 | 1.701748000 | -0.154875000 |
| 6 | 2.822805000 | 2.262281000 | -0.140139000 |
| 6 | 3.716014000 | 1.208376000 | -0.191466000 |
| 6 | 2.950672000 | 0.009309000 | -0.238290000 |
| 6 | 0.524142000 | 3.962156000 | -0.142453000 |
| 6 | 0.591941000 | 4.656878000 | 1.084863000 |
| 6 | 0.785997000 | 6.045529000 | 1.070950000 |
| 6 | 0.910871000 | 6.766361000 | -0.122874000 |
| 6 | 0.842793000 | 6.053517000 | -1.326570000 |
| 6 | 0.651014000 | 4.665153000 | -1.361638000 |
| 6 | 0.457695000 | 3.931110000 | 2.405079000 |
| 6 | 1.085497000 | 8.267339000 | -0.114485000 |
| 6 | 0.585726000 | 3.946568000 | -2.690644000 |
| 6 | -3.795743000 | -0.400236000 | -0.371048000 |
| 6 | -3.461862000 | -1.504603000 | 0.666263000 |
| 6 | -4.436415000 | -2.693564000 | 0.540484000 |
| 6 | -5.874668000 | -2.210832000 | 0.802852000 |
| 6 | -6.240686000 | -1.133701000 | -0.235079000 |
| 6 | -5.262536000 | 0.051403000 | -0.120801000 |
| 6 | -3.736770000 | -1.021176000 | -1.800470000 |
| 6 | -4.713038000 | -2.210838000 | -1.914067000 |
| 6 | -6.153519000 | -1.730482000 | -1.653437000 |
| 6 | -4.336923000 | -3.289200000 | -0.878418000 |
| 6 | 3.536114000 | -1.386453000 | -0.378172000 |
| 6 | 5.069273000 | -1.361415000 | -0.123892000 |
| 6 | 5.683992000 | -2.765879000 | -0.277222000 |
| 6 | 5.441029000 | -3.274203000 | -1.712233000 |
| 6 | 3.924735000 | -3.334966000 | -1.979204000 |
| 6 | 3.309517000 | -1.928491000 | -1.823706000 |
| 6 | 2.908330000 | -2.388706000 | 0.624924000 |
| 6 | 3.266866000 | -4.300792000 | -0.973624000 |
| 6 | 5.033779000 | -3.731398000 | 0.731243000 |

| | | | |
|---|---|---|---|
| 6 | 3.519149000 | -3.794855000 | 0.461344000 |
| 6 | -0.173786000 | -0.160741000 | 3.001714000 |
| 6 | 1.179838000 | 0.020298000 | 3.675563000 |
| 6 | -0.097526000 | -2.579818000 | 2.542154000 |
| 6 | -1.207614000 | -2.979231000 | 3.505394000 |
| 1 | 0.108197000 | 8.784559000 | -0.175585000 |
| 1 | 1.579645000 | 8.613246000 | 0.810015000 |
| 1 | 1.688244000 | 8.610373000 | -0.973486000 |
| 1 | 0.842867000 | 6.578491000 | 2.026546000 |
| 1 | 0.944293000 | 6.593286000 | -2.274542000 |
| 1 | 0.704711000 | 4.653542000 | -3.528589000 |
| 1 | -0.378355000 | 3.423126000 | -2.819829000 |
| 1 | 1.213567000 | 3.131746000 | 2.505850000 |
| 1 | 0.581063000 | 4.625592000 | 3.252972000 |
| 1 | -0.533838000 | 3.452130000 | 2.500700000 |
| 1 | 4.800508000 | 1.280070000 | -0.202405000 |
| 1 | 3.056877000 | 3.324406000 | -0.102410000 |
| 1 | -2.082455000 | 4.018022000 | -0.196797000 |
| 1 | -4.300764000 | 2.509035000 | -0.293817000 |
| 1 | -5.345595000 | 0.516281000 | 0.879256000 |
| 1 | -3.510962000 | -1.074914000 | 1.684505000 |
| 1 | -2.433585000 | -1.868084000 | 0.512835000 |
| 1 | -2.709883000 | -1.354798000 | -2.021648000 |
| 1 | -3.997227000 | -0.243528000 | -2.542408000 |
| 1 | -5.548528000 | 0.820791000 | -0.858986000 |
| 1 | -7.266792000 | -0.768470000 | -0.046679000 |
| 1 | -6.445245000 | -0.971119000 | -2.403587000 |
| 1 | -6.862983000 | -2.573343000 | -1.756405000 |
| 1 | -6.581702000 | -3.059380000 | 0.739320000 |
| 1 | -4.639302000 | -2.634918000 | -2.931788000 |
| 1 | -5.958991000 | -1.797029000 | 1.825948000 |
| 1 | -5.016767000 | -4.157450000 | -0.971620000 |
| 1 | -4.160100000 | -3.463071000 | 1.285278000 |
| 1 | -3.311544000 | -3.653257000 | -1.066353000 |
| 1 | 1.821857000 | -2.453306000 | 0.454232000 |
| 1 | 2.229608000 | -1.964194000 | -2.043589000 |
| 1 | 3.062852000 | -2.022405000 | 1.657126000 |
| 1 | 3.769830000 | -1.229774000 | -2.546684000 |
| 1 | 5.275202000 | -0.966621000 | 0.888468000 |
| 1 | 5.556046000 | -0.678352000 | -0.841795000 |
| 1 | 6.770366000 | -2.702105000 | -0.083855000 |
| 1 | 5.224666000 | -3.386767000 | 1.765660000 |
| 1 | 5.931761000 | -2.601551000 | -2.441001000 |
| 1 | 5.482092000 | -4.738696000 | 0.640121000 |
| 1 | 5.893589000 | -4.275271000 | -1.843994000 |
| 1 | 3.686755000 | -5.317574000 | -1.094116000 |

| | | | |
|---|---|---|---|
| 1 | 3.740374000 | -3.691262000 | -3.008740000 |
| 1 | 3.039513000 | -4.479459000 | 1.185168000 |
| 1 | 2.181941000 | -4.368823000 | -1.167406000 |
| 1 | 0.895777000 | -2.715232000 | 3.006270000 |
| 1 | -0.135612000 | -3.206866000 | 1.639325000 |
| 1 | -1.114203000 | -4.058015000 | 3.723693000 |
| 1 | -2.201630000 | -2.805608000 | 3.059454000 |
| 1 | -1.154628000 | -2.444669000 | 4.469526000 |
| 1 | -0.972631000 | -0.323756000 | 3.746465000 |
| 1 | -0.443476000 | 0.737365000 | 2.426161000 |
| 1 | 1.140418000 | 0.905626000 | 4.335150000 |
| 1 | 1.458219000 | -0.845569000 | 4.301558000 |
| 1 | 1.973952000 | 0.183584000 | 2.927035000 |
| 1 | 1.376395000 | 3.179936000 | -2.775436000 |

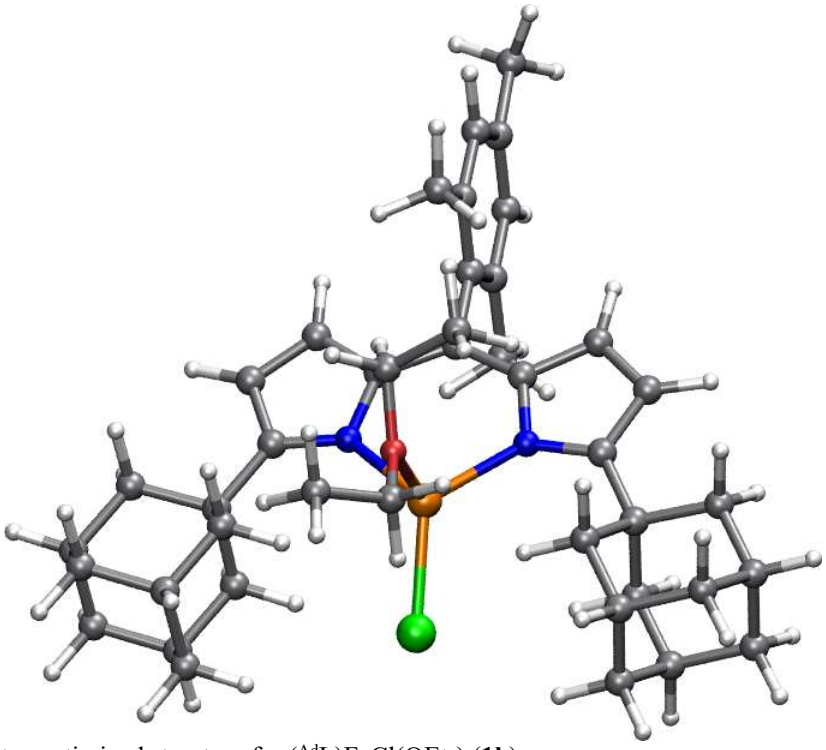

**Figure 5.14** Geometry optimized structure for ($^{Ad}$L)FeCl(OEt$_2$) (**1b**)

**Table 5.5** Optimized geometry coordinates for $OEt_2$

| | | | |
|---|---|---|---|
| 8 | 1.787927000 | 10.588582000 | -0.784521000 |
| 6 | 2.011735000 | 11.962629000 | -0.582561000 |
| 1 | 3.006693000 | 12.255176000 | -0.987722000 |
| 1 | 2.031135000 | 12.194491000 | 0.506265000 |
| 6 | 0.909240000 | 12.750863000 | -1.270462000 |
| 1 | 1.059677000 | 13.835652000 | -1.128169000 |
| 1 | -0.077407000 | 12.475756000 | -0.858294000 |
| 1 | 0.898944000 | 12.536485000 | -2.353501000 |
| 6 | 2.748843000 | 9.749894000 | -0.191121000 |
| 1 | 2.787348000 | 9.924346000 | 0.907862000 |
| 1 | 3.762923000 | 9.985060000 | -0.586112000 |
| 6 | 2.391302000 | 8.301886000 | -0.483442000 |
| 1 | 3.130537000 | 7.619127000 | -0.028450000 |
| 1 | 2.369745000 | 8.121404000 | -1.572479000 |
| 1 | 1.393360000 | 8.060648000 | -0.077294000 |

**Table 5.6** Optimized geometry coordinates for 1-azido-1-phenyl-4-vinylbutane

| | | | |
|---|---|---|---|
| 6 | -3.474074000 | -3.461758000 | 3.787503000 |
| 6 | -1.532901000 | -1.937760000 | 3.200340000 |
| 6 | -1.185312000 | 0.504638000 | 2.300086000 |
| 6 | -3.144075000 | 1.847769000 | 3.167529000 |
| 6 | -4.673689000 | -3.731882000 | 3.261050000 |
| 6 | -4.492917000 | 2.212723000 | 3.174313000 |
| 6 | -4.897722000 | 0.724443000 | 1.314096000 |
| 6 | -0.850975000 | -0.565794000 | 3.363055000 |
| 6 | -2.656039000 | 0.910445000 | 2.243026000 |
| 6 | -5.376204000 | 1.649738000 | 2.246674000 |
| 1 | -2.458256000 | 2.301536000 | 3.891796000 |
| 1 | -4.854127000 | 2.946334000 | 3.901942000 |
| 1 | -6.432008000 | 1.937834000 | 2.246148000 |
| 1 | -5.578979000 | 0.283921000 | 0.579247000 |
| 1 | -0.603458000 | 1.406501000 | 2.571621000 |
| 1 | 0.244976000 | -0.695417000 | 3.326808000 |
| 1 | -1.084435000 | -0.141247000 | 4.356920000 |
| 1 | -0.842077000 | -2.715368000 | 3.576190000 |
| 1 | -1.669991000 | -2.158029000 | 2.126443000 |
| 1 | -5.333744000 | -2.932420000 | 2.898645000 |
| 1 | -5.044619000 | -4.760288000 | 3.174556000 |
| 1 | -2.848495000 | -4.298965000 | 4.133494000 |
| 6 | -2.875917000 | -2.089594000 | 3.943060000 |
| 1 | -3.597249000 | -1.329426000 | 3.599206000 |
| 1 | -2.698490000 | -1.892292000 | 5.020439000 |
| 6 | -3.547580000 | 0.357694000 | 1.311940000 |
| 1 | -3.181967000 | -0.367272000 | 0.579865000 |
| 7 | -0.682683000 | 0.001060000 | 1.001162000 |

| | | | |
|---|---|---|---|
| 7 | -0.515371000 | 0.813651000 | 0.097405000 |
| 7 | -0.311622000 | 1.470224000 | -0.809556000 |

**Table 5.7** Optimized geometry coordinates for $N_2$

| | | | |
|---|---|---|---|
| 7 | 0.092198000 | 0.995000000 | 0.000000000 |
| 7 | -1.008198000 | 0.995000000 | 0.000000000 |

**Table 5.8** Optimized geometry coordinates for ($^{Ad}$L)FeCl(•NR) iminyl intermediate

| | | | |
|---|---|---|---|
| 26 | -0.148142000 | 0.161369000 | -0.497188000 |
| 17 | -1.605835000 | 0.408449000 | -2.212374000 |
| 7 | 1.303732000 | 1.560654000 | -0.454329000 |
| 7 | -0.902313000 | 0.174407000 | 1.098603000 |
| 7 | 1.006171000 | -1.539458000 | -0.708360000 |
| 6 | 1.334089000 | 2.922641000 | -0.462426000 |
| 6 | 2.573523000 | 1.110925000 | -0.047626000 |
| 6 | -0.506242000 | -3.459537000 | -1.478363000 |
| 6 | 2.620796000 | 3.367597000 | -0.059570000 |
| 6 | 5.504299000 | -0.434426000 | -0.382712000 |
| 6 | 3.388295000 | 2.246796000 | 0.203340000 |
| 6 | 4.435874000 | -0.401902000 | 0.541334000 |
| 6 | 3.017307000 | -0.227430000 | 0.055644000 |
| 6 | 6.809821000 | -0.603954000 | 0.099613000 |
| 6 | 4.687809000 | -0.540547000 | 1.924034000 |
| 6 | 0.776859000 | -2.854412000 | -0.930614000 |
| 6 | 0.199446000 | 3.843190000 | -0.883696000 |
| 6 | 2.330580000 | -1.415535000 | -0.251138000 |
| 6 | 6.010255000 | -0.708337000 | 2.358814000 |
| 6 | -3.368993000 | -3.443159000 | 3.801224000 |
| 6 | 7.087987000 | -0.740313000 | 1.465659000 |
| 6 | -1.755446000 | -3.019770000 | -0.666402000 |
| 6 | -0.056146000 | 3.723838000 | -2.417602000 |
| 6 | -1.481841000 | -1.800753000 | 3.404772000 |
| 6 | -1.348869000 | 0.615031000 | 2.355996000 |
| 6 | 1.947555000 | -3.608485000 | -0.613644000 |
| 6 | -3.205416000 | -3.207803000 | -2.717384000 |
| 6 | 2.909089000 | -2.718566000 | -0.187018000 |
| 6 | -3.038859000 | -3.646235000 | -1.248240000 |
| 6 | -1.990719000 | -3.687609000 | -3.538031000 |
| 6 | -3.274546000 | 1.806553000 | 3.513575000 |
| 6 | -4.357465000 | -3.969231000 | 3.068901000 |
| 6 | -1.724544000 | -5.647904000 | -1.991287000 |
| 6 | -0.699740000 | -3.059181000 | -2.973206000 |
| 6 | -4.599537000 | 2.245542000 | 3.583035000 |
| 6 | -5.032620000 | 1.256375000 | 1.422006000 |
| 6 | -0.935873000 | -0.367593000 | 3.501026000 |
| 6 | -2.813226000 | 1.082255000 | 2.402397000 |
| 6 | -1.896840000 | -5.223117000 | -3.463028000 |
| 6 | -5.486232000 | 1.967307000 | 2.537139000 |
| 6 | -2.942028000 | -5.180608000 | -1.172348000 |
| 6 | -0.440337000 | -5.012519000 | -1.422753000 |
| 6 | 8.508160000 | -0.889310000 | 1.960099000 |
| 1 | 8.986540000 | 0.098639000 | 2.106222000 |
| 1 | 8.547117000 | -1.416946000 | 2.928781000 |

| | | | |
|---|---|---|---|
| 1 | 9.131773000 | -1.448166000 | 1.240557000 |
| 6 | 3.561602000 | -0.516477000 | 2.933521000 |
| 1 | 3.006489000 | 0.438172000 | 2.897480000 |
| 1 | 2.827231000 | -1.319050000 | 2.740628000 |
| 1 | 3.947034000 | -0.646540000 | 3.958544000 |
| 6 | 5.262402000 | -0.297763000 | -1.869585000 |
| 1 | 4.611240000 | -1.104806000 | -2.250636000 |
| 1 | 4.761497000 | 0.655926000 | -2.114034000 |
| 1 | 6.212221000 | -0.335401000 | -2.428606000 |
| 6 | -1.120251000 | 3.538523000 | -0.122705000 |
| 1 | -0.946709000 | 3.643863000 | 0.964787000 |
| 1 | -1.437409000 | 2.499405000 | -0.302353000 |
| 6 | -2.248149000 | 4.488983000 | -0.571810000 |
| 1 | -3.169445000 | 4.228410000 | -0.021195000 |
| 6 | -2.484068000 | 4.322534000 | -2.086739000 |
| 1 | -3.308646000 | 4.983519000 | -2.414920000 |
| 1 | -2.788123000 | 3.284816000 | -2.311137000 |
| 6 | -1.191794000 | 4.673756000 | -2.851676000 |
| 1 | -1.359380000 | 4.552558000 | -3.937254000 |
| 6 | -1.848947000 | 5.943884000 | -0.265643000 |
| 1 | -1.695310000 | 6.077548000 | 0.822106000 |
| 1 | -2.659945000 | 6.635248000 | -0.562803000 |
| 6 | 0.571161000 | 5.325237000 | -0.592863000 |
| 1 | 1.496420000 | 5.592590000 | -1.133310000 |
| 1 | 0.776208000 | 5.456046000 | 0.485779000 |
| 6 | -0.555878000 | 6.281509000 | -1.030386000 |
| 1 | -0.247792000 | 7.318526000 | -0.803689000 |
| 6 | -0.795820000 | 6.130471000 | -2.545206000 |
| 1 | -1.593514000 | 6.822632000 | -2.874934000 |
| 1 | 0.119023000 | 6.404144000 | -3.104404000 |
| 1 | 0.875880000 | 3.975248000 | -2.957403000 |
| 1 | -0.314120000 | 2.685298000 | -2.677272000 |
| 1 | 6.200806000 | -0.819604000 | 3.431853000 |
| 1 | 7.635527000 | -0.632626000 | -0.619889000 |
| 1 | 2.943488000 | 4.402041000 | 0.017888000 |
| 1 | 4.427977000 | 2.217582000 | 0.523453000 |
| 1 | 3.926961000 | -2.941937000 | 0.126647000 |
| 1 | 2.056925000 | -4.685942000 | -0.700352000 |
| 1 | 0.175499000 | -3.405649000 | -3.554198000 |
| 1 | -0.741084000 | -1.962890000 | -3.067508000 |
| 1 | -1.630832000 | -3.325593000 | 0.388522000 |
| 1 | -1.852371000 | -1.922292000 | -0.678923000 |
| 1 | -0.287876000 | -5.344245000 | -0.379098000 |
| 1 | 0.425103000 | -5.372004000 | -2.007222000 |
| 1 | -1.633018000 | -6.747694000 | -1.929213000 |
| 1 | -1.041798000 | -5.584028000 | -4.065699000 |

| | | | |
|---|---|---|---|
| 1 | -2.808087000 | -5.684461000 | -3.888464000 |
| 1 | -2.842683000 | -5.503926000 | -0.118967000 |
| 1 | -3.866901000 | -5.643555000 | -1.565541000 |
| 1 | -2.107358000 | -3.371358000 | -4.590540000 |
| 1 | -4.136312000 | -3.635711000 | -3.135807000 |
| 1 | -2.589708000 | 2.038674000 | 4.336163000 |
| 1 | -4.939666000 | 2.811115000 | 4.456338000 |
| 1 | -6.524571000 | 2.309200000 | 2.589086000 |
| 1 | -5.715098000 | 1.040108000 | 0.594083000 |
| 1 | -0.732940000 | 1.529197000 | 2.539029000 |
| 1 | 0.166817000 | -0.412891000 | 3.478792000 |
| 1 | -1.217220000 | 0.080452000 | 4.471684000 |
| 1 | -0.859225000 | -2.438531000 | 4.061191000 |
| 1 | -1.323859000 | -2.180506000 | 2.378888000 |
| 1 | -4.965666000 | -3.349093000 | 2.396864000 |
| 1 | -4.601957000 | -5.037192000 | 3.116444000 |
| 1 | -2.788459000 | -4.108126000 | 4.459165000 |
| 1 | -3.903445000 | -3.297836000 | -0.654470000 |
| 1 | -3.294619000 | -2.108652000 | -2.778654000 |
| 6 | -2.956800000 | -1.995596000 | 3.805413000 |
| 1 | -3.630074000 | -1.412608000 | 3.129508000 |
| 1 | -3.101621000 | -1.579321000 | 4.823261000 |
| 6 | -3.704468000 | 0.820348000 | 1.352796000 |
| 1 | -3.354441000 | 0.278416000 | 0.470763000 |

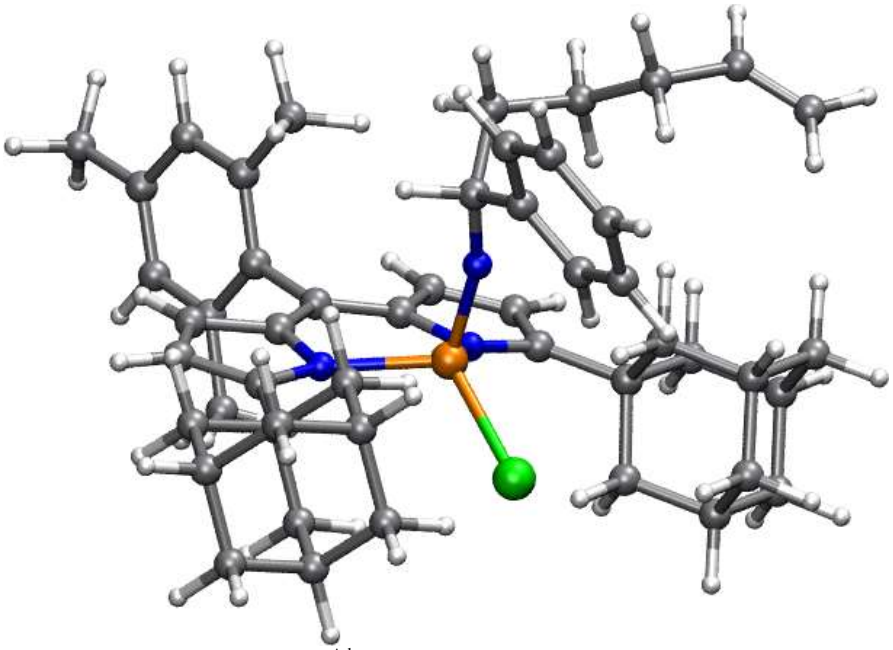

**Figure 5.15** Geometry optimized structure for ($^{Ad}$L)FeCl(ˑNR) iminyl intermediate

**Table 5.9** Optimized geometry coordinates for TS_*syn* configuration

| | | | |
|---|---|---|---|
| 26 | 0.382650000 | 0.138908000 | -0.213849000 |
| 17 | 1.948792000 | 0.686498000 | -1.727951000 |
| 7 | -0.226582000 | -1.840811000 | -0.406046000 |
| 7 | 0.858773000 | 0.503899000 | 1.519791000 |
| 7 | -1.440837000 | 1.046146000 | -0.507754000 |
| 6 | 0.385903000 | -3.046742000 | -0.503837000 |
| 6 | -1.597441000 | -2.087522000 | -0.198487000 |
| 6 | -0.989978000 | 3.510539000 | -1.067695000 |
| 6 | -0.571650000 | -4.090942000 | -0.334502000 |
| 6 | -4.778707000 | -2.045579000 | -1.117821000 |
| 6 | -1.800506000 | -3.497984000 | -0.144644000 |
| 6 | -4.025949000 | -1.724054000 | 0.036398000 |
| 6 | -2.639602000 | -1.142803000 | -0.124757000 |
| 6 | -6.054722000 | -2.603063000 | -0.961471000 |
| 6 | -4.562734000 | -1.967125000 | 1.318669000 |
| 6 | -1.859593000 | 2.327551000 | -0.669932000 |
| 6 | 1.853189000 | -3.294440000 | -0.821249000 |
| 6 | -2.580985000 | 0.261573000 | -0.255093000 |
| 6 | -5.844073000 | -2.529000000 | 1.425364000 |
| 6 | -1.129202000 | 2.557230000 | 3.476966000 |
| 6 | -6.610390000 | -2.852619000 | 0.300355000 |
| 6 | 0.259845000 | 3.672374000 | -0.160070000 |
| 6 | 2.140110000 | -2.978813000 | -2.322672000 |
| 6 | -0.030869000 | 0.379292000 | 4.269843000 |
| 6 | 1.814318000 | 0.095158000 | 2.527749000 |
| 6 | -3.271097000 | 2.396141000 | -0.494394000 |
| 6 | 1.569212000 | 4.671059000 | -2.067785000 |
| 6 | -3.719826000 | 1.114993000 | -0.236159000 |
| 6 | 1.112635000 | 4.876031000 | -0.609234000 |
| 6 | 0.331855000 | 4.557398000 | -2.981288000 |
| 6 | 3.542932000 | 1.732210000 | 1.567784000 |
| 6 | -2.247580000 | 3.233258000 | 3.143315000 |
| 6 | -0.953871000 | 6.043237000 | -1.416322000 |
| 6 | -0.523434000 | 3.349225000 | -2.547409000 |
| 6 | 4.868220000 | 2.132907000 | 1.371269000 |
| 6 | 5.642285000 | 0.126613000 | 2.471590000 |
| 6 | 1.441950000 | 0.636594000 | 3.940248000 |
| 6 | 3.251927000 | 0.524243000 | 2.215147000 |
| 6 | -0.501403000 | 5.849025000 | -2.876635000 |
| 6 | 5.922903000 | 1.333794000 | 1.823429000 |
| 6 | 0.280202000 | 6.166869000 | -0.503521000 |
| 6 | -1.803533000 | 4.833532000 | -0.980789000 |
| 6 | -7.999754000 | -3.430460000 | 0.438746000 |
| 1 | -8.130044000 | -3.946072000 | 1.405881000 |
| 1 | -8.770598000 | -2.637363000 | 0.383654000 |

| | | | |
|---|---|---|---|
| 1 | -8.220778000 | -4.152827000 | -0.366618000 |
| 6 | -3.798918000 | -1.618386000 | 2.576183000 |
| 1 | -2.744974000 | -1.939942000 | 2.521857000 |
| 1 | -3.796423000 | -0.525991000 | 2.748274000 |
| 1 | -4.257229000 | -2.090952000 | 3.461120000 |
| 6 | -4.228267000 | -1.808163000 | -2.506457000 |
| 1 | -4.007992000 | -0.739279000 | -2.677986000 |
| 1 | -3.282640000 | -2.356295000 | -2.666919000 |
| 1 | -4.946495000 | -2.135433000 | -3.276688000 |
| 6 | 2.806308000 | -2.450063000 | 0.062667000 |
| 1 | 2.621445000 | -2.689869000 | 1.126023000 |
| 1 | 2.602726000 | -1.376194000 | -0.072090000 |
| 6 | 4.280748000 | -2.727891000 | -0.292552000 |
| 1 | 4.922326000 | -2.093380000 | 0.343102000 |
| 6 | 4.528238000 | -2.389493000 | -1.776542000 |
| 1 | 5.590090000 | -2.568670000 | -2.031736000 |
| 1 | 4.325330000 | -1.319621000 | -1.959737000 |
| 6 | 3.618510000 | -3.263514000 | -2.662268000 |
| 1 | 3.790596000 | -3.020037000 | -3.726550000 |
| 6 | 4.596433000 | -4.213670000 | -0.040626000 |
| 1 | 4.439354000 | -4.463013000 | 1.026318000 |
| 1 | 5.658729000 | -4.424658000 | -0.266899000 |
| 6 | 2.206162000 | -4.791941000 | -0.589519000 |
| 1 | 1.569215000 | -5.430615000 | -1.225894000 |
| 1 | 1.997449000 | -5.068506000 | 0.460675000 |
| 6 | 3.682011000 | -5.079076000 | -0.926307000 |
| 1 | 3.886255000 | -6.149686000 | -0.742009000 |
| 6 | 3.935772000 | -4.750490000 | -2.410471000 |
| 1 | 4.988157000 | -4.966773000 | -2.674939000 |
| 1 | 3.304040000 | -5.391173000 | -3.054839000 |
| 1 | 1.478703000 | -3.601137000 | -2.954118000 |
| 1 | 1.899327000 | -1.924523000 | -2.534508000 |
| 1 | -6.251212000 | -2.722383000 | 2.423965000 |
| 1 | -6.630272000 | -2.855935000 | -1.858818000 |
| 1 | -0.368503000 | -5.157753000 | -0.362142000 |
| 1 | -2.758262000 | -3.993034000 | 0.002306000 |
| 1 | -4.746434000 | 0.793892000 | -0.069085000 |
| 1 | -3.882246000 | 3.291665000 | -0.566030000 |
| 1 | -1.413337000 | 3.261581000 | -3.198709000 |
| 1 | 0.055045000 | 2.417918000 | -2.658187000 |
| 1 | -0.065104000 | 3.799831000 | 0.888117000 |
| 1 | 0.875763000 | 2.760729000 | -0.195103000 |
| 1 | -2.167521000 | 4.980753000 | 0.052904000 |
| 1 | -2.692362000 | 4.771178000 | -1.633084000 |
| 1 | -1.570298000 | 6.957286000 | -1.335905000 |
| 1 | -1.383312000 | 5.790083000 | -3.542570000 |

| | | | |
|---|---|---|---|
| 1 | 0.095293000 | 6.719119000 | -3.209958000 |
| 1 | -0.035730000 | 6.333510000 | 0.543903000 |
| 1 | 0.888912000 | 7.042108000 | -0.799719000 |
| 1 | 0.656142000 | 4.405916000 | -4.026905000 |
| 1 | 2.200250000 | 5.521487000 | -2.389283000 |
| 1 | 2.723363000 | 2.354498000 | 1.202126000 |
| 1 | 5.076873000 | 3.074697000 | 0.854092000 |
| 1 | 6.959690000 | 1.646972000 | 1.665813000 |
| 1 | 6.458792000 | -0.510447000 | 2.826317000 |
| 1 | 1.811487000 | -1.011385000 | 2.611328000 |
| 1 | 2.107111000 | 0.157699000 | 4.678313000 |
| 1 | 1.657136000 | 1.719797000 | 3.974749000 |
| 1 | -0.246318000 | 0.696899000 | 5.308797000 |
| 1 | -0.236079000 | -0.704689000 | 4.216981000 |
| 1 | -3.103788000 | 2.729877000 | 2.678052000 |
| 1 | -2.334423000 | 4.311555000 | 3.318518000 |
| 1 | -0.297705000 | 3.115568000 | 3.929225000 |
| 1 | 1.997843000 | 4.949151000 | 0.049221000 |
| 1 | 2.185262000 | 3.757855000 | -2.147972000 |
| 6 | -0.925227000 | 1.117535000 | 3.279755000 |
| 1 | -1.845422000 | 0.585437000 | 2.997524000 |
| 1 | -0.190497000 | 0.952321000 | 2.214174000 |
| 6 | 4.316064000 | -0.273658000 | 2.661768000 |
| 1 | 4.104914000 | -1.223782000 | 3.164546000 |

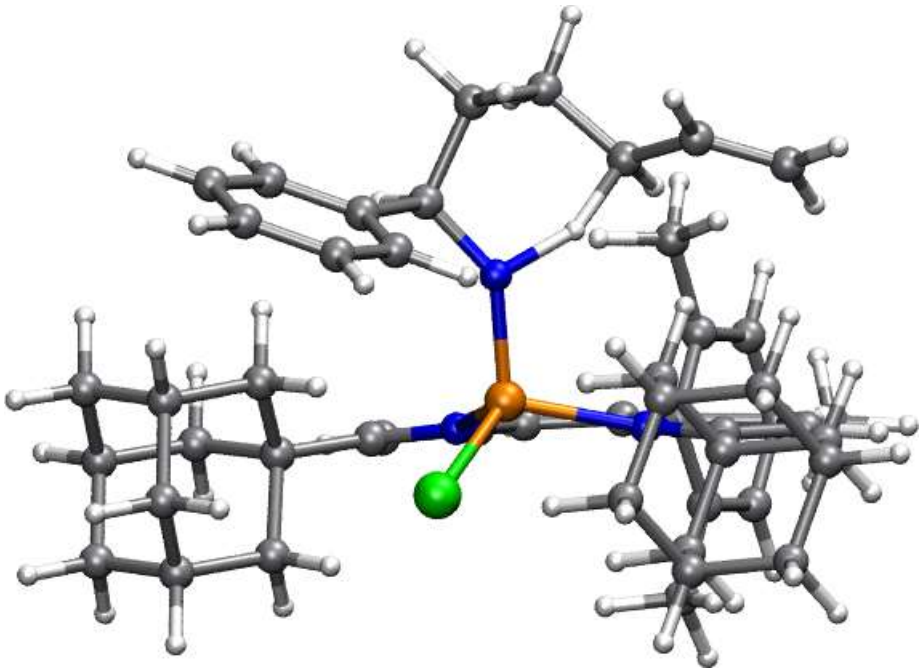

**Figure 5.16** Geometry optimized structure for the TS_*syn* configuration

**Table 5.10** Optimized geometry coordinates for TS_*anti* configuration

| | | | |
|---|---|---|---|
| 26 | 0.389534000 | 0.115271000 | -0.101516000 |
| 17 | 1.883217000 | 0.550646000 | -1.724124000 |
| 7 | -0.343070000 | -1.829053000 | -0.304939000 |
| 7 | 0.985636000 | 0.505891000 | 1.590994000 |
| 7 | -1.382192000 | 1.129725000 | -0.379148000 |
| 6 | 0.195886000 | -3.066101000 | -0.435109000 |
| 6 | -1.736366000 | -1.996945000 | -0.181732000 |
| 6 | -0.797498000 | 3.573270000 | -0.928467000 |
| 6 | -0.832202000 | -4.053849000 | -0.370531000 |
| 6 | -4.911734000 | -1.576049000 | -1.216037000 |
| 6 | -2.029968000 | -3.392512000 | -0.217746000 |
| 6 | -4.146389000 | -1.490876000 | -0.028625000 |
| 6 | -2.719859000 | -0.994258000 | -0.100053000 |
| 6 | -6.232212000 | -2.039688000 | -1.139445000 |
| 6 | -4.709860000 | -1.888964000 | 1.203091000 |
| 6 | -1.725191000 | 2.440040000 | -0.512615000 |
| 6 | 1.652550000 | -3.394734000 | -0.720510000 |
| 6 | -2.569190000 | 0.409763000 | -0.156354000 |
| 6 | -6.038240000 | -2.338541000 | 1.231313000 |
| 6 | -1.884126000 | 1.217346000 | 3.626782000 |
| 6 | -6.821332000 | -2.417515000 | 0.074095000 |
| 6 | 0.476496000 | 3.671266000 | -0.048977000 |
| 6 | 1.957819000 | -3.115987000 | -2.226457000 |
| 6 | 0.556315000 | 1.202025000 | 4.410521000 |
| 6 | 2.056970000 | 0.293994000 | 2.545109000 |
| 6 | -3.126754000 | 2.589186000 | -0.325378000 |
| 6 | 1.804453000 | 4.573461000 | -1.990677000 |
| 6 | -3.651883000 | 1.329298000 | -0.103285000 |
| 6 | 1.390860000 | 4.817924000 | -0.525183000 |
| 6 | 0.544901000 | 4.527519000 | -2.878399000 |
| 6 | 3.796451000 | 1.536933000 | 1.124603000 |
| 6 | -2.970719000 | 1.945994000 | 3.295677000 |
| 6 | -0.620369000 | 6.096885000 | -1.301284000 |
| 6 | -0.372744000 | 3.377029000 | -2.417240000 |
| 6 | 5.119265000 | 1.746669000 | 0.724302000 |
| 6 | 5.821797000 | -0.155989000 | 2.035706000 |
| 6 | 1.941486000 | 1.245226000 | 3.774744000 |
| 6 | 3.468019000 | 0.474227000 | 1.977388000 |
| 6 | -0.208268000 | 5.866968000 | -2.768685000 |
| 6 | 6.137759000 | 0.903047000 | 1.179373000 |
| 6 | 0.637132000 | 6.156287000 | -0.415541000 |
| 6 | -1.531193000 | 4.942009000 | -0.838169000 |
| 6 | -8.261565000 | -2.870923000 | 0.133006000 |
| 1 | -8.442422000 | -3.538932000 | 0.992936000 |
| 1 | -8.947897000 | -2.008271000 | 0.239103000 |

| | | | |
|---|---|---|---|
| 1 | -8.555924000 | -3.407951000 | -0.785701000 |
| 6 | -3.902374000 | -1.866806000 | 2.480538000 |
| 1 | -3.172777000 | -2.697387000 | 2.507919000 |
| 1 | -3.325478000 | -0.933175000 | 2.576753000 |
| 1 | -4.555997000 | -1.965226000 | 3.364015000 |
| 6 | -4.333037000 | -1.188784000 | -2.559117000 |
| 1 | -4.148299000 | -0.101232000 | -2.624021000 |
| 1 | -3.364481000 | -1.686231000 | -2.743335000 |
| 1 | -5.019803000 | -1.464496000 | -3.376966000 |
| 6 | 2.640479000 | -2.584138000 | 0.154569000 |
| 1 | 2.439585000 | -2.793332000 | 1.221920000 |
| 1 | 2.491198000 | -1.503880000 | 0.001148000 |
| 6 | 4.100413000 | -2.937694000 | -0.193602000 |
| 1 | 4.770895000 | -2.326732000 | 0.433162000 |
| 6 | 4.366484000 | -2.628784000 | -1.680791000 |
| 1 | 5.420245000 | -2.856945000 | -1.930328000 |
| 1 | 4.211215000 | -1.553153000 | -1.876937000 |
| 6 | 3.421149000 | -3.471683000 | -2.558629000 |
| 1 | 3.606757000 | -3.250641000 | -3.625579000 |
| 6 | 4.346631000 | -4.432810000 | 0.078098000 |
| 1 | 4.176860000 | -4.660956000 | 1.147862000 |
| 1 | 5.398453000 | -4.695682000 | -0.143324000 |
| 6 | 1.932897000 | -4.905239000 | -0.468128000 |
| 1 | 1.270512000 | -5.522062000 | -1.099550000 |
| 1 | 1.706469000 | -5.158363000 | 0.584520000 |
| 6 | 3.394640000 | -5.265552000 | -0.798381000 |
| 1 | 3.547482000 | -6.342277000 | -0.600178000 |
| 6 | 3.667980000 | -4.968158000 | -2.286250000 |
| 1 | 4.709901000 | -5.237832000 | -2.543131000 |
| 1 | 3.009050000 | -5.586976000 | -2.924747000 |
| 1 | 1.269628000 | -3.717566000 | -2.849149000 |
| 1 | 1.765019000 | -2.055601000 | -2.454911000 |
| 1 | -6.470307000 | -2.640539000 | 2.191860000 |
| 1 | -6.818008000 | -2.109239000 | -2.062725000 |
| 1 | -0.693002000 | -5.128938000 | -0.443320000 |
| 1 | -3.024065000 | -3.830317000 | -0.152302000 |
| 1 | -4.695331000 | 1.066682000 | 0.058849000 |
| 1 | -3.684337000 | 3.520891000 | -0.369706000 |
| 1 | -1.281494000 | 3.340943000 | -3.046930000 |
| 1 | 0.143086000 | 2.411075000 | -2.535006000 |
| 1 | 0.181078000 | 3.834962000 | 1.004190000 |
| 1 | 1.032445000 | 2.722252000 | -0.080412000 |
| 1 | -1.867203000 | 5.121490000 | 0.200301000 |
| 1 | -2.434524000 | 4.926760000 | -1.472750000 |
| 1 | -1.180751000 | 7.045833000 | -1.216511000 |
| 1 | -1.104182000 | 5.856220000 | -3.418017000 |

| | | | |
|---|---|---|---|
| 1 | 0.432621000 | 6.698279000 | -3.118566000 |
| 1 | 0.354517000 | 6.351041000 | 0.636639000 |
| 1 | 1.289506000 | 6.991564000 | -0.733086000 |
| 1 | 0.838686000 | 4.348696000 | -3.928659000 |
| 1 | 2.479375000 | 5.381257000 | -2.332057000 |
| 1 | 3.009667000 | 2.202317000 | 0.764720000 |
| 1 | 5.353934000 | 2.575226000 | 0.048947000 |
| 1 | 7.173041000 | 1.068465000 | 0.865220000 |
| 1 | 6.608887000 | -0.825137000 | 2.397666000 |
| 1 | 1.994142000 | -0.741725000 | 2.941347000 |
| 1 | 2.720741000 | 0.959371000 | 4.500864000 |
| 1 | 2.170929000 | 2.274478000 | 3.444921000 |
| 1 | 0.529099000 | 1.868464000 | 5.296368000 |
| 1 | 0.337638000 | 0.181615000 | 4.778542000 |
| 1 | -2.878051000 | 2.926651000 | 2.814793000 |
| 1 | -3.984481000 | 1.578157000 | 3.488436000 |
| 1 | -2.030743000 | 0.238237000 | 4.103284000 |
| 1 | 2.291911000 | 4.844137000 | 0.115111000 |
| 1 | 2.361936000 | 3.623573000 | -2.075395000 |
| 6 | -0.497262000 | 1.622723000 | 3.402477000 |
| 1 | -0.004850000 | 1.017726000 | 2.345309000 |
| 1 | -0.398260000 | 2.673514000 | 3.084334000 |
| 6 | 4.495723000 | -0.368269000 | 2.426506000 |
| 1 | 4.255665000 | -1.202515000 | 3.094434000 |

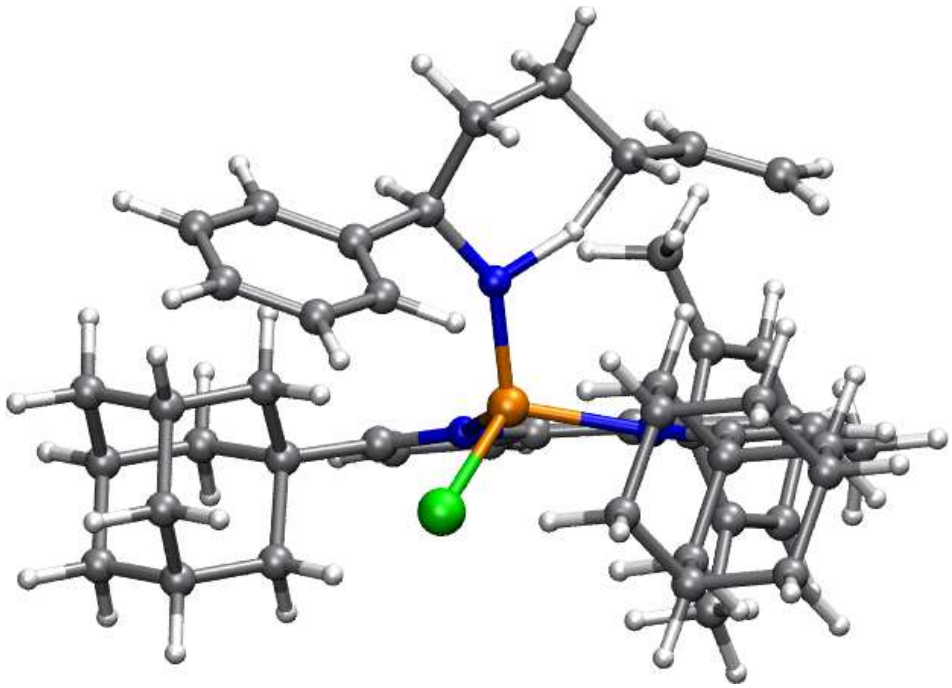

**Figure 5.17** Geometry optimized structure for the TS_*anti* configuration

**Table 5.11** Optimized geometry coordinates for ($^{Ad}$L)FeCl(NHR$^{\bullet}$) amide intermediate

| | | | |
|---|---|---|---|
| 26 | -0.410367000 | 0.211944000 | -0.273438000 |
| 17 | -1.980813000 | 0.378896000 | -1.905728000 |
| 7 | 1.107832000 | 1.625586000 | -0.321412000 |
| 7 | -1.201779000 | -0.122845000 | 1.562388000 |
| 7 | 0.812636000 | -1.509308000 | -0.429757000 |
| 6 | 1.140884000 | 2.971892000 | -0.466429000 |
| 6 | 2.437965000 | 1.195778000 | -0.186764000 |
| 6 | -0.699417000 | -3.491950000 | -1.008096000 |
| 6 | 2.486000000 | 3.440157000 | -0.403895000 |
| 6 | 5.139858000 | -0.530126000 | -1.155651000 |
| 6 | 3.294439000 | 2.335599000 | -0.232174000 |
| 6 | 4.402147000 | -0.285570000 | 0.024489000 |
| 6 | 2.899834000 | -0.133065000 | -0.072636000 |
| 6 | 6.533522000 | -0.671260000 | -1.070979000 |
| 6 | 5.074575000 | -0.174490000 | 1.263100000 |
| 6 | 0.589144000 | -2.838829000 | -0.522995000 |
| 6 | -0.055940000 | 3.868781000 | -0.742701000 |
| 6 | 2.174403000 | -1.343310000 | -0.126958000 |
| 6 | 6.466728000 | -0.327295000 | 1.299514000 |
| 6 | 0.511844000 | -1.576899000 | 4.078242000 |
| 6 | 7.219119000 | -0.578622000 | 0.144584000 |
| 6 | -1.951082000 | -3.039122000 | -0.209644000 |
| 6 | -0.463184000 | 3.759217000 | -2.245475000 |
| 6 | -0.364704000 | 0.819692000 | 4.180904000 |
| 6 | -2.166238000 | 0.625222000 | 2.363593000 |
| 6 | 1.785437000 | -3.562919000 | -0.223447000 |
| 6 | -3.420822000 | -3.347056000 | -2.228629000 |
| 6 | 2.774055000 | -2.632257000 | 0.017047000 |
| 6 | -3.228332000 | -3.719136000 | -0.744266000 |
| 6 | -2.204598000 | -3.834915000 | -3.041098000 |
| 6 | -4.057241000 | -1.107690000 | 2.399304000 |
| 6 | 1.305637000 | -2.580210000 | 3.595511000 |
| 6 | -1.881213000 | -5.723460000 | -1.416383000 |
| 6 | 0.538678000 | -0.234965000 | 3.623429000 |
| 6 | -0.923668000 | -3.155163000 | -2.514635000 |
| 6 | -5.374931000 | -1.492520000 | 2.136835000 |
| 6 | -5.829914000 | 0.696896000 | 1.221443000 |
| 6 | -1.852552000 | 0.544143000 | 3.881418000 |
| 6 | -3.607053000 | 0.184315000 | 2.078783000 |
| 6 | -4.508712000 | 1.076788000 | 1.481232000 |
| 6 | -2.077122000 | -5.363786000 | -2.902529000 |
| 6 | -6.267629000 | -0.589115000 | 1.548830000 |
| 6 | -3.099379000 | -5.246482000 | -0.604341000 |
| 6 | -0.604678000 | -5.039160000 | -0.888820000 |
| 6 | 8.720923000 | -0.730322000 | 0.218696000 |

| | | | |
|---|---|---|---|
| 1 | 9.205339000 | 0.213265000 | 0.533636000 |
| 1 | 9.013560000 | -1.502584000 | 0.953615000 |
| 1 | 9.148263000 | -1.014680000 | -0.757612000 |
| 6 | 4.325372000 | 0.094704000 | 2.548549000 |
| 1 | 3.691448000 | 0.994502000 | 2.468449000 |
| 1 | 3.662403000 | -0.747275000 | 2.813928000 |
| 1 | 5.023913000 | 0.243838000 | 3.388613000 |
| 6 | 4.460631000 | -0.635898000 | -2.502914000 |
| 1 | 3.820267000 | -1.534103000 | -2.564569000 |
| 1 | 3.807390000 | 0.232656000 | -2.697489000 |
| 1 | 5.204746000 | -0.693134000 | -3.314932000 |
| 6 | -1.284335000 | 3.510259000 | 0.130610000 |
| 1 | -1.009592000 | 3.595193000 | 1.199625000 |
| 1 | -1.584503000 | 2.465711000 | -0.059726000 |
| 6 | -2.478440000 | 4.433598000 | -0.186895000 |
| 1 | -3.337131000 | 4.142652000 | 0.447119000 |
| 6 | -2.860964000 | 4.283438000 | -1.673430000 |
| 1 | -3.731632000 | 4.926532000 | -1.904566000 |
| 1 | -3.155862000 | 3.240455000 | -1.885737000 |
| 6 | -1.659824000 | 4.683218000 | -2.553463000 |
| 1 | -1.929962000 | 4.572483000 | -3.619227000 |
| 6 | -2.093847000 | 5.895018000 | 0.107847000 |
| 1 | -1.836322000 | 6.015956000 | 1.177646000 |
| 1 | -2.951137000 | 6.564608000 | -0.094628000 |
| 6 | 0.299511000 | 5.357780000 | -0.467517000 |
| 1 | 1.151734000 | 5.662091000 | -1.099077000 |
| 1 | 0.617562000 | 5.480258000 | 0.584945000 |
| 6 | -0.893764000 | 6.284161000 | -0.774166000 |
| 1 | -0.598203000 | 7.327765000 | -0.560898000 |
| 6 | -1.277268000 | 6.146740000 | -2.261188000 |
| 1 | -2.122209000 | 6.820113000 | -2.500198000 |
| 1 | -0.429098000 | 6.455511000 | -2.901211000 |
| 1 | 0.403557000 | 4.039037000 | -2.872504000 |
| 1 | -0.719831000 | 2.714825000 | -2.485709000 |
| 1 | 6.979386000 | -0.245648000 | 2.264562000 |
| 1 | 7.098312000 | -0.859045000 | -1.990403000 |
| 1 | 2.813031000 | 4.473608000 | -0.485326000 |
| 1 | 4.379958000 | 2.317497000 | -0.158403000 |
| 1 | 3.820084000 | -2.823538000 | 0.249580000 |
| 1 | 1.899392000 | -4.643675000 | -0.215078000 |
| 1 | -0.046405000 | -3.499898000 | -3.093477000 |
| 1 | -0.994518000 | -2.063509000 | -2.645407000 |
| 1 | -1.810903000 | -3.290869000 | 0.860645000 |
| 1 | -2.074854000 | -1.947641000 | -0.287216000 |
| 1 | -0.433257000 | -5.324731000 | 0.166143000 |
| 1 | 0.261303000 | -5.405897000 | -1.467209000 |

| | | | |
|---|---|---|---|
| 1 | -1.767733000 | -6.818030000 | -1.310260000 |
| 1 | -1.220051000 | -5.732012000 | -3.497847000 |
| 1 | -2.982160000 | -5.862437000 | -3.298603000 |
| 1 | -2.980422000 | -5.526033000 | 0.460445000 |
| 1 | -4.019216000 | -5.744072000 | -0.966403000 |
| 1 | -2.338179000 | -3.565677000 | -4.104657000 |
| 1 | -4.347215000 | -3.812675000 | -2.616295000 |
| 1 | -3.376198000 | -1.832909000 | 2.858272000 |
| 1 | -5.705994000 | -2.503808000 | 2.393784000 |
| 1 | -7.299261000 | -0.890424000 | 1.341567000 |
| 1 | -6.515989000 | 1.409661000 | 0.753192000 |
| 1 | -2.073932000 | 1.680032000 | 2.066126000 |
| 1 | -2.495211000 | 1.267484000 | 4.415488000 |
| 1 | -2.126630000 | -0.456433000 | 4.261330000 |
| 1 | -0.248430000 | 0.864846000 | 5.283158000 |
| 1 | -0.081287000 | 1.809844000 | 3.786545000 |
| 1 | 2.003661000 | -2.411980000 | 2.767882000 |
| 1 | 1.240472000 | -3.595193000 | 4.000129000 |
| 1 | -0.202224000 | -1.822401000 | 4.876619000 |
| 1 | 1.327535000 | 0.060902000 | 2.927045000 |
| 1 | -1.279194000 | -1.128722000 | 1.767537000 |
| 1 | -4.092945000 | -3.358354000 | -0.158011000 |
| 1 | -3.533405000 | -2.253500000 | -2.332698000 |
| 1 | -4.172807000 | 2.082942000 | 1.210937000 |

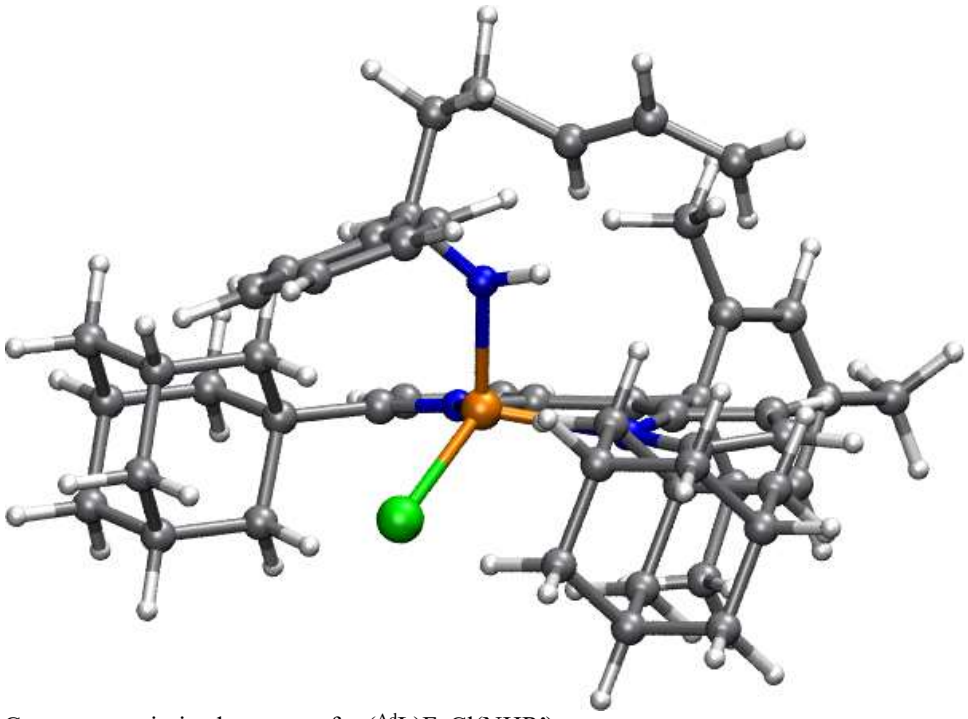

**Figure 5.18.** Geometry optimized structure for ($^{Ad}$L)FeCl(NHR$^{\bullet}$)

**Table 5.12** Optimized geometry coordinates for (**1b**)[2-phenyl-5-vinylpyrrolidine]

| | | | |
|---|---|---|---|
| 26 | -0.282451000 | 0.318862000 | -0.418901000 |
| 17 | -1.840969000 | 0.902688000 | -1.969468000 |
| 7 | 1.498010000 | 1.345152000 | -0.301769000 |
| 7 | -1.104910000 | 0.133679000 | 1.669370000 |
| 7 | 0.461872000 | -1.638374000 | -0.518003000 |
| 6 | 1.857269000 | 2.651956000 | -0.360509000 |
| 6 | 2.676373000 | 0.602990000 | -0.112846000 |
| 6 | -1.494441000 | -3.187680000 | -1.094402000 |
| 6 | -0.318078000 | 5.048146000 | -2.518134000 |
| 6 | 3.263620000 | 2.780702000 | -0.180802000 |
| 6 | 4.998471000 | -1.618604000 | -1.019128000 |
| 6 | 3.774564000 | 1.506941000 | -0.027529000 |
| 6 | 4.220465000 | -1.306431000 | 0.120135000 |
| 6 | 2.806240000 | -0.803578000 | -0.065210000 |
| 6 | 6.310962000 | -2.076226000 | -0.839918000 |
| 6 | 4.772047000 | -1.449665000 | 1.411832000 |
| 6 | 4.443294000 | -1.460545000 | -2.417072000 |
| 6 | -1.638965000 | 4.905601000 | -1.735910000 |
| 6 | -0.411468000 | 3.717326000 | 0.110518000 |
| 6 | -0.068008000 | -2.872535000 | -0.661617000 |
| 6 | 0.925132000 | 3.814530000 | -0.663924000 |
| 6 | -1.339719000 | 4.902395000 | -0.223308000 |
| 6 | 1.827163000 | -1.807365000 | -0.222433000 |
| 6 | 6.089276000 | -1.914971000 | 1.541564000 |
| 6 | -0.359952000 | -1.334609000 | 3.557062000 |
| 6 | 6.877054000 | -2.238137000 | 0.431087000 |
| 6 | -2.558200000 | -2.384585000 | -0.300434000 |
| 6 | 0.607534000 | 3.857538000 | -2.191256000 |
| 6 | -0.022405000 | 1.190161000 | 3.506572000 |
| 6 | -2.057670000 | 1.198438000 | 2.187298000 |
| 6 | 0.931970000 | -3.868028000 | -0.427915000 |
| 6 | 0.666474000 | 6.356114000 | -0.610188000 |
| 6 | 1.592184000 | 5.167013000 | -0.285683000 |
| 6 | -4.126936000 | -2.404114000 | -2.267406000 |
| 6 | 2.109351000 | -3.206879000 | -0.155147000 |
| 6 | 0.369629000 | 6.369193000 | -2.122852000 |
| 6 | -3.986570000 | -2.732649000 | -0.767634000 |
| 6 | -3.106748000 | -3.233880000 | -3.071879000 |
| 6 | 8.283230000 | -2.766909000 | 0.594798000 |
| 6 | 3.978166000 | -1.107597000 | 2.652843000 |
| 6 | -0.651444000 | 6.220582000 | 0.175159000 |
| 6 | -4.041789000 | -0.194340000 | 3.012164000 |
| 6 | 0.157290000 | -2.553026000 | 3.358952000 |
| 6 | -3.227759000 | -5.052286000 | -1.341421000 |
| 6 | -0.039049000 | -0.124848000 | 2.711415000 |

| | | | |
|---|---|---|---|
| 6 | -1.676504000 | -2.879119000 | -2.612956000 |
| 6 | -5.381983000 | -0.581227000 | 2.930134000 |
| 6 | -5.704577000 | 0.935539000 | 1.076673000 |
| 6 | -1.503656000 | 1.583237000 | 3.576076000 |
| 6 | -3.511861000 | 0.764931000 | 2.131046000 |
| 6 | -4.361606000 | 1.317753000 | 1.159848000 |
| 6 | -3.373659000 | -4.734328000 | -2.842272000 |
| 6 | -6.219720000 | -0.014247000 | 1.963003000 |
| 6 | -4.251307000 | -4.231138000 | -0.536021000 |
| 6 | -1.798833000 | -4.698628000 | -0.886191000 |
| 1 | 8.950670000 | -2.398039000 | -0.203911000 |
| 1 | 8.717020000 | -2.472422000 | 1.565963000 |
| 1 | 8.303033000 | -3.873129000 | 0.548444000 |
| 1 | 4.072212000 | -0.435288000 | -2.592646000 |
| 1 | 3.590762000 | -2.140467000 | -2.593213000 |
| 1 | 6.511681000 | -2.023286000 | 2.546609000 |
| 1 | 6.910720000 | -2.310635000 | -1.726396000 |
| 1 | 4.573911000 | -1.285027000 | 3.563818000 |
| 1 | 3.059288000 | -1.714707000 | 2.729429000 |
| 1 | 3.663861000 | -0.048613000 | 2.654064000 |
| 1 | 4.815938000 | 1.227350000 | 0.118924000 |
| 1 | 3.829750000 | 3.708637000 | -0.175486000 |
| 1 | 1.852697000 | 5.168124000 | 0.789307000 |
| 1 | 2.535062000 | 5.290792000 | -0.845796000 |
| 1 | 1.555007000 | 3.945683000 | -2.754253000 |
| 1 | -0.926240000 | 2.780897000 | -0.160220000 |
| 1 | -0.204237000 | 3.691110000 | 1.196885000 |
| 1 | 0.129705000 | 2.912206000 | -2.497950000 |
| 1 | -2.150571000 | 3.970190000 | -2.023688000 |
| 1 | -2.318711000 | 5.742914000 | -1.983576000 |
| 1 | -2.283498000 | 4.788246000 | 0.341602000 |
| 1 | -1.314960000 | 7.079227000 | -0.039882000 |
| 1 | -0.449425000 | 6.234100000 | 1.263315000 |
| 1 | -0.279194000 | 7.228842000 | -2.376084000 |
| 1 | 1.176494000 | 7.293496000 | -0.322422000 |
| 1 | 1.309718000 | 6.496492000 | -2.692335000 |
| 1 | -0.529202000 | 5.047188000 | -3.602740000 |
| 1 | -1.473081000 | -1.812090000 | -2.801771000 |
| 1 | -2.453493000 | -2.608113000 | 0.778787000 |
| 1 | -2.400836000 | -1.304478000 | -0.449202000 |
| 1 | -1.663093000 | -4.964987000 | 0.178677000 |
| 1 | -1.083226000 | -5.307886000 | -1.465041000 |
| 1 | -0.936151000 | -3.462830000 | -3.191005000 |
| 1 | -3.398092000 | -6.131195000 | -1.171418000 |
| 1 | -2.662132000 | -5.344532000 | -3.430453000 |
| 1 | -4.389472000 | -4.999790000 | -3.191480000 |

| | | | |
|---|---|---|---|
| 1 | -3.203059000 | -2.997867000 | -4.147198000 |
| 1 | -5.280528000 | -4.491891000 | -0.847340000 |
| 1 | -4.170321000 | -4.472005000 | 0.541318000 |
| 1 | -4.705493000 | -2.129066000 | -0.185615000 |
| 1 | -3.956955000 | -1.326138000 | -2.435502000 |
| 1 | -5.154713000 | -2.632670000 | -2.608504000 |
| 1 | 0.790761000 | -4.944707000 | -0.469753000 |
| 1 | 5.214524000 | -1.679054000 | -3.174492000 |
| 1 | 3.080319000 | -3.647812000 | 0.061770000 |
| 1 | -3.405200000 | -0.653716000 | 3.774475000 |
| 1 | -5.774773000 | -1.328179000 | 3.627137000 |
| 1 | -7.270067000 | -0.315348000 | 1.899970000 |
| 1 | -6.347255000 | 1.379645000 | 0.310418000 |
| 1 | -3.962238000 | 2.047659000 | 0.449362000 |
| 1 | -1.950953000 | 2.063128000 | 1.521612000 |
| 1 | -2.017233000 | 1.023023000 | 4.375270000 |
| 1 | -1.656740000 | 2.654478000 | 3.786012000 |
| 1 | 0.554369000 | 1.948692000 | 2.949396000 |
| 1 | 0.445956000 | 1.071420000 | 4.497593000 |
| 1 | 0.915878000 | -0.298155000 | 2.194654000 |
| 1 | -1.077798000 | -1.187861000 | 4.376427000 |
| 1 | 0.867451000 | -2.754129000 | 2.546489000 |
| 1 | -0.122827000 | -3.399896000 | 3.996709000 |
| 1 | -1.628717000 | -0.734310000 | 1.523036000 |

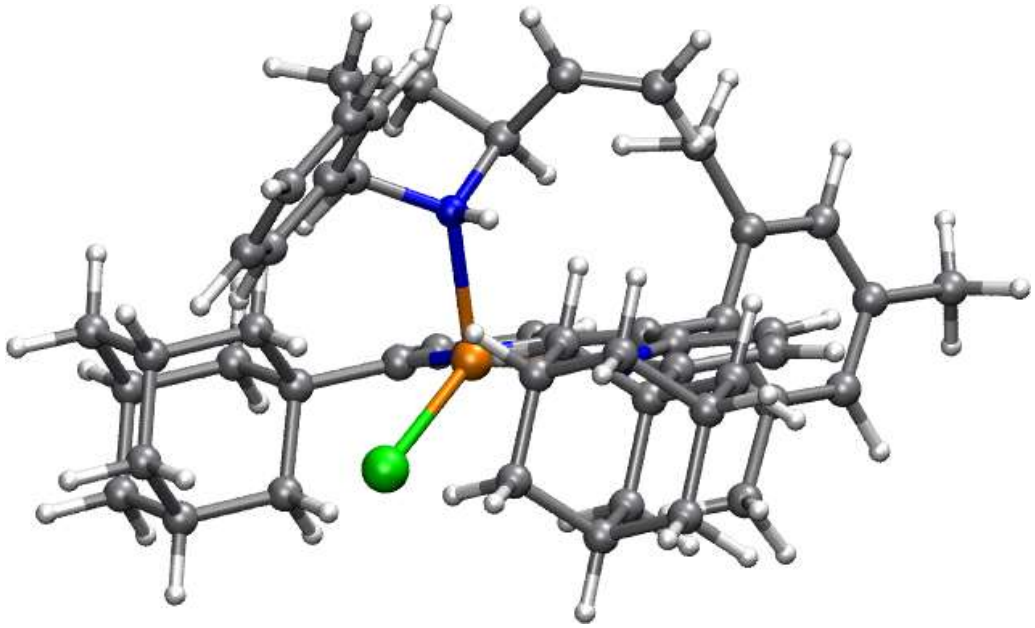

**Figure 5.19** Geometry optimized structure for (**1b**)[2-phenyl-5-vinylpyrrolidine]

**Table 5.13** Final energies from optimized geometries

| Species | Final energy (Hartrees) |
|---|---|
| ($^{Ad}$L)FeCl($OEt_2$) (**1b**) | -3541.17319195 |
| $Et_2O$ | -233.46917586 |
| $N_2$ | -109.43922207 |
| 1-azido-1-phenyl-4-vinylbutane | -629.98534136 |
| ($^{Ad}$L)FeCl(•NR) | -3828.31147095 |
| TS_*syn* | -3828.29297211 |
| TS_*anti* | -3828.29148671 |
| ($^{Ad}$L)FeCl(NHR•) | -3828.31328788 |
| (**1b**)[2-phenyl-5-vinylpyrrolidine] | -3828.38982901 |

.